The Oriented-Eddy Collision Model

THE ORIENTED-EDDY COLLISION MODEL

A Dissertation Presented

by

MICHAEL B MARTELL JR

Submitted to the Graduate School of the
University of Massachusetts Amherst in partial fulfillment
of the requirements for the degree of

DOCTOR OF PHILOSOPHY

May 2012

Mechanical and Industrial Engineering

THE ORIENTED-EDDY COLLISION MODEL

A Dissertation Presented

by

MICHAEL B MARTELL JR

Approved as to style and content by:

J. Blair Perot, Chair

Stephen M. de Bruyn Kops, Member

David M. Ford, Member

Donald Fisher, Department Head
Mechanical and Industrial Engineering

"I am an old man now, and when I die and go to heaven there are two matters on which I hope for enlightenment. One is quantum electrodynamics, and the other is the turbulent motion of fluids. And about the former I am rather optimistic." Sir Horace Lamb

ACKNOWLEDGMENTS

Thank you to Blair Perot for his endless patience, guidance and support. Thank you to my family for pushing me up the ladder. Thank you to my wife Amy for her kindness and understanding. Thank you to my coworkers in the CFD lab, past and present, for their help and friendship. Thank you to Profs. Ford, de Bruyn Kops, and Schmidt for their time and helpful input. Finally, the author would like to acknowledge the Office of Naval Research for their support under grant N00014-08-1-0275 and the National Science Foundation.

Written in LaTeX 2_ε

ABSTRACT

THE ORIENTED-EDDY COLLISION MODEL

MAY 2012

MICHAEL B MARTELL JR

B.S., NORWICH UNIVERSITY

M.S., UNIVERSITY OF MASSACHUSETTS AMHERST

Ph.D., UNIVERSITY OF MASSACHUSETTS AMHERST

Directed by: Professor J. Blair Perot

The physical and mathematical foundations of the Oriented-Eddy Collision turbulence model are provided through a discussion of the Reynolds averaged Navier-Stokes (RANS) equations, probability density functions (PDF), PDF collision models, Reynolds stress transport models (RSTM), and two-point correlations. Behavior of the Oriented-Eddy Collision turbulence model near solid boundaries is examined in depth. The Oriented-Eddy Collision turbulence model treats turbulence in a novel way: the average behavior of a turbulent flow can be modeled as a collection of interacting fluid particles, or eddies, which have inherent orientation. The model is cast in the form of a collection of Reynolds stress transport models. Underlying this approach is a unique PDF collision model that departs from more common PDF methods as it includes orientation information along with the usual position and velocity information. This adds important physics and differentiates it from other PDF collision treatments that return RANS-type models.

To operate in physical space, the model is cast as a unique decomposition to the two-point velocity correlation transport equation. The Oriented-Eddy Collision turbulence model accurately captures fast pressure-strain in rapid distortion, which is a major shortcoming of nearly all Reynolds stress transport models. The Oriented-Eddy Collision turbulence model contains no special provisions to satisfy realizability, and maintains frame and coordinate invariance. Models to account for turbulent dissipation, diffusion, and system rotation are presented with canonical benchmark flows for validation. Inhomogeneous, anisotropic cases are also considered. Model to capture non-local pressure effects near solid boundaries are proposed in the form of turbulent eddy reorientation schemes with associated Reynolds stress treatments. These schemes aim to capture the asymptotic approach of the Reynolds stress components and basic turbulent, wall-bounded flows are investigated as a means of validation. Boundary conditions for solid and shear-free surfaces are discussed and several alternatives to the standard viscous diffusion model proposed.

TABLE OF CONTENTS

LIST OF TABLES

Table **Page**

LIST OF FIGURES

Figure **Page**

CHAPTER 1

INTRODUCTION

Capturing the behavior of turbulent flows is both a challenge and a necessity. Hundreds of methods have been devised. Those based on Reynolds decomposition of the Navier-Stokes equations (the Reynolds averaged Navier-Stokes, or RANS, equations [70]) include zero-equation (so-called algebraic) models like Prandtl's mixing length model [67, 68] and the Cebeci-Smith [71] and Baldwin-Lomax [4] models, and one-equation arrangements like the popular Spalart-Allmaras model [89] which is used heavily in aeronautical flows. Two-equation models exist, such as the widely-used $K - \epsilon$ [17, 29] and $K - \omega$ [17, 105, 104] models, and those proposed by Kolmogorov [91, 32]. Following two-equation models are non-linear eddy viscosity models such as the cubic $K - \epsilon$ model [11] and the $\overline{v^2} - f$ model [16]. Other RANS-based models include the relatively new and complex Reynolds stress transport (RST) models, first proposed by Rotta in 1951 [79], as well as others, such as hybrid Reynolds averaged Navier-Stokes / large eddy simulation models [20, 58] and probability density function based methods [63, 64, 65, 66, 42, 100]. The most accurate methods are computationally costly for many flows of interest, while faster methods often fail to capture important physics or are unphysical in their predictions. All are subject to certain restrictions such as realizability which can lend to a model's complexity. Direct numerical simulation of turbulent flows at the Reynolds numbers and scales that interest most engineers are only now becoming feasible with current state-of-the-art facilities. Such simulations are only computationally efficient for simple flows. As

such, researchers must often rely upon experiment or turbulence models to answer their questions about the nature of such flows.

Many mathematicians, scientists, engineers, and physicists have attempted to describe turbulent flows through various intuitions, simplifications, assumptions, tricks, omissions, and ideas from other areas of research. Few have achieved models which are predictive outside of specific flow regimes. The first models were based on physical intuition and careful observation. Osborne Reynolds' landmark 1895 paper [70] paved the way for nearly all modern turbulence models by introducing the then-novel concept of decomposing pressure and velocity into mean and fluctuating components. Taylor [96, 97] did pioneering work on describing turbulence using statistics, along with Rotta's work published in 1951 [79]. Many of the first turbulence models were based on the hypothesis of eddy viscosity, which is physically incorrect and can lead to inaccurate predictions of turbulent flows. A discussion of this is deferred to §D.1. Models which use transport equations for the turbulent kinetic energy and length scales can be better, but have difficulty solving the evolution of turbulent flows in curvilinear domains or limits such as those described by rapid distortion theory. Rotta [79] proposed the first model which attempted to explain the behavior of the *Reynolds stress tensor*, which is a quantity that results from performing Reynolds averaging on the Navier-Stokes equations (see §1.2.1). At the time (the early 1950s) the idea was considered both brilliant and intractable (for practical flows, at least) as the method introduced further equations to be solved (the components of the Reynolds stress tensor) and greatly increased the cost of solving turbulent flow problems.

1.1 Turbulence

Before any turbulence modeling is discussed, it is necessary to understand the basic physical nature of turbulence and some observations that have been made about its behavior. Although this is by no means an exhaustive survey of turbulent flow

physics, it is instructive to introduce a few concepts. Many more complete reviews of turbulence can be found in books by Pope [66], Durbin [17], Tennekes and Lumley [98] and others. Turbulence is irregular fluid flow which is characterized by numerous disparate length and time scales, as well as chaotic fluctuations inherent to it. Turbulence develops from instabilities present in the flow, usually emanating from the regions of flow close to objects or boundaries. Coherent structures exist in turbulence, and are often called eddies, vortices, bursts, patches, streaks, and other imaginative but descriptive names. Figure 1.1(a) illustrates the type of structures present in tur-

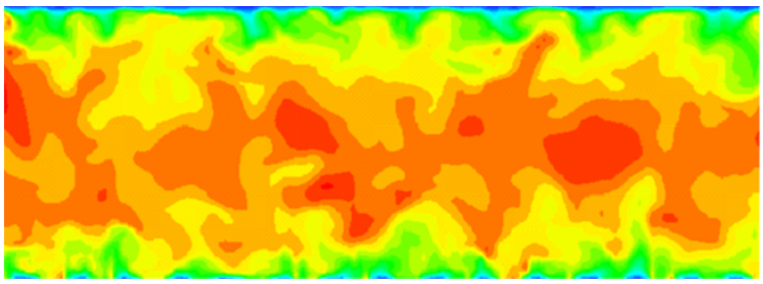

(a) A snapshot in time.

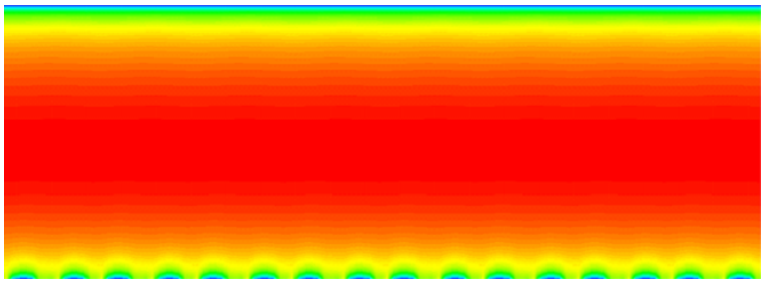

(b) A time average of Figure 1.1(a).

Figure 1.1. Results from direct numerical simulation of turbulent channel flow over streamwise ridges, adapted from Martell [45].

bulent flows, in this case turbulent channel flow over an array of streamwise ridges from a direct numerical simulation running at a fairly low Reynolds number (see [44]). Non-uniform regions of high and low velocity are present, with certain structures seeming to grow outward from solid boundaries. Patches, streaks, and other vaguely similar features populate the flow. It is difficult to exactly describe the na-

ture of Figure 1.1(a), except perhaps to say it is chaotic or, of course, turbulent. The contours are colored by streamwise velocity (in this case going into the page). The top of the domain is bounded by a uniform solid wall while the bottom of the domain has regions of solid boundaries (so-called *no-slip* boundary conditions where all fluid motion comes to rest save for molecular motion) and regions of *shear-free* boundaries which damp only wall-normal velocity. Figure 1.1(b), the time-averaged version of Figure 1.1(a), is much easier to understand: The time-averaged velocity peaks near the channel's center, while it tends to zero near the top wall. Although surely not a complete characterization of even the average behavior, looking at a turbulent flow in such a way makes a description practical, is often employed in modeling efforts, and served as partial inspiration for Reynolds' averaging technique.

Turbulence is strongly rotational, fully three dimensional, and varies in time [66, 17, 105]. Another important aspect of turbulence is its unpredictability. Wilcox [105] explains this tenet of turbulence by example: Suppose one were to observe a turbulent flow's evolution for a fixed amount of time, perhaps by inspecting the results of a simulation with a given set of initial conditions (using a method which presumably captured the physics of the process properly, such as direct numerical simulation, discussed in §1.2.4). Then suppose a second identical simulation was performed (a second *realization*), except the initial conditions were perturbed slightly. One might expect nearly identical results after the same fixed observation period. This, however, is not the case - the flow may (or may not) evolve in a drastically different manner. This result, of course, is referring to the *instantaneous* flow field and not the statistics of the flow field. This is a very important distinction to make, as the statistics of the turbulence will tend to evolve in the same manner (otherwise turbulence modeling would be a lost cause). Interestingly, this is true even of unsteady flows. Turbulence is fundamentally a characteristic of fluid *flows* and not of fluid itself. Turbulence is the result of highly complex non-linear interactions between the viscous and non-

linear inertial terms in the Navier-Stokes equations which come from the fully three-dimensional vortical structure interactions found in any truly turbulent flow [98].

One of the most important and studied aspects of turbulent flows is the energy cascade mechanism, first introduced by Richardson in 1922 [77]. The energy cascade is responsible for transferring energy from the largest and most energetic turbulent structures present in the flow downward to the smallest scales where viscosity dominates and acts to dissipate energy [98, 66, 17, 105]. Note that there needn't be a "mean flow" present. Richardson hypothesized that the rate at which energy was dissipated, ϵ, was dictated by the rate at which it was transferred to the flow, and thus governed by the largest eddies in the flow, $\epsilon \sim u_0^3/L_0$. The largest eddies are often comparable to the macroscopic scale of the flow (say, the channel height) and are given characteristic length, velocity, and time scales of L_0, u_0 and $t_0 = L_0/u_0$ respectively. Note that a large eddy may contain many other eddies with length scales smaller than its own [66]. The smallest scales were investigated and characterized by Kolmogorov, and are dictated by the viscosity. Figure 1.2 shows a schematic representation of the structural hierarchy thought to be present in a turbulent flow. The large scale structures are created by shear present in the flow and "add" energy to the cascade. Small structures are dissipated by viscosity and "take energy away" from the cascade. Kolmogorov formed three hypotheses concerning the characterization of the smallest turbulent scales, which must similarly govern (or be governed by) the rate at which energy is transferred into, and dissipated out of, the smallest turbulent scales. Kolmogorov's first hypothesis states that at high Reynolds numbers, the smallest length scales are much smaller than the largest, $L << L_0$, thus the small scale turbulent structures are statistically isotropic [66]. The second claims that the flow statistics below a finite length scale are solely dependent on the kinematic viscosity ν and dissipation ϵ. From this, single length, time, and velocity scales can be formed, namely the Kolmogorov length scale $\eta = (\nu^3/\epsilon)^{1/4}$, the Kolmogorov

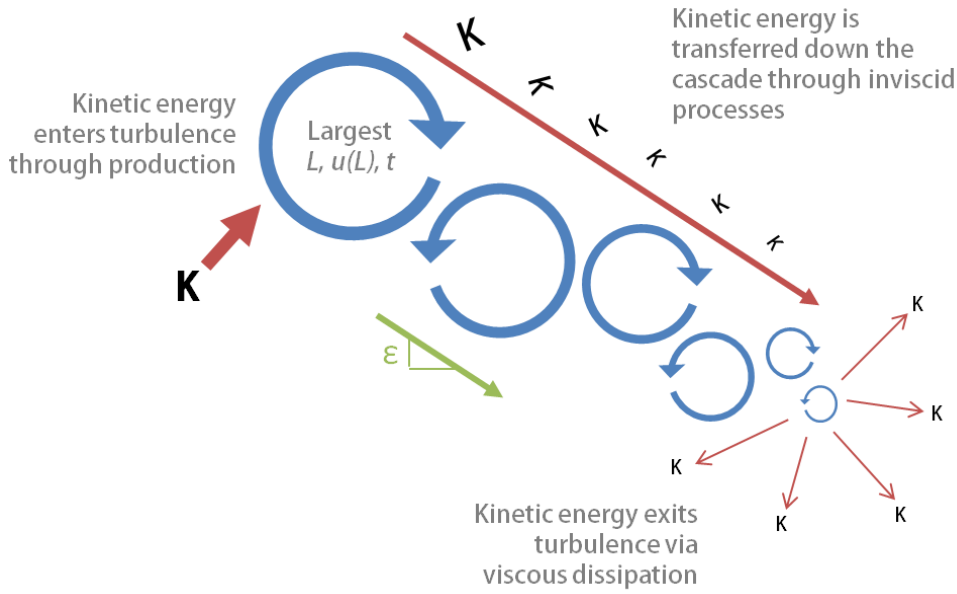

Figure 1.2. A schematic diagram of the eddy sizes present in a turbulent flow, along with the length scales proposed by Richardson and Kolmogorov. Modern interpretations of turbulence reveal this to be an oversimplified view of the energy cascade mechanism in turbulence.

velocity scale $u_\eta = (\epsilon\nu)^{1/4}$, and the time scale $t_\eta = (\nu/\epsilon)^{1/2}$. From this conclusion Kolmogorov further supposed that three length scale regimes existed at sufficiently high Reynolds numbers, implying that $L_0 >> L >> \eta$ and, more importantly, that this intermediate range of length scales (the *inertial subrange*) was characterized by the dissipation ϵ alone and not affected by the viscosity [66]. This lack of dependence on viscosity led Kolmogorov to conclude that dissipation mustn't occur within this subset of turbulent structures.

In between the largest and smallest turbulent scales, a mechanism exists to transfer energy between various size structures down the cascade. This cascade is continuous, and constitutes an energy spectrum present in the flow. Often, the concept of a turbulent eddy is employed to visualize this and understand the phenomenon more easily. Eddies of all sizes populate turbulent flows, the largest of which are affected by the mean flow and the smallest of which are affected by viscous dissipa-

tion. Operating under the hypothesis that a spectrum of energy across a range of lengthscales (eddy sizes) exists, turbulence is often visualized in wave space, that is the energy is represented as a function of wave number, which has units of inverse length where the length can be considered the size of a representative turbulent eddy. Keeping this in mind, energy at the highest wavenumbers very roughly corresponds to that contained within the *smallest* eddies, while energy at the lowest wavenumbers is contained within the *largest* eddies. Characterizing the way in which energy is distributed throughout this spectrum, specifically through the inertial subrange, was a task tackled originally by Kolmogorov [17]. Kolmogorov already believed that the largest structures in the flow could not depend upon viscosity, and the smallest could not depend on the flow geometry, leaving the inertial subrange, common to both the large and small scale ranges, to be governed by the dissipation alone. Using this reasoning and applying dimensional analysis, Kolmogorov concluded that the energy of an eddy in this range must be of order $(\epsilon L)^{2/3}$ with L the eddy size. This became Kolmogorov's law, stating that the energy of an eddy in the inertial subrange increases with their length by $L^{2/3}$. When translated into Fourier (wave) space, this exponent becomes -5/3 [66, 17]. Figure 1.3 illustrates this concept, and introduces three common families of turbulence models, Reynolds averaged Navier-Stokes (RANS), Large-eddy simulation (LES), and direct numerical simulation (DNS). While useful in understanding the role of kinetic energy in turbulence, modern interpretations of turbulence reveal a more complex dissipation mechanism. Figure 1.3, portions of which were adapted from the work of Perot and Gadebusch [20, 58], contains a few new concepts. First, the shape of the energy curve $E(\kappa)$, with wavenumber κ: The majority of the energy in a turbulent flow is contained within the largest eddies (at the smallest wavenumbers), shown by the peak. As the wavenumber increases and eddy size decreases, the energy decreases. In homogeneous isotropic turbulence a region exists where $E(\kappa)$ appears linear on the log-log plot with a slope of approx-

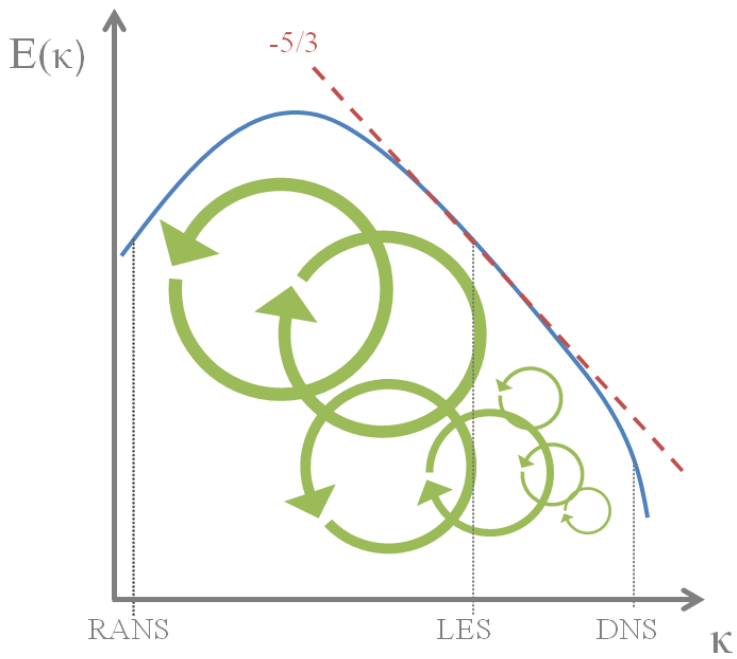

Figure 1.3. A log-log schematic representation of the energy spectrum $E(\kappa)$ as a function of wavenumber κ typically present in a turbulent flow. The locations of minimum scales at which RANS, LES, and DNS are able to resolve adapted from [20].

imately -5/3, which was expected. This region, often called the *inertial subrange*, was investigated by Kolmogorov [17, 32] and forms the basis for the concept of a turbulent energy cascade. It is within this region that the energy transfer mechanism - the cascade - exists. Energy is not being added to the spectrum through shear, nor is it being taken away through dissipation. It is simply being handed off, from one scale eddy to another, down to the smallest scales. Another way to think of this is that eddies in this range are not affected by eddies outside of this range, larger or smaller [17]. Although the size, nature, and associated decay exponent of this region are not universally agreed upon, its presence and importance to turbulent physics are. Furthermore, mounting evidence suggests that this is an overly-simplistic view of the structures present in a turbulent flow, and that in fact eddies within the inertial subrange are surely affected by those outside of this range. Figure 1.3 contains three

labels along the κ axis. These labels denote the extent to which the energy cascade, and thus the physics of a turbulent flow, are modeled. For example, methods which employ the Reynolds averaged Navier-Stokes equations (discussed in §1.2.1) model all scales to the right of the label, that is to say they model the entire spectrum. Large-eddy simulations (LES) resolve (*i.e.* solve for) the larger scales (to the left of the label) while relying on a *subgrid model* for the scales to the right of the label. Direct numerical simulation (DNS) numerically solves the equations which describe turbulent fluid flow thereby resolving *all* relevant scales (one hopes) and requiring no model. DNS and LES will be discussed in §1.2.4.

Much research has focused on characterizing and understanding the turbulent energy cascade, and it has led to numerous insights about the physics of turbulence. Several physical interpretations of the behavior of turbulent structures, including vortex or eddy stretching, flow instabilities, complex folding and transformation of structures, or random convection [17], all attempt to explain the mechanism by which energy is transferred from the largest eddies downward to the smallest. This is brought about by the interactions between structures at different sizes and energy levels. Energy increases when vortices are stretched in the direction of the average velocity gradient [105]. This is postulated to be the way in which larger eddies transfer energy to smaller eddies, and so on down the energy cascade. This description of turbulence, although incomplete, has aided in the development of turbulence models and furthered understanding of the complex phenomenon.

1.2 Reynolds averaged Navier-Stokes Equations

A brief history of turbulence modeling, along with some fundamental mathematics behind those efforts, is considered. By no means can an exhaustive survey of turbulence modeling (or even a specific branch of turbulence modeling, such as Reynolds stress transport models) be presented: it is clearly outside the scope of

this paper. Instead, the information will serve as a means to contrast past modeling efforts with the Oriented-Eddy Collision turbulence model ideas which are taken from collision models for probability density functions first investigated by Taylor [96, 97], and extensively investigated by Perot, Pope, Van Slooten, Lundgren, and others [63, 64, 23, 100, 42, 66].

1.2.1 Derivation

The Navier-Stokes equations exactly describe the motion of fluid but cannot be solved analytically (the term "exactly" may be somewhat contentious, but it is an operating assumption here). Direct numerical simulation (DNS) overcomes this issue by solving the Navier-Stokes equations numerically. This method is the most accurate, but suffers from an enormous computational cost and for many flows is intractable even with today's state of the art computational resources. Reynolds averaged Navier-Stokes (RANS) approaches model the average behavior of turbulence but require human intervention in order to be closed. These closure models lead to inaccuracies in the predictions made by RANS approaches, but also make RANS approaches some of the most computationally tractable methods available. Large Eddy Simulations (LES) accurately solve for large scale motions present in the turbulent flow, but resort to modeling for small scales. The method is less computationally expensive than DNS, but still suffers from the inaccuracies present in modeling.

The incompressible Navier-Stokes equations, which govern all incompressible, viscous fluid flows, serve as a basis for most turbulence models [17, 66, 105]:

$$\frac{\partial \tilde{u}_i}{\partial t} + \tilde{u}_j \frac{\partial \tilde{u}_i}{\partial x_j} = -\frac{1}{\rho}\frac{\partial \tilde{p}}{\partial x_i} + \nu \frac{\partial^2 \tilde{u}_j}{\partial x_i^2} \tag{1.1a}$$

$$\frac{\partial \tilde{u}_i}{\partial x_i} = 0 \tag{1.1b}$$

where x_i is a direction in space, $\tilde{u}_i$ is the (total) instantaneous turbulent fluid velocity, $\tilde{p}$ the total pressure, and ν the kinematic viscosity. Equation (1.1a) above

represents conservation of momentum, while Equation (1.1b) comes about due to the incompressibility of the fluid, which is equivalent to conservation of mass. For more details on Reynolds' derivation, see Appendix C. Equations (1.1a) and (1.1b) can be further simplified by realizing that, by definition, the ensemble average (denoted by an overbar) of the fluctuating component of the velocity is zero, $\overline{u_i'} = 0$ and the ensemble average of the mean velocity is simply the mean velocity:

$$\frac{\partial \overline{u}_i}{\partial t} + \overline{u}_j \frac{\partial \overline{u}_i}{\partial x_j} = -\frac{1}{\rho}\frac{\partial P}{\partial x_i} + \nu \frac{\partial^2 \overline{u}_j}{\partial x_i^2} - \frac{\partial \overline{u_j' u_i'}}{\partial x_j} \tag{1.2a}$$

$$\frac{\partial \overline{u}_i}{\partial x_i} = 0 \tag{1.2b}$$

Equations (1.2a) and (1.2b) represent the basic form of the Reynolds averaged Navier-Stokes (RANS) equations. The last term in Equation (1.2a), $\partial \overline{u_j' u_i'}/\partial x_j$, is the only one that involves something other than the average velocity or pressure, $\overline{u}_i$ or $\overline{p}$. This term originates from the convective derivative when expanding Equation (C.1a). The term is the spatial derivative of the *Reynolds stress tensor* $\overline{u_i' u_j'}$, and is the average of the products of the fluctuating velocities present in the turbulent flow [17]. The term is a rank two tensor, symmetric, and responsible for adding additional unknowns to Equations (1.2a) and (1.2b), thus making the equation set unclosed. This term represents the average effect of turbulent convection but is diffusive in nature, in this case being responsible for diffusing momentum [17]. The thought of a convection term diffusing is interesting, and is cause for further comment.

To better understand how a convective term might diffuse momentum, it is necessary to make comments on the statistical nature of turbulence. Doing so is appropriate, as the formative ideas behind the Oriented-Eddy Collision turbulence model involve equations which are governed by probability density functions. The topic will be introduced here and expanded upon later. Taylor first related correlations to turbulence, observing that turbulent motion was diffusive in nature similar to molecular

diffusion resulting from random molecular motion [96]. Taylor went on to observe that, while it had been known the average Reynolds stresses were proportional to spatial velocity correlations, the relationship between temporal velocity correlations and turbulent stresses plays a key role in defining relevant turbulent lengthscales [97]. Durbin [17] provides a succinct description of this statistical relationship. If a set of particles is considered with positions $X(t)$, moved by some velocity $u(t)$, the trajectories of these particles represent a random collection of positions which have inherent to them a probability distribution at any given position and time, $f(x,t)$. The evolution of $f(x,t)$ is chosen to be the standard diffusion equation, namely

$$\frac{\partial}{\partial t} f(x,t) = \alpha \frac{\partial^2}{\partial x^2} f(x,t) \tag{1.3}$$

with α as a diffusion coefficient. If the variance of $X(t)$ is defined as $\overline{X^2} = \int_{-\infty}^{\infty} f(x) x^2 dx$ then, recognizing that by definition $x^2 f(x) = \overline{X^2}$, one can multiply Equation (1.3) by x^2 and integrate. This yields $d\overline{X^2}/dt = 2\alpha$, which shows that the ensemble average of a convective quantity, in this case $\overline{X^2}$, can be diffusive in nature. Related to this is the *Langevin equation*, which is relevant to any discussion of turbulence models which employ PDFs. The Langevin equation is an ordinary differential equation which is Lagrangian in nature. The Langevin equation follows the motion of something (a particle, a volume of fluid) through time. The equation was originally developed to describe the velocity of particles experiencing Brownian motion [40]. The equation can also describe the velocity of a particle in a turbulent flow and, as stated above, is related to diffusion processes, in this case turbulent diffusion of momentum [66, 23]. In general, the Langevin equation is a *stochastic* ordinary differential equation which describes the physics of a continuous, stochastic (*i.e.* not deterministic) process that has no history effects present [40]. Consider velocity $u(t)$ as a discrete stochastic process which is described by $u(t+\Delta t) = ru(t) + s\xi(t)$ with $\xi(t)$ a standardized Gaussian random variable with zero mean, unit variance, and one which is uncorrelated with

itself in time ($\overline{\xi(t)\xi(t+\Delta t)} = 0$) and uncorrelated with the velocity $u(t)$ for all previous times, $\overline{\xi(t+\Delta t)u(t)} = 0$ for $\Delta t > 0$ [66]. It can be shown [17] that $r = 1 - dt/T_L$ as $\Delta t \to dt$ with T_L the Lagrangian integral time scale (Lagrangian because the correlation function is that of a Lagrangian velocity) and $s = \sqrt{(1-r^2)\sigma} \approx \sqrt{2dt}\sigma$, noting that $\sigma = \overline{u^2}$, the variance of the fluctuating velocity. Substituting in r and s arrives at $u(t+\Delta t) = (1 - dt/T_L)u(t) + \sqrt{2dt/T_L}\sigma\xi(t)$. Completing the transformation from discrete to continuous and defining the infinitesimal increment $du = u(t+dt) - u(t)$ [66], the Langevin equation is obtained [17, 66]:

$$du(t) = -u(t)\frac{dt}{T_L} + \sqrt{\frac{2\overline{u^2}}{T_L}}\sqrt{dt}\xi(t) \tag{1.4}$$

noting that the final term in Equation (1.4) may be re-written as $\sqrt{dt}\xi(t) = dW(t)$ with $W(t)$ being a *Wiener process*. A Wiener process represents the most basic diffusion process with a zero drift coefficient and diffusion coefficient of unity [66]. Equation (1.4) is the stochastic differential equation representing a diffusion process with drift coefficient $-u(t)/T_L$ and diffusion coefficient $\sqrt{2\overline{u^2}/T_L}$. Equation (1.4) is less complex than it appears: the first term simply relaxes u toward the mean value while the second randomly perturbs u at regular intervals. The Langevin equation is often employed as a means of numerically solving a PDF-based turbulence model as will be discussed in Chapter 2. A discussion of the gradient diffusion hypothesis and turbulent viscosity, while related to turbulence modeling, is tangent to this work and thus presented in Appendix D.

1.2.2 Reynolds stress transport models

All zero-, one-, and two-equation models (see Appendix D) fundamentally rely on the Boussinesq approximation (or some variant thereof) as a foundation for modeling. The basic idea behind these efforts is that the Reynolds stresses are related to the strain by the eddy viscosity, which is little more than a constant of proportionality re-

liant on the flow under consideration [105]. For many simple flow situations, including some which are important to engineers, this works well. The approximation (and thus any model based on it) fails, however, in some other very important cases. Wilcox and others [105, 66, 17] provide a succinct list of deficiencies: Any flow subject to sudden changes in strain (to be precise, changes in the *mean rate-of-strain*) will cause problems in eddy-viscosity based models. Curved surfaces, secondary flows, rotating flows, fully three dimensional flows and any flow with a detached boundary layer also present obstacles to such models. In addition, the eddy viscosity assumption forces Reynolds stresses to change instantly when the strain changes, a restriction which denies the possibility of a loss-of-equilibrium in the flow. A lack of equilibrium between the stress and mean rate-of-strain does in fact exist in flows such as fully three dimensional boundary layers [17]. With such a wide variety of flow situations unsolvable by eddy viscosity models, it is no surprise that since the 1950s (and surely prior to that) researchers have endeavored to find an alternative. Returning to the RANS equations (Equations (C.1a) - (1.2b)) and developing a model for the evolution of the Reynolds stresses $\overline{u_i' u_j'}$ themselves has a few automatic advantages: First, convection and diffusion are accounted for and history effects of the flow can be realized more accurately compared to classic two-equation models [105]. Also, curvilinear flows will be captured exactly, and the previously assumed relationship between the stresses and the strain is now obviated, meaning that non-zero Reynolds stresses may exist even if the mean rate-of-strain is zero [94, 20, 66, 105].

The concept of modeling the transport of the Reynolds stress tensor R_{ij} was first explored by Rotta in 1951 [79]. Proposing a turbulence model that did not rely on the Boussinesq approximation was a fairly new idea [105]. All stress-equation models incorporate PDEs for the components of the Reynolds stress tensor $\overline{u_i' u_j'}$ [71] or some variant thereof. Returning to the Reynolds averaged Navier-Stokes equations (Equations (1.2a) and (1.2b)), an equation for the evolution of the Reynolds stresses

$\overline{u_i^{'}u_j^{'}}$ can be obtained, as described in Durbin [17], by subtracting Equations (1.2a) and (1.2b) from Equations (C.1a) and (C.1b), multiplying the entire equation by $u_j^{'}$ and then swapping the i and j indices:

$$\frac{\partial \overline{u_i^{'}u_j^{'}}}{\partial t} + \overline{u}_k \frac{\partial \overline{u_i^{'}u_j^{'}}}{\partial x_k} = -\frac{1}{\rho}\left(\overline{u_j^{'}\frac{\partial p^{'}}{\partial x_i}} + \overline{u_i^{'}\frac{\partial p^{'}}{\partial x_j}}\right) - 2\nu\overline{\frac{\partial u_i^{'}}{\partial x_k}\frac{\partial u_j^{'}}{\partial x_k}} - \frac{\partial \overline{u_k^{'}u_i^{'}u_j^{'}}}{\partial x_k} - \left(\overline{u_j^{'}u_k^{'}}\frac{\partial \overline{u}_i}{\partial x_k} + \overline{u_i^{'}u_k^{'}}\frac{\partial \overline{u}_j}{\partial x_k}\right) + \nu\frac{\partial^2 \overline{u_i^{'}u_j^{'}}}{\partial x_k^2} \quad (1.5)$$

The first term on the right hand side of Equation (1.5) represents turbulent redistribution, the second term accounts for dissipation, the third term being turbulent transport, the fourth term handling turbulent production, and the fifth term being viscous diffusion from the Navier-Stokes equation. Equation (1.5) is the Reynolds stress transport equation, governing the evolution of the Reynolds stress tensor $\overline{u_i^{'}u_j^{'}}$. Only the production and viscous diffusion terms are closed, and the rest must be modeled. Hypothesizing closures for the Reynolds stress transport equation is a popular way to approach turbulence modeling but has serious limitations, some of which are overcome by employing a PDF collision model instead of the Reynolds stress transport equations. The procedure outlined above is somewhat nebulous, and can be stated more simply: Take the Navier-Stokes momentum equation for the *fluctuating* velocity:

$$\frac{\partial u_i^{'}}{\partial t} + u_j^{'}\frac{\partial u_i^{'}}{\partial x_j} = -\frac{1}{\rho}\frac{\partial \tilde{p}}{\partial x_i} + \nu\frac{\partial^2 u_i^{'}}{\partial x_j^2} \quad (1.6)$$

and multiply by the fluctuating velocity $u_j^{'}$ (that is, take the first moment of the fluctuating Navier-Stokes equations) and then average. This results in an unclosed set of equations. One could take higher and higher moments of the Navier-Stokes equations, but for every higher moment achieved, more unknowns would be introduced. This is due to the simple yet unavoidable fact that taking the moment of an equation does not introduce any new *physics*, only new *math*. As such, it is not possible to introduce any means of simplifying or closing the problem without new physics.

Most second-order closures based on the Reynolds stress transport equation rely upon a model to close the third-order correlation term, $\partial\overline{u_k' u_i' u_j'}/\partial x_k$. This follows logic employed in zero and first-order models: simplifying approximations for a correlation one order *above* that of the model (in this case, a model for the *third* order correlation in a second-order model) yields good approximations for orders below the modeled level. More specifically, any unclosed terms from Equation (1.5) must be replaced by a model which relates the term in question to known quantities, such as those involving the mean flow and its gradients, the kinetic energy, or the dissipation. It is desirable to make these unclosed terms functions of past quantities in order to incorporate history, but usually history effects are realized through the evolution of the PDE itself [17]. Determining the form of these model terms is a complicated process with many possible paths, and the procedure will not be detailed here. It is instructive to note that most often unknown terms are split into two distinct categories: those which involve the gradient of the mean velocity (usually called "rapid" terms), and those which do not (not surprisingly called "slow" terms). Rapid terms involve the physical process of rapid pressure strain and constitute the majority of effort devoted to stress closures, while slow terms involve return to isotropy for the Reynolds stresses [17]. Several well-known models have been developed for these terms, including the Launder, Reece, and Rodi (LRR) model [35], and the more recent Speziale, Sarkar, and Gatski (SSG) model [95] which, rather than casting the relationship between the pressure and strain as linear (which is used by many RST models), the relationship is quadratic. As a final note, the triple (third-order) correlation may in fact not be the key to a more accurate RST model. Recent work with PDF-based turbulence models by Perot, Pope, Reynolds and others [65, 100, 56, 10, 30] has suggested that an RST model may still suffer from deficiencies even if given a perfect triple correlation. It may be the case that the pressure term contains the important physics, and thus being able to model this term properly (or use direct numerical simulation to ob-

tain the exact answer) is of utmost importance. The questionable significance of the triple correlation is brought to light with PDF-based models (see Chapter 2) where the triple correlation is exact, yet the model still suffers from deficiencies common to RST models. Few turbulence models (the Oriented-Eddy Collision turbulence model being one of the exceptions) are able to capture the pressure term properly.

Despite the many advantages that RST models offer, and the many flow situations in which they return more physically correct results compared to eddy-viscosity based models, stress tensor models have their own set of deficiencies. To begin with, great care must be taken when attempting to use RST models near solid boundaries where the velocity and Reynolds stresses tend to zero. At the moment, wall functions and damping are the most popular methods employed to handle solid boundaries. Not only is it imperative that the value at the boundary be prescribed, but the model must also behave properly as it *approaches* the wall, meaning the model's asymptotic behavior must be considered. If the fluctuating velocity is considered to be a smooth function of the distance from the solid boundary x_2, then it can be expanded as a Taylor series, *viz.* $u_i^{'} = p_i + q_i x_2 + r_i x_2^2$ with p_i, q_i, and r_i functions of the wall-tangent directions, and truncating higher order terms. If the velocity at the wall is zero, $u_i^{'}(x_2 = 0) = 0$, then $p_i = 0$ which implies $u_1^{'}$ and $u_3^{'}$ (in the tangential x_1 and x_3 directions, respectively) approach the boundary like x_2. Furthermore, if continuity is invoked, it is found that velocity in the wall normal direction $u_2^{'}$ approaches the wall like x_2^2. Using this information, the near wall asymptotic behavior of the individual Reynolds stress tensor components can be assessed: $\overline{u_1^{'}u_1^{'}}$, $\overline{u_3^{'}u_3^{'}}$, and $\overline{u_1^{'}u_3^{'}}$ will approach like x_2^2. $\overline{u_1^{'}u_2^{'}}$ and $\overline{u_2^{'}u_3^{'}}$ will go like x_2^3, and $\overline{u_2^{'}u_2^{'}}$ like x_2^4 [17, 66]. Figure 1.4 illustrates this. It is not trivial to ensure this behavior, and is an area of focus for the Oriented-Eddy Collision turbulence model. The near-wall region creates other difficulties: the highest shear rate is often located at a solid wall, and the normal

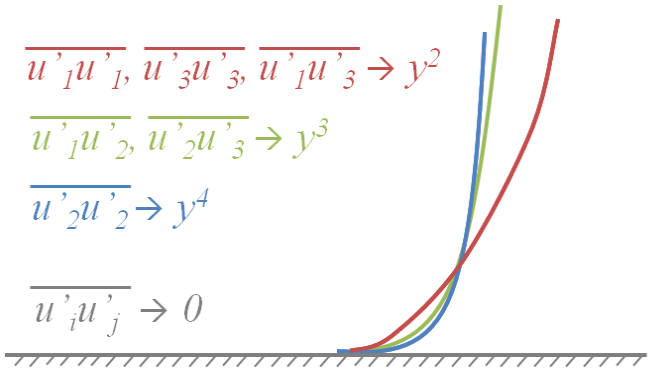

Figure 1.4. A schematic of the desired near-wall asymptotic behavior of various Reynolds stress components. Here, $x_2 = y$.

velocity being forced to zero at the wall tends to affect the flow away from the wall via pressure (often called "wall blocking") [66].

Aside from near-wall asymptotic difficulties, RANS-based RST models suffer from several other problems: Due to their RANS foundation, they cannot provide any information about the specific structure of turbulent flows, only the average structures - the mean velocity, mean pressure, and Reynolds stresses. Furthermore, flows that have rapidly changing energy spectra, flows with separation, and flows with spreading jets all pose difficulties for RST models [95].

A survey of RANS-based model would not be complete without a brief mention of unsteady Reynolds averaged Navier-Stokes based methods, or URANS. Such models still employ a basic RANS approach but also incorporate the unsteady term (that is, the time derivative term in the convective derivative) in calculations [17]. This is done to capture the behavior of flows which are not stationary in time (not statistically stationary) like flow past a bluff body which includes vortex shedding [88], such as that shown in Figure 1.5, adapted from [9]: In order to properly capture the turbulent flow, two steps are employed. First, the "steady" solution is found via RANS computations, and then a "deterministic shedding" [17] is added in order to capture the downstream eddies properly. The turbulence model itself is solely

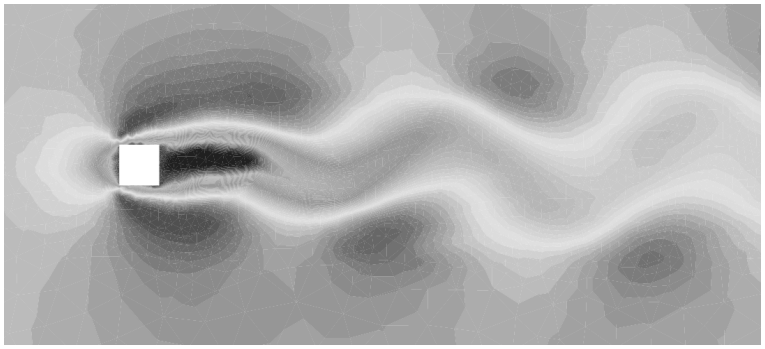

Figure 1.5. An example of the unsteady, time dependent structures that can be present in flow past a bluff body. Adapted from [9].

employed to capture the statistics of unsteady velocity fluctuations [17]. URANS models are relatively new and still an area of active research.

1.2.3 Invariance, Realizability, and Consistency

Now that a basis for RANS/URANS turbulence models has been established (with some foreshadowing about the upcoming statistical discussion), it is important to recognize that there are several traits that turbulence models should possess. The first two are *frame invariance*, (also referred to as Galilean invariance), and coordinate system independence (or coordinate invariance). Galilean invariance ensures that the modeling equations remain unaltered even if the frame of reference they are cast in varies. More specifically, the model should remain consistent in any reference frames having constant relative velocities, which is usually automatically satisfied by use of the material derivative [17]. In the case of non-inertial frames (first considered by Lumley [41] and again by Speziale [93]), such as a fluid undergoing solid-body (*i.e.* time-dependent) rotation and translation, additional terms must be added to the model to account for accelerations such as the Coriolis force. Such a term often takes the form $\Omega_{ij} + \epsilon_{ijk}\Omega_k$ with Ω_{ij} the fluid rotation tensor relative to the frame (the mean rate of rotation), ϵ_{ijk} the permutation tensor, and Ω_k the frame rotation vector [17, 93, 94, 66]. It is important to note that in RST-like models, an additional term

may be added to the material derivative in order to account for rotation relative to the non-inertial frame [17]. Spalart and Speziale [90] point out an important subtlety: in the limit of two-dimensional turbulent flows, the flow is insensitive to constant (not time varying) rotation, but this is not necessarily the case in three dimensions. This is a special case, such as certain approximations of atmospheric flow, where the gradients of turbulent quantities are zero in the same direction as the rotation vector.

Coordinate system invariance is a somewhat simpler concept, ensuring that a given model responds identically to translations, reflections, and accelerations regardless of whether they are occurring in the flow itself or arise from the coordinate system. Interestingly, coordinate invariance requires that any Reynolds stress transport equation model be cast in tensor form [8], which is not always the case [94]. A positive side effect of a tensor-based model is that it ensures the model can be extended to complex flow situations, such as those with curved streamlines. This is related to the previous discussion of frame invariance, as a model which does not account for noninertial frame rotation will most likely be unable to properly handle curvature, even in inertial reference frames [93]. Closely tied to this is grid or mesh independence, which essentially states the model must not change if the computational mesh changes. That is not to say the solution returned by the model may not improve or degrade depending on the mesh resolution, only that the *underlying equations* remain unaltered.

The concept of realizability was introduced first by Schumann [86] and applied to Reynolds stress transport equations by Lumley [41]. Simply stated, realizability requires that the diagonal components of the Reynolds stress tensor, introduced above in Equations (1.2a) and (1.2b), are all greater than zero and, more generally, that the Reynolds stress tensor be positive semi-definite. The magnitudes of *all* components of the Reynolds stress tensor are related to realizability through the Schwartz inequality [17], which states the normalized covariance of the velocity components must be less

than unity, $\overline{u_j' u_i'} / \sqrt{\overline{(u_i')^2}\ \overline{(u_j')^2}} \leq 1$. This condition, along with the requirement that the diagonal components be greater than zero $u_i' u_i' = (u_i')^2 > 0$ imply the eigenvalues of $\overline{u_i' u_j'}$ must also be positive [17]. If these conditions are violated, then the turbulence model is not realizable, which in this context means that it cannot represent statistics of a random process. More specifically, if one of the diagonal terms (component energies) of $\overline{u_i' u_j'}$ drops below zero, this means that a statistic, in this case the fluctuating velocity component, say u_i', has a negative variance $\overline{(u_i')^2} < 0$ which is impossible. Although not immediately obvious, this, along with Schwartz's inequality brings to light an important fact about the Reynolds stress tensor: the components of the stress tensor returned from a model usually represent the result from an evolution equation for the correlation $\overline{u_i' u_j'}$ itself, not the underlying fluctuating velocities. Since $\overline{u_i' u_j'}$ is a correlation and not a velocity, it makes sense that it is subject to *statistical* constraints such as the Schwartz inequality above. Most often realizability is ensured through careful turbulence model coefficient tuning [17, 66].

Finally, dimensional consistency, although seemingly obvious, is important to consider and has aided greatly in the formulation of turbulence models. Dimensional consistency simply states that quantities represented within a turbulence model such as the kinetic energy K or the dissipation ϵ must have units consistent with their physical counterparts. This also relates to the concept of a turbulence model exhibiting physicality (or physical coherence), meaning the model must not return results which are physically impossible and models themselves must bear resemblance to the real-world physics they are meant to represent.

1.2.4 Large-Eddy and Direct Numerical Simulations

Large-eddy simulation (LES) and direct numerical simulation (DNS) are popular means of solving the turbulence problem. Large-eddy simulations entail computations of large-scale turbulent structures that are present in three-dimensional, time-varying

turbulent flows [71]. For scales smaller than those captured by LES, a "subgrid model", such as the zero-equation Smagorinsky model, is employed [87]. LES relies on a "filtering" approach, whereby all but the largest scales of turbulence are removed from the velocity field. This operation can be thought of as applying a mesh (computational grid) to the turbulence, which spatially discretizes the flow, and is a form of weighted averaging. The mesh resolution dictates the smallest features that will be resolved by the LES. Naturally, anything under the mesh resolution will have to be handled in some other way. Turbulent features lying below this filter are modeled in the expectation that the use of modeling has a negligible impact on the overall simulation results [105]. In addition, it is plausible to assume that only the large scale turbulent eddies are affected by the flow geometry, boundary conditions, etc. and therefore are the only features "deserving" of computational effort. This implies that the small scales are of an isotropic, universal nature [105]. LES has returned reasonable results for a variety of wall-bounded flows as well as simpler cases. The fact that LES relies on so-called "subgrid" models means that these models must be able to handle energy dissipation (especially near walls) properly [105]. Note that LES also operates under the restrictions of realizability, frame, and coordinate invariance.

Finally, direct numerical simulation (DNS) of turbulent flows is considered. DNS is only tangentially related to the Oriented-Eddy Collision turbulence model, other PDF models, and RANS-based models as *the method is not based on the RANS equations or probability density functions.* DNS does not rely on the eddy viscosity hypothesis which forms the basis for popular zero-, one-, and two-equation models. DNS involves no modeling, and solves all lengthscales relevant to the Navier-Stokes equations numerically for all time and space for a given flow [66]. DNS is expensive, and requires enormous computational power in order to solve even moderate Reynolds number flows. Recent advances in computational efficiency have greatly extended the usability of DNS, and the method may one day replace turbulence models for certain

complex, high Reynolds number flows. DNS may be performed in both physical and wave space (Fourier space), or in a mixture of the two (pseudo-spectral methods), where velocity is kept in Fourier space but the more challenging non-linear terms in the Navier-Stokes equations ($u_i^{'}u_j^{'}$) are considered by transforming the velocity into physical space, forming the nonlinear terms, and finally transforming these back into Fourier space [66]. DNS is primarily used for research purposes or the study of turbulent decay or other isotropic or homogeneous flow situations, and cannot be used in many high Reynolds number flows. DNS is often employed to study fundamental physics such as turbulent drag reduction [44, 45, 46], isotropic turbulence (see the work of de Bruyn Kops, for example [12]), scalar mixing [13], the energy spectrum noted in the introduction, and many, many other topics. DNS can be considered an experimental method as it returns truly physical results [105]. Such is the case with Kim [31], Moser [49], and their study of turbulent channel flow. Aside from computational cost, two additional difficulties arise when attempting DNS. One is numerical accuracy. A DNS is only as good as the underlying numerical method it employs, and it is imperative to use proper spatial and temporal discretization schemes. Open (far field) boundaries present another issue, as they require knowledge of the flow *outside* of the computational domain. Periodic boundary conditions - that is, boundary conditions which "wrap around" in one or more directions - are very often employed ([44, 45, 46, 51, 20, 12, 13, 31, 49] and many others). Initial conditions are also a major challenge (see, for example, work done by Nilsson [51]). In order to properly advance the Navier-Stokes equations in time and space it is imperative to provide proper starting conditions. Results from a previous simulation are ideal, but the "chicken and egg" scenario dictates that initial conditions must be created in some original form. Many methods have been employed to overcome this difficulty, including the use of random fields, experimental data, perturbations applied to the

mean flow, and others. With the increase of computational resources available, DNS promises to be a major player in turbulence research for the foreseeable future.

1.3 Problems with RST approaches

1.3.1 Nonlocality of Rapid Pressure Redistribution

Rapid pressure strain (also called redistribution) is an unclosed term in the Reynolds stress transport equation that requires modeling. Most traditional RST modeling approaches are single-point closure methods, meaning they do not contain information about surrounding turbulent quantities (the Oriented-Eddy Collision turbulence model is *not* a single-point method). While this restriction suffices for other unclosed terms in the RST equation, one term - redistribution - cannot be captured with single-point approaches. Numerous efforts, spanning multiple decades, have failed to properly capture the physics of rapid distortion theory [17] in traditional single-point, second-moment closures in any general method. This effort is frustrated by the presence of turbulence in the rapid distortion theory (RDT) limit, which is linear turbulence dominated by rapid pressure strain effects. An analytical solution exists for homogeneous RDT, and yet most models fail in the presence of such a turbulent flow.

Figure 1.6 is the familiar Lumley triangle, adapted from [66], which plots the second and third invariants of Reynolds stress anisotropy. The second invariant is defined as $\eta = (1/6)\left(B_{ij}B_{ji}\right)^{1/2}$ and the third invariant defined as $\xi = (1/6)\left(B_{ij}B_{jk}B_{ki}\right)^{1/3}$ where Reynolds stress anisotropy is $B_{ij} = (R_{ij}/k) - (1/3)\delta_{ij}$. A model which can capture the extremes of the Lumley triangle - that is isotropic turbulence, one component turbulence, two component turbulence, and axisymmetric two component turbulence - may be able to capture *arbitrary* anisotropy. While the ability to capture linear turbulence is appealing, predicting turbulence of arbitrary anisotropy while remaining realizable (*i.e.* within the bounds of the Lumley triangle) is the ultimate goal.

Arbitrary anisotropy aside, the task at hand remains to predict linear turbulence. The

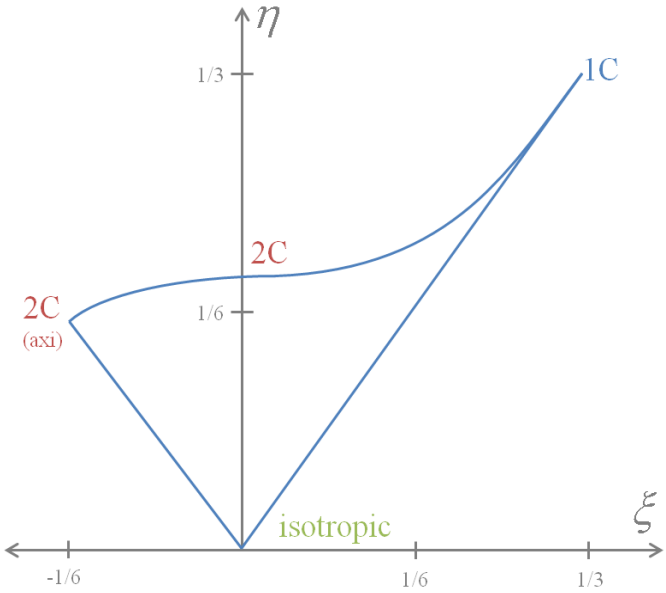

Figure 1.6. A Lumley triangle showing the limits of anisotropy in a turbulent flow. η and ξ are the second and third invariants of the Reynolds stress anisotropy. Plot adapted from [66].

rapid pressure-strain term in any Reynolds stress transport model should exhibit certain behavior: if no anisotropy production is present, the rapid pressure-strain term should be zero. Furthermore, when approaching a two component limit in turbulence, the rapid pressure-strain should generally decrease. The magnitude of rapid pressure-strain should be less than that of production [28]. While several models are capable of meeting some of these requirements, models such as SSG and LRR typically return unphysical, unrealizable results without special modification [17]. As the section title suggests, the reason for this has to do with the nonlocality of pressure redistribution. RST models contain information about the componentality of turbulence through the Reynolds stress tensor, but lack any means of representing the *dimensionality* of turbulence [73, 76]. Redistribution can be thought of as the correlation between fluctuating velocity and the fluctuating pressure gradient, $\phi_{ij} = \left(\overline{u'_j p'_{,i}} + \overline{u'_i p'_{,j}}\right)$. Note that Cartesian notation is used here and "$_{,i}$" refers to a spatial derivative (gradi-

ent). This term in the Reynolds stress transport equation serves to transfer variance from one stress component into others while keeping kinetic energy constant [17]. This requires that the redistribution term be traceless, and therefore redistribution is sometimes defined as $\prod_{ij} = \phi_{ij} - (1/3)\phi_{kk}\delta_{ij}$ [17]. While the term *contains* rapid pressure strain effects, it also contains other physics as well, often called "pressure diffusion" and slow pressure-strain. As such, ϕ_{ij} may be separated into these separate portions [17],

$$-\phi_{ij} = -\overline{u_j' \frac{\partial p'}{\partial x_i}} - \overline{u_i' \frac{\partial p'}{\partial x_j}} \qquad = \underbrace{-\left(\frac{\partial \overline{u_j' p'}}{\partial x_i} + \frac{\partial \overline{u_i' p'}}{\partial x_j}\right)}_{\text{pressure-diffusion}} + \underbrace{\overline{p'\left(\frac{\partial u_j'}{\partial x_i} + \frac{\partial u_i'}{\partial x_j}\right)}}_{\text{pressure-strain}} \tag{1.7}$$

In Equation (1.7), the pressure diffusion expression is of less concern than the pressure-strain not only due to its relation to rapid distortion, but also due to the nature of turbulence near solid boundaries - that is, in highly inhomogeneous and anisotropic circumstances. In the next sections, several RDT turbulence cases and turbulent channel flow will be considered and the performance of several popular RST methods analyzed.

The exact but unclosed Reynolds stress tensor transport equation contains a redistribution term $\wp_{ij}$ which may be defined as $\wp_{ij} = \phi_{ij}$ or, including dissipation anisotropy, $\wp_{ij} = -\left(\phi_{ij} + \epsilon_{ij} - (2/3)\epsilon\delta_{ij}\right)$ [17]. Redistribution must be expressed in terms of known quantities such as the stress tensor (R_{ij}) or its anisotropy (B_{ij}), the mean velocity ($\overline{u_i}$) and its gradients, the kinetic energy, and the dissipation. Casting redistribution as a function of these terms implies both spatial and temporal locality, which is major assumption. This assumption is most clear when the redistribution is separated into portions which include the mean velocity gradient, $\partial\overline{u_i}/\partial x_j$, and those terms which do not. The terms which do *not* include the mean velocity gradient are often referred to as "slow" and modeled with return-to-isotropy concepts [17]. Of greater concern are the "rapid" terms which depended upon gradients of $\overline{u_i}$.

Durbin [17] provides a detailed description of the origins of non-locality in rapid pressure strain. A summary will be presented here. To begin with, in homogeneous flows redistribution reduces to

$$\phi_{ij} = -(1/\rho)\overline{p'\left(\frac{\partial u_j'}{\partial x_i'} + \frac{\partial u_i'}{\partial x_j}\right)} \tag{1.8}$$

which is the second term on the right hand side of Equation (1.7). A relation between the pressure and velocity can be made by way of the Poisson equation. Taking the divergence of Navier-Stokes and invoking continuity yields [17]

$$\nabla^2 p' = -\rho \underbrace{\left(\frac{\partial u_l'}{\partial x_k}\frac{\partial u_k'}{\partial x_l} - \overline{\frac{\partial u_l'}{\partial x_k}\frac{\partial u_k'}{\partial x_l}}\right)}_{\text{slow}} - \underbrace{2\rho\frac{\partial \overline{u}_k}{\partial x_l}\frac{\partial u_l'}{\partial x_k}}_{\text{rapid}} \tag{1.9}$$

for p', the fluctuating pressure. Taking only the linear ("rapid") portion of Equation (1.9) one arrives at

$$\nabla^2 p' = -2\rho\frac{\partial \overline{u}_k}{\partial x_l}\frac{\partial u_l'}{\partial x_k} \tag{1.10}$$

which can be solved using a free-space Green's function for Laplace's equation of the form $1/(4\pi|x_i - \tilde{x}_i|)$ [17] which involves information about an additional point in space, $\tilde{x}_i$. Herein lies the problem - the solution for the redistribution ϕ_{ij}, which is a single point quantity, involves a Greens function which is a *two-point* quantity. Pressure forces acting at a distance cause this non-locality to be present and are the source of many single-point, second moment modeling difficulties.

1.3.2 RDT and channel flow examples

Several sources ([66, 17, 21]) provide a convenient overview of various popular RST models' pressure-strain term performance when subjected to common rapid distortion theory (RDT) cases including axisymmetric expansion, axisymmetric contraction, plane strain, and homogeneous shear. The Speziale-Sarkar-Gatski (SSG)

model [95], Launder-Reece-Rodi (LRR) model [35], isotropization of production (IP) model [50], and LRR-IP model are all examined below. Figure 1.7 compares the ratio of the second invariant of the redistribution tensor, $\wp_{ij}$ [17], to the second invariant of production $P_{ij} = -\overline{u'_j u'_i}\overline{u}_{i,k} - \overline{u'_i u'_k}\overline{u}_{j,k}$. Recall $\prod_{ij} = \phi_{ij} - (1/3)\phi_{kk}\delta_{ij}$, $\phi_{ij} = (1/\rho)\left(\overline{u'_j p'_{,i}} + \overline{u'_i p'_{,j}}\right)$, $\epsilon_{ij} = \overline{u'_i u'_j}(\epsilon/k)$ and $\epsilon = \nu\left(\overline{u_{i,j}u_{i,j}}\right)$ [17]. Note that $\phi_{kk} = 0$

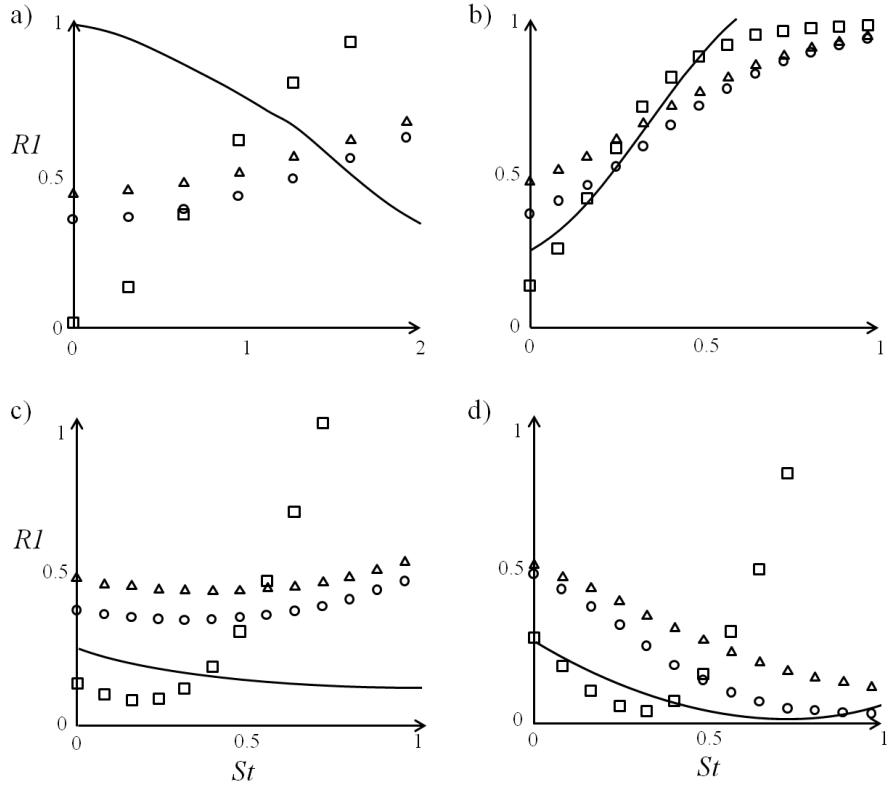

Figure 1.7. RDT [21] (—) versus SSG [95] (□), IP [50] (○), and LRR-IP [35] (△) models for a) homogeneous shear, b) axisymmetric expansion, c) axisymmetric contraction, and d) plane strain. Plot adapted from [21]. $R1 = \wp_{ij}\wp_{ij}/P_{ij}P_{ij}$.

in homogeneous incompressible turbulence. Figure 1.8 focuses on the LRR-IP model [35] subjected to homogeneous shear and compared to DNS data from Rogers and Moin [78]. Anisotropy is reported in the form of $B_{ij} = R_{ij}/2K - \frac{1}{3}\delta_{ij}$. It is critically important to notice that LRR-IP predicts $B_{22} = B_{33}$ which is physically incorrect. The model is incapable of representing the (large) differences between these anisotropy components.

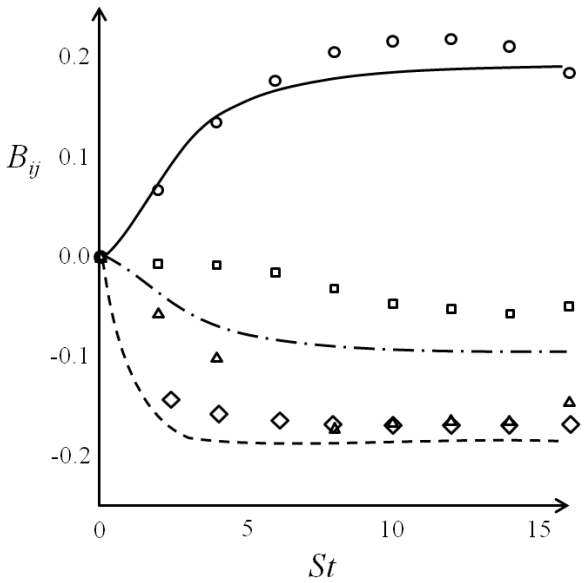

Figure 1.8. Performance of the LRR-IP turbulence model [35] subjected to homogeneous shear: B_{11} (—), B_{12} (- - -), $B_{22} = B_{33}$ (–·–); compared to DNS [78]: B_{11} (○), B_{12}(◇), B_{22}(△), and B_{33}(□). $B_{ij} = R_{ij}/2K - \frac{1}{3}\delta_{ij}$.

Figure 1.9, adapted from [17], tells a similar story in that both the SSG and IP turbulence models, when predicting flow in a turbulent channel at a friction Reynolds number of $Re_\tau = 395$ [49], drastically over predict redistribution near the solid boundary.

It should be mentioned that Durbin [17] and others have proposed numerous solutions to the redistribution problem presented in Figure 1.9 including elliptical relaxation and isotropization of production. While these near-wall treatments work well for channel flow and similar wall-bounded cases, they fail to address the more fundamental problem of non-local effects being both present and in some cases dominant in an otherwise single point model. With the physical and mathematical origins of non-locality, as well as the consequences of ignoring such physics, presented above, it is clear that a model which actually includes non-local information (perhaps in the form of a two-point correlation) could not only capture rapid distortion properly, but may also capture arbitrary levels of anisotropy, and non-local wall effects, as

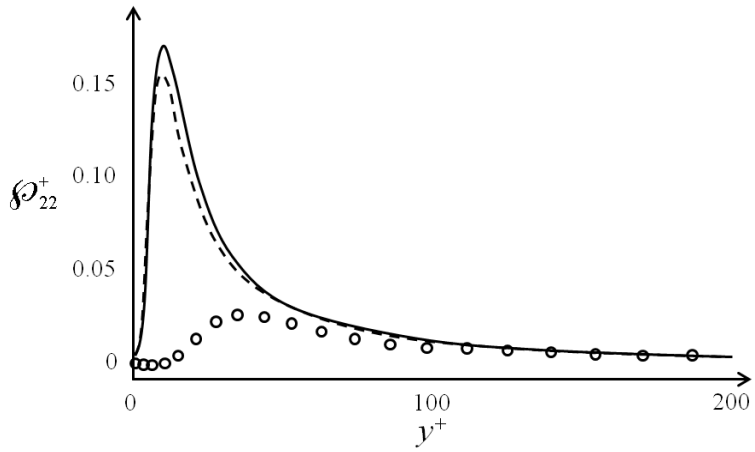

Figure 1.9. Performance of the SSG [95] (—) and IP [36] (- - -) turbulence models subjected to turbulent channel flow at a friction Reynolds number $Re_\tau = 395$; compared to DNS [49] (∘). $\wp_{ij}^{+}$ is the normalized redistribution tensor [17]. Plot adapted from [17].

well. This is the main motivation for the development of the Oriented-Eddy collision turbulence model.

CHAPTER 2

MOTIVATION

2.1 Statistical & Structure-based methods

Turbulence modeling can now be examined as a whole. Methods such as LES and DNS are expensive but accurate. They are not burdened by complex modeling terms (save for whatever subgrid model LES might employ). Some day these methods may be tractable for high Reynolds number turbulent flows. Zero-, one-, and two-equation models, of which there are many, are based on some simple assumptions about the nature of turbulence and often have a limited set of physical situations in which they are accurate. Nevertheless, many models such as $K-\epsilon$ or Spalart-Allmaras are widely used. Reynolds stress transport models are the most complicated of those considered thus far and, when posed properly, can achieve a wider range of physically accurate results. Unfortunately, these models have their own set of limiting assumptions, and for the most part cannot capture linear turbulence. Linear turbulence (turbulence in the rapid distortion theory limit [66]) is often strongly non-isotropic and initially unsteady, that is, it is far from equilibrium. A model is sought that can accurately capture linear turbulence.

An entire set of turbulence models are based on probability density functions (PDFs), which represent the fluid as a collection of fluid elements (or particles, blobs, packets, etc.). Lundgren was the first to consider such models [42]. PDF-based models form the inspiration for the Oriented-Eddy Collision turbulence model as well as models proposed by Pope and others [66, 63, 64, 65, 10, 56]. The Oriented-Eddy Collision turbulence model treats turbulent flows as a collection of colliding eddies

that have inherent orientation. Collision rules can be constructed for turbulent eddies such that the resulting collective system behaves in a manner consistent with mean turbulent flow governed by the RANS hypothesis. A number of advantages over classic Reynolds stress transport models result: turbulent transport does not require a model (when cast as a PDF), frame invariance, realizability, and tensor consistency are easily satisfied.

Traditional turbulence modeling methods involve educated guesses for the equations that govern the Reynolds stress tensor. Turbulent structures contained within a flow are proportional to the velocity gradients present in the mean flow, meaning these eddies respond on similar time scales as the mean flow. Transport equations, taken from work with non-Newtonian stress tensors, make non-Newtonian fluid dynamics an excellent source for insight into turbulence modeling. Transport equation models have serious limitations for non-Newtonian fluids and often the fluid is modeled at the particle collision level rather than using a transport equation for the stress. The impetus for the eddy-collision method is derived from the relationship between turbulent and granular flows. Complex, non-Newtonian fluids, such as colloidal suspensions, result from the interaction of their constituent particles and are solved using non-Newtonian fluid models such as the finitely extensible non-linear elastic (FENE-P) dumbbell model [24] or the Oldroyd model [52]. PDF collision models for turbulence aim to create an analogy between such flows and turbulence.

2.1.1 Boltzmann and Fokker-Planck

It is helpful to begin with a simple case, and not consider complications such as colliding oriented eddies. Instead, imagine a collection of particles: an expression can be found for the number of particles that have some velocity v_i at location x_i and time t, called a number density function. The more familiar probability density function is simply the number density divided by the total number of particles under

consideration. Let $f(v_i, x_i, t)$ be the probability density function. Using this function, one can arrive at several useful quantities: multiplying f by v_i and integrating over all of the possible velocities (that is, taking the first moment of f and integrating over velocity space), one can arrive at the mean velocity for the collection of particles, $\overline{u}_i$:

$$\overline{u}_i = \int_{v_i} v_i f(v_i, x_i, t) dv_i \tag{2.1}$$

where $\int_{v_i}$ and dv_i imply a triple integral over $v_i, i = 1, 2, 3$. If the mean velocity can be found, perhaps another quantity of interest, $\overline{u_i' u_j'}$ can be found. Taking the second moment of f with the fluctuating velocities $v_i - \overline{u}_i$, recalling the fluctuating velocities are the total velocity of a given particle v_i with the mean velocity of all particles $\overline{u}_i$ subtracted off:

$$\overline{u_i' u_j'} = \int_{v_i} (v_i - \overline{u}_i)(v_j - \overline{u}_j) f(v_i, x_i, t) dv_i \tag{2.2}$$

once again recognizing that a triple integral exists in Equation (2.2). Equations (2.1) and (2.2) represent the statistical mechanics of the collection of particles but say nothing about the physics present in that f has yet to be prescribed. One of the simplest ways to describe the time evolution of a PDF is through the Boltzmann equation:

$$\frac{\partial}{\partial t} f(v_i, x_i, t) + v_i \frac{\partial}{\partial x_i} f(v_i, x_i, t) + a_i \frac{\partial}{\partial v_i} f(v_i, x_i, t) = \frac{\partial}{\partial t} f(v_i, x_i, t) \bigg|_{collisions} \tag{2.3}$$

with a_i representing the acceleration, usually due to some body (external) force that may be acting on the fluid (such as a Coriolis term) and the right hand side representing the way in which the average of all collisions over time affects the PDF. The left hand side of Equation (2.3) is exact, while the right hand side is that which requires a model, the so-called "collision" term. A hierarchy of treatments for the right hand side of Equation (2.3) exists. The first and simplest option is to set the collision term

to zero, that is $\frac{\partial}{\partial t} f(v_i, x_i, t)|_{collisions} = 0$. This would imply that in between particle collisions, the distribution f advects ballistically. This is the so-called "equilibrium" Boltzmann equation. Its solution is the Maxwell-Boltzmann distribution. This distribution is not employed by the Oriented-Eddy Collision turbulence model and will not be considered further.

Boltzmann originally considered a "hard-sphere gas" when formulating his collision operator. This collision term is complex and often approximations are sought to simplify calculation. One such approximation to the Boltzmann collision operator is the "BGK" model proposed by Bhatnagar, Gross, and Krook [5, 56]. This term slowly brings f to a local equilibrium value, which usually means a Gaussian distribution. Once a form of f has been chosen, it can be used in Equation (2.1) and the mean velocity found (the method in which this is done will be discussed later). Employing the BGK-approximation has several benefits, including a transport equation which can be shown to obey mass, momentum, and energy conservation. The equilibrium distribution toward which the collision operator strives is Maxwellian. This makes the BGK-approximation capable of reproducing the behavior of Boltzmann's original collision operator without adding undue complexity.

A slightly more complex linear relaxation model may also be employed (see Perot & Chartrand [56]). Interestingly, for low density flows (meaning flows in which few particle collisions occur), a simple collision model returns the ideal gas law, the viscous terms of the Navier-Stokes equations, Fourier heat conduction and many other physical processes. Thus, this method is suited for Newtonian flows, but might not work well as a turbulence model. Inspecting the second moment and plugging the Boltzmann equation in to Equation (2.2) yields an unfortunate result: simple relaxation models predict that the Reynolds stresses are zero, $\partial \overline{u_i' u_j'}/\partial t = 0$. Not only is this approach flawed, it is in fact useless for capturing the behavior of a turbulent flow. This is due to the fact that the BGK-Boltzmann equations look at fluid inter-

actions purely as a viscous phenomena with a single relevant time scale. It is well understood that a single length or time scale can never capture turbulence properly, and so it is no surprise that this simple collision model fails.

An alternative to the BGK-approximation for collisions is the Fokker-Planck (FP) collision model (also referred to as the Kolmogorov forward equation), which describes the time evolution of a PDF in a more complicated way:

$$\frac{\partial}{\partial t} f(v_i, x_i, t) + v_i \frac{\partial}{\partial x_i} f(v_i, x_i, t) + a_i \frac{\partial}{\partial v_i} f(v_i, x_i, t) = \\ - \alpha \frac{\partial}{\partial v_i}(v_i - \overline{u}_i) f(v_i, v_i, t) + \beta \frac{\partial^2}{\partial v_i^2} f(v_i, x_i, t) \quad (2.4)$$

with α and β the collision model constants. Equation (2.4) (adapted from [56, 10]) represents one of the simplest Fokker-Planck collision models (appropriate for modeling Brownian motion) the right hand side of Equation (2.3) replaced by two terms. The right hand side of Equation (2.4) must be generalized in order to be employed for PDF turbulence model methods. Pope and others proposed a generalized form with a tensor constant, and use this extensively in their PDF modeling work [66, 63, 64, 56]:

$$\frac{\partial}{\partial t} f(v_i, x_i, t) + v_i \frac{\partial}{\partial x_i} f(v_i, x_i, t) + a_i \frac{\partial}{\partial v_i} f(v_i, x_i, t) = \\ - \frac{\partial}{\partial v_j} \left[G_{ij}(v_i - \overline{u}_i) f(v_i, x_i, t) \right] + \beta \frac{\partial^2}{\partial v_i^2} f(v_i, x_i, t) + \nu \frac{\partial^2}{\partial x_i^2} f(v_i, x_i, t) \quad (2.5)$$

where G_{ij} is a tensorial modeling parameter, ν the fluid viscosity, and noting the addition of a second order spatial derivative (Laplacian) of the PDF. Unlike the simple BGK collision model, the Fokker-Planck collision model is complex enough to ensure that the resulting second moment (Reynolds stress) transport equation is not zero.

The two methods mentioned above relate to the aforementioned Langevin equation: a Langevin approach can be employed to solve the resulting PDF transport

equations arrived at from plugging either the Boltzmann or the Fokker-Planck collision models into Equation (2.3) and the resulting expression for f into Equations (2.1) or (2.2). This is because the equations may be solved using "normal" methods, that is using a finite-difference or finite-element method to discretize both physical *and* velocity space, or may be solved by using a particle approach which represents velocity space statistically (using many particles at different speeds), the details of which will be avoided here. Using a Langevin approach makes no changes to the underlying physics - it is simply a particle method solution. When a Langevin method is used with a BGK-approximated Boltzmann equation, this is often referred to as a Lattice-Boltzmann method (as the velocities are restricted to a small "lattice" of possibilities). Solving a PDF collision method in this way is a way of solving the Navier-Stokes equations. Using the Fokker-Planck collision term (on the right hand side) with a Langevin method results in a numerical method for solving the Reynolds averaged Navier-Stokes equations along with a Reynolds stress transport model. This method is referred to by Pope as the Generalized Langevin Method (GLM) [66, 65, 23]. Various forms of the Fokker-Planck model lead to various forms of Reynolds stress transport models, ranging from the simpler Launder, Reece, and Rodi to more complex forms.

The fact that well-known turbulence models emerge from the steps above could be considered affirmation that collision modeling is a viable approach. However, simply returning to a statistical mechanics-based version of a well known turbulence model family also means that this PDF method inherits almost all of the previous problems associated with RST models, most important of which is the inability to capture linear (rapid distortion theory limit) turbulence. While classic PDF methods require no model for the triple correlation $\overline{u_k' u_i' u_j'}$, they still suffer from an inability to capture pressure effects properly. Including pressure effects into the turbulence model allows linear and non-equilibrium turbulence to be accurately predicted.

Perot & Chartrand [10, 56] originally proposed a very general but unoriented Fokker-Planck collision model with more unknowns than the classic Fokker-Planck model proposed by Pope [66]:

$$\frac{\partial f}{\partial t} + v_i \frac{\partial f}{\partial x_i} + a_i \frac{\partial f}{\partial v_i} = -\frac{\partial}{\partial v_j}\left[G_{ij}(v_i - \overline{u}_i)P\right] + \frac{\partial}{\partial v_j}\left[H_{ij}\frac{\partial f}{\partial v_j}\right] + \frac{\partial}{\partial v_j}\left[\left(J_{ij} + \nu \overline{u}_{i,j}\right)\frac{\partial f}{\partial x_j}\right] + \frac{\partial}{\partial x_i}\left[\nu \frac{\partial f}{\partial x_i}\right] + \frac{\partial}{\partial v_i}\left[\nu K_{,n}\frac{\partial}{\partial x_n}\left(\frac{P v_i}{K}\right)\right] \quad (2.6)$$

An additional term may be added to the end of Equation (2.6) to account for mesh motion, which was related to a numerical method used by Perot & Chartrand to solve their generalized Fokker-Planck method using an adaptive three-point mesh in velocity space [56]. In Equation (2.6), G_{ij}, H_{ij} and J_{ij} are tensorial modeling terms, $\overline{u}_{i,j}$ is the mean velocity gradient and $K_{,n}$ the physical-space gradient of the kinetic energy.

Van Slooten and Pope [100], as well as Perot and others [56, 2, 10], have attempted to overcome the inherent limitations of classic Fokker-Planck based PDF turbulence models. Work by Perot determined that any complex extension of the basic Fokker-Planck model (such as the example shown in Equation (2.6)) would simply result in a slightly more complex but still inherently limited RST model. The only way to add substantially more physics was to add orientation to the fluid particles, that is a Fokker-Planck collision model was formed for something like rods or disks (later called eddies) rather than particles which are spheres and have no orientation (see [10]). This can be achieved by adding an "extra" unknown to a Fokker-Planck like collision model yielding derivatives with respect to time, space, and "something else", which could be thought of as eddy orientation.

The work of Reynolds and Kassinos, discussed in the next section, produced a powerful idea: Perhaps the failure of PDF-based turbulence models lies not in the formation of the PDF collision model (*e.g.* Fokker-Planck) but instead in a previously

unimagined missing unknown, perhaps related to orientation of turbulent eddies or, in the case of PDF methods, fluid particles. Van Slooten and Pope took these ideas and applied them to a PDF-based method solved with a particle-based approach (a Monte-Carlo solution), and then using this new method to simulate *inhomogeneous* linear turbulence [100]. They implemented this extra information via a joint PDF of velocity and a "wave vector" [100] which is related to the unit wave vector tied to a given turbulent eddy size. The collection of these vectors are referred to as the directional spectrum. This was a major step forward in PDF-based turbulence modeling, but the method is both difficult to understand and expensive to solve, requiring a large statistical sample in order to return reasonable results from the particle-based solution. Furthermore, Van Slooten & Pope point out the need for improved dissipation models. Perot and Chartrand picked up where Van Slooten

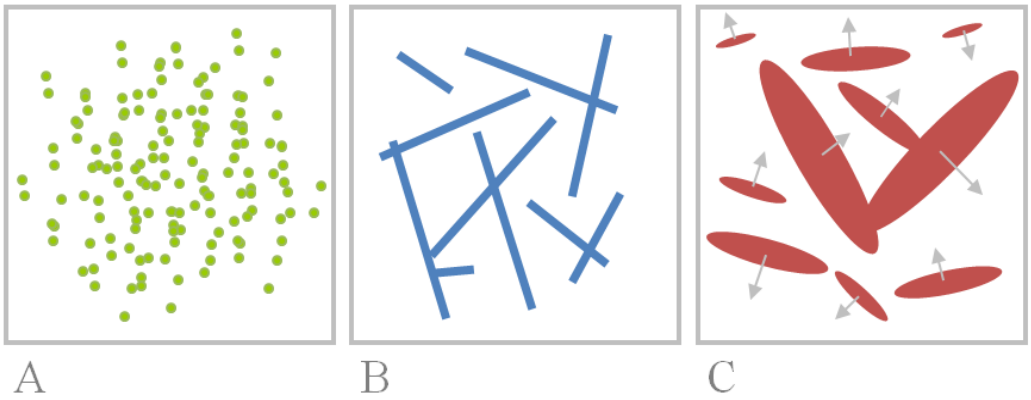

Figure 2.1. Box **A** illustrates a hypothetical region of turbulent fluid as a classic particle collision model, like Fokker-Planck or BGK-Boltzmann. The particles are spheres and cannot have any orientation. Box **B** is a schematic of the same flow but with a collision model that treats particles as rods rather than spheres, thus including orientation information. Finally, box **C** illustrates disks (eddies), which appear to be the shape necessary in order to capture linear turbulence [10].

and Pope left off, believing that the key to linear turbulence was indeed the extra "information" contained within the wave vectors. They chose to add this information as a second derivative to the generalized Fokker-Planck equation (Equation (2.5)):

$$\frac{\partial}{\partial t}f + v_i\frac{\partial}{\partial x_i}f + a_i\frac{\partial}{\partial v_i}f = -\frac{\partial}{\partial v_j}\left[G_{ij}(v_i - \overline{u}_i)f\right] + \frac{\partial}{\partial q_j}\left[H_{ij}q_i f\right] + \beta\frac{\partial^2}{\partial v_i^2}f + \nu\frac{\partial^2}{\partial x_i^2}f \quad (2.7)$$

Note the variable for *orientation* space is denoted here by the vector q_i. Perot and Chartrand interpreted this extra information as eddy orientation (similar to Reynolds' and Kassinos' hypothesis), but chose to transform the PDF collision model into an RST equation form. The resulting model is like a collection of classic RST models (having one Reynolds stress transport equation for each possible orientation), resulting in a model which could capture fast pressure strain exactly, yielded excellent experimental agreement in elliptical flows, and calculated linear turbulence exactly [10].

The oriented model still required model tuning, but the primary RST modeling issue (*i.e.* how to accurately capture pressure effects) had been resolved. Furthermore, unlike the PDF form, when cast as an RST model the turbulent transport term requires treatment, but options for this term are abundant and not difficult to form. A critical difference exists between the model proposed by Reynolds & Kassinos [30] and that of Perot: Perot's real-space eddy orientation model did not take the moment of and subsequently integrate over orientation space, whereas Reynolds & Kassinos did. This step allowed Reynolds & Kassinos to cast their model in the form of a single Reynolds stress transport model for a symmetric, rank three (18 component) tensor transport equation. By choosing to forgo this moment, Perot had to keep orientation in the Reynolds stress equation itself and solve a family of Reynolds stress transport equations (one corresponding to each eddy orientation). Both approaches include orientation information and are exact in the limit of linear turbulence [10].

2.1.2 PRM/IPRM

Taking a step back from PDF methods for a moment, the work of Reynolds and Kassinos [30] should be considered. Reynolds and Kassinos wished to capture rapidly deforming homogeneous turbulence with a Reynolds stress transport model. They

hypothesized that the stress tensor was not enough to capture rapid distortion theory limit turbulence as information about the turbulent structure was not contained within such a quantity. Among other proposals, they suggested a general model which transports a single, rank two tensor, the "eddy axis tensor" which characterizes the shape and orientation of a turbulent eddy. The model employed algebraic equations of state (as opposed to a stress tensor) and two scalar quantities thus containing information about the dimensionality and "componentality" of the turbulence [30]. The model managed to capture many linear turbulence cases exactly, which was the first ever demonstration of an RST-like turbulence model providing accurate solutions in this limit of turbulence [30].

Reynolds and Kassinos furthered this idea with the Particle Representation Model (PRM) [73] and later extended by Kassinos and Akylas with the Interacting Particle Representation Model (IPRM) [1]. Two main differences exist between the PRM / IPRM approaches and the Oriented-Eddy Collision turbulence model. First, PRM / IPRM approaches account for all turbulent structure information whereas the Oriented-Eddy Collision turbulence model approach averages over structures which have the same orientation. Second, PRM / IPRM approaches represent structure via dimensionless, unit vectors and, in order to provide a lengthscale, later solve for an additional quantity which scales the structure vectors. The Oriented-Eddy Collision turbulence model approach folds both structure magnitude and direction into one quantity, the eddy orientation vector.

2.2 Alternative Approaches

2.2.1 Models for Linear Turbulence

One fairly limiting aspect of most turbulence models, including structureless PDF methods, is that they do not capture the linearized Navier-Stokes equations. In theory, a linear equation system should not require a model at all (and should therefore

be trivial to model) as all modes or solutions to the linear equations are uncoupled and do not interact with one another. If one considers the case of incompressible fluid flow, the transport equation for the fluctuating velocity (or turbulence) in a noninertial reference frame is,

$$\frac{\partial u_i^{'}}{\partial t} + \overline{u}_j u_{i,j}^{'} = -\overline{u}_{i,j} u_j^{'} + 2\epsilon_{ijl}\Omega_l u_j^{'} + \nu u_{i,jj}^{'} - p_{,i}^{'} - (u_i^{'} u_j^{'} - \overline{u_i^{'} u_j^{'}})_{,j} \tag{2.8}$$

where $\overline{u}_j$ is the mean velocity, $u_j^{'}$ the fluctuating velocity, ν the kinematic viscosity, ϵ_{ijl} the permutation tensor and Ω_l is the external system rotation rate. This equation also assumes constant viscosity and density, so the fluctuating incompressibility constraint also holds, $u_{i,i}^{'} = 0$, and determines the fluctuating pressure, $p^{'}$. Note that only the final term is nonlinear. If any of the other terms on the right hand side are very large, then the last term can be neglected, the equation system becomes linear, and it is often analytically solvable. The classic case of exact turbulence solutions is rapid distortion theory (RDT), where the first term on the right hand side (involving the mean strain) is large.

It is important to note that the pressure term is always the same order of magnitude as the largest term on the right hand side of Equation (2.8), and therefore never can be neglected. It is key to obtaining the correct solution. The pressure is also the key difficulty with existing turbulence models. Reynolds stress transport (RST) models are derived directly from Equation (2.8). They capture the first term on the right-hand-side (the production term) exactly, but they model the pressure term (which is the same size and therefore always important). Reynolds stress transport models therefore cannot represent the simple case of linearized turbulence (RDT) properly. In fact, it has been shown that models for the pressure effects that only involve the fluctuating velocity are fundamentally incapable of representing all RDT flows correctly [72] regardless of how many tuning constants are involved.

Fundamentally, the problem stems from the nature of the fluctuating pressure which is elliptic and depends strongly on the neighboring velocity field, not the local one. The pressure therefore depends on the shape or structure of the turbulent eddies present in a given flow. The eddies generated by thermal buoyancy in the atmosphere tend to be oblate (flattened) spheroids, while the eddies generated by strong shear tend to be prolate (elongated) spheroids. The local velocity fluctuation levels (Reynolds stresses) may be identical in both flows; however, the turbulence (and therefore the mean flow) evolves differently in the two cases. A model which can predict RDT exactly must somehow capture the effect of these different turbulent eddy structures correctly.

The focus of turbulence modeling has long been on the Reynolds stress tensor (or its divergence, the body force vector [2]) as this is the critical variable needed to predict the mean flow evolution. What has recently become clear is that predicting the Reynolds stress tensor evolution requires knowledge of the local turbulent structure. The equations cannot be closed adequately at the Reynolds stress tensor level. Adding more information leads to a closure approach which captures a great deal more of the physics exactly (including the RDT limit). It is hypothesized that at this level of closure, existing modeling approaches are sufficiently accurate to predict the remaining physics which is not captured by the addition of turbulent structure information.

Pope and Van Slooten [100] extended the concept of probability density function (PDF) models by adding turbulent structure information. A typical PDF model computes the probability of a certain velocity fluctuation at a certain location and time. In [30], the PDF was expanded to compute the probability of a certain velocity and a certain "wavevector" at some location and time (a 10 dimensional space). This model is also capable of exactly predicting linearized turbulence (or rapid distortion theory) in homogeneous conditions.

The Oriented-Eddy Collision turbulence model incorporates turbulence structure information. In this case, the model is derived from the exact two-point velocity correlation transport equation. Two-point correlations are an intuitive representation for turbulence structure. If two separated points have velocities that are closely correlated, they are likely to belong to the same eddy. When a correlation gets close to zero that represents the final extent of the average eddy. It is therefore possible that two-point correlations are a reasonable environment in which to construct a general model for engineering applications (with inhomogeneous turbulence, walls, and other complications), that is still capable of capturing rapid distortions (the linearized limit) exactly.

The derivation of the model is presented. The final result of this section is a collection of Reynolds stress transport (RST) equations. There is one tensor transport equation for each representative eddy orientation. Many existing computational fluid dynamics (CFD) codes have RST models implemented already. This makes the OEC model reasonably simple to incorporate into existing CFD infrastructure. To illustrate this, the results in Chapters 4, 5, and 6 were computed with the Oriented-Eddy Collision turbulence model implemented in the open source collection of computational fluid dynamics libraries, OpenFOAM [27], [81]. Exact results in the RDT limit are shown as well as other important limits, such as rotating decay and return to isotropy, that test the other (inexact) aspects of the model.

2.2.2 Two-point correlations

The general form for the exact but unclosed equation for the evolution of the two-point velocity correlation tensor is

$$
\begin{aligned}
&\frac{\partial}{\partial t}Q_{ij}\left(\mathbf{x},\mathbf{r}\right)+\overline{u}_k(\mathbf{x})\frac{\partial Q_{ij}}{\partial \mathbf{x_k}}=-\left(\overline{u}_{i,k}(\mathbf{x})+2\epsilon_{kil}\Omega_l\right)Q_{kj}-\left(\overline{u}_{j,k}(\tilde{\mathbf{x}})+2\epsilon_{kjl}\Omega_l\right)Q_{ik}\\
&+\left(\overline{u}_k(\mathbf{x})-\overline{u}_k(\tilde{\mathbf{x}})\right)\frac{\partial Q_{ij}}{\partial r_k}-\left(\frac{\partial Q_{(ik)j}}{\partial x_k}-\frac{\partial Q_{(ik)j}}{\partial r_k}\right)-\frac{\partial Q_{i(kj)}}{\partial r_k}\\
&-\left(\frac{\partial \overline{pu_j'}}{\partial x_i}-\frac{\partial \overline{pu_j'}}{\partial r_i}\right)-\frac{\partial \overline{u_i'p}}{\partial r_j}+\nu\left(\frac{\partial^2 Q_{ij}}{\partial x_k\partial x_k}-2\frac{\partial^2 Q_{ij}}{\partial x_k\partial r_k}+2\frac{\partial^2 Q_{ij}}{\partial r_k\partial r_k}\right)
\end{aligned}
\tag{2.9}
$$

In the context of two point correlations, $\mathbf{x}$ is the vector representing the physical location of the first point in a two point correlation and $\mathbf{r}$ a vector pointing toward the second point $\tilde{\mathbf{x}}\equiv\mathbf{x}+\mathbf{r}$. Note that explicit dependence on $\mathbf{x}$ and $\tilde{\mathbf{x}}$ is implied by the index order and is not explicitly stated. In Equation (2.9) above, the notation $Q_{(ik)j}$ implies a triple correlation *viz.* $\overline{u_i'(\mathbf{x})u_k'(\mathbf{x})u_j'(\tilde{\mathbf{x}})}$, and similarly $Q_{i(kj)}=\overline{u_i'(\mathbf{x})u_k'(\tilde{\mathbf{x}})u_j'(\tilde{\mathbf{x}})}$. Note that an external forcing given by the term $\overline{f_i(\mathbf{x})u_j'(\tilde{\mathbf{x}})}+\overline{u_i'(\mathbf{x})f_j(\tilde{\mathbf{x}})}$ has not been explicitly included. In the homogeneous turbulence limit, where the spatial derivatives of turbulence quantities are zero and the mean flow gradients are constant, this becomes [98],

$$
\begin{aligned}
&\frac{\partial}{\partial t}Q_{ij}\left(\mathbf{x},\mathbf{r}\right)=-\left(\overline{u}_{i,k}+2\epsilon_{kil}\Omega_l\right)Q_{kj}-\left(\overline{u}_{j,k}+2\epsilon_{kjl}\Omega_l\right)Q_{ik}-r_l\frac{\partial\overline{u}_k}{\partial x_l}\frac{\partial Q_{ij}}{\partial r_k}\\
&+\left(\frac{\partial \overline{u_j'p}(\tilde{\mathbf{x}},-\mathbf{r})}{\partial r_i}-\frac{\partial \overline{u_i'p}}{\partial r_j}\right)+2\nu\frac{\partial^2 Q_{ij}}{\partial r_k\partial r_k}+\left(\frac{\partial Q_{(ik)j}}{\partial r_k}-\frac{\partial Q_{i(kj)}}{\partial r_k}\right)
\end{aligned}
\tag{2.10}
$$

For an incompressible flow it can be shown that

$$
\frac{\partial Q_{ij}}{\partial r_j}=0 \tag{2.11}
$$

which allows the pressure-velocity correlations (4th term on the right hand side of Equation (2.10)) to be determined. In fact, the only unclosed terms in the two-point evolution equation are the terms involving the two-point triple-velocity correlations (the last term in Equation (2.10)). If the triple-velocity correlations are neglected, Equation (2.10) represents linearized turbulence (RDT).

2.2.3 The Linear OEC Model

To derive the model it is assumed that the correlations can be decomposed using

$$Q_{ij} = \frac{1}{N}\sum_{n=0}^{N} R_{ij}^{n}(t)\frac{\partial F}{\partial \eta}(\eta^{n}) \text{ and } \overline{u_i' p} = \frac{1}{N}\sum_{n=0}^{N} w_i^{n}(t)F(\eta^{n}) \tag{2.12}$$

is employed, where $\eta^n = |r_i q_i^n|$ and $q_i^n(t)$ is the eddy orientation direction. The shape function, $F = F(\eta)$ is some function (like a decaying exponential $\frac{\partial F}{\partial \eta} = e^{-\eta}$) that has a derivative equal to unity at $\eta = 0$ and which drops quickly off to zero at infinity. The function F implies an assumption as to the shape of the two-point correlation subsets. No assumptions are made about the variance. In each direction, given by the orientation vector q_i^n, that eddy's contribution to the correlation will drop off according to the inverse of the length of q_i^n in the direction of q_i^n and will not approach zero in the plane perpendicular to q_i^n. The summation allows different correlation lengths in different directions. As long as the number of eddies, N, is very large, the total correlation will still go towards zero at infinite separation even though individual contributions to the summation may not. In practical computations, a finite sum (often around 20-100 eddies) is used, and the modeled correlations drop to a maximum of 5%-1% at infinite separation. In what follows the orientation superscript, n, is dropped, and summation is assumed over all orientations. Subscripts continue to refer to Cartesian tensor notation.

The decomposition given by Equation (2.12) is powerful. First, it allows complex correlations to be represented simply. When Equation (2.12) is plugged into the two-point evolution equations for homogeneous turbulence (Equations (2.9) and (2.11)) the equations for RDT are recovered (see §2.2.4 for the derivation). For RDT these equations do not depend at all on the choice of F. If the two-point correlation is required, a form for F must be assumed. If the Reynolds stress tensor is the only necessary quantity (which is often the case) then $\overline{R}_{ij} = Q_{ij}(\mathbf{r} = 0) = \frac{1}{N}\sum R_{ij}$ and the system is again independent of the choice of F. It is *very important* to note that

an overbar for turbulent quantities such as $\overline{K}$ and $\overline{R_{ij}}$ refer to **global quantities** in the modeling framework; that is, those averaged over all eddies at a given location in physical space. It does *not* imply ensemble or Reynolds averaging. The context should provide enough information to distinguish between the two definitions of overbars employed.

§2.2.4 shows that the following equations for the decomposition coefficients is a solution for the inviscid two-point RDT equations (Equations (2.10) and (2.11)),

$$\frac{DR_{ij}}{Dt} = \left[\overline{u}_{i,k} + \left(\frac{q_i q_l}{q^2} - \delta_{il}\right) 2\overline{u}^*_{l,k}\right] R_{kj} + \left[\overline{u}_{j,k} + \left(\frac{q_j q_l}{q^2} - \delta_{jl}\right) 2\overline{u}^*_{l,k}\right] R_{ki} \tag{2.13a}$$

$$\frac{Dq_i}{Dt} = -q_k \overline{u}_{k,i} \tag{2.13b}$$

where δ_{ij} is the Kronecker delta, $\overline{u}_i$ the mean velocity, and $\overline{u}^*_{i,j} = \overline{u}_{i,j} + \epsilon_{ikj}\Omega_k$ the transformation-invariant velocity gradient tensor accounting for system rotation effects. Equation (2.13a) accounts for the advection and production of the Reynolds stress tensor as well as the rapid pressure-strain redistribution. Equation (2.13b) is the same as the equation for the normal vector of passive disk embedded in a mean flow. As a result, eddies are often referred to as disk-like (or planar) in shape. This does not imply that the two-point correlation is disk-like, as it is a sum over many eddies all located at the same place and time.

This system (Equations (2.13a) and (2.13b)) can be solved numerically to obtain exact RDT results. The form of the equations is nearly identical in form to the analytical Fourier solution for exact rapid distortion theory from Pope [66]. However, it should be remembered that Equations (2.13a) and (2.13b) were not derived with any relation to Fourier space, and the ideas behind their construction can easily be extended to Equation (2.10) and general turbulence in non-periodic domains, with walls, inhomogeneity, and slow or no strain. While not common, other solutions in the form of correlations exist, such as those proposed by Deissler [15].

2.2.4 Basis

Begin with the simplified transport equation for the two point correlation $Q_{ij}(\mathbf{x},\mathbf{r}) \equiv \overline{u_i'(\mathbf{x})u_j'(\tilde{\mathbf{x}})}$ (Equation (2.10) above),

$$\frac{\partial Q_{ij}}{\partial t}(\mathbf{x},\mathbf{r}) = -\left(\overline{u}_{i,k} + 2\epsilon_{kil}\Omega_l\right)Q_{kj} - \left(\overline{u}_{j,k} + 2\epsilon_{kjl}\Omega_l\right)Q_{ik} - r_l\frac{\partial \overline{u}_k}{\partial x_l}\frac{\partial Q_{ij}}{\partial r_k}$$
$$+\left(\frac{\partial \overline{u_j'p}(\tilde{\mathbf{x}},-\mathbf{r})}{\partial r_i} - \frac{\partial \overline{u_i'p}}{\partial r_j}\right) + 2\nu\frac{\partial^2 Q_{ij}}{\partial r_k \partial r_k} + \left(\frac{\partial Q_{(ik)j}}{\partial r_k} - \frac{\partial Q_{i(kj)}}{\partial r_k}\right) \tag{2.14}$$

and recall that incompressibility requires

$$\frac{\partial Q_{ij}}{\partial r_j} = 0 \tag{2.15}$$

The pressure velocity correlation equation can be expressed as

$$\frac{\partial \overline{u_i'p}}{\partial r_j \partial r_j} = -2\overline{u}^*_{k,j}(\tilde{\mathbf{x}})\frac{\partial Q_{ij}}{\partial r_k} - \frac{\partial^2}{\partial r_k \partial r_k}\left(\overline{u_i'(\mathbf{x})u_k'(\tilde{\mathbf{x}})u_j'(\tilde{\mathbf{x}})}\right) + \overline{u_i'(\mathbf{x})f_{j,j}(\tilde{\mathbf{x}})}. \tag{2.16}$$

The two point fluctuating velocity correlation Q_{ij}, as well as the pressure correlation $\overline{u_i'p}$, and the triple correlation $\overline{u_i'(\mathbf{x})u_k'(\tilde{\mathbf{x}})u_j'(\tilde{\mathbf{x}})}$, may be decomposed as

$$Q_{ij} = \sum_0^\infty R_{ij}\frac{\partial F}{\partial \eta}\overline{u_i'p} = \sum_0^\infty u_i'pF\overline{u_i'(\mathbf{x})u_k'(\tilde{\mathbf{x}})u_j'(\tilde{\mathbf{x}})} = \sum_0^\infty u_i'u_k'u_j'F \tag{2.17}$$

respectively. Note the difference between Equation (2.17) and Equation (2.12) where again $\eta = (q_i r_i)$ and $F = F(\eta) = F(q_i r_i)$ is some positive function. Note that several useful derivatives involving the decompositions above can be calculated,

$$\frac{\partial Q_{ij}}{\partial r_k} = \sum \frac{\partial^2 F}{\partial (q_k r_k)^2} q_k R_{ij},\ \frac{\partial \overline{u_i'p}}{\partial r_j} = \sum \frac{\partial F}{\partial (q_j r_j)} q_j u_i' p,\ \frac{\partial^2 \overline{u_i'p}}{\partial r_j \partial r_j} = \sum \frac{\partial^2 F}{\partial (q_j r_j)^2}(q_j)^2 u_i' p \tag{2.18}$$

noting that the summation limits have been dropped. Starting with Equation (2.16) and using the decompositions in Equation (2.17) and derivatives in Equation (2.18) and simplifying the second derivative of the triple correlation, one arrives at

$$\sum \frac{\partial^2 F}{\partial \eta^2} q^2 u_i^{'} p = -2\overline{u}_{k,j}^{*}(\tilde{\mathbf{x}}) \sum \frac{\partial^2 F}{\partial \eta^2} q_k R_{ij} - \sum u_i^{'} u_k^{'} u_j^{'} q_k q_j \frac{\partial^2 F}{\partial \eta^2} \tag{2.19}$$

noting the last term in Equation (2.16) has been neglected. Dividing though by $\sum \left[\left(\partial^2 F / \partial \eta^2 \right) \left(q_j \right)^2 \right]$ yields

$$\overline{u_i^{'} p} = -2\overline{u}_{k,j}^{*}(\tilde{\mathbf{x}}) \frac{q_k}{q^2} R_{ij} - \frac{q_k q_j}{q^2} u_i^{'} u_k^{'} u_j^{'} \tag{2.20}$$

Moving on to the two point velocity correlation equation, substituting decompositions and evaluating derivatives yields

$$\begin{aligned} &\sum \left(R_{ij,t} \frac{\partial F}{\partial \eta} + \frac{\partial^2 F}{\partial \eta^2} q_{l,t} r_l R_{ij} \right) = \left(2\epsilon_{ikl} \Omega_l - \overline{u}_{i,k} \right) \sum \left(R_{kj} \frac{\partial F}{\partial \eta} \right) \\ &+ \left(2\epsilon_{jkl} \Omega_l - \overline{u}_{j,k} \right) \sum \left(R_{ik} \frac{\partial F}{\partial \eta} \right) - r_l \overline{u}_{k,l} \sum \frac{\partial^2 F}{\partial \eta^2} q_k R_{ij} \\ &- \sum u_j^{'} u_k^{'} u_i^{'} q_k \frac{\partial F}{\partial \eta} - \sum u_i^{'} u_k^{'} u_j^{'} q_k \frac{\partial F}{\partial \eta} - \sum q_i u_j^{'} p \frac{\partial F}{\partial \eta} \\ &- \sum q_j u_i^{'} p \frac{\partial F}{\partial \eta} + 2\nu \sum R_{ij} q^2 \frac{\partial^3 F}{\partial \eta^3} \end{aligned} \tag{2.21}$$

noting again that in Equation (2.21) the forcing terms have been neglected. Equation (2.21) must be simplified. This can be achieved by moving all terms to the right hand side of the equation, grouping with respect to $\sum \partial F / \partial \eta$ (and higher order derivatives), and recalling $\overline{u}_{i,j}^{*} = \overline{u}_{i,j} + \epsilon_{ikj} \Omega_k$,

$$\begin{aligned} 0 = &\sum \frac{\partial F}{\partial \eta} \Big[-R_{ij,t} + [\overline{u}_{i,k} + 2\overline{u}_{l,k}^{*} (\tfrac{q_i q_l}{q^2} - \delta_{il})] R_{jk} + [\overline{u}_{j,k} + 2\overline{u}_{l,k}^{*} (\tfrac{q_j q_l}{q^2} - \delta_{jl})] R_{ik} \\ &- u_i^{'} u_k^{'} u_l^{'} (\delta_{jl} - \tfrac{q_j q_l}{q^2}) q_k - u_j^{'} u_k^{'} u_l^{'} (\delta_{il} - \tfrac{q_i q_l}{q^2}) q_k \Big] - \sum \frac{\partial^2 F}{\partial \eta^2} r_l [q_{l,t} + \overline{u}_{k,l} q_k] R_{ij} \\ &+ \sum \frac{\partial^3 F}{\partial \eta^3} 2\nu k^2 R_{ij} \end{aligned} \tag{2.22}$$

In order to arrive at the fundamental basis for the Oriented-Eddy Collision turbulence model, the flow is assumed to be subject to rapid distortion. This is sensible considering the basis for the model returns the RDT equations. To begin with, terms involving the triple correlation are removed along with the viscous term involving $\partial^3 F/\partial\eta^3$. This reduces Equation (2.22) to

$$0 = \sum \frac{\partial F}{\partial \eta}\left[\overbrace{-R_{ij,t} + [\overline{u}_{i,k} + 2\overline{u}^*_{l,k}(\tfrac{q_i q_l}{q^2} - \delta_{il})]R_{jk} + [\overline{u}_{j,k} + 2\overline{u}^*_{l,k}(\tfrac{q_j q_l}{q^2} - \delta_{jl})]R_{ik}}^{\text{Expression "Y"}}\right] \tag{2.23}$$

$$- \sum \frac{\partial^2 F}{\partial \eta^2} r_l [\overbrace{q_{l,t} + \overline{u}_{k,l} q_k}^{\text{Expression "Z"}}] R_{ij}$$

In Equation (2.23), two expressions have been labeled, "Y" and "Z". Equation (2.23) represents an infinite number of equations involving q_i and r_i. As such, a collection of equations can be assembled representing this summation,

$$\begin{aligned}
0 &= \tfrac{\partial F}{\partial \eta}(q_1, r_1)Y_1(q_1) + \tfrac{\partial F}{\partial \eta}(q_2, r_1)Y_2(q_2) + ... + \tfrac{\partial^2 F}{\partial \eta^2}(q_1, r_1)Z_1(q_1) + \tfrac{\partial^2 F}{\partial \eta^2}(q_2, r_1)Z_2(q_2) + ... \\
0 &= \tfrac{\partial F}{\partial \eta}(q_1, r_2)Y_1(q_1) + \tfrac{\partial F}{\partial \eta}(q_2, r_2)Y_2(q_2) + ... + \tfrac{\partial^2 F}{\partial \eta^2}(q_1, r_2)Z_1(q_1) + \tfrac{\partial^2 F}{\partial \eta^2}(q_2, r_2)Z_2(q_2) + ... \\
0 &= \tfrac{\partial F}{\partial \eta}(q_1, r_3)Y_1(q_1) + \tfrac{\partial F}{\partial \eta}(q_2, r_3)Y_2(q_2) + ... + \tfrac{\partial^2 F}{\partial \eta^2}(q_1, r_3)Z_1(q_1) + \tfrac{\partial^2 F}{\partial \eta^2}(q_2, r_3)Z_2(q_2) + ...
\end{aligned} \tag{2.24}$$

Equation set (2.24) can be assembled into a linear system:

$$\begin{bmatrix} \frac{\partial F}{\partial \eta}(q_1, r_1) + \frac{\partial F}{\partial \eta}(q_2, r_1) + ... + \frac{\partial^2 F}{\partial \eta^2}(q_1, r_1) + \frac{\partial^2 F}{\partial \eta^2}(q_2, r_1) + ... \\ \frac{\partial F}{\partial \eta}(q_1, r_2) + \frac{\partial F}{\partial \eta}(q_2, r_2) + ... + \frac{\partial^2 F}{\partial \eta^2}(q_1, r_2) + \frac{\partial^2 F}{\partial \eta^2}(q_2, r_2) + ... \\ \frac{\partial F}{\partial \eta}(q_1, r_3) + \frac{\partial F}{\partial \eta}(q_2, r_3) + ... + \frac{\partial^2 F}{\partial \eta^2}(q_1, r_3) + \frac{\partial^2 F}{\partial \eta^2}(q_2, r_3) + ... \\ \vdots \end{bmatrix} \begin{bmatrix} Y_1(q_1) \\ Y_2(q_2) \\ \vdots \\ Z_1(q_1) \\ Z_2(q_2) \\ \vdots \end{bmatrix} = \begin{bmatrix} 0 \\ 0 \\ \vdots \\ 0 \\ 0 \\ \vdots \end{bmatrix} \tag{2.25}$$

Considering the restrictions placed upon the function $F(\eta)$, $Y_1(q_1)$, $Y_2(q_2)$, ... and $Z_1(q_1)$, $Z_2(q_2)$, ... must all equate to zero in order to satisfy Equation (2.25). This implies that for any q_i and r_i

$$Y_i(q_i) = -R_{ij,t} + [\overline{u}_{i,k} + 2\overline{u}^*_{l,k}(\tfrac{q_i q_l}{q^2} - \delta_{il})]R_{jk} + [\overline{u}_{j,k} + 2\overline{u}^*_{l,k}(\tfrac{q_j q_l}{q^2} - \delta_{jl})]R_{ik} = 0 \tag{2.26}$$

$$Z_i(q_i) = q_{l,t} + \overline{u}_{k,l} q_k = 0 \tag{2.27}$$

Thus, Equation set (2.27) returns the desired RDT equations and forms the fundamental basis for the Oriented-Eddy Collision turbulence model. Note that neglecting the viscous term in Equation (2.22) is not strictly necessary and the argument above still holds if the term is included in Equation (2.23). This is because any Sturm-Liouville-type ordinary differential equation obeys $\partial^3 F/\partial\eta^3 = C_1(\eta)\partial F/\partial\eta + C_2\eta\,[\partial^2 F/\partial^2\eta]$ and therefore $F(\eta)$ must satisfy this condition.

The decomposition for the two-point velocity correlation $Q_{ij} = \sum R_{ij}\frac{\partial F}{\partial\eta}$ must also be considered in the continuity equation,

$$\frac{\partial}{\partial r_j}\left(\sum R_{ij}\frac{\partial F}{\partial\eta}\right) = 0 \tag{2.28}$$

Expanding the derivative and rearranging yields

$$\sum \frac{\partial^2 F}{\partial\eta^2} R_{ij} q_j = 0 \tag{2.29}$$

noting that this assumes homogeneous flow. By the same argument employed to arrive at Equation set (2.25), one may conclude that $R_{ij}q_j = 0$ and therefore maintaining incompressibility in a homogeneous flow is akin to ensuring orthogonality between R_{ij} and q_j.

CHAPTER 3

THE MODEL

While the basic model presented in the previous chapter is sufficient for simple flows like those considered in Chapter 4, wall bounded flows present a difficult challenge to the model and necessitate a deeper analysis. Much of this effort focused on recasting the model in terms of lengthscales $L_i = q_i/q_i^2$ and normalized Reynolds stress tensors, $R^*_{ij} = R_{ij}/K$. An additional transport equation for the local kinetic energy K was also formulated. Most of these attempts aimed to ensure a stable system close to solid boundaries, where many classic Reynolds stress transport models tend to have stability problems. While future efforts may revisit these ideas (found in Appendix A), they are only briefly considered here.

The reasoning behind using L_i as opposed to q_i is straightforward: avoid infinite boundary conditions on q_i for no-slip walls while employing "easy" boundary conditions on L_i for a solid boundary, namely $L_i|_{wall} = 0$ for $i = 1, 2, 3$. While the units of the eddy orientation vectors change due to the conversion, the relative sizes of the eddy vectors' individual components do not. For example, if the wall-normal direction is 2 (1 and 3 are wall-tangent), then one suspects $q_2 > q_1$ as eddies will tend to align themselves to the walls (recalling q_i has units of *inverse* length). This means that the eddies are small in the wall-normal direction when compared to the wall-tangent directions. But what if this same thought process is applied to the new L_i vectors? In this case, $L_2 > L_1$, meaning the eddies are *smaller* in the plane of the wall and *larger* in the wall normal direction. In addition, as is seen in Appendix A, the conversion from q_i to L_i flips the signs of many terms in the eddy orienta-

tion evolution equation, making source terms appear as sinks and visa versa. This trend continues when considering the relative sizes of eddies in the limit of low or no turbulence. L_i becomes *large* in low Reynolds number flows. It is interesting to consider turbulent eddies *growing* as the Reynolds number decreases. In turbulent flows, eddies (especially those near walls; see, for example, [44]), tend to shrink with increasing Reynolds number. This aligns with the behavior of L_i (or q_i). As a flow becomes laminar, however, a characteristic eddy should in fact vanish as turbulence itself vanishes. Constructing a model which behaves like this is difficult without some unphysical "switch" that alters the eddies in some way. In the current interpretation, eddies would become infinitely-sized in laminar flows.

Close analysis of the eddy orientation vector transport equation prompted a comparison of the existing q_i equation to the K equation from the "qkR*" model variant (see Appendix A). If one were to inspect the evolution of $q^2 = q_i q_i$ rather than q_i itself, corollaries could be drawn between this and the K equation. A sanity check can then be performed on the K equation by comparing it to kinetic energy equations from other well-known turbulence models such as the famous $K - \epsilon$ model, discussed in Appendix D.4. The goal of such an exercise is to find a term which is always a source for q_i and determine a stable method of imposing the necessary boundary conditions. The nature of boundary conditions applied to q_i can be understood by examining the equation for K, seen below in a slightly modified form:

$$\frac{DK}{Dt} = \tag{3.1a}$$

$$\left[\overline{u}_{i,k} + \left(\frac{q_i q_l}{q^2} - \delta_{il}\right) 2\overline{u}^*_{l,k}\right] R_{ki} \tag{3.1b}$$

$$- \left(\alpha\nu\overline{q^2}\right) K - \frac{1}{\tau_R} K \tag{3.1c}$$

$$+ \left[\left(\nu + \nu_t\right) K_{,k}\right]_{,k} \tag{3.1d}$$

$$- E\left(\nu + \nu_t\right) \frac{1}{2} \frac{(K)_{,k}(K)_{,k}}{K} \tag{3.1e}$$

$$+ \frac{1}{2} W_{ii} \tag{3.1f}$$

noting that

$$\left[\overline{u}_{i,k} + \left(\frac{q_i q_l}{q^2} - \delta_{il}\right) 2\overline{u}^*_{l,k}\right] R_{ki} = \left[\overline{u}^*_{l,k} R_{ki}\right] \tag{3.2}$$

as $R_{ki} q_i = 0$; pressure effects (the terms which involve q_i) do not affect the kinetic energy. Expression (3.1b) includes the production-like terms, Expression (3.1c) is a decay term, Expression (3.1d) is the viscous diffusion term, Expression (3.1f) is a remnant from the Reynolds stress near-wall reorientation term (which should be identically zero), and of most interest Expression (3.1e) is taken from previous work by Perot and Natu [61] on the Reynolds stress evolution equation. Previous versions of the Oriented-Eddy Collision turbulence model ignored this term, effectively setting the scalar $E = 0$. This is theoretically possible as $\nu\left(q_i q_i\right)$ in term (3.1c) accomplished the same objective if $q_i q_i$ were to approach a solid boundary like $\frac{2}{\alpha/y^2}$. However, it was hypothesized that $q_i q_i$ is *not* infinite at a solid boundary and the "E" term in fact plays a crucial role in dictating the behavior of the Oriented-Eddy Collision turbulence model near walls. If the desired asymptotic behavior of the kinetic energy K is assumed, that is $K \sim y^2$ or a Taylor series $K \sim ay^2 + by^3 + ...$, the equation above can be written as:

$$O(y^2) = \tag{3.3a}$$

$$[\overline{u}_{1,2}]\, O\left(y^2\right) \tag{3.3b}$$

$$-\left(\alpha\nu\overline{q^2}\right)\left(ay^2 + by^3 + ...\right) - \frac{1}{\tau_R} O\left(y^2\right) \tag{3.3c}$$

$$+ \left(\nu + \nu_t\right)\left(2a + 6by + ..\right) + \nu_{t,k}\left(2ay + ...\right) \tag{3.3d}$$

$$- E\left(\nu + \nu_t\right)\left(2a + 4by + ...\right) \tag{3.3e}$$

$$+ \frac{1}{2} W_{ii} \tag{3.3f}$$

Without term (3.3e), the only way to enforce the desired asymptotic behavior of K was to require that $\overline{q^2} \sim \frac{1}{y^2}$. This approach was theoretically feasible, but very difficult numerically due to q_i becoming infinite at solid boundaries. Now, with term (3.1e), the desired asymptotic behavior can be realized without resorting to infinite boundary conditions. The boundary conditions for q_i

$$q_i|_{wall} = \begin{bmatrix} q_1 = 0 \\ \frac{\partial q_2}{\partial y} = 0 \\ q_3 = 0 \end{bmatrix} \tag{3.4}$$

should be sufficient. As will be discussed in Chapter 5, these boundary conditions are open to interpretation.

3.1 OEC in Simple Flows

For a full Oriented-Eddy Collision turbulence model, the equation system must be generalized to account for diffusion, as well as the nonlinear affects of turbulent dissipation, and return to isotropy. These effects may appear in either or both Equations (2.13a) and (2.13b). The turbulent dissipation term is discussed in detail in de Bruyn Kops and Perot [62]. In summary, the decay equations are

$$\frac{\partial R_{ij}}{\partial t} = -\left(2\alpha\nu\overline{q^2} + \frac{1}{\tau_R}\right) R_{ij} \tag{3.5a}$$

$$\frac{\partial q_i}{\partial t} = -\frac{1}{3}\left(2\alpha\nu\overline{q^2} + \frac{1}{\tau_R}\right) q_i \tag{3.5b}$$

where $\frac{1}{\tau_R}$ is the inverse turbulent timescale. These equations will produce the exact decay behavior for isotropic turbulence in both the high Reynolds number (Re) limit and the low Reynolds number limit. The constant α, which is often set to 15.0, determines the Reynolds number at which the switch from high to low Reynolds number behavior occurs. The fraction 1/3 is exact for Saffman decay [84], [82] (a low wavenumber spectrum of K^2) which was determined to be appropriate for turbulence generated by walls [55]. Note that a fraction of 1/5 is correct for Kolmogorov/Bachelor decay (a low wavenumber spectrum of K^4), if that is desired. It is important to note that the viscous inverse time-scale is $2\alpha\nu\overline{q^2}$, the turbulent inverse time-scale is $1/\tau_R$, and their effect is additive in this model.

The positive definite inverse eddy turnover time can be constructed as $1/\tau_R = \left(\overline{Kq^2}\right)^{1/2} = \overline{K}^{1/2}\left(\frac{1}{N}\sum q^2\right)^{1/2}$. Alternatives exist, and are discussed briefly later in this chapter. The average kinetic energy over all eddies is defined as $\overline{K} = \frac{1}{N}\sum\left(\frac{1}{2}R_{ii}\right)$ where N is the number of eddies employed in a given simulation of turbulent flow. Recall the overbar is used to indicate a quantity which has been averaged over all eddies. The quantities of interest to the engineer returned by this model are not the individual eddies' statistics but those quantities averaged over all eddies.

Return-to-isotropy is another important result of the nonlinear turbulence-turbulence interactions. A number of return-to-isotropy models are considered in Chartrand and Perot [57], including one just on the cusp of strong realizability that has no tunable constants. In this work a modified version of Rotta's linear return-to-isotropy model [79] is employed for the orientation stresses in Equation (2.13a).

$$-\frac{1}{\tau_R}\left(\frac{C_R}{1+C_B\nu/\nu_T}\right)\left[R_{ij} - \overline{K}\left(\delta_{ij} - \frac{q_i q_j}{q^2}\right)\right] \tag{3.6}$$

In Expression (3.6), C_R and C_B are tunable constants. The first is quite important and is set to 1.375. The latter, set to 1.0, is only active in the very low Reynolds number limit where it sets the Re where return-to-isotropy goes to zero, recalling that at very low Reynolds numbers the flow becomes Stokes flow and is once again linear with effectively no modal interactions.

The positive definite turbulent viscosity is given by $\nu_T = \left(\overline{K^2}/\overline{Kq^2}\right)^{1/2}$, noting that alternatives are explored at the end of this chapter. The Reynolds stress isotropy is typically defined as the scalar kinetic energy multiplied by the identity tensor, $\frac{2}{3}\overline{K}\delta_{ij}$. In Expression (3.6), however, this tensor is modified by the normalized outer product of the orientation vector $q_i q_j/q^2$. This modification of the term means that this return term is always orthogonal to the orientation vector. §2.2.4 shows how orthogonality of the orientation stress and the orientation vector is a direct result of the fluctuating incompressibility constraint. This form of the return term means that this orthogonality is maintained even during return-to-isotropy. While the two terms are similar in form, note that the formulation of the eddy viscosity is not related to the formulation of the turbulent time scale.

Return-to-isotropy of the orientation vectors is similar but operates on a vector rather than a tensor term:

$$A_i = -\frac{1}{\tau_R}\left(\frac{C_Q}{1+C_B\nu/\nu_T}\right)\left[3\frac{\overline{q_i q_k}}{\overline{q^2}} - \delta_{ki}\right] q_k \tag{3.7}$$

The tensor $\overline{q_i q_k}/\overline{q^2}$ represents the average orientations of the eddies. When one of the diagonal components of this tensor is large, then most of the eddies point in that direction, or the eddies that point in that direction have small sizes (and hence large q^2). The value of C_Q is typically larger than C_R and is set to 2.75 in this work. Isotropy in the Oriented-Eddy Collision turbulence model therefore occurs when the oriented stresses become isotropic, but also when the eddy orientations become uniformly distributed on a sphere. Note that mean flow gradients tend to

distort the orientation distribution, and random mixing by turbulence tends to return orientations to the isotropic state. Again, some novel alternatives to the eddy vector return term are covered at the end of this chapter.

In order to maintain orthogonality (or fluctuating incompressibility), a term must be added to the stress equation to account for the orientation return to isotropy:

$$\left(R_{lj}\frac{q_i}{q^2} + R_{li}\frac{q_j}{q^2}\right)(A_l) \tag{3.8}$$

§3.2 shows how this term makes $\frac{\partial(R_{ij}q_j)}{\partial t} = 0$, which implies that orthogonality is preserved by the transport equations if the system starts in an orthogonal state which is necessary in order to be a consistent incompressible initial condition.

For flows far from features such as solid boundaries or shear free interfaces, accounting for viscous diffusion is straightforward. The Laplacian of the effective viscosity and the quantity of interest - the eddy orientation vector or Reynolds stress tensor - should suffice:

$$+\left[(\nu + \nu_T)\, R_{ij,k}\right]_{,k} \text{ and } + \frac{1}{3}\left[(\nu + \nu_T)\, q_{i,k}\right]_{,k} \tag{3.9}$$

although complications in non-homogeneous flows arise, and are discussed briefly at the end of this chapter. The factor of 1/3 is included to be consistent with the dissipation models but has no real theoretical basis for inclusion in the diffusion term. Initial tests of the Oriented-Eddy Collision turbulence model in wall bounded flows revealed troublesome behavior coming from terms such as $\left[(\nu + \nu_T)\, q_{i,k}\right]_{,k}$, the diffusion of q_i. The turbulent viscosity, calculated as $\nu_T = \sqrt{\overline{K^2}/\overline{Kq^2}}$ in the original "qR" model, can be compared to its corollary from the $K - \epsilon$ model. Although previously unstated, formally a constant coefficient C_μ should be prepended to the turbulent viscosity formula, *viz.* $\nu_T = C_\mu\sqrt{\overline{K^2}/\overline{Kq^2}}$. In the past, $C_\mu = 1$. Typically, the corresponding eddy viscosity from the $K-\epsilon$ model uses $C_\mu = 0.09$. This indicated

that the value of the eddy viscosity in early versions of the Oriented-Eddy Collision turbulence model was an order of magnitude higher than it should have been. This discovery added to the suspicion that diffusion was somehow incorrect. With all of the previous points in place, the current version of the Oriented-Eddy Collision turbulence model may be proposed.

It is also important for the Oriented-Eddy Collision turbulence model to respond properly to system rotation either due to the mean flow or due to a non-inertial frame. This may be achieved by modifying the decay rate of the orientation vectors to account for system rotation:

$$-\frac{1}{\tau_R}\left[\frac{\overline{\left(q_k\Omega_k^*\right)^2/q^2}}{20\overline{q^2}\,\overline{K}+0.25\left(\Omega_k^*\right)^2}\right]q_i \tag{3.10}$$

where the absolute vorticity is $\Omega_k^* = \epsilon_{ijk}\overline{u}_{k,j} + \Omega_i$. The term $q_k\Omega_k^*$ implies that turbulence that is two-dimensional (*i.e.* has one component of the orientation always zero) will not be affected by system rotation perpendicular to that plane (as theory dictates). At low rotation rates this term becomes negligible, with the value of "low" dictated by the constant 20. At high rotation rates the term in square parenthesis approaches 4/3, leading to a theoretical decay rate for the kinetic energy of 6/13. A value of 0.4 (rather than 0.25) for the second constant leads to a kinetic energy decay rate of 3/5 (as cited in [48]). The two numerical constants in the Equation (3.10) were determined empirically through the work of Perot and Chartrand [10]. A somewhat simpler rotation model is considered later.

The complete transport equations for the Oriented-Eddy Collision turbulence model away from solid boundaries can now be constructed. The orientations obey the equation,

$$q_{i,t} + \left(\overline{u}_j q_i\right)_{,j} = -q_k \overline{u}_{k,i} - \tfrac{1}{3}\left(\alpha\nu\overline{q^2} + \tfrac{1}{\tau_R}\left\{1 + \frac{3\overline{\left(q_k\Omega_k^*\right)^2/q^2}}{20.0\overline{q^2}\overline{K} + 0.25\left(\Omega_k^*\right)^2}\right\}\right) q_i$$
$$+ \tfrac{1}{3}\left[\left(\nu + \nu_T\right) q_{i,k}\right]_{,k} - \tfrac{1}{\tau_R}\left(\tfrac{C_Q}{1+C_B\nu/\nu_T}\right)\left[3\tfrac{\overline{q_i q_k}}{\overline{q^2}} - \delta_{ki}\right] q_k \tag{3.11}$$

Similarly, the evolution equation for the Reynolds stress tensor becomes

$$R_{ij,t} + \left(\overline{u}_k R_{ij}\right)_{,k} = \left[\overline{u}_{i,k} + \left(\tfrac{q_i q_l}{q^2} - \delta_{il}\right) 2\overline{u}_{l,k}^*\right] R_{kj} + \left[\overline{u}_{j,k} + \left(\tfrac{q_j q_l}{q^2} - \delta_{jl}\right) 2\overline{u}_{l,k}^*\right] R_{ki}$$
$$- \left(\alpha\nu\overline{q^2} + \frac{1}{\tau_R}\right) R_{ij} - \tfrac{1}{\tau_R}\left(\tfrac{C_R}{1+C_B\nu/\nu_T}\right)\left[R_{ij} - \overline{K}\left(\delta_{ij} - \tfrac{q_i q_j}{q^2}\right)\right]$$
$$+ \left(R_{lj}\tfrac{q_i}{q^2} + R_{li}\tfrac{q_j}{q^2}\right) A_l + \left[\left(\nu + \nu_T\right) R_{ij,k}\right]_{,k} \tag{3.12}$$

Equations (3.11) and (3.12) represent the form of the Oriented-Eddy Collision turbulence model used for benchmark cases in Chapter 4.

3.2 Maintaining orthogonality between q_i and R_{ij}

Equation (2.29) requires that the transport equations for R_{ij} and q_j maintain orthogonality between the two quantities for all time. More succinctly, it is necessary that

$$\tfrac{\partial}{\partial t}\left(R_{ij} q_j\right) = 0 \tag{3.13}$$

In order to ensure Equation (3.13) is satisfied, Expression (3.8) was added to the Reynolds stress transport equation (Equation (3.12) above). Expanding Equation (3.13) illustrates this,

$$
\begin{aligned}
&\tfrac{\partial}{\partial t}\left(R_{ij}q_j\right) = q_j\tfrac{\partial R_{ij}}{\partial t} + R_{ij}\tfrac{\partial q_j}{\partial t} \\
&= q_j\Big\{-\left(\overline{u}_k R_{ij}\right)_{,k} + \left[\overline{u}_{i,k} + \left(\tfrac{q_i q_l}{q^2} - \delta_{il}\right)2\overline{u}^*_{l,k}\right]R_{kj} + \left[\overline{u}_{j,k} + \left(\tfrac{q_j q_l}{q^2} - \delta_{jl}\right)2\overline{u}^*_{l,k}\right]R_{ki} \\
&- \left(\alpha\nu\overline{q^2} + \frac{1}{\tau_R}\right)R_{ij} - \tfrac{C_R}{\tau_R}\left(\tfrac{1}{1+C_B\nu/\nu_T}\right)\left[R_{ij} - \overline{K}\left(\delta_{ij} - \tfrac{q_i q_j}{q^2}\right)\right] \\
&+ \left(R_{lj}\tfrac{q_i}{q^2} + R_{li}\tfrac{q_j}{q^2}\right)A_l + \left[\left(\nu+\nu_T\right)R_{ij,k}\right]_{,k}\Big\} \\
&+ R_{ij}\Big\{-\left(\overline{u}_k q_j\right)_{,k} - q_l\overline{u}_{l,j} - \tfrac{1}{3}\left(\alpha\nu\overline{q^2} + \tfrac{1}{\tau_R}\left\{1 + \tfrac{3\overline{\left(q_l\Omega^*_l\right)^2/q^2}}{20.0\overline{q^2}\,\overline{K} + 0.25\left(\Omega^*_l\right)^2}\right\}\right)q_j \\
&+ \tfrac{1}{3}\left[\left(\nu+\nu_T\right)q_{j,l}\right]_{,l} - \tfrac{C_Q}{\tau_R}\left(\tfrac{1}{1+C_B\nu/\nu_T}\right)\left[3N_{lj} - \delta_{lj}\right]q_l\Big\}
\end{aligned}
\tag{3.14}
$$

Equation (3.14) is cumbersome and must be simplified. To begin with, again assume homogeneous turbulence and neglect the viscous terms as well as any expression involving the gradient of the mean velocity. Multiplying through by q_j and R_{ij}, Equation (3.14) reduces to

$$
\begin{aligned}
&q_j\tfrac{\partial R_{ij}}{\partial t} + R_{ij}\tfrac{\partial q_j}{\partial t} = q_j\left[\overline{u}_{i,k} + \left(\tfrac{q_i q_l}{q^2} - \delta_{il}\right)2\overline{u}^*_{l,k}\right]R_{kj} + q_j\left[\overline{u}_{j,k} + \left(\tfrac{q_j q_l}{q^2} - \delta_{jl}\right)2\overline{u}^*_{l,k}\right]R_{ki} \\
&- q_j\left(\alpha\nu\overline{q^2} + \frac{1}{\tau_R}\right)R_{ij} - q_j\tfrac{C_R}{\tau_R}\left(\tfrac{1}{1+C_B\nu/\nu_T}\right)\left[R_{ij} - \overline{K}\left(\delta_{ij} - \tfrac{q_i q_j}{q^2}\right)\right] \\
&+ q_j\left(R_{lj}\tfrac{q_i}{q^2} + R_{li}\tfrac{q_j}{q^2}\right)A_l - R_{ij}q_l\overline{u}_{l,j} - \tfrac{1}{3}R_{ij}\left(\alpha\nu\overline{q^2} + \tfrac{1}{\tau_R}\left\{1 + \tfrac{3\overline{\left(q_l\Omega^*_l\right)^2/q^2}}{20.0\overline{q^2}\,\overline{K} + 0.25\left(\Omega^*_l\right)^2}\right\}\right)q_j \\
&- R_{ij}\tfrac{C_Q}{\tau_R}\left(\tfrac{1}{1+C_B\nu/\nu_T}\right)\left[3N_{lj} - \delta_{lj}\right]q_l
\end{aligned}
\tag{3.15}
$$

Assume that the stress tensor and eddy orientation vector begin orthogonal $R_{ij}q_j|_{t=0} = 0$ (which the code ensures). In this case, all terms in Equation (3.15) which involve this product must be zero initially. This further simplifies Equation (3.15),

$$
\begin{aligned}
&q_j\tfrac{\partial R_{ij}}{\partial t} + R_{ij}\tfrac{\partial q_j}{\partial t} = q_j\overline{u}_{j,k}R_{ki} + R_{li}A_l - R_{ij}q_l\overline{u}_{l,j} \\
&- R_{ij}\tfrac{C_Q}{\tau_R}\left(\tfrac{1}{1+C_B\nu/\nu_T}\right)\left[3N_{lj} - \delta_{lj}\right]q_l
\end{aligned}
\tag{3.16}
$$

By substituting the definition of the eddy orientation vector return-to-isotropy A_l (Equation (3.7)) into Equation (3.16),

$$q_j \frac{\partial R_{ij}}{\partial t} + R_{ij} \frac{\partial q_j}{\partial t} = q_j \overline{u}_{j,k} R_{ki} + R_{li} \left[\frac{C_Q}{\tau_R} \left(\frac{\nu_T}{\nu_T + C_B \nu} \right) [3N_{kl} - \delta_{kl}] \, q_k \right]$$
$$- R_{ij} q_l \overline{u}_{l,j} - R_{ij} \frac{C_Q}{\tau_R} \left(\frac{1}{1 + C_B \nu / \nu_T} \right) [3N_{lj} - \delta_{lj}] \, q_l. \tag{3.17}$$

and rearranging subscripts it is easily shown that $q_j \frac{\partial R_{ij}}{\partial t} + R_{ij} \frac{\partial q_j}{\partial t} = \frac{\partial}{\partial t} (R_{ij} q_j) = 0$ and thus the transport equations maintain orthogonality between q_j and R_{ij} for homogeneous turbulent flows.

The complete Oriented-Eddy Collision turbulence model presented in the preceding sections (Equations (3.11) and (3.12)) was employed for the benchmark cases presented in Chapter 4. Several terms in the model warrant discussion when wall-bounded flows are considered. While most of the discussion pertaining to solid boundaries is considered in Chapter 5, some alternatives to existing model terms will be presented here for completeness.

3.3 Diffusion Near Walls

The diffusion term in the eddy orientation transport equation involves taking the divergence of the effective viscosity $\nu + \nu_T$ multiplied by the gradient of the orientation vector q_i

$$\left[(\nu + \nu_t) \, q_{i,k} \right]_{,k} \tag{3.18}$$

When the Oriented-Eddy Collision turbulence model was first developed and the viscous diffusion term first constructed, nearly all flows of interest were isotropic or homogeneous (*i.e.* zero diffusion). As such, for a given eddy (say, perhaps, eddy #36), the direction of that eddy at one cell was identical to the direction of the same eddy in another cell. The only difference that might exist between the two eddy #36s would be their magnitude. Thus, the diffusion term would be reduced to a measure of the difference between eddy vector magnitudes amongst neighboring cells. As was demonstrated extensively in Chapter 4, this term operated as expected. A subtlety arises when considering nonhomogeneous flows. The Laplacian operator applied to

two eddies widely differing in direction may return incorrect results. Figure 3.1(a) illustrates the simpler case where the direction of an eddy in one cell is aligned to that eddy's counterpart in any other cell. This is case where the standard approach to viscous diffusion is permissible. Figure 3.1(b) illustrates the problematic case where a given eddy and its counterpart may be pointing in different directions across neighboring cells. A diffusion term for q_i is supposed to be a measure of the differences

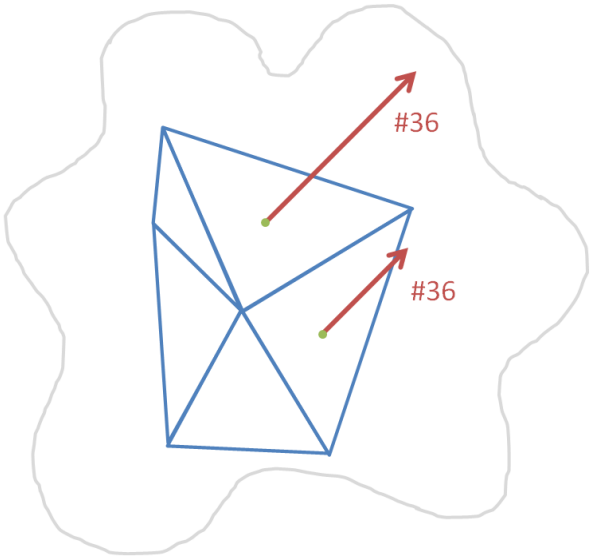

(a) Far away from any source of anisotropy, eddy #36 in one cell points in the same direction as eddy #36 in another cell, even if their magnitudes differ.

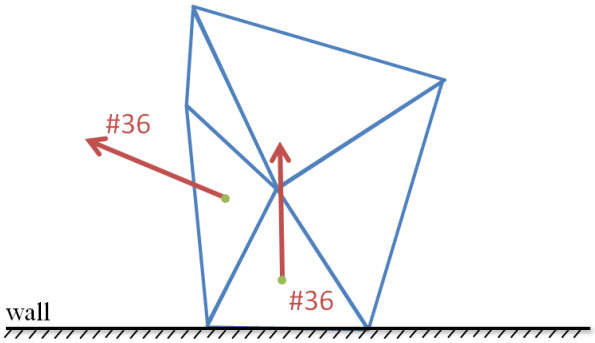

(b) In anisotropic situations (such as near a wall), eddy #36 may be very different from its partner in a neighboring cell.

Figure 3.1. Possible pitfalls of using classic diffusion for eddy orientation vectors.

in magnitude amongst eddy orientation vectors, not the difference in direction - that is the job of the return-to-isotropy model. It was believed that may lead to unstable or erroneous behavior of the viscous diffusion term in the eddy orientation evolution equation near solid boundaries where anisotropy dominates. As such, diffusion and turbulent viscosity were closely examined.

3.3.1 Statistical Approach

One way to overcome the difficulty above is to tackle viscous diffusion statistically. This novel approach removes the viscous diffusion term entirely from the eddy orientation transport equation. Rather than relying on viscosity and gradients, a randomly selected fraction of eddies at each cell may be swapped across a cell's face to a neighboring cell according to the likelihood that a swap might occur across that face. The likelihood of a swap is dictated by the "normal distance" dx between cell centers, that is the distance between cell centers dotted with the shared face normal. This distance dx is used to calculate the probability of a swap occurring across the face shared between a cell and its neighbor, $D = C\sqrt{(\nu dt)/dx^2}$ with ν the kinematic viscosity, dt the simulation time step, and C a tunable constant which represents the ratio of "statistical" to kinematic viscosity. This procedure is repeated at every cell in a given mesh, for every neighbor of that cell. OpenFOAM provides ample mesh connectivity information making implementation of this algorithm trivial.

For every shared face between a cell and its neighbors, a loop over every eddy stored at the parent cell assigns a random number between zero and one to that eddy. If this random number (the eddy's swap probability) lies below D, the eddy is swapped with its partner in the neighboring cell. For example, if $D \approx 0.2$, on average 20% of the eddies contained at the parent cell would be swapped with the neighbor cell whose shared face was employed to calculate D. If 10 eddies are stored at each cell, then on average two will swap across the face in question at every time step.

The higher the probability, the more chance of a swap (*i.e.* the greater chance that the eddy's swap probability will fall below D). Note that at first glance D appears to have an upper limit of unity, as $D = 1$ would indicate that all eddies are swapped across a shared face at every time step. This, however is not the case. "Substepping" could be employed in the event that $D > 1$: If, for example, $D \approx 2$, the eddies could be given not one but *two* opportunities to swap over a given face, effectively doubling their odds of swapping.

The user-set constant C is necessary to fine tune the statistical diffusion algorithm. The higher the swap probability D, the more swaps will occur on average across faces at every time step. More swaps translates into higher effective (statistical) diffusion. Even if the seed for the random number generator is fixed (thus making the procedure perfectly reproducible), there is no way to fine tune the probability (without altering the kinematic viscosity, the time step, or the mesh). To overcome this obstacle, the algorithm was employed to replace viscous diffusion in a laminar Poiseuille flow simulation where a known analytical solution existed. Instead of swapping turbulent eddies (which makes little sense in a laminar flow), a collection of velocity vectors was stored at each cell. The basic algorithm is outlined in Algorithm 1. Algorithm 1 relies on the existence of neighboring cells to identify shared faces and eventually swap eddies across those faces. This works well for internal cells, but what of cells that lie on a boundary? For channel flow, the ability for viscosity and pressure to transmit information about the presence of a wall to the interior of the flow is of paramount importance. Statistical diffusion must handle walls properly. In OpenFOAM, a cell which lies on a boundary has no neighbor cell across that boundary (a method often employed to enforce boundary conditions using "ghost" or "halo" cells which lie *outside* the domain; see, for example, [44]). Boundary cells must receive eddies from the wall, but the wall contains no eddies to swap. A slight modification to Algorithm 1 can be made by looping over all faces which belong to a cell and determining if a face

```
for all cells do {Loop over all cells in a given mesh}
  ⋮
  myCenter = cell(center)
  myNeighbors = cell(neighbors)
  ⋮
  for all neighbors do {Loop over neighbors}
    ⋮
    neighborCenter = neighbor(center)
    distance = neighborCenter - cellCenter
    sharedFace = getSharedFace(cell, neighbor)
    ⋮
    dx = distance · sharedFace(normal) {dx is the normal distance}
    D = C√((νdt)/dx²)
    chance = random[0,1] {The probability of an eddy swap, between 0 and 1}
    ⋮
    for all eddies(cell) do {Loop over all eddies stored at this cell}
      ⋮
      if chance ≤ D then
        Swap this eddy(cell) with eddy(neighbor)
      end if
      ⋮
    end for
    ⋮
  end for
  ⋮
end for
```

Algorithm 1: An algorithm for performing statistical diffusion on eddy orientation vectors.

belongs to a boundary patch (which is easily accomplished in OpenFOAM). Algorithm 2 outlines the basic method of handling cells with faces that lie on boundaries. Note that no swap actually occurs - if an eddy is selected for a swap across a face on a boundary patch, that eddy instead has its boundary conditions applied. Also note that the wall needn't ever "receive" an eddy into it. As was mentioned previously, laminar Poiseuille flow was employed to test the method and a collection of velocity vectors were stored at cells rather than eddy orientation vectors. The procedures out-

```
for all faces do {Loop over this cell's faces}
  if face ∈ boundary patch then
    for all eddies(cell) do
      if chance ≤ D then
        Apply wall BC to eddy
      end if
    end for
  end if
end for
```

Algorithm 2: A method to handle statistical diffusion at walls properly.

lined in Algorithms 1 and 2 succeeded in returning laminar Poiseuille flow in a channel after the constant C was tuned. Initial tests showed good agreement. Unfortunately, after extensive testing, the statistical diffusion proved sensitive to changes in viscosity and was computationally expensive. While capable of replacing the typical diffusion term in laminar channel flow cases, the cost, numerical sensitivity, tight dependence on viscosity, as well as the necessity to employ large numbers of eddies, led to the method being abandoned.

3.3.2 Average Eddy Magnitude Approach

The statistical approach outlined above is only useful if it is both computationally efficient and stable. An alternative approach was formulated which does not rely on a statistical interpretation of diffusion. Recall the issues with viscous diffusion centered around differences in eddy vector orientation, for the same eddy, across different cells. Furthermore, in the case of eddy orientation vectors, the differences in *magnitude* amongst eddies and their counterparts in other cells is the relevant quantity for viscous diffusion. A method was sought to determine a cell's average eddy size in *all* directions. If this information were available, a cell may gain access to its neighbor's average eddy size information *in the direction of all of its own eddies.* Figure 3.2 illustrates this concept. To give a concrete example: Consider an eddy, perhaps eddy #36, in cell A (in Figure 3.2). This eddy requires access to the average

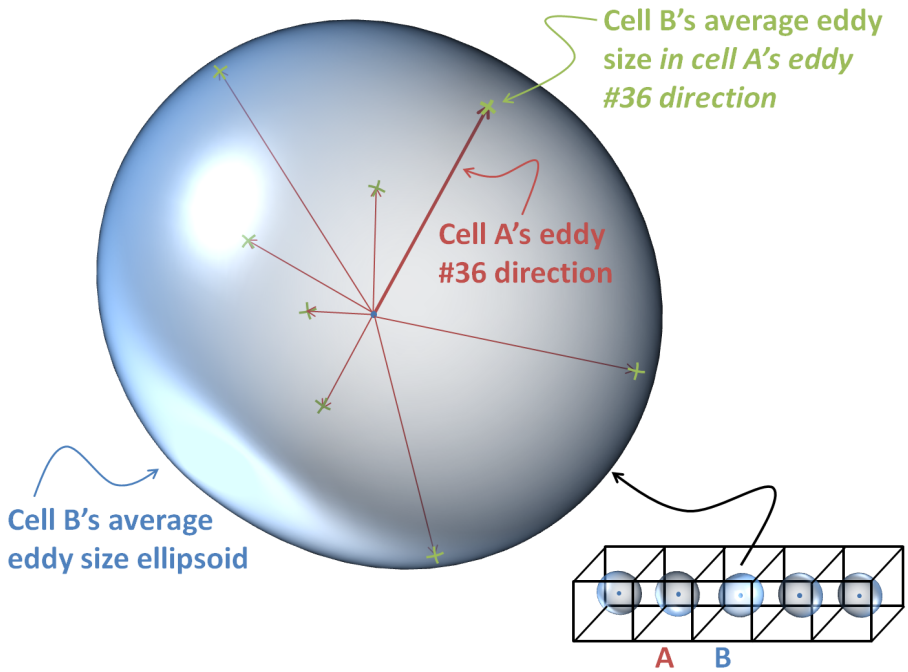

Figure 3.2. An ellipsoid representing the average eddy size in all directions can be computed for each cell. To calculate diffusion for a given eddy at a neighboring cell, the "average eddy size" ellipsoid provides the average eddy size in the direction of the neighboring cell's eddy.

eddy size for neighboring cells *in the direction of cell A's eddy #36*. As such, the average eddy size ellipsoid in cell B (a neighbor of cell A) is polled for its value in the direction of cell A's eddy #36. This effectively eliminates the problem of misaligned eddy pairs while preserving vital eddy magnitude information and enabling the calculation of viscous diffusion for cell A's eddy #36. See Appendix H for details on the calculation of the "average eddy" ellipse.

While appealing on paper and for the eddy orientation vectors, this method has its own set of difficulties. First, while the construction of the average eddy ellipse (Appendix H) is possible, construction of the corresponding structure for R_{ij} is difficult. In addition, calculation of the structure information at each cell and each time step is expensive. An analysis of q_i in the log layer (see Appendix G) reveals that 1) local R_{ij} and q_i should in fact vary slowly in space thus avoiding the issues associated

with taking their Laplacian; and 2), the coefficient scaling the turbulent viscosity ν_T, C_ν should be order $\mathcal{O}(0.1)$, opposed to order $\mathcal{O}(1)$ as it had been previously. This observation provided a more reasonable explanation for the instabilities previously associated with diffusion.

3.3.3 Current Approach

With the reduction of C_ν from $\mathcal{O}(1)$ to $\mathcal{O}(0.1)$, wall bounded flows - specifically turbulent channel flow run at a friction Reynolds number $Re_\tau = 395$ - appeared much more stable than previous attempts. With this progress came the suspicion that the formulation of turbulent viscosity

$$\nu_T = C_\nu \left(\frac{\overline{K^2}}{\overline{Kq^2}} \right)^{\frac{1}{2}} \tag{3.19}$$

may be incorrect and in fact too large. To understand why, an examination of the classic diffusion model is necessary. While the term is often written as

$$(\nu + \nu_T) \nabla^2 \phi \tag{3.20}$$

the operation is actually performed as

$$\nabla (\nu + \nu_T) \cdot \nabla \phi \tag{3.21}$$

where ϕ is the field of interest, in this case q_i or R_{ij}. OpenFOAM implements the Laplacian operator properly, adhering to Equation (3.21). Examination of the behavior of diffusion near solid boundaries revealed that, when the effective viscosity $\nu + \nu_T$ was included in the Laplacian as is usually the case, the gradient of ν_T was quite large and led to stability issues. It became clear that the eddy viscosity itself - and *not* the Laplacian - may be to blame for instabilities exhibited in wall-bounded

simulations. The diffusion term was reimplemented in the form of Equation (3.20) with promising results. This is not proper diffusion, however (or, at least "proper enough" - Equation (3.21) is a model, after all) and should be avoided, particularly when casting the Laplacian operator implicitly in OpenFOAM. In fact, multiplying an implicit Laplacian operator by *any* varying quantity in OpenFOAM is a recipe for disaster. These observations led to new ideas about the form of ν_T.

3.4 Redefining ν_T and $1/\tau_R$

The turbulent viscosity ν_T and turbulent time scale $1/\tau_R$ were previously defined as $\nu_T = C_\nu \left(\overline{K^2}/\overline{Kq_i^2}\right)^{1/2}$ and $1/\tau_R = \left(\overline{K}\overline{q_i^2}\right)^{1/2}$. These definitions worked well for flows away from solid boundaries presented in Chapter 4, but warrant additional consideration for the flows discussed in the next chapter. To begin with, while convenient, the kinetic energy (both local K and global $\overline{K}$) quickly approaches zero near a solid boundary, and is identically so at a no-slip wall. The average eddy vector magnitude $\overline{q^2}$ is non-zero at the wall, and therefore the behavior of ν_T and $1/\tau_R$ is dominated by $\overline{K}$. Both cases go like $\overline{K}^{1/2}$ which is correct. Very close to a wall, and at a solid boundary, however, both quantities are zero. While this is physically appropriate for the turbulent viscosity, this behavior is worrisome for the turbulent time scale $1/\tau_R$. This quantity scales both dissipation and return-to-isotropy for both the eddy orientation vectors and Reynolds stress tensors. While at the wall itself these terms are irrelevant, very close to a boundary they both play an important role. In order to ensure these terms in the transport equations do not become vanishingly small, the turbulent timescale was redefined to be non-zero close to and on a no-slip wall, *viz.*

$$\frac{1}{\tau_R} = \left(\overline{K}\overline{q_i^2}\right)^{1/2} + \alpha\nu\overline{q^2} \tag{3.22}$$

where the addition of $\alpha\nu\overline{q^2}$ ensures the timescale (and therefore the return and dissipation terms scaled by the timescale) remains larger very close to a solid boundary.

The asymptotic behavior of the turbulent viscosity (which is also important in many modeling terms) can be modified as well: rather than scaling directly with the kinetic energy, the wall-normal component of the average Reynolds stress tensor can be employed:

$$\nu_T = C_\nu \left[\left(\overline{R_{ij}}^{-1} \right)^{-1}_{kk} \right] / \left(\overline{Kq^2} \right)^{1/2} \tag{3.23}$$

This definition avoids large peaks associated with $\overline{K}$ while remaining smooth as a solid boundary is approached, and zero on the boundary itself.

3.5 Modifying the rotation model

The original system rotation model, proposed in Chapter 2, was tested extensively, and validation cases were presented in Chapter 4 for a variety of flows. It was originally constructed as

$$A_i = -\frac{1}{\tau_R} \left[\frac{\overline{\left(q_k \Omega^*_k\right)^2 / q^2}}{20\overline{q^2}\,\overline{K} + 0.25\left(\Omega^*_k\right)^2} \right] q_i \tag{3.24}$$

Note that this term is a scalar modification to the eddy orientation vector q_i; that is, it affects all components of the vector equally. Recent observations of turbulent shear flows by Perot suggests that correlations in the spanwise direction (in the case of a channel flow) tend to be suppressed. A new rotation model for the Oriented-Eddy Collision turbulence model was proposed which tends to suppress the spanwise component of the eddy orientation vector (q_3 in the channel flow cases considered where x_3 is the spanwise direction):

$$A_i = -C_{A_i} \left(\frac{\Omega^*_k q_k}{|\Omega^*_k|} \right) \Omega^*_i \tag{3.25}$$

recalling $\Omega^*_k = \epsilon_{ijk} \overline{u}_{k,j} + \Omega_i$. This rotation model was primarily tested in turbulent channel flow cases but can be employed in any of the canonical rotating flows considered in Chapter 4.

3.6 Issues with return-to-isotropy for q_i

The original return-to-isotropy model for the eddy orientation vectors, proposed in Chapter 2, is based on Rotta's linear return model [79]:

$$A_i = -\frac{1}{\tau_R}\left(\frac{C_Q}{1+C_B\nu/\nu_T}\right)\left[3\frac{\overline{q_iq_k}}{\overline{q^2}} - \delta_{ki}\right]q_k \tag{3.26}$$

Investigation of this return model when subjected to wall-bounded shear revealed instabilities, and a tendency for the streamwise component of the eddy orientation vectors, q_1, to return little or not at all. Several other models were proposed, including

$$A_i = -\frac{1}{\tau_R}\left(\frac{C_Q}{1+C_B\nu/\nu_T}\right)\left[\delta_{ki} - \frac{\overline{q^2}}{3}\left(\overline{q_iq_k}\right)^{-1}\right]q_k \tag{3.27}$$

Unfortunately, inverting the tensor $\overline{q_iq_j}$ in Equation (3.27) becomes impossible near to and on solid boundaries where $\overline{q_iq_j}$ can become singular. A similar model which avoided inversion was constructed:

$$A_i = -\frac{1}{\tau_R}\left(\frac{C_Q}{1+C_B\nu/\nu_T}\right)\left[\frac{\overline{q_iq_k}}{\overline{q^2}} - \frac{\overline{q_iq_kq_iq_k}}{\overline{q^2q^2}}\delta_{ik}\right]q_k \tag{3.28}$$

While the return model for the eddy orientation vectors proposed in Equation (3.28) avoids inverting singular $\overline{q_iq_j}$ and the instabilities associated with the original return to isotropy model (Equation (3.26)), it reveals yet another shortcoming: all previously proposed return to isotropy models fail to adequately influence the streamwise eddy orientation vector component (q_1 in the case of turbulent channel flow). Consider a simplified evolution equation for the "eddy structure tensor", $N_{ij} = \overline{q_iq_j}$, and specifically N_{11} - it contains no production sources but contains both dissipation and decay. Return-to-isotropy is the only means of preventing N_{11} (that is, $\overline{q_1}$) from decaying to zero short of an additional production term. Unfortunately, return tends to act only weakly on q_1. This leads q_1 to rapidly approach zero, which severely damps N_{12}, and

eventually inhibits all N_{ij} production. Either the return to isotropy model must be modified or an additional production term for $\overline{q_1}$ (or all components of $\overline{q_i}$) employed.

One novel approach to modeling return to isotropy for the eddy orientation vectors, originally investigated by Perot and Chartrand [10], treats the endpoints of the orientation vectors (which all share a common origin for a given location in physical space) as particles. These particles, which all lie on the surface of a spheroid, can be made to either attract or repulse one another based on their separation and the average distribution of vectors. A term can then be added to the eddy vector transport equation, O_i, which replaces the standard return to isotropy model:

$$O_i = \frac{C_O}{\tau_R}\frac{1}{\overline{q^2}}\left(\overline{q^2}p_i - \overline{q_k p_k}q_i\right) \tag{3.29}$$

where p_i is a list of vector fields, one for every eddy at every physical location, which dictates the distance each eddy should maintain from every other eddy. $\overline{q_k p_k}$ is the inner product of the eddy orientation vector and the eddy repulsion vector, averaged over all eddies. The eddy repulsion vector is calculated via:

```
p_i[*] = 0
for n = 1:N do
   for m = n+1:N do
      d_i = (q_i[n] − q_i[m]) / |q_i[n] − q_i[m]|^3
      p_i[n] = p_i[n] + d_i
      p_i[m] = p_i[m] − d_i
   end for
end for
```

Algorithm 3: Calculating eddy repulsion vectors for return-to-isotropy.

where N is the total number of eddies employed for a given flow, and $[i]$ refers to the eddy repulsion vector at the ith eddy. This novel method for modeling eddy orientation vector return to isotropy was primarily tested under turbulent channel flow conditions, and once tuned accurately captured return. While an improvement

over the older models, this method requires N^2 operations at every time step and is sensitive to shrinking $\overline{q^2}$, as is obvious from Equation (3.29).

3.7 Producing q_i

As is hinted at in the previous sections, prescribing a suitable return-to-isotropy model for the eddy orientation vectors may not be enough to prevent exponential decay, especially in regions far from high shear (and thus production) such as the center of a turbulent channel flow. While production and dissipation should theoretically balance, experience has shown that this balance is difficult to achieve, and extremely sensitive. Taking inspiration from the dissipation evolution equation in the $K-\epsilon$ turbulence model, a production term can be constructed for the eddy orientation vectors which acts in addition to the rapid-distortion-theory production term but does not affect the model's performance when subject to linear turbulence:

$$P_j^{\epsilon} = C_{P_\epsilon} \left(\frac{-\overline{R}_{ij}\overline{u}_{i,j}}{\overline{K}} \right) q_j \tag{3.30}$$

recalling $\overline{u}_{i,j}$ is the velocity gradient tensor, and in the case of a shear flow is zero aside from the shear component $\overline{u}_{1,2}$. This "ϵ-like" production term is capable of forestalling unbounded decay. A closer examination of the dissipation equation from the $K-\epsilon$ turbulence model and its relationship to the evolution q_i^2, assuming $q_i^2 \sim \frac{1}{L^2} \sim \frac{\epsilon^2}{K^3}$ reveals that terms based on the gradient of $\overline{R}_{ij}$ or $\overline{q}_i$ are necessary. There is no unique expression which fulfills this need, and in fact many were formulated and tested. A particularly appealing gradient-like production term of the form

$$P_i^G = C_{P_G} \left(\nu + \nu_T\right) \left[\frac{\nabla \overline{q_i^2}}{\overline{q_i^2}} \right]^2 q_i \tag{3.31}$$

is employed in the eddy orientation transport equation both alone and in combination with Equation (3.30). The turbulent channel flow cases considered in Chapter 6 make

use of Equation (3.31) in order to prevent the decay of the eddy orientation vectors far from high shear regions.

3.8 Initial Conditions for local R_{ij}

Figure 3.3 illustrates an eddy, with associated local, two-dimensional, orthogonal Reynolds stress, as well as a family of eddies present at some cell in physical space. A variety of initial conditions for the eddy vectors q_i are available for use within the

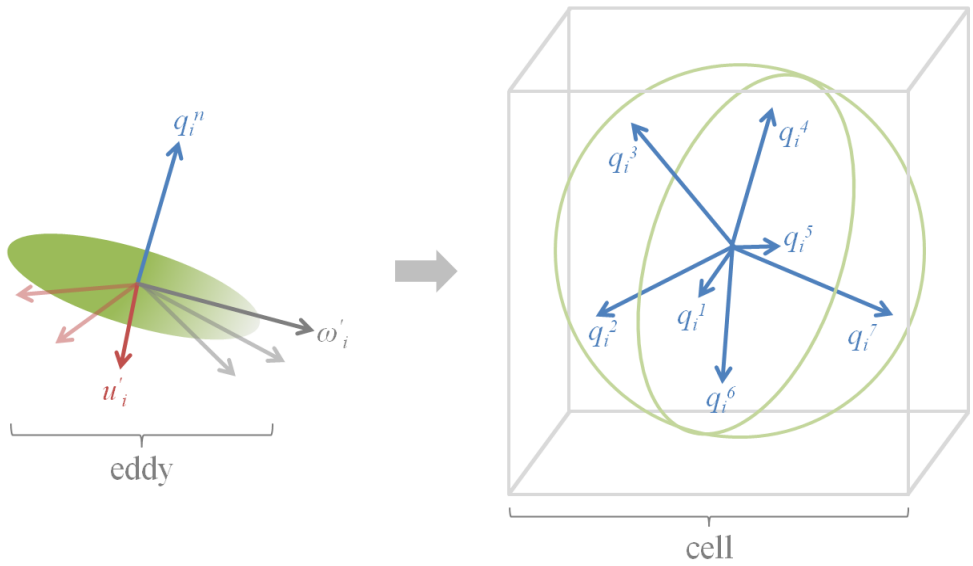

Figure 3.3. A family of eddies is located at every cell in physical space. For most simulations, the eddies begin uniformly distributed on a unit sphere. As a simulation progresses, the directions of these eddy orientation vectors will distort.

Oriented-Eddy Collision turbulence model. These initial conditions are in the form of a collection of vectors which are uniformly distributed on the unit sphere. These vector lists were originally created by Chartrand [10] and have been adapted for use in OpenFOAM. The number of eddies employed in a given simulation is akin to the size of the statistical sampling space given to the underlying probability density function evolution equation. In theory, the more statistical sample space (eddies) given to the model, the better representation of the underlying physics. This, however, comes at

a cost, one which is brought to light as the details of implementing such a system in OpenFOAM are considered. Specifically, a method is required by which an arbitrary number of eddy vectors may be used in any given simulation. Based on the number of eddies (N), each cell in the computational domain must be populated with N Reynolds stress tensors, N eddy vectors, and N transport equations for each. Two transport equations for each eddy at each physical location in the computational mesh (i.e., at each cell) requires precise accounting. Pointer lists are employed for this purpose in FOAM. For some number of initial eddy vectors N, a pointer list with N entries is constructed for the eddy vectors themselves, for the corresponding Reynolds stress tensors, and if necessary for the scalar kinetic energy. As mentioned above, the eddies are arranged on a unit sphere and are thus unit vectors.

In Appendix B, the original scheme to determine the proper initial conditions for the individual (local) Reynolds stress tensors based on the initial turbulent Reynolds number, initial global Reynolds stresses (or global kinetic energy), and the initial eddy orientation vectors (scaled by the initial dissipation) is outlined. This equation is not presented in the main body of the text because its use is limited to homogeneous cases. When nonhomogeneous, anisotropic cases such as wall-bounded flows are considered, Equation (B.2) fails. This is because there exists no *unique* set of local Reynolds stress tensors which corresponds to a given set of global initial conditions. While the evolution of turbulent statistics for most flows (such as channel flow) should be independent of the initial condition, being able to begin a simulation with a set of local Reynolds stresses that corresponds to the flows' global initial conditions and are orthogonal to their eddy orientation vectors is vital when evaluating the model's performance in complex flows. It is difficult (perhaps impossible) to construct an equation similar to Equation (B.2) which is applicable to nonhomogeneous initial conditions. To avoid this problem, a simple iterative method was devised which results in correct, local Reynolds stress tensors given any initial condition, provided

that the global stress tensor / kinetic energy values and initial eddy orientation vectors are known. The "project and correct" method projects the initial local stress tensors to be orthogonal to their corresponding eddy orientation vectors employing either Equation (5.15) or Equation (5.17), discussed in the near-wall reorientation section of Chapter 5. Then, the difference between the updated global stress tensor and the desired initial condition is calculated, and used to correct the local stress tensors. Once this correction is applied, the local tensors are once again projected to be orthogonal to their eddy orientation vectors. This process quickly converges the local Reynolds stresses to a state where they satisfy the global initial conditions and are orthogonal to the eddy orientation vectors.

CHAPTER 4

VALIDATION IN SIMPLE FLOWS

While the Oriented-Eddy Collision turbulence model has been tested in the past by Chartrand [10] and Andeme [2], recent changes to the Oriented-Eddy Collision turbulence model necessitated additional benchmarking. Furthermore, implementation of the Oriented-Eddy Collision turbulence model into the open-source collection of computational fluid dynamics libraries OpenFOAM [27, 81] requires that the model be retested. This chapter provides a thorough test of the Oriented-Eddy Collision turbulence model as the model is presented in §3.1 while avoiding wall-bounded flows, which are addressed after the near-wall behavior of the Oriented-Eddy Collision turbulence model is considered in Chapter 5. In general, the latest version of the Oriented-Eddy Collision turbulence model performs quite well when predicting a variety of canonical flows.

4.1 Regular and Rotating Isotropic Decay

The most basic test of the Oriented-Eddy Collision turbulence model is isotropic decaying turbulence. Direct numerical simulation data from de Bruyn Kops and Riley [20] is employed. The initial kinetic energy for this case is $\overline{K}^0 = 0.075\ m^2/s^2$ and the initial turbulent Reynolds number is $Re_T^0 = 665$. It is important to recall that an overbar implies a "global" quantity in the Oriented-Eddy Collision turbulence model; that is, one which is averaged over all eddies at each physical location. The Oriented-Eddy Collision turbulence model accurately predicts the decay of the turbulent kinetic energy, even though the decay process is non-linear and therefore

an entirely modeled phenomenon. In addition, nine cases of turbulent rotating decay

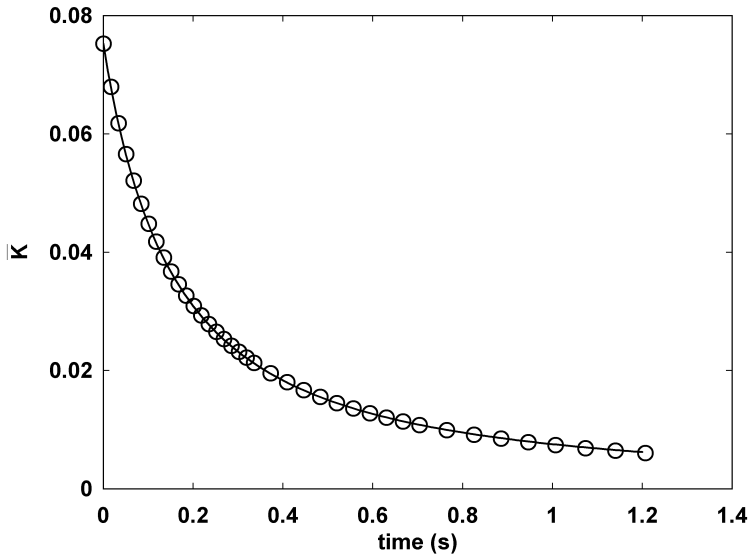

Figure 4.1. Isotropic, homogeneous decay of kinetic energy predicted by the Oriented-Eddy Collision turbulence model (—) compared to DNS data from de Bruyn Kops and Riley [12] (∘).

with varying turbulent Rossby and Reynolds numbers, from Wigeland and Nagib [103], are calculated. The initial conditions are summarized in Table 4.1, noting the definition of the turbulent Reynolds number $Re_T \equiv \overline{K}^2/\nu\overline{\epsilon}$ and turbulent Rossby number $Ro_T \equiv \overline{\epsilon}/\left(|\Omega_i|\,\overline{K}\right)$.

Table 4.1. Initial conditions for Wigeland and Nagib [103]

Rotating and non-rotating decay initial conditions									
	A			**B**			**C**		
$\overline{\epsilon}\,(m^2/s^3)$	14.85	14.67	14.94	2.96	3.49	3.36	2.77	3.36	22.26
$\overline{K}\,(m^2/s^2)$	0.098	0.0975	0.105	0.045	0.0462	0.051	0.029	0.033	0.096
$\nu\,(m^2/s)$	1.85E-5	1.8E-5	1.85E-5	1.85E-5	1.85E-5	1.85E-5	1.85E-5	1.85E-5	1.85E-5
Re_T	36	36	41	38	34	43	17	18	23
Ro_T	∞	7.52	1.78	∞	3.77	0.82	∞	5.09	2.9
$\lvert\Omega_i\rvert$	0	20	80	0	20	80	0	20	80

The Oriented-Eddy Collision turbulence model predicts the decay of turbulent kinetic energy for all nine cases within reasonable accuracy compared to data from Wigeland

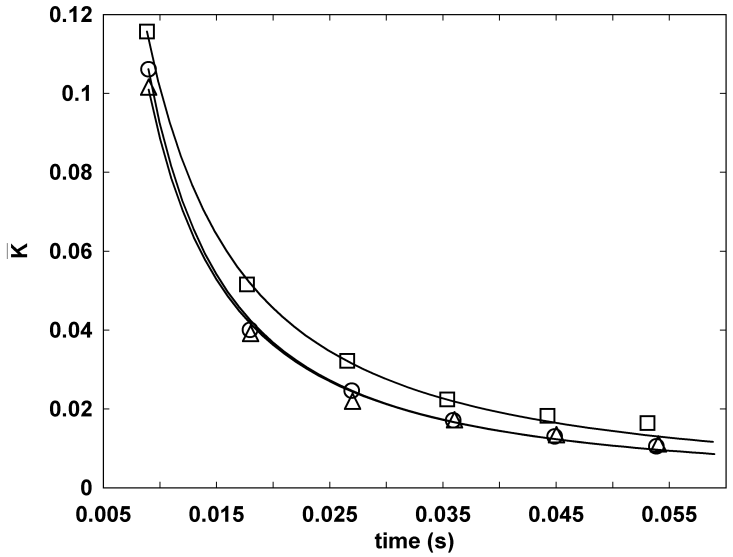

Figure 4.2. Rotating and non-rotating decay of kinetic energy from Wigeland and Nagib [103], case A: $|\Omega_i| = 0$ ($\circ$), $|\Omega_i| = 20$($\triangle$), $|\Omega_i| = 80$($\square$), compared to predictions from the Oriented-Eddy Collision turbulence model (—).

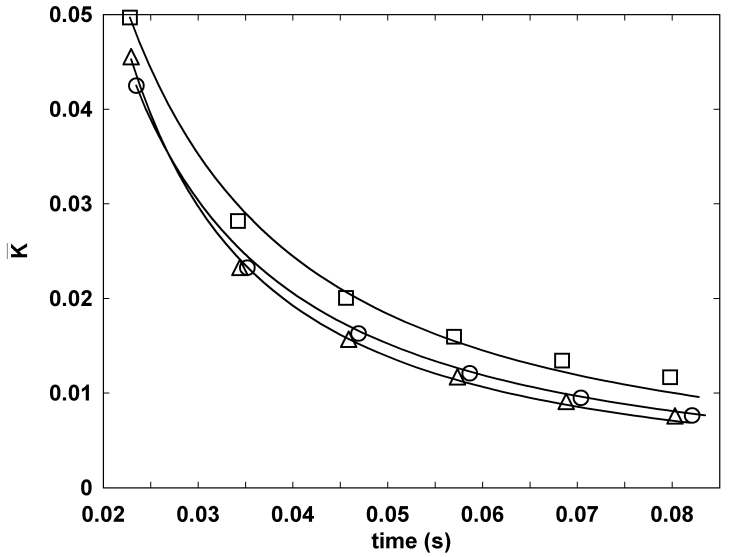

Figure 4.3. Rotating and non-rotating decay of kinetic energy from Wigeland and Nagib [103], case B: $|\Omega_i| = 0$ ($\circ$), $|\Omega_i| = 20$($\triangle$), $|\Omega_i| = 80$($\square$), compared to predictions from the Oriented-Eddy Collision turbulence model (—).

and Nagib. Figures 4.2 through 4.4 show the model's performance. A more marked deviation from the benchmark data are noted for the three cases with the highest

rotation rate, especially at long times. Rotating decay was also tested with data taken

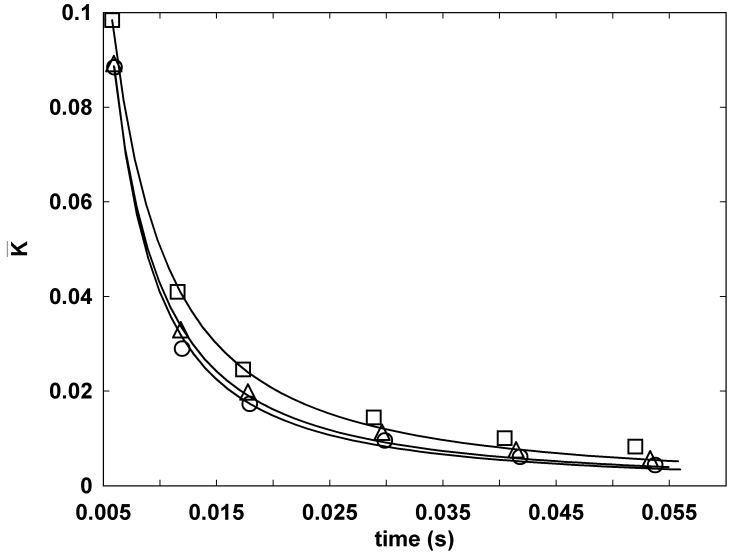

Figure 4.4. Rotating and non-rotating decay of kinetic energy from Wigeland and Nagib [103], case C: $|\Omega_i| = 0$ ($\circ$), $|\Omega_i| = 20$($\triangle$), $|\Omega_i| = 80$($\square$), compared to predictions from the Oriented-Eddy Collision turbulence model (—).

from Jacquin, *et al.* [26]. Note that only the highest Reynolds number case is shown here, as agreement at lower Reynolds numbers was excellent and tested previously. For the case considered, the initial dissipation was $\overline{\epsilon} = 30.96\ m^2/s^3$, the initial kinetic energy $\overline{K} = 0.444\ m^2/s^2$, and the initial kinematic viscosity $\nu = 1.51E{-}5\ m^2/s$. The case began with a turbulent Reynolds number of $Re_T = 457$ and initial turbulent Rossby number of $Ro_T = 1.10$. Figure 4.5 compares the Oriented-Eddy Collision turbulence model's predictions to data from Jacquin, *et al.* (case C), the highest Reynolds number considered. Even at high Reynolds numbers the model deviates from the experimental data by less than 5%.

The results of Mansour, Cambon, and Speziale's [43] simulations of turbulent rotating decay were employed as a final test of the Oriented-Eddy Collision turbulence model's ability to predict such flows. The initial conditions for the four cases considered are

Table 4.2. Initial conditions from Jacquin *et al.* [26] turbulent rotating decay. Note that cases A and B are not shown

Rotating decay initial conditions			
	A	**B**	**C**
$\bar{\epsilon}\left(m^2/s^3\right)$	11.73	16.43	30.96
$\overline{K}\left(m^2/s^2\right)$	0.153	0.288	0.444
$\nu\left(m^2/s\right)$	1.51E-5	1.51E-5	1.51E-5
Re_T	127	281	457
Ro_T	1.22	0.91	1.10

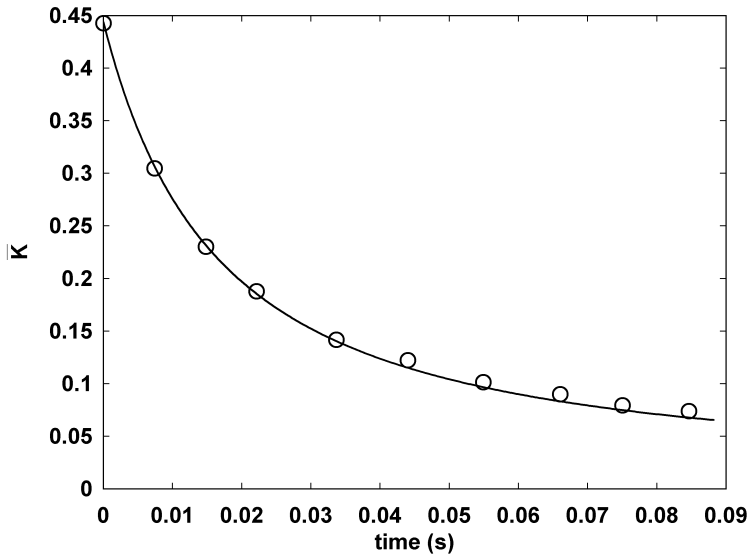

Figure 4.5. Rotating and non-rotating decay of kinetic energy from Jacquin, *et al.* [26] (∘) with $Ro_T = 1.10$ (case C) compared to predictions from the Oriented-Eddy Collision turbulence model (—).

listed in Table 4.3. Thoroughly testing the model's ability to accurately predict rotating decay was necessary as the rotating dissipation model must remain stable for long times in order to compute cases such as steady state shear flow.

Figures 4.6(a) and 4.6(b) show the Oriented-Eddy Collision turbulence model's prediction of normalized kinetic energy as a function of time when subjected to the conditions presented in Table 4.3. Interestingly, cases A and C, which were run at the highest turbulent Rossby numbers, show the closest agreement to Mansour, Cambon,

Table 4.3. Initial conditions for Mansour, Cambon, and Speziale [43] rotating decay cases

Rotating decay initial conditions				
	A	**B**	**C**	**D**
$\bar{\epsilon}\left(m^2/s^3\right)$	0.93		0.95	
$\overline{K}\left(m^2/s^2\right)$	0.964		0.977	
$\nu\left(m^2/s\right)$	3.67E-2		1.49E-2	
Re_T	27.2		67.1	
Ro_T	0.37	0.037	0.24	0.1

and Speziale's data and matched to within 5%. Cases B and D, with lower Rossby numbers, showed agreement only to within 10%. Note that data from Mansour, *et al.* [43] cases C and D run for relatively brief periods of time, possibly indicating difficulty in attaining accurate DNS simulations, especially case C (□) which only provides data up to 0.8 seconds.

4.2 Inhomogeneous decay

Shear-less turbulent mixing layer direct numerical simulation data (performed at a resolution of 256^3 grid points) from Winckelmans, Jeanmart, and Carati [109, 108] is used to examine the model's ability to capture the decay of kinetic energy and dissipation which is not spatially uniform. Note that these results employ the diffusion terms presented in §3.1 (Expression (3.9)). Kinetic energy results are shown in Figure 4.7 and dissipation results in Figure 4.8. The Oriented-Eddy Collision turbulence model's ability to predict the decay of both the average kinetic energy $\overline{K}$ and average (calculated) dissipation $\bar{\epsilon} = \overline{q^2 K}\nu\alpha + \overline{K}^{\frac{3}{2}}\overline{|q_i|}$ is reasonable at time t = 0.071 seconds. However, the model seems to slightly over predict the kinetic energy at the latest times and under predict the dissipation at time t = 0.191 seconds.

4.3 Rapid Distortion Theory

The addition of orientation information to the Oriented-Eddy Collision turbulence model enables it to accurately capture turbulence in highly non-equilibrium condi-

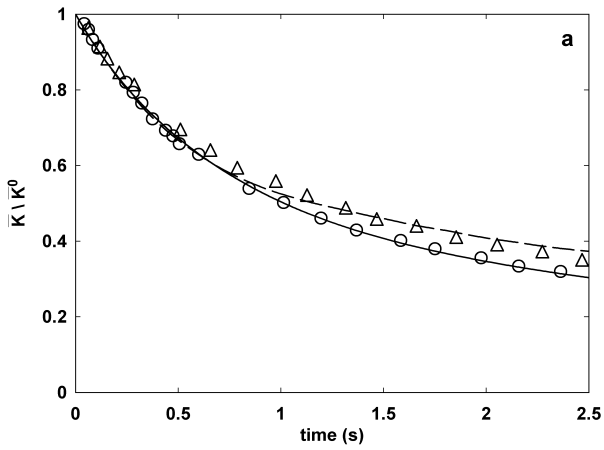

(a) Cases A and B from [43].

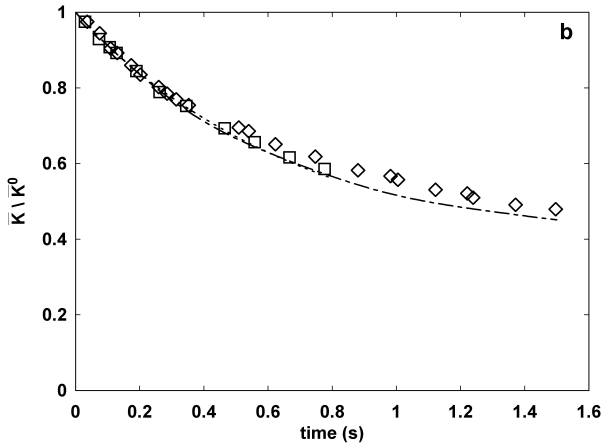

(b) Cases C and D from [43].

Figure 4.6. The Oriented-Eddy Collision turbulence model's predictions for normalized kinetic energy of rotating decay compared to data from Mansour, Cambon, and Speziale [43]. Figure 4.6(a): Cases A (○) and B (△) data from Mansour, *et al.* compared to OEC's predictions for cases A (—) and B (- - -). Figure 4.6(b): Mansour cases C (□) and D (◇), compared to OEC's predictions,(- - -) and (· · ·) respectively.

tions, such as those described by rapid distortion theory (RDT). Among the RDT cases considered and used for validation were the following: Axisymmetric expansion, akin to an expansion in a wind tunnel in directions transverse to the mean flow; axisymmetric contraction in which the turbulent flow is contracted in the transverse directions, plane strain, and finally shear. The four cases are summarized in Table 4.4. The tensor $\overline{u}_{i,j}$ is the mean velocity gradient tensor applied to the turbulent flow

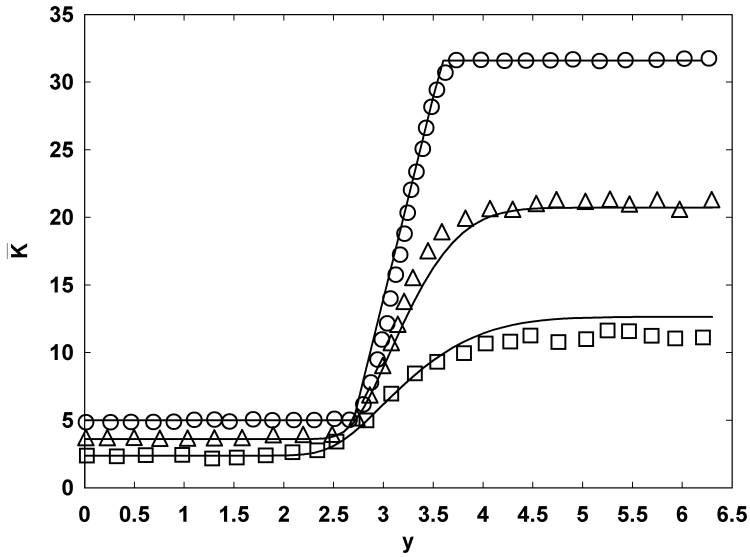

Figure 4.7. Non-homogeneous decay of kinetic energy from Winckelmans, Jeanmart, and Carati [109], [108]: t = 0s (○), t = 0.071s (△), t = 0.191s (□); compared to predictions from the Oriented-Eddy Collision turbulence model (—).

to produce rapid distortion, and S a scalar quantity which controls the amount of strain. The exact RDT solutions can be found in numerous references [66, 17].

Table 4.4. Rapid distortion theory cases used for testing the Oriented-Eddy Collision turbulence model

	Axisymmetric Contraction	Axisymmetric Expansion	Plane Strain
$\overline{u}_{i,j}$	$\begin{bmatrix} S & 0 & 0 \\ 0 & -\frac{1}{2}S & 0 \\ 0 & 0 & -\frac{1}{2}S \end{bmatrix}$	$\begin{bmatrix} -2S & 0 & 0 \\ 0 & S & 0 \\ 0 & 0 & S \end{bmatrix}$	$\begin{bmatrix} S & 0 & 0 \\ 0 & -S & 0 \\ 0 & 0 & 0 \end{bmatrix}$

As shown in Figure 4.9, the Oriented-Eddy Collision turbulence model is capable of predicting plane strain to within less than 1% of what rapid distortion theory predicts. This is not surprising considering the two-point correlation basis of the model and its ability to capture rapid pressure strain exactly. It should be noted that, while agreement with RDT is reasonable when only a small number of eddies (say, 22) are employed for a simulation, the best agreement occurs when the largest number of

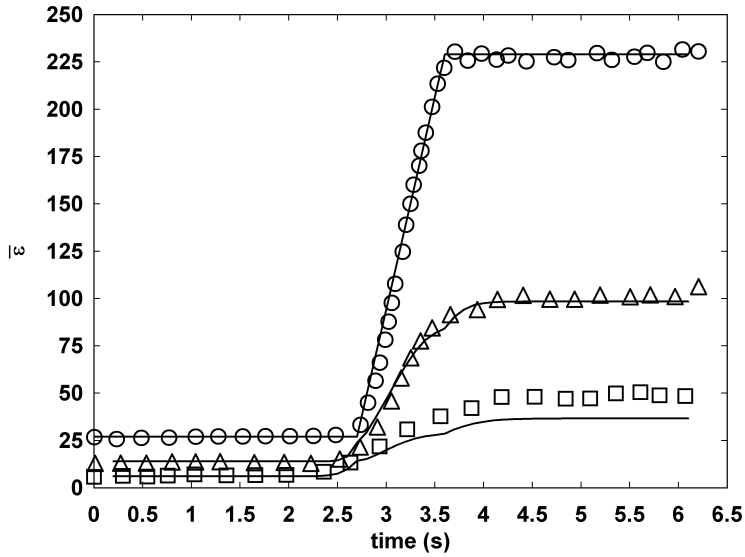

Figure 4.8. Non-homogeneous decay of dissipation from Winckelmans, Jeanmart, and Carati [109], [108]: t = 0s (○), t = 0.071s (△), t = 0.191s (□); compared to predictions from the Oriented-Eddy Collision turbulence model (—).

eddies (1,257) are used for a given RDT case. As such, all RDT cases shown employ 1,257 eddies. Figure 4.10 shows results from axisymmetric expansion compared to theoretical limits from Pope [66]. Once again, agreement is excellent. Figures 4.11 and 4.12 both compare the Oriented-Eddy Collision turbulence model's performance when subjected to axisymmetric contraction. The model performs well, capturing the theoretical limits predicted by RDT closely especially when a large number of eddies are employed. Figure 4.12 details the asymptotic development of $\overline{R}_{22}/\overline{K}^0$ as it approaches and meets the theoretical limit of $\frac{1}{2}e^{St}$. Before moving on, one last and somewhat unusual case related to rapid distortion theory will be considered.

4.4 Slow Axisymmetric Expansion

One case related to axisymmetric expansion, investigated by Lee and Reynolds [75] among others, is that of slow axisymmetric expansion. Challenges inherent to modeling such a flow are detailed by Kassinos, Reynolds and Rogers [76]. Single point

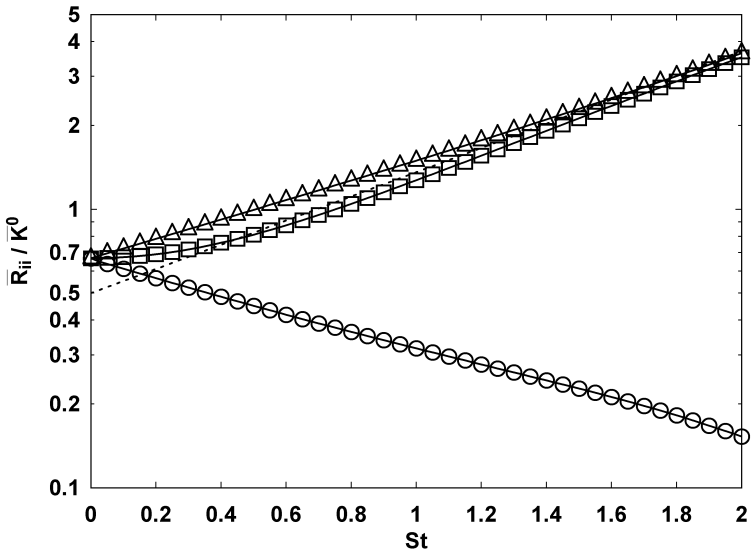

Figure 4.9. Plane strain data of principal Reynolds stresses. Symbols from RDT: $\overline{R}_{11}/\overline{K}^0$ ($\circ$), $\overline{R}_{22}/\overline{K}^0$($\triangle$), $\overline{R}_{33}/\overline{K}^0$($\square$), compared to the Oriented-Eddy Collision turbulence model (—), and the theoretical limit $\frac{1}{2}e^{St}$ ($\cdots$).

closure methods have difficulty capturing slow strain as the Reynolds stress anisotropy is greater than that found in rapidly distorted cases. The Oriented-Eddy Collision turbulence model was subjected to slow axisymmetric expansion with $S\overline{K}^0/\overline{\epsilon}^0 = 0.41$ and compared to RDT case at a much higher $S\overline{K}^0/\overline{\epsilon}^0 = 20.0$, both at a turbulent Reynolds number of $Re_T^0 = 200$. Similar to the observations made by Kassinos and Reynolds [74], [30], slow axisymmetric strain exhibits higher initial anisotropy when compared to standard RDT. Figure 4.13 shows this interesting phenomenon.

4.5 Return to Isotropy

Data from Le Penven, *et al.* [39] is widely used to test return-to-isotropy. The flow, which is initially isotropic, is rapidly strained to an anisotropic state and then allowed to relax back toward isotropy. The velocity gradient tensor employed for the two cases considered is shown in Table 4.5 and causes very different types of anisotropy. Case A has one large stress value and Case B has two large stress values.

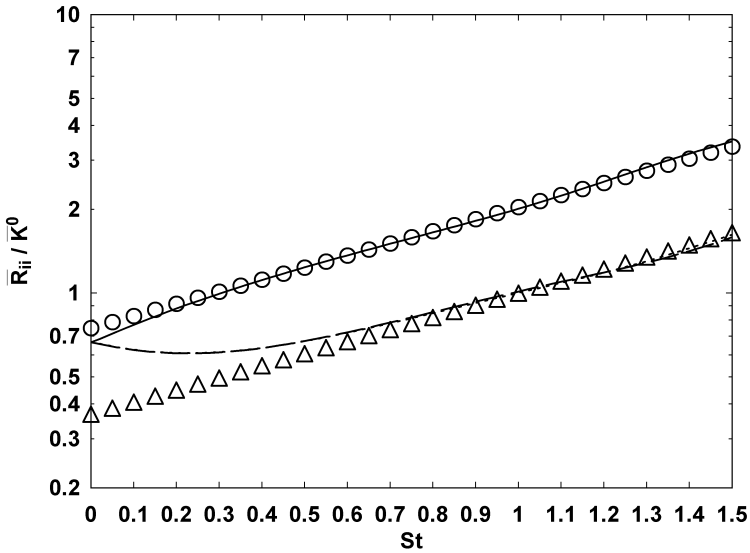

Figure 4.10. Axisymmetric expansion data of principal Reynolds stresses as predicted by the Oriented-Eddy Collision turbulence model: $\overline{R}_{11}/\overline{K}^0$ (—), $\overline{R}_{22}/\overline{K}^0 = \overline{R}_{33}/\overline{K}^0$ (- - -), compared to the theoretical long-time asymptotic growth rates: $e^{St+log(0.75)}$ ($\circ$), $e^{St+log(0.36)}$($\triangle$).

The initial values for the Reynolds number are not provided in the data, and were deduced by what produced the correct conditions at the end of the straining region.

Table 4.5. Summary of initial conditions for shear flow cases Le Penven, *et al.* [39]

	Le Penven, *et al.* Case A	Le Penven, *et al.* Case B
$S\overline{K}/\overline{\epsilon}$	0.43	0.33
Re_T	612	846
$\overline{u}_{i,j}$	$\begin{bmatrix} 5.48 & 0 & 0 \\ 0 & 1.99 & 0 \\ 0 & 0 & -7.47 \end{bmatrix}$	$\begin{bmatrix} 8.86 & 0 & 0 \\ 0 & -2.36 & 0 \\ 0 & 0 & 6.50 \end{bmatrix}$

Agreement between data from L. Le Penven, J. N. Gence, and G. Comte-Bellot, Case A [39] and the Oriented-Eddy Collision turbulence model is within 8%, as shown in Figures 4.14. While Case B (Figure 4.15) shows less agreement, the model's prediction for the return to isotropy of stress tensor is reasonably accurate for both cases, and possibly within the error levels of the experiment and initial condition specification.

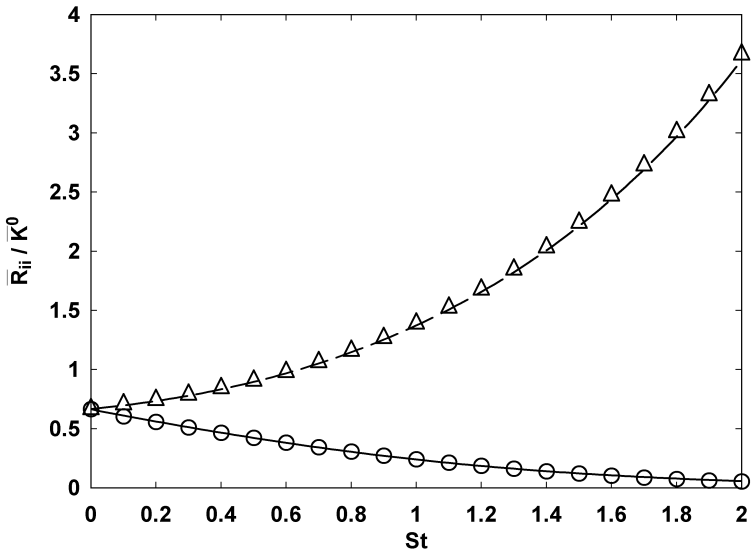

Figure 4.11. Axisymmetric contraction data of principal Reynolds stresses: RDT results, $\overline{R}_{11}/\overline{K}^0$ ($\circ$), $\overline{R}_{22}/\overline{K}^0 = \overline{R}_{33}/\overline{K}^0$($\triangle$), compared to predictions from the Oriented-Eddy Collision turbulence model $\overline{R}_{11}/\overline{K}^0$ (—), $\overline{R}_{22}/\overline{K}^0 = \overline{R}_{33}/\overline{K}^0$ (- - -).

4.6 Shear

The shear flow benchmark comes from the 64x256x64 (X x Y x Z) grid point simulation data of Matsumoto, Nagano, and Tsuji [47], the initial conditions and strain tensor of which are detailed in Table 4.6. Unlike the previous return cases, the flow is subject to a constant shear that persists for all time. The first case is at a very low turbulent Reynolds number, $Re_T = 18$, and is only considered for a short dimensionless time, $St \leq 4$. The data are presented in the form of the anisotropy tensor, $\overline{A}_{ij} = \left(\overline{R}_{ij}/\overline{K}\right) - 2\delta_{ij}/3$. Of primary interest is the Oriented-Eddy Collision turbulence model's ability to predict the shear stress, $\overline{A}_{12}$, over short times. Also important to recall is the inability of popular single-point Reynolds stress transport models to predict the separate evolution of $\overline{B}_{22}$ and $\overline{B}_{33}$. This is clearly corrected in the Oriented-Eddy Collision transport model due to its two-point correlation basis and ability to account for the underlying structure of a turbulent flow.

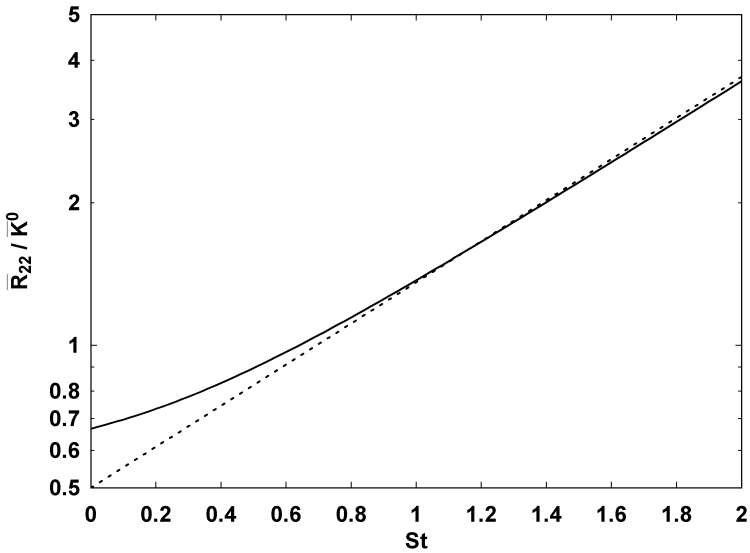

Figure 4.12. A closer look at the Oriented-Eddy Collision turbulence model's prediction of $\overline{R}_{22}/\overline{K}^0$ (—) compared to the asymptotic growth rate $\frac{1}{2}e^{St}(\cdots)$ for axisymmetric contraction.

Table 4.6. Initial conditions for the shear flow cases of Matsumoto, Nagano, and Tsuji [47]

$S\overline{K}/\overline{\epsilon}$	30.6	4.71
Re_T	18.18	152
$\overline{u}_{i,j}$	$\begin{bmatrix} 0 & 28.28 & 0 \\ 0 & 0 & 0 \\ 0 & 0 & 0 \end{bmatrix}$	$\begin{bmatrix} 0 & 30.0 & 0 \\ 0 & 0 & 0 \\ 0 & 0 & 0 \end{bmatrix}$

Agreement between OEC's prediction of the evolution of stresses and available data from Matsumoto, *et al.* is reasonable and within 4%. The ability of the model to remain accurate over such a short time is not surprising since this is almost a rapid distortion theory case. The higher Reynolds number case, $Re_T = 152$, runs for a much longer time and is the more difficult case. The data are also presented in the form of the anisotropy tensor and shown in Figure 4.17 against predictions of the Oriented-Eddy Collision turbulence model. Unlike the low Reynolds number case, the current data extends to relatively long dimensionless time $St \approx 14.4$. By time $St \approx 8$ the flow has reached a steady, anisotropic state and should remain so indefinitely. Agreement between the OEC model and data from Matsumoto, *et al.* is quite good considering

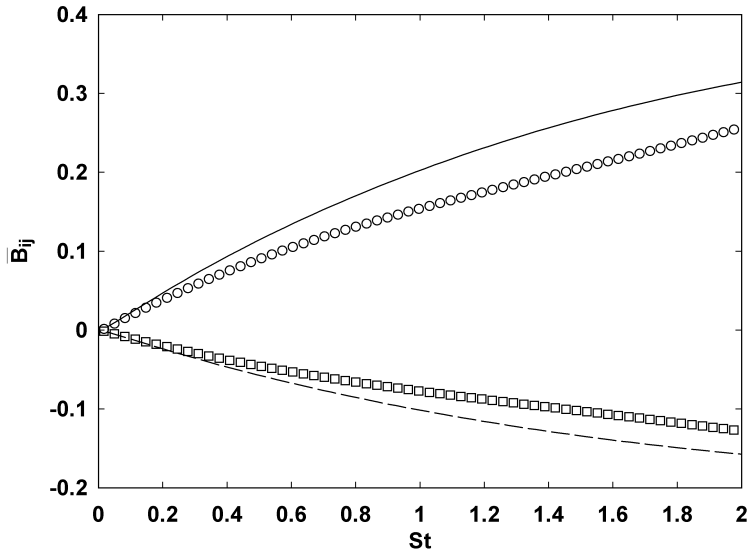

Figure 4.13. Anisotropy predictions of the Oriented-Eddy Collision turbulence model for slow axisymmetric expansion, $S\overline{K}^0/\overline{\epsilon}^0 = 0.41$: $\overline{B}_{11}$ (—), $\overline{B}_{22} = \overline{B}_{33}$ (- - -). Compared to RDT with $S\overline{K}^0/\overline{\epsilon}^0 = 20.0$: $\overline{B}_{11}$ ($\circ$), $\overline{B}_{22} = \overline{B}_{33}(\square)$. Anisotropy is defined as $\overline{B}_{ij} = \overline{R}_{ij}/2\overline{K} - \frac{1}{3}\delta_{ij}$.

the challenging nature of the benchmark. It is interesting to note that $\overline{A}_{11}$ ($\circ$) and $\overline{A}_{22}(\triangle)$ from Matsumoto, *et al.* appear to begin to return despite the presence of shear. This behavior may be due to the finite size of the simulation domain for the DNS data.

The validation of the Oriented-Eddy Collision turbulence model presented in this chapter supports both the exact (rapid pressure strain) and modeled (diffusion, dissipation, and return to isotropy) portions of the model. Several new cases such as slow axisymmetric expansion, are presented to further validate the model and its implementation for "non-standard" benchmarks. While the fundamentals of the Oriented-Eddy Collision turbulence model are outlined in Chapter 2 are validated above, the behavior of the model near solid boundaries must still be assessed. A brief introduction was provided in Chapters 2 and 3 and the ideas will be explored in the next chapter. Changes made to the model to account for solid boundaries and

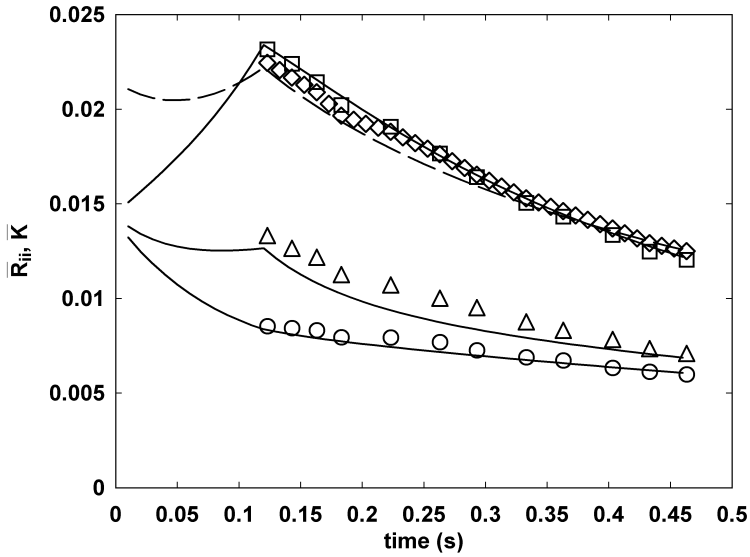

Figure 4.14. Principal Reynolds stress and kinetic energy decay. Symbols are data from L. Le Penven, J. N. Gence, and G. Comte-Bellot, Case A [39]: $\overline{R}_{11}$ ($\circ$), $\overline{R}_{22}$($\triangle$), $\overline{R}_{33}$($\square$), $\overline{K}$($\diamond$); compared to the Oriented-Eddy Collision turbulence model: $\overline{R}_{ii}$ (—), $\overline{K}$ (- - -).

non-local pressure effects do not affect the model's performance in simple canonical flows.

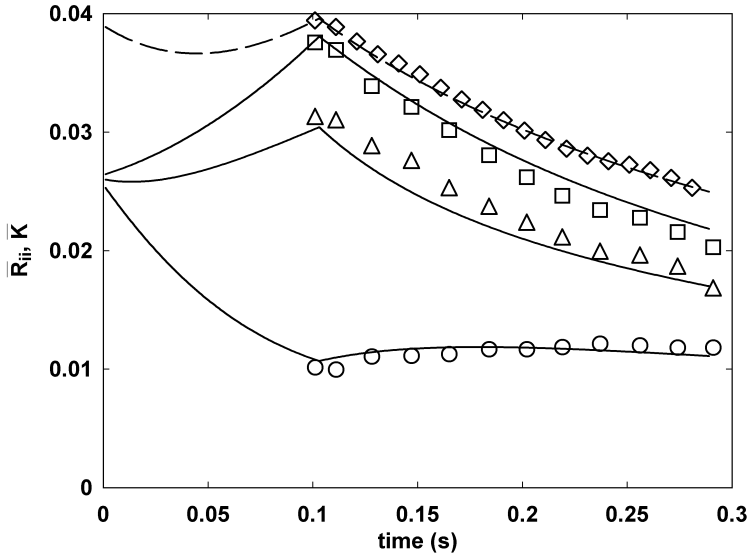

Figure 4.15. Principal Reynolds stress and kinetic energy decay. Symbols are data from L. Le Penven, J. N. Gence, and G. Comte-Bellot, Case B [39]: $\overline{R}_{11}$ ($\circ$), $\overline{R}_{22}$($\triangle$), $\overline{R}_{33}$($\square$), $\overline{K}$($\diamond$); compared to the Oriented-Eddy Collision turbulence model: $\overline{R}_{ii}$ (—), $\overline{K}$ (- - -).

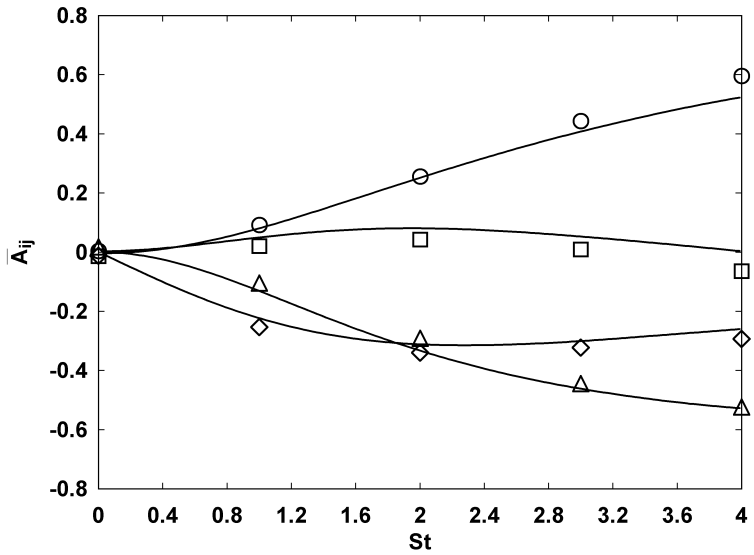

Figure 4.16. Anisotropy data $\overline{A}_{ij} = \left(\overline{R}_{ij}/\overline{K}\right) - 2\delta_{ij}/3$ at $Re_T = 18$ from Matsumoto, Nagano, and Tsuji [47]. $\overline{A}_{11}$ ($\circ$), $\overline{A}_{22}$($\triangle$), $\overline{A}_{33}$($\square$), $\overline{A}_{12}$($\diamond$); compared to results from the Oriented-Eddy Collision turbulence model (—).

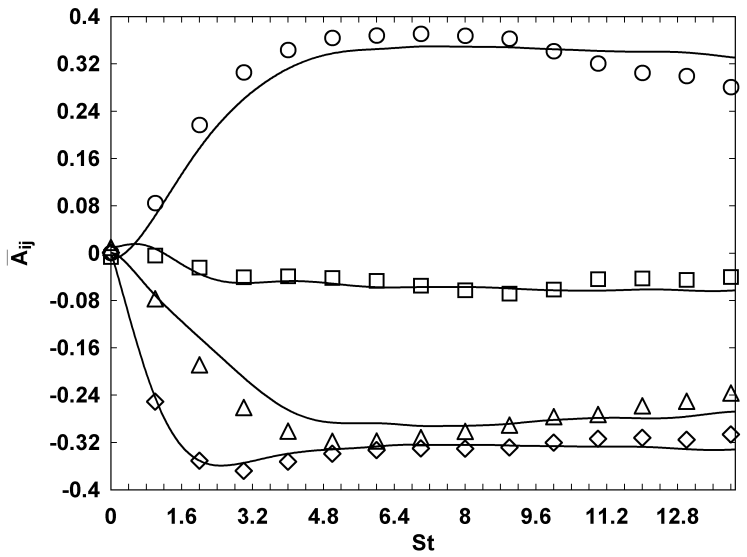

Figure 4.17. Anisotropy data $\overline{A}_{ij} = \left(\overline{R}_{ij}/\overline{K}\right) - 2\delta_{ij}/3$ at $Re_T = 152$ from Matsumoto, Nagano, and Tsuji [47]. $\overline{A}_{11}$ ($\circ$), $\overline{A}_{22}$($\triangle$), $\overline{A}_{33}$($\square$), $\overline{A}_{12}$($\diamond$); compared to results from the Oriented-Eddy Collision turbulence model (—).

CHAPTER 5

SOLID BOUNDARIES

5.1 Slip and no-slip boundary conditions

In Chapter 4, progressively more complex turbulent flows were simulated and compared with existing experimental or direct numerical simulation benchmarks. This is the same procedure used by Chartrand [10] and Andeme [2] during the formative years of the Oriented-Eddy Collision turbulence model. This lengthy endeavor is employed by turbulence modelers to validate components of their models, such as return to isotropy, turbulent dissipation, and terms responsible for frame invariance. The initial and boundary conditions employed for such simplistic test cases are often themselves quite simple. Furthermore, many of the test cases discussed in Chapter 4 are limited in their dimensionality, componentality, homogeneity, or isotropy. Isotropic, homogeneous decay is, obviously, isotropic and homogeneous. Such a benchmark is limited in its ability to test a turbulence model, and the Oriented-Eddy Collision turbulence model is no exception. Even flows which are non-homogeneous (Section 4.2) are still isotropic, and more complex cases (such as shear data from Matsumoto, *et al.* [47]) are not spatially dependent and rely solely on the velocity gradient tensor to drive the shear. Turbulence in the rapid distortion theory (RDT) limit approaches two-componentality, but is still quite simple spatially compared with turbulent flows of interest to most engineers. In all test cases mentioned above, cyclic (also called periodic) boundary conditions were employed in all directions, which essentially gives the simulation an infinite domain (see [44] or [20] for more details). In sharp contrast

to these simple boundary conditions are those which many engineers are concerned with, so-called slip and no-slip boundary conditions.

As a brief review, "slip" or "shear-free" boundary conditions (see, for example, [59]) provide no resistance to motion tangential to the plane of the boundary but prevent normal motion, a so-called "no-penetration" condition. The physical translation of such a condition to velocity is both intuitive and trivial, and can be thought of, for example, as an ideal (flat) air-water interface. Translating a slip condition to other quantities, such as eddy orientations and Reynolds stresses, is not as straight-forward. "No-slip" boundary conditions (solid walls, as they are often called) resist all motion (at least down to a level where the continuum assumption for fluids holds) meaning that both tangential and normal motion is damped. Once again, translating such a condition to velocity is easy, but imposing such conditions on turbulent quantities, especially eddy vectors, can be tricky. Many flows of interest to engineers (exceptions include [12, 13] and many more) employ one or both of these boundary conditions. Use of such boundary conditions immediately implies non-homogeneity and possibly a loss of isotropy. Furthermore, such boundary conditions emphasize many previously untested components of a turbulence model, including the model's ability to handle shear and sharp spatial gradients, the stability of the viscous diffusion term, and coupling between the turbulence model and momentum equation.

It is beneficial to test turbulence models one term at a time, but once such tests have been completed, more complex benchmarks are required. Decaying turbulence near a solid wall tests non-local effects and diffusion while not emphasizing terms that depend on shear. Turbulent Couette flow between two infinite parallel plates with one fixed (no-slip) and one moving (fixed streamwise velocity but otherwise no-slip) wall is a common test. This flow imparts a fixed shear across the entire domain (except in the boundary layers) and reaches a known steady state (for average quantities - see, for example, [33]). Another common benchmark is turbulent Poiseuille flow between

two infinite parallel plates, often called turbulent channel flow. A plethora of direct numerical simulation and experimental data exists for this flow including that of Kim *et al.* [31] and Moser, *et al.* [49] whose data have been used extensively to benchmark simulations of turbulent channel flow. Turbulent flow over a backward facing step, as described in [38] among others, is often the next step in validating a turbulence model as it not only involves complex boundary conditions but also challenges the model to accurately predict reattachment length and circulation (directly after the step). Unfortunately, as is discussed in §1.2.2, most models which involve turbulent quantities such as Reynolds stresses require special attention close to and on solid boundaries. The Oriented-Eddy Collision turbulence model is no exception. Capturing the proper turbulent behavior at and near a wall (in order to ensure the Reynolds stresses and eddy orientations asymptotically approach the boundary correctly) without resorting to arbitrary wall functions is far from trivial.

A wall, whether it be a slip or no-slip boundary, immediately presents problems for turbulence modelers. Certain quantities, like velocity, have physically intuitive boundary conditions. Others, especially the Reynolds stresses $\overline{R}_{ij}$, require more thought. The Reynolds stresses are defined via fluctuating velocities $u_i^{'}$ (discussed in §1.2.1), namely $\overline{R}_{ij} = \overline{u_i^{'} u_j^{'}}$. As such, it would make sense that the boundary conditions on $\overline{R}_{ij}$ are based on those imposed on velocity. For a no-slip wall, where all velocity is damped, all components of the Reynolds stresses are also damped (set to zero at the wall). For a slip wall, one condition cannot be applied to all components. In both cases, the asymptotic behavior of the stress tensor's components as they approach the wall must be ensured (first introduced in §1.2.2 and discussed below in §5.3.1). Specifying boundary conditions for the velocity and Reynolds stress tensor is not enough - boundary conditions for the eddy vector q_i must also be considered. But what does an eddy do at a wall, either slip or no-slip? In its current state, an eddy vector q_i represents neither vorticity nor velocity and therefore has no obvious

boundary conditions. Instead, the original form of the Oriented-Eddy Collision turbulence model casts q_i as representative of the size of a characteristic turbulent eddy (properly, the inverse size of an eddy as q_i has units of inverse length) and is related to the dissipation and correlation length. Over a no-slip wall, do eddies shrink to zero size? What about over a slip wall? Also, how do these representative eddy vectors approach a wall asymptotically?

5.2 Two interpretations

There are at least two ways to interpret an eddy's behavior on and near a wall. One claims that a turbulent eddy should be aligned with vorticity, while the other places eddies perpendicular to vorticity. The relationship between vorticity and eddy orientation vectors is still unclear, and the truth likely lies somewhere between these two extremes. These interpretations are outlined below, along with the boundary conditions for the eddy orientation vectors and Reynolds stress tensors which apply to each. In addition, two algorithms are developed to capture pressure echo effects, one for each interpretation. A brief review of non-local pressure effects is given. In order to test the new theory developed, data from instantaneous wall-insertion in a turbulent flow is employed. Under either interpretation, the wall-normal components of the Reynolds stresses tend to be suppressed and go to zero at a solid boundary, while the wall-tangent components tend to increase, at least initially. This behavior is consistent with what is observed for cases where a wall is instantaneously inserted into a turbulent flow, and is primarily due to pressure echo. The focus of this chapter is to understand the relationship between the stress tensor behavior, vorticity, and eddy orientation vectors.

In the case where eddies are aligned with vorticity, the wall-tangent components of the eddy orientation vectors are damped when approaching a no-slip wall, and zero on the wall itself. The wall-normal components tend to increase. This is opposite

to the observed behavior of the Reynolds stress tensor. If eddies are perpendicular to vorticity, however, the wall-normal components of the eddy orientation vectors are damped, and the tangential components increase (or, at the very least, are not damped). While this corresponds well with the behavior of the Reynolds stress tensor components, it is not clear that this interpretation is superior to one in which eddies are aligned to vorticity. As is discussed below, both ideas yield reasonable results. At first, eddies aligned with vorticity are considered, boundary conditions proposed, and a simplistic near-wall damping and reorientation scheme developed. This idea is then abandoned for the perpendicular interpretation discussed in the works of Reynolds & Kassinos [30]. Boundary conditions are reformulated, and a more complex eddy orientation vector and Reynolds stress tensor damping and reorientation scheme proposed and tested against wall-insertion data. Finally, the original interpretation is considered once again, a new reorientation algorithm formulated, and the ideas tested against the same turbulent wall-insertion data.

5.2.1 Pressure echo

Before tackling the nature of the eddy orientation vectors, a brief review of non-local wall effects (taken mostly from Durbin, *et al.* [17]) is in order. If, in a given flow, one neglects viscosity and there is no shear present, the inviscid effect of a boundary (in this case, slip or no-slip) is reduced to a pressure effect (a "pressure-" or "wall-echo") and the surface acts as a sort of mirror, reflecting flow structures across the boundary (which acts as a reflection plane, as it were). This observation has led to the idea of so-called "image vortices", non-physical entities which can be used to approximate the presence of a solid boundary. If these image vortices were to be introduced to a flow by mirroring existing vortices across the wall plane (*i.e.* placing them on the other side of the surface), and the surface then removed, the flow would be unaware that the surface had disappeared (keeping the simplifying

assumptions in mind). As a concrete example, consider a surface in the XZ-plane, shown in Figure 5.1. In this case, Y is positive in the wall-normal direction. The vortex and corresponding image vortex are comprised of three vorticity components, ω_x, ω_y, and ω_z: Note that the sign of ω_y is the same for both the vortex and its image.

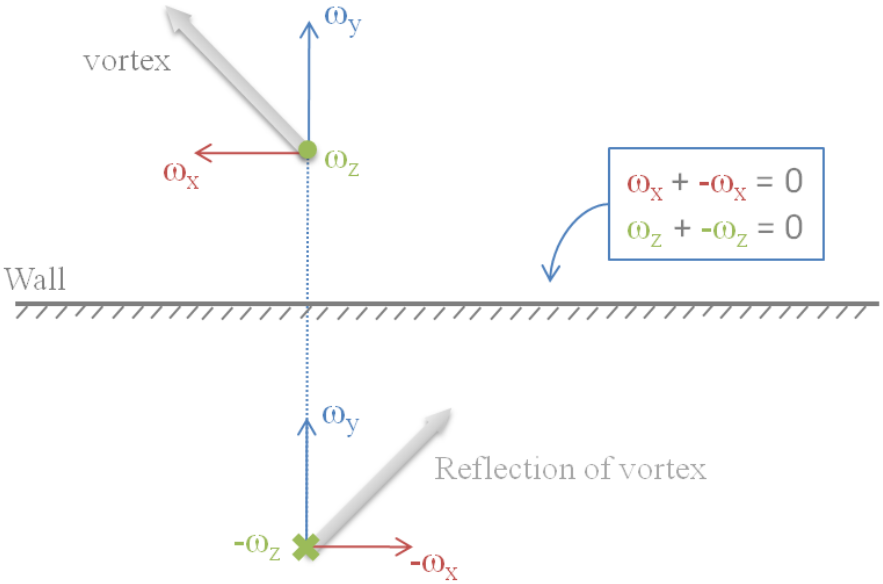

Figure 5.1. In shear-free, inviscid flow, a wall can be replaced by a collection of image vortices. Note the "dot" for ω_z in the upper vortex, and the "cross" for ω_z in the lower vortex, represent ω_z out of and into the page, respectively.

The signs of both ω_x and ω_z are reversed but their magnitudes identical, noting ω_z is out of the page for the original vortex and subsequently into the page for the image vortex. This is an important observation: in the inviscid, shear-free case, vorticity in the wall-tangent directions (X and Z) appears to cancel, meaning tangential vorticity at a solid boundary vanishes. These ideas are particularly useful when considering the relationship between an eddy orientation vector and vorticity.

5.3 Initial thoughts: Eddies aligned to vorticity

Two types of solid boundaries are considered: first, a classic "slip" wall where surface-normal velocities are forced to zero (a no-penetration condition) but tangential

components are undamped, that is a zero gradient condition is set as the boundary condition. The appropriate boundary conditions for velocity are obvious. Boundary conditions for the eddy vectors and Reynolds stress tensors are less obvious, however. Equation (5.1) proposes slip wall boundary conditions for the local Reynolds stress tensor R_{ij}:

$$R_{ij}|_{slip-wall} = \begin{bmatrix} \frac{\partial R_{11}}{\partial x_i} = 0 & R_{12} = 0 & \frac{\partial R_{13}}{\partial x_i} = 0 \\ & R_{22} = 0 & R_{23} = 0 \\ & & \frac{\partial R_{33}}{\partial x_i} = 0 \end{bmatrix} \tag{5.1}$$

and for the eddy vectors q_i.

$$q_i|_{wall} = \begin{bmatrix} q_1 = 0 \\ \frac{\partial q_2}{\partial x_i} = 0 \\ q_3 = 0 \end{bmatrix} \tag{5.2}$$

This assumes that the x_2 direction is normal to the free surface. Curved surfaces with spatially changing normals are not considered at this time. Note that R_{ij} and q_j do *not* have overbars indicating they are "local" quantities. Equation (5.2) above implies that the eddy orientation vectors are perfectly aligned with vorticity, which is open to interpretation. The boundary conditions described above are appealing as they ensure that eddy orientation vectors at a solid boundary are automatically orthogonal to the Reynolds stress tensor corresponding to the given eddy. Although the orthogonal restriction is necessary in order for the model to maintain fluctuating incompressibility, this restriction may be unnecessary in nonhomogeneous or anisotropic conditions.

In Equation (5.1), all the components of the stress tensor which involve a vertical (x_2) component are set to zero, while those independent of the vertical component are set to zero gradient in the vertical direction. A different idea is applied to the eddy vectors in Equation (5.2). At a slip wall (and a solid boundary), only the vertical component of the eddy vector is allowed to grow or shrink (once again assuming x_2 is the wall-normal direction), and the two tangential components of the eddy vector are

forced to zero. Selecting tensor components to be no-slip or zero gradient in a certain direction is difficult in OpenFOAM. A boundary condition does exist which allows certain components of a vector or tensor to have zero gradient boundary conditions applied while others can have a fixed value (*i.e.* zero) condition applied. The current implementation of this boundary condition does not, however, allow for a zero gradient boundary condition *in a certain direction* to be applied - the zero gradient is applied to all directions of a given component.

The second case considered is somewhat simpler, as appropriate boundary conditions at a no-slip wall have quantities that are forced to zero. Again, many boundary conditions are obvious: all three velocity components are forced to zero, the kinetic energy is forced to zero as are all six components of the symmetric Reynolds stress tensor. The eddy vector q_i is left in the form of Equation (5.2) above. Note that one might wish to introduce a new quantity L_i which redefines the eddy orientation vector such that $L_i = q_i/q^2$ (see §A.2 and §A.4). All components of L_i could be set to zero at a solid boundary, essentially forcing all eddies at the wall to be of zero size. This seems physically intuitive. Unfortunately, this intuition leads to an impossible boundary condition on the eddy vector q_i itself, namely that if the eddy size goes to zero at a no-slip wall ($L_i \to 0$) then $q_i \to \infty$. Even if q_i is abandoned all together in favor of L_i, the prescription of such boundary conditions, while convenient in the case of a no-slip wall, causes several numerical issues that must be taken into consideration. Specifically, forcing the eddy vectors L_i to be zero at solid boundaries can lead to unstable behavior.

5.3.1 A first look at eddy reorientation

Stability at solid boundaries is dependent on several factors, two of which are considered here: First, the boundary conditions for all relevant quantities must be set properly. Second, the way in which quantities asymptotically approach a wall is

also vital (for a review, see §1.2.2). The presence of walls in a turbulent flow impart so-called non-local effects on the flow, specifically affecting turbulent redistribution. Durbin [17] discusses two of the most common methods that near-wall modeling employs, pressure echo and elliptical relaxation. Both methods seek to alter turbulence quantities near to but not at a wall in order that the model return more realistic results. The effects of walls are felt instantaneously and up to an eddy-length away from the wall. This is because the pressure and incompressibility constraint cause a sudden and long range change in the velocity field. As a result, solid boundaries tend to cause regions of strong inhomogeneity, production, and shear. Near wall pressure echo acts to suppress wall-normal turbulence, which can have a drastic effect on the nature of the near-wall Reynolds stress tensor. Unfortunately, most Reynolds stress transport models lack a mechanism to ensure this behavior, thus special consideration must be made. The Oriented-Eddy Collision turbulence model is no different, and the aforementioned "near wall reorientation" of the eddy vectors is this model's solution to the problem. Great care must be taken when attempting to use Reynolds stress transport models near solid boundaries where the velocity and Reynolds stresses tend to zero. At the moment, wall functions and damping are the most popular methods employed to handle solid boundaries.

Recall from §1.2.2: the fluctuating velocity can be considered a smooth function of the distance from the solid boundary y and expanded as a Taylor series $u_i^{'} = p_i + q_i x_2 + r_i x_2^2$ with p_i, q_i, and r_i functions of the wall-tangent directions. If the velocity at the wall is zero, $u_i^{'}(x_2 = 0) = 0$, then $p_i = 0$ which implies $u_1^{'}$ and $u_3^{'}$ (in the tangential x_1 and x_3 directions) approach the boundary like x_2. Invoking continuity reveals that velocity in the wall normal direction $u_2^{'}$ approaches the wall like x_2^2. The near wall asymptotic behavior of the individual Reynolds stress tensor components can be assessed: $\overline{u_1^{'}u_1^{'}}$, $\overline{u_3^{'}u_3^{'}}$, and $\overline{u_1^{'}u_3^{'}}$ will approach like x_2^2. $\overline{u_1^{'}u_2^{'}}$ and $\overline{u_2^{'}u_3^{'}}$ will go like x_2^3, and $\overline{u_2^{'}u_2^{'}}$ like x_2^4 ([17], [66]). A similar analysis can be performed

for the eddy vector q_i asymptotic behavior revealing $\overline{q^2}$ should approach the wall like $1/x_2^2$, at least in the log layer. In order for the Oriented-Eddy Collision turbulence model to return reasonably accurate results near a solid boundary it is necessary - and not trivial - to ensure this behavior.

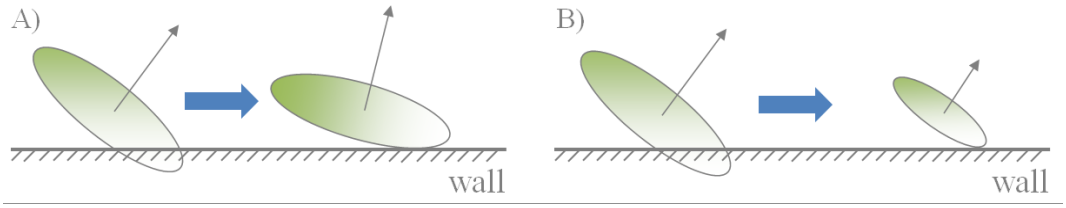

Figure 5.2. Eddies that intersect solid boundaries may be "rotated out of the way". A) This reorientation preserves the magnitude of the eddy, which does not affect the near-wall dissipation. B) This scaling achieves the same goal, but affects the near-wall dissipation. Arrows indicate the direction of vorticity. The eddy orientation vector is often perpendicular to the vorticity and lies in the plane of the eddies shown in this figure.

In order to achieve proper near-wall asymptotic behavior, the eddy orientation vectors q_i and subsequently the per-eddy Reynolds stresses (R_{ij}) must interact with the region near a wall (the large-scale damping effect) properly. The eddies must align themselves to ensure they are not embedded within the solid boundary. As such, an additional term is effectively added to both the evolution equations for q_i and R_{ij}. This "term" in the R_{ij} transport equation ensure that once an eddy is reoriented, the stress tensor corresponding to that eddy is also reoriented such that is remains orthogonal to the new q_i. Expressing near-wall reorientation as a term in the transport equation is somewhat misleading as the reorientation process is handled by a correction performed after the evolution equation is advanced in time. Any eddy embedded in a wall (there is nothing in place to guarantee this doesn't occur) must be rotated out of the wall or resized such that it no longer interacts with the wall. One method rotates the eddy vector away from the wall while maintaining its magnitude, shown in Figure 5.2A, while the second method shrinks the eddy away

from the wall and does not maintain the eddy's original magnitude. The first method was initially chosen as it does not affect the near-wall dissipation. The second method, illustrated in Figure 5.2B, always decreases the magnitude of the eddy vector thus affecting the near wall dissipation. Both methods are performed as a post-calculation correction to q_i and are not contained in the evolution equations themselves. For the first case, the angle between the old and new eddy vectors is calculated once the proper reorientation has been applied. Then, the tensor R_{ij} must be aligned with the new eddy vector. This enforces the incompressibility constraint on q_i and R_{ij} (*i.e.* orthogonality between q_i and R_{ij}). For a given eddy vector q_i, the following transformation can be applied until the eddy has been rotated far enough from the wall making sure that the magnitude of q_i remains unchanged:

$$q_i = \gamma \left[q_i - \chi \begin{pmatrix} q_1 \\ 0 \\ q_3 \end{pmatrix} \right] \tag{5.3}$$

with the scalar coefficients

$$\chi = 1 - \frac{x_2^{cell}}{({q_1}^2 + {q_3}^2)^{\frac{1}{2}}} \tag{5.4}$$

and

$$\gamma = \left[\frac{|q_i|^2}{(1-\chi^2)\,({q_1}^2 + {q_3}^2) + {q_2}^2} \right]^{\frac{1}{2}} \tag{5.5}$$

where ${x_2}^{cell}$ is the distance from the eddy in question to the nearest wall. The loop terminates when $|a_i|^2 \leq ({x_2}^{cell})^2$ where $a_i = q_i \times n_i$ and n_i is the unit normal vector of the nearest wall. Once an eddy is reoriented, the corresponding Reynolds stress tensor must also be rotated. Rodrigues' rotation formula can be employed:

$$T_{ij} = P_{ij} + (\delta_{ij} - P_{ij}) \cos\phi + L_{ij} \sin\phi \tag{5.6}$$

with ϕ the angle between the original and reoriented eddy vector, the cosine between the old and new vectors is defined as $\cos\phi = \left({q_i}^{old} q_i\right) / \left(\left|{q_i}^{old}\right| |q_i|\right)$, the sine subsequently calculated via $\sin\phi = \sqrt{1-\cos^2\phi}$, and $P_{ij} = a_i a_j$. The skew-symmetric tensor L_{ij} is defined for each eddy as

$$L_{ij} = \begin{bmatrix} 0 & -a_3 & a_2 \\ a_3 & 0 & -a_1 \\ -a_2 & a_1 & 0 \end{bmatrix} \tag{5.7}$$

recalling $a_i = \epsilon_{ijk} q_j n_k$.

Finally, employing Equation (5.6) above, R_{ij} is rotated via $R_{ij} = T_{ji} R_{ij} T_{ij}$. Several ideas are implicit to this selection of a near wall reorientation algorithm. The procedure outlined above decouples the near wall dissipation from the reorientation operation. Whether this is physically correct or not is questionable, as dissipation is not constant when approaching a solid boundary [60]. A near wall realignment can be formulated to affect the magnitude of the eddy vectors. Independent of the magnitude of the eddy vectors, a similar argument can be made for the Reynolds stress tensor reorientation; that is, kinetic energy can be conserved locally, globally, or not at all. The method presented above conserves local kinetic energy (*i.e.* the trace of the stress tensor remains constant) and validation cases have shown that global kinetic energy (the trace of the average stress tensor) is also preserved. Once again, conserving kinetic energy is not necessarily the desired behavior as direct numerical simulations of near-wall turbulence reveal that kinetic energy is not constant as it approaches a solid boundary [60]. For the most part, eddy orientation vectors have at least two non-zero components and in theory associated orientation vectors are neither perfectly normal nor perfectly tangent to a solid boundary, as illustrated in Figure 5.3(a). Figure 5.3(b) illustrates two troublesome situations. In Figure 5.3(b), the eddy on the left is perfectly tangential to the wall while the eddy on the right

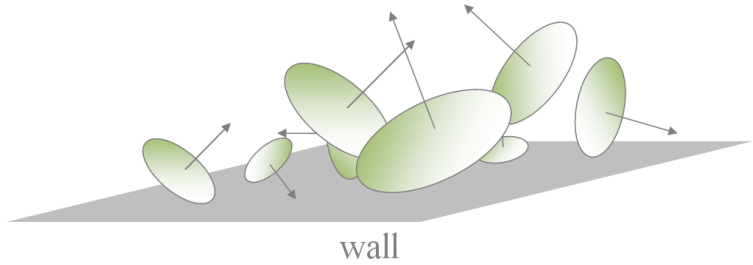

(a) Most eddies are not aligned tangential or normal to a solid boundary.

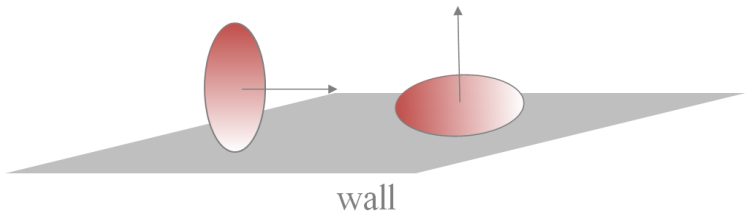

(b) Some eddies may be normal to (right) or tangential to (left) a wall.

Figure 5.3. Possible alignments for eddies near a wall.

is perfectly normal to the wall. The above reorientation algorithm fails in these situations. If the eddy is normal, the eddy should never be reoriented as it cannot be intersecting the wall. This case is rare, but must be accommodated for. In the event of a perfectly tangential eddy, the problem becomes more serious. In this case, the normal component of the eddy vector (in this case, the x_2 component) is identically (or vanishingly close to) zero. Even if the eddy is embedded in a wall (see Figure 5.2), the algorithm above will not work. Either it will fail to reorient the eddy (as no changes to the tangential x_1 or x_3 components can possibly reorient the eddy away from the wall) or it will spin the eddy about its wall-normal (x_2) axis forever. Neither case is desirable, as the eddy must be rotated out of the wall. Several possible solutions exist, including "nudging" the eddy away from the wall by forcing the wall-normal (x_2) component to be non-zero. Of course, the sign of the arbitrary non-zero x_2 component will dictate whether the resulting eddy vector points toward or away from the wall. There is no clear answer to this question, and the original Oriented-Eddy

Collision turbulence model near-wall algorithm chose to point all perfectly-tangential eddies slightly away from the solid boundary they are embedded in. The necessity for arbitrary reorientation led to this method being abandoned, and alternatives sought.

5.4 Another approach: The "sub-eddy" interpretation

Previous ideas about boundary conditions for eddy orientation vectors were based on physical intuition about the size and orientation of turbulent eddies near solid boundaries. This procedure falls victim to the nebulous nature of q_i, which is more mathematical than physical in nature. Humans tend to understand fluids (turbulent or otherwise) in terms of velocities, densities, and pressures. Those with more experience in the field might also think in terms of vortices or gradients. Eddy orientation vectors, at least in the context of the Oriented-Eddy Collision turbulence model, are less straightforward. In Chapter 1, the work of Reynolds & Kassinos [30] and Van Slooten & Pope [100] were cited as cousins and predecessors of the OEC model. Although not identical to q_i in the Oriented-Eddy Collision turbulence model, Reynolds & Kassinos employed the concept of a "sub-eddy" which is composed of vorticity and fluctuating velocity vectors as well as a third vector perpendicular to those two. Considering the relative ease in which the behavior of vorticity and velocity can be described (especially near solid boundaries), q_i could be interpreted in a similar manner. This interpretation could shed light on the otherwise obscure behavior of q_i at and near walls.

The eddy orientation vectors may not represent vorticity lines but may still be related to vorticity. As was mentioned previously, Kassinos and Reynolds [30] argued that a "sub-eddy" (which is *not* q_i) is comprised of three vectors: a fluctuating vorticity vector $\omega_i^{'}$, a fluctuating velocity vector $u_i^{'}$ (which is by definition perpendicular to the vorticity vector) and finally some other vector r_i which is perpendicular to both $\omega_i^{'}$ and $u_i^{'}$. Note that, given $\omega_i^{'} \perp u_i^{'}$, these two vectors define a plane or a planar disk

which may be circular or elliptical. With $r_i \perp \omega_i^{'}$ and $r_i \perp u_i^{'}$, r_i must in fact be normal to the plane defined by $\omega_i^{'}$ and $u_i^{'}$. This means that, neglecting the magnitude of r_i, $r_i = \omega_i^{'} \times u_i^{'}$. It is important to point out *why* $r_i \neq q_i$: r_i is defined by a unique pair of $\omega_i^{'}$ and $u_i^{'}$. In the Oriented-Eddy Collision turbulence model, the local Reynolds stress tensor R_{ij} is an *average* over all pairs of $\omega_i^{'}$ and $u_i^{'}$ with the same r_i direction. The vector q_i is therefore an average over all r_i that have the same direction but potentially different magnitudes, different $u_i^{'}$, and different $\omega_i^{'}$. Note that many r_i may be normal to one given plane, and an infinite number of pairs of orthogonal $\omega_i^{'}$ and $u_i^{'}$ may lie in that given plane. The Oriented-Eddy Collision turbulence model is equivalent to an average over all pairs in that plane.

Imagine the face of a clock, where $\omega_i^{'}$ is the hour hand and $u_i^{'}$ the minute hand, and the two hands define the face (a planar disk which happens to be circular). For every possible "time" told by $\omega_i^{'}$ and $u_i^{'}$ there exists a unique r_i. In essence, q_i could be interpreted as the average of all possible "sub-eddy" r_i, meaning the average of all possible $\omega_i^{'}$ and $u_i^{'}$ that r_i (and therefore q_i) is orthogonal to. This is consistent with the previous understanding of the transport equation for q_i as an equation for a passive planar disk in the rapid distortion theory limit. This concept is illustrated in Figure 5.4. An important subtlety arises with this new interpretation of the eddy orientation vector: The Oriented-Eddy Collision turbulence model contains no vector representing the velocity fluctuations $u_i^{'}$; instead, it has a tensor, namely the Reynolds stress tensor that is orthogonal to (that is, lies in the plane perpendicular to) q_i. In addition, the vorticity vector is not part of the model. Recalling q_i is an average over all "sub-eddy" r_i at a given location, the stress tensor R_{ij} local to the eddy (*i.e.* attached to the given q_i) is in fact an average over all $u_i^{'}$, which is consistent with the definition of R_{ij}. This supports the conjecture that q_i represents an average over all the fluctuating velocities that lie in the plane perpendicular to q_i. With this

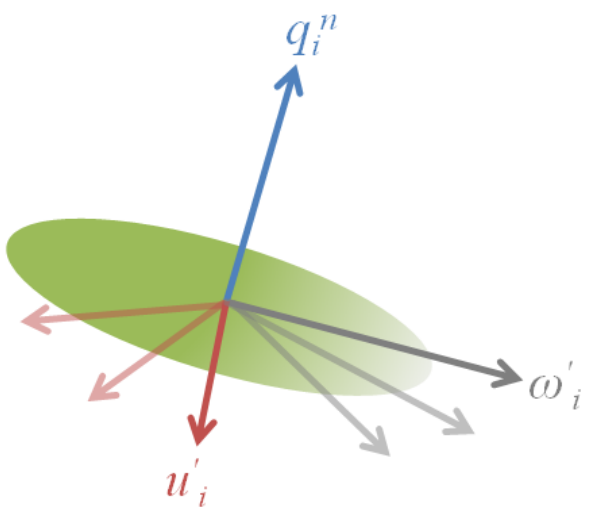

Figure 5.4. Rather than thinking of a turbulent eddy as a singular entity, one might imagine it consists of many orthogonal fluctuating velocity vectors $u_i^{'}$ and vorticity vectors $\omega_i^{'}$, themselves orthogonal to the eddy vector q_i^n.

interpretation of the eddy orientation vector in mind, boundary conditions for q_i can be reconsidered.

5.4.1 Boundary conditions for the "sub-eddy" interpretation

At a slip wall, all sub-eddies have vorticity $\omega_i^{'}$ normal to the wall (as was shown above). This restricts the possible orientations of $u_i^{'}$ and q_i to be tangent to the wall, with q_i still perpendicular to $u_i^{'}$. This restriction on the orientation of $\omega_i^{'}$ and $u_i^{'}$ is so severe that the number of possible sub-eddy vorticity and velocity vectors drops to one for each q_i. Thus, at a wall, there exists a *single* sub-eddy vorticity vector $\omega_i^{'}$ (normal to the wall) and a *single* sub-eddy fluctuating velocity vector $u_i^{'}$ (tangential to the wall and perpendicular to the eddy orientation vector) for each q_i vector. This is good news. Rather than guessing at the *average* behavior of all sub-eddy vortices and fluctuating velocities to divine the proper boundary conditions on q_i, understanding the behavior of *one* $\omega_i^{'}$ and *one* $u_i^{'}$ at a solid boundary will suffice. This can be interpreted as the Reynolds stress tensor R_{ij} collapsing from a disk to a line in the

wall plane. Furthermore, the eddy vectors will all lie in the wall plane with each q_i being orthogonal to the new "R_{ij} line".

The wall-tangent inviscid boundary condition requires that $q_2 = 0$ (continuing with the standard of declaring x_2 the wall normal direction) as any eddy orientation vector q_i normal to the wall is an average of sub-eddies with vortices in the wall plane which are, by definition, all zero. This is *precisely opposite* to what was proposed for a q_2 boundary condition when q_i was aligned with vorticity. The previous boundary condition on q_i, which damped all wall-normal fluctuations, was attractive as it automatically satisfied the no-fluctuation requirement. The Reynolds stress tensor R_{ij} associated with each q_i will once again have all components which include a wall-normal component set to zero. This, at least, is consistent with the previous version of R_{ij} boundary conditions for a wall. Again, only components which do *not* include the wall-normal direction will remain non-zero at a wall, namely R_{11}, R_{13}, and R_{33}. Furthermore, R_{ij} must remain perpendicular to q_i, which places additional constraints on two of the three remaining "free" stress tensor components. This reduces the Reynolds stress boundary condition to one free parameter which is intuitive as this one free parameter represents the amount of fluctuation that is both in the wall plane and perpendicular to q_i.

Specifying boundary conditions for the Reynolds stress tensor and the wall normal component of the eddy vector is not enough. Boundary conditions for the tangential components of q_i are still required. Viscous effects at a no-slip wall force the normal vorticity to zero, $\omega_2^{'} = 0$ while the tangential vorticity components $\omega_1^{'}$ and $\omega_3^{'}$ are no longer zero (with the same assumptions for the x_2 direction). Tangential vorticity is actually generated by the solid boundary and tends to flux away from the wall. Considering vorticity must lie in the wall plane, and the fluctuating velocity must be tangential to the wall (when sufficiently close), these two conditions force the eddy orientation vector q_i associated with this pair to be perfectly normal to the wall. Even

though the velocity vector very close to the wall is tangential and non-zero, it quickly approaches zero at the wall. This indicates that, although normal to the wall, the magnitude of the eddy orientation vectors quickly approaches zero as well. In the case of an inviscid boundary, the wall-normal component of the orientation vector is zero (as was the case previously), $q_2 = 0$, while tangential components q_1 and q_3 have no such requirement and thus may be set to be zero-derivative. Again, this is exactly opposite to what was proposed previously. With this in mind, the boundary conditions for the eddy orientation vector q_i can be restated:

$$q_i|_{wall} = \begin{bmatrix} \frac{\partial q_1}{\partial x_i} = 0 \\ q_2 = 0 \\ \frac{\partial q_3}{\partial x_i} = 0 \end{bmatrix} \tag{5.8}$$

This method should work both as a slip and no-slip boundary condition for q_i as q_i is normal to the wall and the normal component should vanish. Boundary conditions for the Reynolds stress tensor R_{ij} at a shear-free surface are unchanged:

$$R_{ij}|_{slip-wall} = \begin{bmatrix} \frac{\partial R_{11}}{\partial x_i} = 0 & R_{12} = 0 & \frac{\partial R_{13}}{\partial x_i} = 0 \\ & R_{22} = 0 & R_{23} = 0 \\ & & \frac{\partial R_{33}}{\partial x_i} = 0 \end{bmatrix} \tag{5.9}$$

5.4.2 Reorientation for the "sub-eddy" interpretation

With a shift in the interpretation of the eddy orientation vectors and changes to the boundary conditions applied to q_i at walls comes the need to reassess the near-wall reorientation. While many concepts developed in the previous section - the need to prevent "embedded eddies" and the need to rotate the Reynolds stresses such that they remain orthogonal to the reoriented eddy orientation vectors - are valid, the re-orientation algorithm and dissipation / kinetic energy conservation must be carefully reconsidered. Sub-eddy vortices had been helpful in the past can be employed to

determine the proper eddy reorientation algorithm for this case. Any vorticity which is entirely normal to the wall is not affected by the solid boundary as only $\omega_1^{'}$ and $\omega_3^{'}$ are damped by the image vortices. Thus, if all sub-eddies for a given q_i contain only wall-normal vorticity the eddy orientation vector would never "feel" the presence of the wall; all q_i and R_{ij} would be tangent to the solid boundary. This is a highly unusual case. Normally, for a given q_i sub-eddy vortices will contain some non-zero $\omega_1^{'}$ and $\omega_3^{'}$ components. As was shown in §5.4, any wall-tangent vorticity components will be damped as the wall is approached, and at the wall these components will become zero. This is the first clue as to how near-wall reorientation operates in this case: as an eddy orientation vector q_i approaches a wall, the tangential components of the sub-eddy vorticity vectors represented by that eddy vector should be damped. This will cause the overall sub-eddy vorticity vector $\omega_i^{'}$ to shrink and its wall-normal component $\omega_2^{'}$ will begin to dominate. This will appear to tilt $\omega_i^{'}$ more normal to the wall. Recalling that q_i and the sub-eddy fluctuating velocity vector $u_i^{'}$ are both perpendicular to $\omega_i^{'}$, this apparent tilt also changes the direction of q_i and $u_i^{'}$, where again $u_i^{'}$ is represented on average as this eddy's associated stress tensor R_{ij}. This causes the eddy vector q_i to become more tangent to the wall plane regardless of whether or not the velocity vector was already tangential to the wall plane. Conveniently, this also satisfies the requirement for q_i and R_{ij} to remain orthogonal. If, however, the eddy orientation vector was perfectly normal to the wall plane, a change in $\omega_i^{'}$ would not affect $u_i^{'}$ (which already lies in the wall plane), meaning the Reynolds stresses would not be altered. Also note that in the rare case that the vorticity vector $\omega_i^{'}$ is *already* perfectly tangent to the wall, as the wall is approached the magnitude of $\omega_i^{'}$ will shrink but the vector itself will not change direction, thus q_i and $u_i^{'}$ will be unaltered. Figures 5.5 and 5.6 illustrate the behavior of q_i and associated sub-eddy vorticity and fluctuating velocities above both a slip and no-slip wall. What if eddies are perfectly aligned to the wall plane? Figure 5.6 illustrates this case. Such eddies,

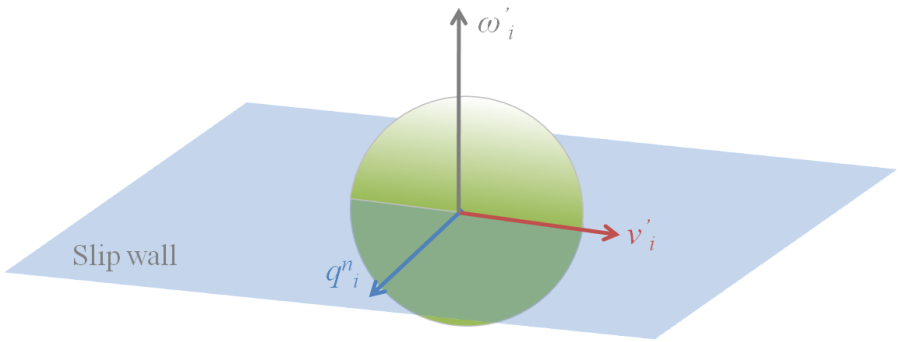

Figure 5.5. Behavior of the eddy's components slightly above a slip wall. The eddy itself can be embedded in the wall as the fluctuating velocity $u_i^{'}$ (and eddy vector q_i^n) is forced to be tangential (a no-penetration condition). The vorticity $\omega_i^{'}$ is therefore entirely perpendicular to the boundary with no tangential component.

when moved slightly away from a solid wall, experience no change in the direction of their associated orientation vector q_i though their magnitude will change considerably. Recalling that the eddy orientation vectors q_i are actually averages over all sub-eddies which share a certain q_i, this presents a problem. The sub-eddy vorticity vectors should become more wall-normal and the fluctuating velocity vectors more tangential as the eddy moves away from the solid boundary. If q_i is unaltered, however, the sub-eddy quantities which lie below q_i have no means of changing. A change in the sub-eddy fluctuating velocities also dictates a change in their Oriented-Eddy Collision turbulence model surrogate, the local Reynolds stresses. One way to overcome this complication involves changing the magnitude of q_i. But what does the magnitude of the eddy orientation vector represent in terms of sub-eddy quantities? The size of q_i could represent the number of sub-eddies averaged over to obtain q_i. Reducing the magnitude of q_i (specifically q_2) as an eddy approaches a wall is akin to reducing the number of sub-eddies that have an r_i in the wall-normal direction. It may also represent $\epsilon_{ijk}\omega_j^{'}u_k^{'}$ in which case vorticity would be damped considerably. In any case, a reduction of the eddy magnitude is necessary. What if q_i is perfectly normal to the wall? This would entail sub-eddy vorticity vectors perfectly tangent to

the wall. As was the case with a perfectly tangential q_i, the sub-eddy vorticity will not change direction as the eddy's distance to the wall changes but should experience a change in magnitude. The sub-eddy velocities, and thus the Reynolds stresses, will neither change in direction nor magnitude. The eddy orientation vectors themselves will also not change direction, but should reduce in magnitude as the solid boundary is approached. A perfectly tangential q_i will do exactly nothing and damp the wall-normal components of the stress tensor R_{ij}. With the observations above in place,

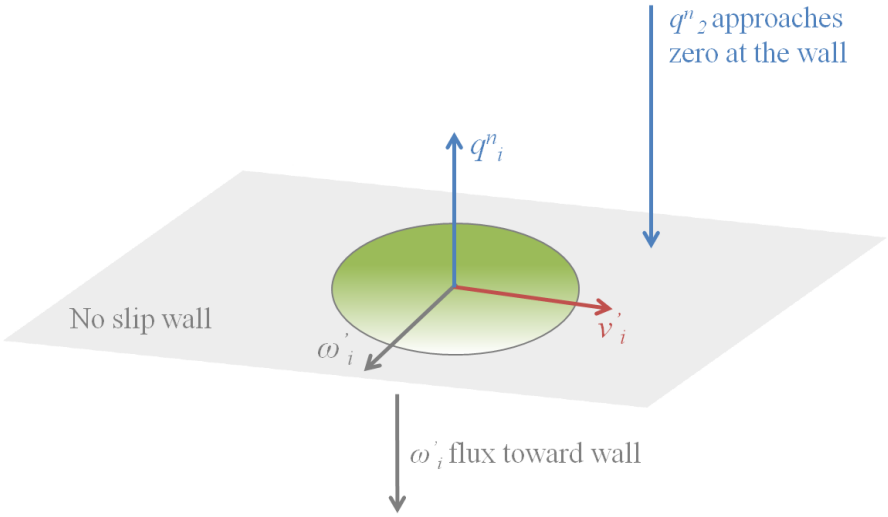

Figure 5.6. Behavior of the eddy's components slightly above a no-slip wall. Here, all fluctuating velocities u_i' are zero at the wall therefore q_2 approaches zero heading toward the wall.

near-wall reorientation of turbulent eddy orientation vectors can be summarized: First and foremost, solid boundaries tend to reorient sub-eddy quantities, specifically the vorticity ω_i' and fluctuating velocity u_i'. Vorticity tends to align normal to the wall plane forcing q_i and u_i' to be more tangential to the wall plane. There tends to be more sub-eddies with tangential q_i and fewer with normal q_i which can be reflected by damping the normal component of q_i. While it appears that tangential q_i should be unaffected as they approach a wall because they correspond to wall-normal vorticity (which is unaffected by the presence of a solid boundary), this is not the case. While

exact conservation of dissipation and kinetic energy is debatable, the need to transfer energy from certain components of the eddy orientation vectors and Reynolds stress tensors to other components of q_i and R_{ij} - specifically from q_2 to q_1 and q_3 and R_{11} to R_{22} and R_{33} - is highly desirable in cases such as turbulent channel flow, discussed in the next section.

In the unusual (and avoidable) case of *perfectly* normal q_i, the direction of q_i remains normal but the normal component is damped. Reorientation of q_i can be achieved either by shrinking normal components or increasing tangential components. Of the two options, only the former works reasonably well for purely normal orientations. Reducing the normal component of a given q_i to produce an overall tangential tilt is preferred as it is most closely aligned with the suspected changes experienced by the sub-eddy vorticity vectors as a wall is approached, and gracefully handles the case of a perfectly wall-normal eddy orientation vector. The corresponding Reynolds stresses will continue to also rotate and align themselves to be orthogonal to the new q_i. The Reynolds stress tensor must also be damped such that its wall-normal components approach zero as the wall is approached in this interpretation of q_i.

Data from direct numerical simulations of instantaneous wall insertion into a turbulent flow, provided by Perot and Moin [60], was employed to test the reorientation scheme and boundary conditions outlined above. The aim was to capture wall insertion as closely as possible. There are several ways to approach this. First, one might choose to rely on eddy damping and reorientation alone to control the behavior of the stress tensor components. Second, one may reorient and damp the eddy orientation vectors, damp certain components of the stress tensor, and realign the local stress tensors to ensure orthogonality. Furthermore, as has been discussed before, it is possible to preserve local eddy orientation vector magnitude and local kinetic energy throughout these operations. The term "damping" implies an operation that not only rotates eddy vectors and stress tensors, but also provides some additional

modification to component sizes, or, alternatively, uses more than just the eddy's wall-normal component as a metric for rotation candidacy. These ideas are explored below. It is important to note that reorientation applied to a stress tensor means keeping the tensor orthogonal to the local eddy orientation vector and not a separate rotation operation.

Two basic approaches to damping may be employed - one which uses error functions, and the other which uses exponential functions. The exponential version is appealing as it enjoys popularity amongst turbulence wall treatments. In either case, a function of the form

$$E = 1 - exp(L),\ E = 1 - erf(L) \tag{5.10}$$

is considered, where L provides a length scale which controls the error / exponential function, E. These functions can then be employed to calculate a control constant which approaches unity at the upper limit of the damping and reorientation scheme (where the effects of pressure echo become negligible); and becomes large close to solid boundaries to affect strong damping:

$$\alpha = \frac{|q_i|}{\left|q_i^{||}\right|} E \tag{5.11}$$

Here, $q_i^{||}$ represents the wall-tangent components of the eddy orientation vector being operated on. The magnitude of the perpendicular portions of the eddy orientation vector, $\left|q_i^{\perp}\right|$ can then be tested against the product of the eddy orientation vector magnitude and the damping function, $(|q_i|\, E)$ and damped if necessary, $q_i^{\perp(new)} = \alpha q_i^{\perp}$. The operation can be reversed, testing and damping the tangential components of q_i. As will be discussed later, this is appealing in certain cases where damping the Reynolds stress tensor is avoided and instead the asymptotic behavior of the stresses is

dictated by the behavior of the eddy orientation vectors alone. The unitless damping lengthscale L is typically of the form $L = -Cy\left|\overline{q_i}^{(old)}\right|$, recalling $|\overline{q_i}|$ is the *average* of the magnitudes of the eddy orientation vectors. The constant C is typically chosen to be 6. If the local eddy orientation vector magnitude $|q_i|$ is to be preserved across the damping and reorientation operations, whichever components were not damped must be adjusted accordingly. This is trivial, and can be achieved by calculating the difference between the old and new eddy orientation magnitudes,

$$\beta = \frac{\left(\left|q_i^{old}\right|^2 - \left|q_i^{\perp}\right|^2\right)^{1/2}}{\left|q_i^{||}\right|} \tag{5.12}$$

and the tangential components scaled, $q_i^{||} = (\beta - 1)\, q_i^{||} + q_i^{||}$. Again, this operation can be applied to the perpendicular components of the orientation vector $q_i^{\perp}$ if tangential damping were performed, as is the case when q_i is interpreted as being aligned to vorticity, covered later in this chapter.

In this scheme, damping must be applied to the Reynolds stresses. Similar to the damping mechanism for the eddy orientation vectors outlined above, a test must be performed in order to determine eligibility for damping. Rather than employing an "if" statement, a minimum can be used to calculate γ, which controls (in this case) the damping of the wall-normal components of the local Reynolds stress tensor:

$$\gamma = min\left(1, \frac{E}{\frac{n_i R_{ij} n_j}{K}}\right) \tag{5.13}$$

where n_i is the unit wall-normal, E is the familiar exponential / error function, and K the local kinetic energy. If local kinetic energy is to be conserved, an additional control variable δ can be calculated where C, the control constant in the exponential / error function damping unitless lengthscale L, is typically half of that employed in the calculation of γ, that is $C_\delta = \frac{1}{2}C_\gamma$ and typically $C_\gamma = C_\beta = 6$.

Once the eddy orientation vectors are rotated and damped, and the appropriate damping for the Reynolds stresses calculated, it is necessary to rotate the Reynold stresses such that they remain orthogonal to the new eddy orientation vectors, and of course damp the appropriate stress components. This can be achieved in one step, via

$$
\begin{aligned}
R_{nm}^{(new)} = (2-\delta^2) & \left(\frac{t_i^{(old)} R_{ij} t_j^{(old)}}{t_k^{(old)} t_k^{(old)}} \right) \left(\frac{t_n^{(old)} t_m^{(old)}}{t_k^{(old)} t_k^{(old)}} + \frac{t_m^{(old)} t_n^{(old)}}{t_k^{(old)} t_k^{(old)}} \right) \\
& + \gamma^2 \left(\frac{c_i^{(old)} R_{ij} c_j^{(old)}}{c_k^{(old)} c_k^{(old)}} \right) \left(\frac{c_n^{(new)} c_m^{(new)}}{c_l^{(new)} c_l^{(new)}} + \frac{c_m^{(new)} c_n^{(new)}}{c_l^{(new)} c_l^{(new)}} \right) \\
& + \gamma \left(\frac{c_i^{(old)} R_{ij} t_j^{(old)}}{\left[\left(c_k^{(old)} c_k^{(old)} \right) \left(t_l^{(old)} t_l^{(old)} \right) \right]^{1/2}} \right) \left(\frac{c_m^{(new)} t_n^{(new)} + c_n^{(new)} t_m^{(new)}}{\left[\left(c_l^{(old)} c_l^{(old)} \right) \left(t_k^{(old)} t_k^{(old)} \right) \right]^{1/2}} \right)
\end{aligned}
\tag{5.14}
$$

where $t_i = \epsilon_{ijk} q_j n_k$ with (old) and (new) referring to whether the original (old) or reoriented (new) eddy orientation vector is being considered. The vector c_i is defined as $c_i = \epsilon_{ijk} q_j t_k$, where once again (old) and (new) refers to whether the original or reoriented eddy orientation vector is being considered. Unfortunately, Equation (5.14) does not perfectly conserve local kinetic energy across the rotation operation, and acts as a small but unphyscial dissipation term.

5.4.3 Testing "sub-eddy" reorientation

Data from Perot and Moin [60] provides Reynolds stress, kinetic energy, and dissipation data from a direct numerical simulation of turbulent Reynolds number $Re_T = 137$ flow very close to a solid boundary. Data at very short times provides validation for the near-wall damping and reorientation scheme developed in the last section, while long-time results provide a means of evaluating dissipation and diffusion models. Agreement between the DNS data and the model is quite good, which indicates the exponential reorientation scheme under the "sub-eddy" interpretation

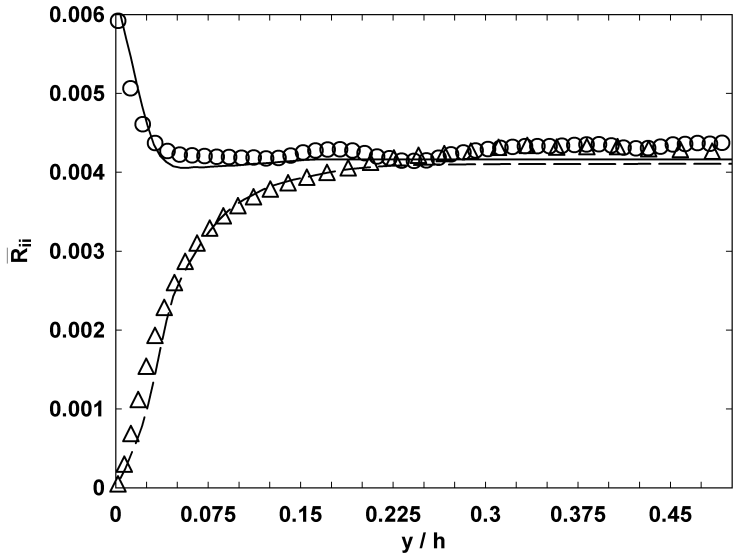

Figure 5.7. Reynolds stress data taken from direct numerical simulations performed by Perot and Moin [60]: $\overline{R}_{11} = \overline{R}_{33}$ ($\circ$), $\overline{R}_{22}(\triangle)$; compared to the Oriented-Eddy Collision turbulence model $\overline{R}_{11} = \overline{R}_{33}$ (—), $\overline{R}_{22}$ (- - -). The DNS data is at t = 2.0E-3 seconds, and considered the initial condition.

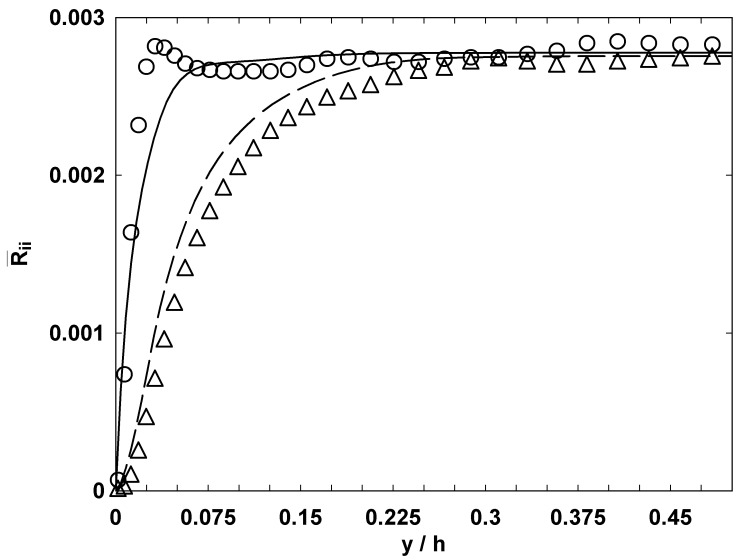

Figure 5.8. Reynolds stress data taken from direct numerical simulations performed by Perot and Moin [60]: $\overline{R}_{11} = \overline{R}_{33}$ ($\circ$), $\overline{R}_{22}(\triangle)$; compared to the Oriented-Eddy Collision turbulence model $\overline{R}_{11} = \overline{R}_{33}$ (—), $\overline{R}_{22}$ (- - -). The DNS data is at t = 1.004560 seconds, while the models data is sampled at t = 1.0 seconds.

outlined above works reasonably well. Recall one challenge was to efficiently and accurately "test" the eddies and Reynolds stresses to determine their eligibility for damping and rotation. It is possible to devise a scheme that, independent of the time step taken, can cause unbounded decay of both the eddy orientation vectors and Reynolds stress tensors. As such, the results shown in Figure 5.7 are collected after taking many small time steps. The slight underestimation of the center channel stress values is due to initial stress values slightly lower than that of the DNS data. Kinetic energy and dissipation are not shown for simplicity.

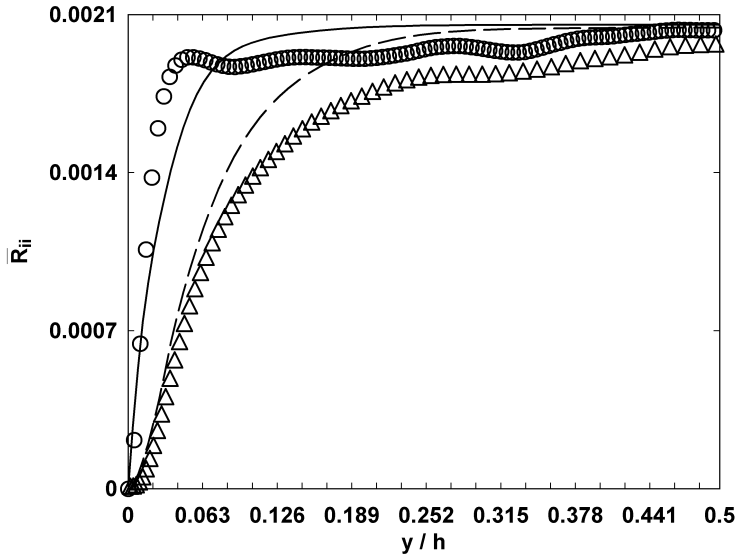

Figure 5.9. Reynolds stress data taken from direct numerical simulation performed by Perot and Moin [60]: $\overline{R}_{11} = \overline{R}_{33}$ (∘), $\overline{R}_{22}$(△); compared to the Oriented-Eddy Collision turbulence model $\overline{R}_{11} = \overline{R}_{33}$ (—), $\overline{R}_{22}$ (- - -). The DNS data is at t = 2.012613 seconds, while the models data is sampled at t = 2.0 seconds.

Reynolds stress data is provided at four additional times from Perot and Moin [60]. Reynolds stress data from direct numerical simulation is provided at time t = 1.004560 seconds, t = 2.012613 seconds, t = 3.013826 seconds, and t = 4.014137 seconds, and compared to the Oriented-Eddy Collision turbulence model's predictions of the stresses at time t = 1.0 seconds, t = 2.0 seconds, t = 3.0 seconds, and t = 4.0 seconds. The differences between sample times is necessitated first by the relatively

large time step employed for model simulations and the negligible difference between the stresses at the two different times reported. For all cases presented below, the exponential reorientation algorithm outlined in §5.4.2 is employed.

Agreement between the model and DNS data is quite good for $\overline{R}_{22}$ in Figure 5.8, while less so for $\overline{R}_{11}$ and $\overline{R}_{33}$. Considering near-wall damping and reorientation algorithms developed focus on this component, this is no surprise. Furthermore, the dominant effect of pressure echo is felt in the wall-normal components of the Reynolds stresses. These trends continue for the subsequent samples. Agreement between the

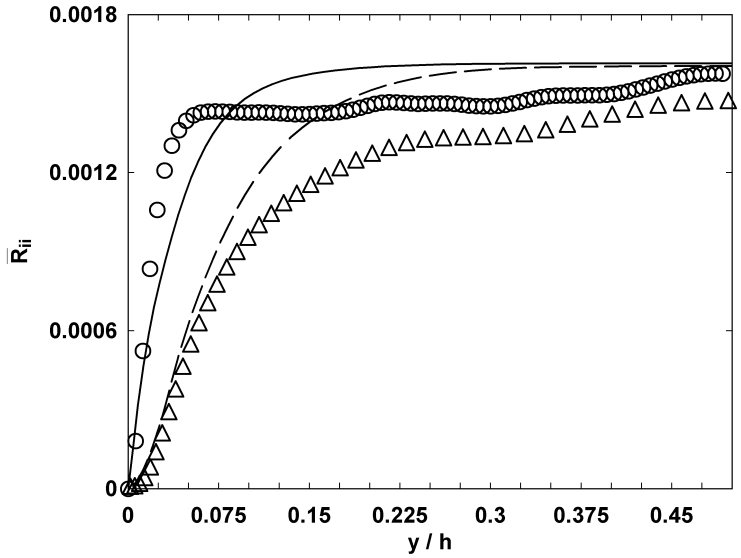

Figure 5.10. Reynolds stress data taken from direct numerical simulation performed by Perot and Moin [60]: $\overline{R}_{11} = \overline{R}_{33}$ (∘), $\overline{R}_{22}$(△); compared to the Oriented-Eddy Collision turbulence model $\overline{R}_{11} = \overline{R}_{33}$ (—), $\overline{R}_{22}$ (- - -). The DNS data is at t = 3.013826 seconds, while the models data is sampled at t = 3.0 seconds.

direct numerical simulation data from Perot and Moin [60] and the Oriented-Eddy Collision turbulence model becomes progressively worse. While the curvature for the principle Reynolds stresses predicted by the model remains reasonable, the model appears to over-predict the stress components by more than 20% in the 4.0 second data sample. This is not the case, however. The domain employed for the DNS is too small, and the structures are interacting with the DNS simulation boundaries.

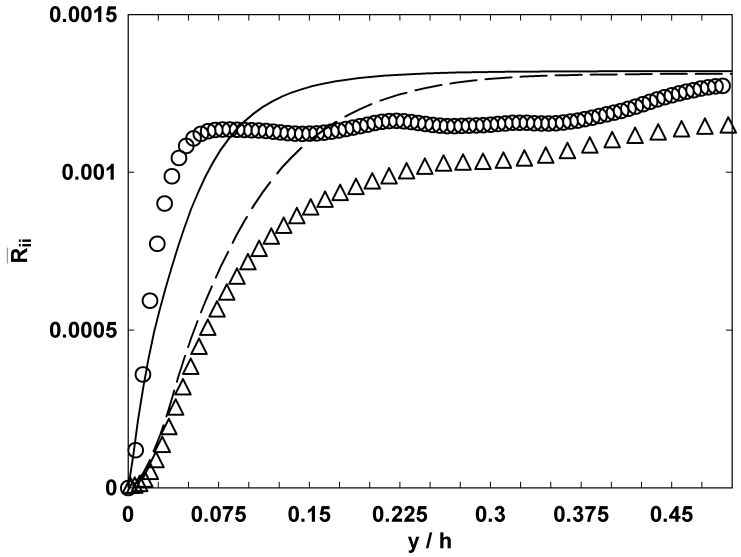

Figure 5.11. Reynolds stress data taken from direct numerical simulation performed by Perot and Moin [60]: $\overline{R}_{11} = \overline{R}_{33}$ ($\circ$), $\overline{R}_{22}$($\triangle$); compared to the Oriented-Eddy Collision turbulence model $\overline{R}_{11} = \overline{R}_{33}$ (—), $\overline{R}_{22}$ (- - -). The DNS data is at t = 4.014137 seconds, while the models data is sampled at t = 4.0 seconds.

This makes long-time data from this test case only partially useful: indeed, the Oriented-Eddy Collision turbulence model is stable next to a solid boundary even at long times, and can certainly predict the correct magnitude and curvature of the stress profiles. This reorientation scheme has succeeded. The decay of the stresses, however, is exaggerated by the underresolved DNS data and therefore cannot be used for anything more than qualitative comparisons.

5.5 Revisiting q_i aligned to ω_i

In §5.3, the original interpretation of the eddy orientation vector q_i being aligned to the vorticity vector ω_i was proposed along with boundary conditions and a simple scheme to capture pressure echo effects. This idea is revisited, and a new reorientation method proposed of the form developed and tested in the previous section. Such a method is appealing as it does not require any damping to be performed on the

stresses themselves, and instead relies on the eddy orientation vectors alone to capture non-local wall effects in the Reynolds stresses.

Rather than directly damping the stresses, the relationship between the eddy orientation vector damping the Reynolds stresses can be exploited to simplify the reorientation procedure. Stress components will respond opposite to eddy orientation vector damping; that is, if the perpendicular components of the orientation vector $q_i^{\perp}$ are damped, the wall-tangent components of the Reynolds stresses will respond by increasing. While a detailed justification of damping $q_i^{\perp}$ based on vorticity arguments was provided in preceding sections, if one were to instead damp the wall-tangent components of the eddy orientation vectors $q_i^{||}$, this would in turn damp the wall normal components of the local Reynolds stresses, which is exactly what non-local pressure effects dictate. This is very appealing, as it simplifies the reorientation and damping algorithm. Near-wall treatments for the Reynolds stresses would be reduced to maintaining orthogonality with the altered eddy orientation vectors. While Equation (5.14) could be employed with $\gamma = \delta = 1$, this equation tends to lose kinetic energy via imperfect reorientation, and therefore could be replaced by a version which exactly conserves the trace of the local Reynolds stresses. A projection method for the stresses can be formulated which does just that:

$$R_{ij}^{(new)} = R_{ij} - \left[\frac{R_{ki}q_j}{q_l q_l} + \frac{R_{kj}q_i}{q_l q_l}\right] q_k + \left[\frac{q_n q_m R_{nm}}{q_l q_l}\right] \left[\frac{q_i q_j}{q_l q_l} + \frac{t_i t_j}{t_l t_l}\right] \tag{5.15}$$

where all eddy orientation vectors q_i and direction of invariance vectors t_i in the equation above are "new", in that they have already been rotated and damped. By properly constructing L for use in the exponential or error function damping E above, reducing the wall-tangent eddy vector components $q_i^{||}$ and allowing the wall-normal eddy vector components $q_i^{\perp}$ to respond accordingly due to preservation of local eddy vector magnitude $|q_i|$ results in properly damped Reynolds stress components which predict wall insertion fairly well.

In a real wall insertion scenario, kinetic energy is not conserved, and the damping of wall-normal and wall-tangent components of the Reynolds stress tensor occur on different lengthscales [60]. In the first exponential damping and reorientation scheme, this was accounted for by essentially prescribing a different damping function for each tangential and normal component of the Reynolds stress tensor and eddy orientation vector. The simplified, single damping function prescribed above is appealing but must accommodate for alterations in kinetic energy. In this case, the damping function E, and its unitless control lengthscale L, are unaltered; the damping coefficient α, however, becomes

$$\alpha = \frac{|q_i|}{\left|q_i^{||}\right|} E^{1/2} \tag{5.16}$$

where the only difference between Equations (5.11) and (5.16) is the power of the damping function E. The test on the wall-tangent components of the eddy orientation vector is slightly altered, and now $q_i^{||} > |q_i|\, E^{1/2}$. While changes to the damping of the eddy orientations improved the damping curvature, the reorientation via projection method from Equation (5.15) must account for changes in kinetic energy due to sudden wall insertion. Equation (5.15) can be modified slightly to achieve this goal:

$$R_{ij}^{(new)} = R_{ij} - \left[\frac{R_{ki}q_j}{q_l q_l} + \frac{R_{kj}q_i}{q_l q_l}\right] q_k + \left[\frac{q_n q_m R_{nm}}{q_l q_l}\right]\left[\delta_{ij} - C_{RP1}\frac{t_i t_j}{t_l t_l} + C_{RP2}\left(\frac{q_i q_j}{q_l q_l} - \delta_{ij}\right)\right] \tag{5.17}$$

where C_{RP1} controls the contributions from the tangential components of q_i and C_{RP2} controls the loss of kinetic energy. Due to the sensitivity of the solution to t_i, $C_{RP1} = 0$. With $C_{RP2} = \frac{1}{2}$, local kinetic energy is conserved. Altering its form slightly

$$C_{RP2} = \tfrac{1}{2} + 2.0\left(\frac{q_i^{||} q_i^{||}}{q_l q_l}\right) \tag{5.18}$$

yields reasonable agreement with existing Reynolds stress data from the wall insertion case considered. Results for this reorientation approach, which interprets q_i as aligned to ω_i, are presented below.

5.5.1 Testing "aligned" reorientation

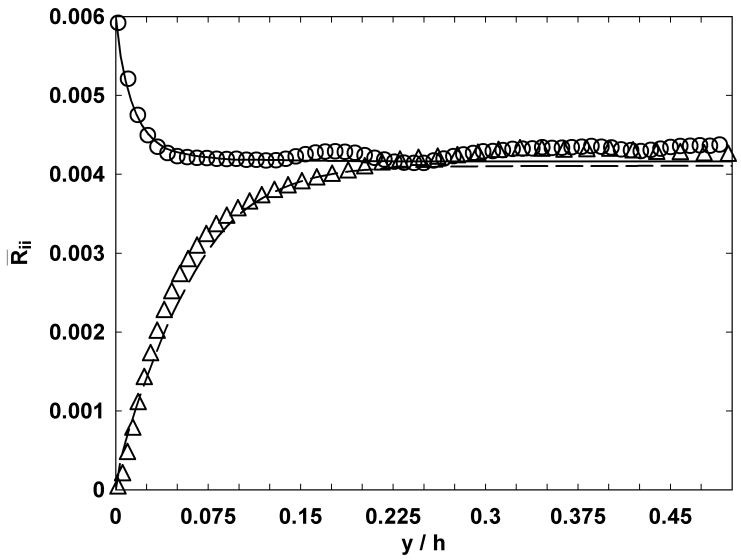

Figure 5.12. Reynolds stress data taken from direct numerical simulations performed by Perot and Moin [60]: $\overline{R}_{11} = \overline{R}_{33}$ (○), $\overline{R}_{22}$(△); compared to the Oriented-Eddy Collision turbulence model $\overline{R}_{11} = \overline{R}_{33}$ (—), $\overline{R}_{22}$ (- - -) employing the simplified damping algorithm. The DNS data is at t = 2.0E-3 seconds, and considered the initial condition.

The previous section proposes an alternative to the reorientation and damping scheme from §5.4.3, one which damps the components of the eddy orientation vector which are tangent to the solid surface $q_i^{||}$, maintains the local eddy orientation vector magnitude by adjusting the wall-normal component $q_i^{\perp}$, and performs no damping operations on the local Reynolds stresses whatsoever; the only alterations made to the local stress tensors would maintain orthogonality via the projection method presented in Equation (5.17).

Figure 5.12 reveals that the damping and reorientation algorithm outlined in §5.5 in a form which does not exactly conserve kinetic energy, predicts the initial pressure

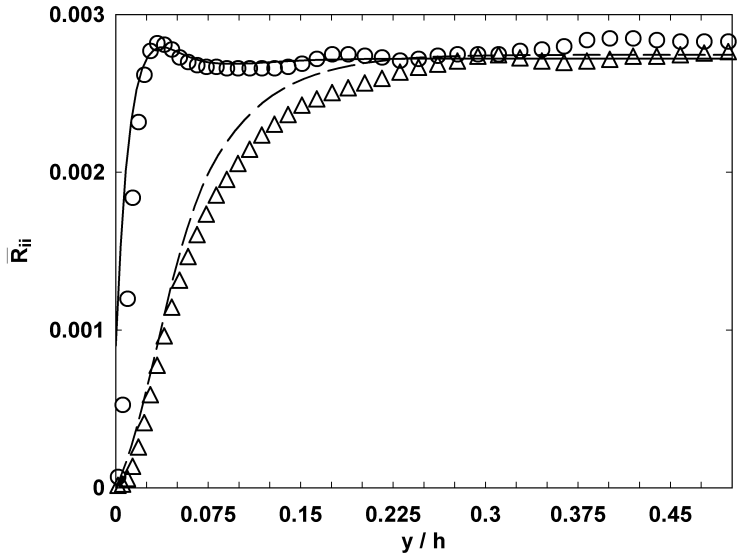

Figure 5.13. Reynolds stress data taken from direct numerical simulations performed by Perot and Moin [60]: $\overline{R}_{11} = \overline{R}_{33}$ (∘), $\overline{R}_{22}$(△); compared to the Oriented-Eddy Collision turbulence model $\overline{R}_{11} = \overline{R}_{33}$ (—), $\overline{R}_{22}$ (- - -) employing the simplified damping algorithm. The DNS data is at t = 1.004560 seconds, while the models data is sampled at t = 1.0 seconds.

echo effects due to wall insertion better than the more complex method initially developed. As was the case previously, the Oriented-Eddy Collision turbulence model's performance over long times was also compared to the DNS data from Perot and Moin [60] at times ranging from one to four seconds. Agreement at one second is quite good compared to the previous method, especially for the tangential components of the stress tensor, $\overline{R}_{11}$ and $\overline{R}_{33}$, indicating the modified projection method was an improvement.

Unfortunately, the stresses in the direct numerical simulation data decay too quickly, causing increasing disagreement between predictions from the Oriented-Eddy Collision turbulence model and the wall insertion data. Nevertheless, the ability to capture the slight increase in $\overline{R}_{11}$ and $\overline{R}_{33}$ near the wall, as well as reasonable agreement when predicting $\overline{R}_{22}$, demonstrates the simplified reorientation's feasibility.

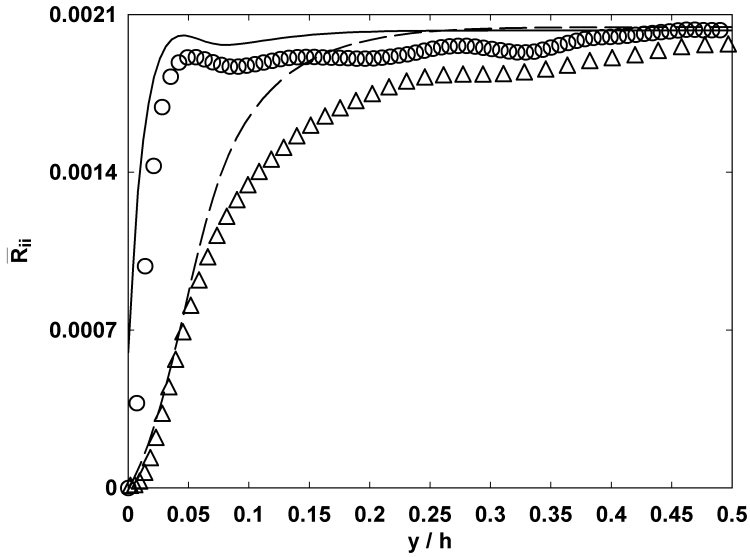

Figure 5.14. Reynolds stress data taken from direct numerical simulation performed by Perot and Moin [60]: $\overline{R}_{11} = \overline{R}_{33}$ ($\circ$), $\overline{R}_{22}$($\triangle$); compared to the Oriented-Eddy Collision turbulence model $\overline{R}_{11} = \overline{R}_{33}$ (—), $\overline{R}_{22}$ (- - -) employing the simplified damping algorithm. The DNS data is at t = 2.012613 seconds, while the models data is sampled at t = 2.0 seconds.

Two proposals for the relationship between the eddy orientation vector q_i and vorticity vector ω_i have been presented along with the physical interpretation of these ideas. Appropriate boundary conditions for the eddy orientation vectors and Stress tensors were reported, and methods to capture pressure echo proposed and tested. The next step involves testing these schemes under more complex flow conditions, and turbulent channel flow is considered in the following chapter.

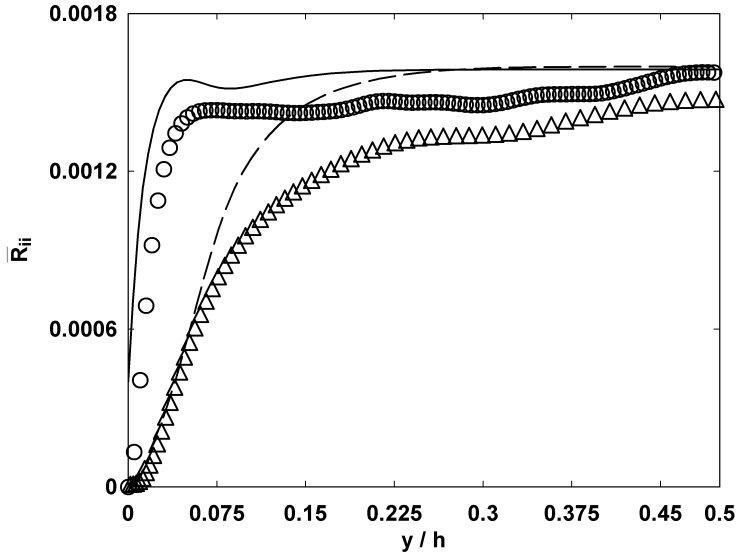

Figure 5.15. Reynolds stress data taken from direct numerical simulation performed by Perot and Moin [60]: $\overline{R}_{11} = \overline{R}_{33}$ ($\circ$), $\overline{R}_{22}$($\triangle$); compared to the Oriented-Eddy Collision turbulence model $\overline{R}_{11} = \overline{R}_{33}$ (—), $\overline{R}_{22}$ (- - -) employing the simplified damping algorithm. The DNS data is at t = 3.013826 seconds, while the models data is sampled at t = 3.0 seconds.

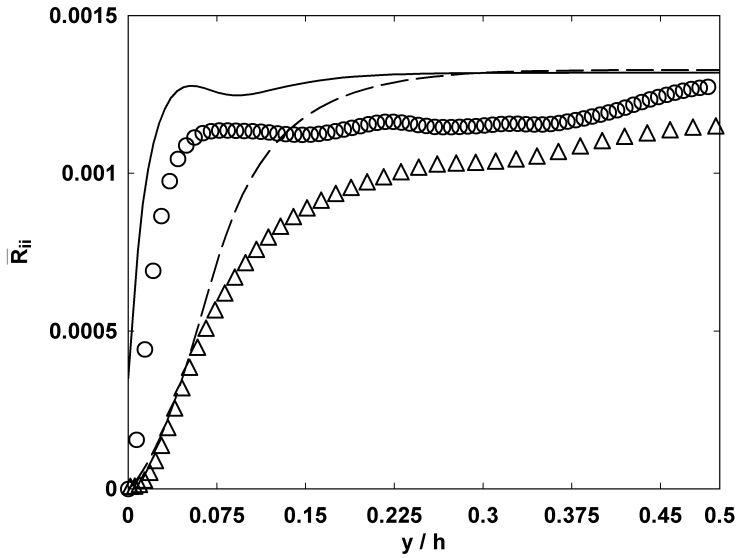

Figure 5.16. Reynolds stress data taken from direct numerical simulation performed by Perot and Moin [60]: $\overline{R}_{11} = \overline{R}_{33}$ ($\circ$), $\overline{R}_{22}$($\triangle$); compared to the Oriented-Eddy Collision turbulence model $\overline{R}_{11} = \overline{R}_{33}$ (—), $\overline{R}_{22}$ (- - -) employing the simplified damping algorithm. The DNS data is at t = 4.014137 seconds, while the models data is sampled at t = 4.0 seconds.

CHAPTER 6

CHANNEL FLOW

With the theory developed in Chapter 5, the Oriented-Eddy Collision turbulence model must now be tested using turbulent channel flow. Assessing the performance of the model is less straightforward than it might appear. While ample data exists to scrutinize a model's performance in predicting velocity fields, dissipation, kinetic energy, and Reynolds stresses, the task of evaluating (and inevitably troubleshooting) the Oriented-Eddy Collision turbulence model's ability to evolve the eddy orientation vectors is difficult. Validation data only exists in the form of two-point correlations, which do not aid in evaluating a specific decomposition of those correlations. While other structure-based turbulence models do exist, few (if any) have ever been subjected to wall-bounded flows. Furthermore, data about turbulent structure is rarely considered - only basic statistics are typically reported. The same is true here - the nature of the eddy orientation vectors is not reported in the wall-bounded validation cases, despite the fact that it was subject to intense scrutiny. This is related to the difficulties encountered in Chapter 5 - a combination of intuition and analysis of dependent statistics must be employed. While corollaries exist between, say, the eddy orientation vectors q_i and dissipation $\bar{\epsilon}$, the overbar betrays an even larger issue. Transport equations for *individual* eddy orientation vectors and Reynolds stress tensors are prescribed. These values are "local", and are not reported. Only their "global" counterparts, those which are averaged over all eddies at a given location in physical space, are reported.

Intuition breaks down below the "global" level. Even if the behavior of $\overline{q_i}$ can be divined from dissipation or two-point correlation data, what are the local q_i or two-dimensional R_{ij} supposed to look like as they are subjected to turbulent channel flow? The local q_i is a statistical quantity, representing one portion of a two-point correlation, which in turn represents the structure of turbulence. Examining the behavior of all local eddies *en masse* (whether 22 or 1,257) can be helpful. For example, in turbulent channel flow, individual eddies near a wall tend to align themselves in the streamwise direction, which can be thought of as long, streamwise structures (streaks) establishing themselves. Nevertheless, testing and development of near-wall treatments must be done with care. It should be noted that shear-free surfaces are not considered in this validation. Despite the development of boundary conditions and reorientation prescriptions for slip surfaces in Chapter 5, the simple and ubiquitous nature of no-slip boundaries, coupled with the difficulty in implementing mixed Neumann / Dirichlet boundary conditions for tensors in OpenFOAM, led to shear-free surfaces being avoided.

6.1 Turbulent Channel Flow at $Re_\tau = 395$

Simulating basic, canonical flows such as those in Chapter 4, and wall-insertion with near-wall turbulent decay, fails to test many of the assumptions underlying the Oriented-Eddy Collision turbulence model, or any structure-based model. Many of the models employed for return-to-isotropy, the turbulent time scale, the eddy viscosity, and so on behave contrary to intuition in the presence of shear and a solid wall. Shear alone is not the culprit, nor are anisotropy and inhomogeneity; instead, it is the combination of these. Furthermore, unlike in a backwards-facing-step flow, many definite, measurable benchmarks exist for turbulent channel flow with high order statistics available. This makes such a flow both appealing and difficult.

Direct numerical simulation data from Moser, Kim, and Mansour [49] of turbulent channel flow at a friction Reynolds number $Re_\tau = 395$ is employed to benchmark the Oriented-Eddy Collision turbulence model's ability to handle a non-decaying wall bounded flow and predict the Reynolds stresses. Results are shown in Figure 6.1.

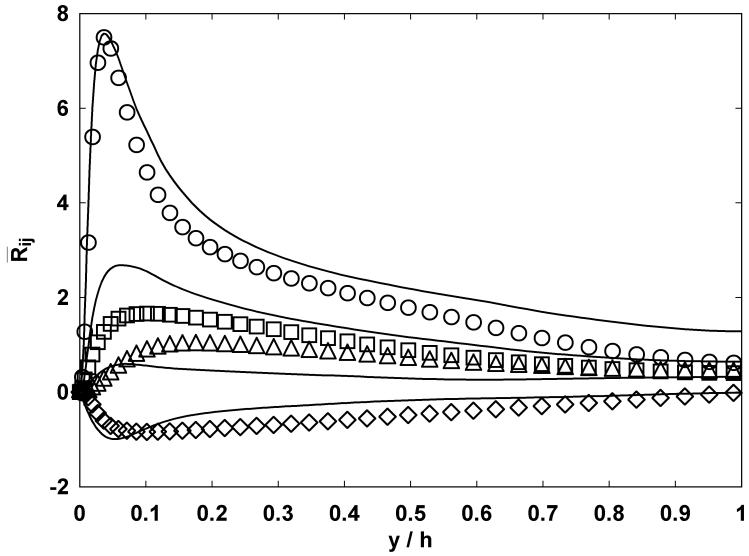

Figure 6.1. Reynolds stress data taken from direct numerical simulations of Moser, Kim, and Mansour [49] of turbulent channel flow at a friction Reynolds number $Re_\tau = 395$: $\overline{R}_{11}$ ($\circ$), $\overline{R}_{22}$($\triangle$), $\overline{R}_{33}$($\square$), $\overline{R}_{12}$($\diamond$); compared to results from the Oriented-Eddy Collision turbulence model (—). The data is symmetric across the channel, and $\overline{R}_{13} = \overline{R}_{23} \approx 0$.

While agreement between the model and available channel flow data is not excellent, the model is capable of returning *an* answer for the flow which is stable and of the correct order of magnitude. Agreement between the Oriented-Eddy Collision turbulence model's prediction of $\overline{R}_{11}$ and DNS data is quite good near the peak, but poor very close to the wall (see Figure 6.2) and further into the channel. The over-prediction of $\overline{R}_{11}$ in the center channel region indicates average eddy vector magnitudes $|\overline{q}_i|$ which are too small. $\overline{R}_{22}$ is too damped, while $\overline{R}_{33}$ not damped enough. The general shape of $\overline{R}_{12}$ is reasonable, but the peak is too close to the wall and too large. Looking closely at the region near to the solid boundary, it is clear that

the model captures the asymptotic approach of the Reynolds stress tensor components reasonably well, as is demonstrated in Figure 6.2. The slope of the relevant Reynolds

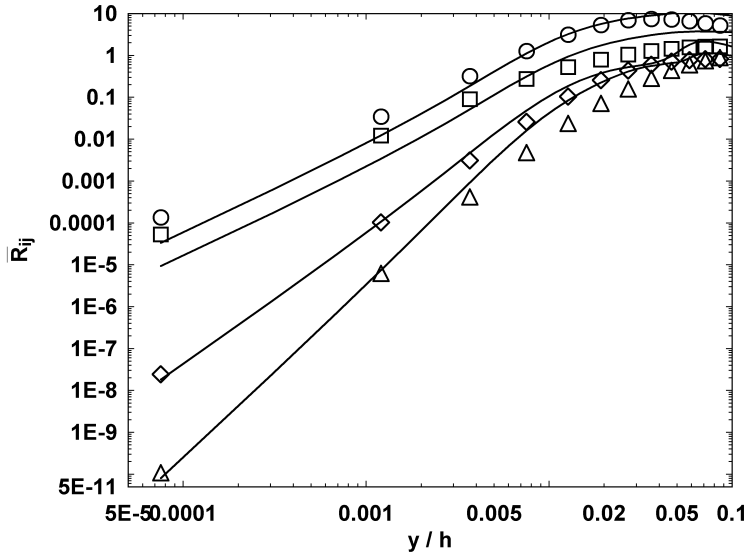

Figure 6.2. A closer look at the near-wall asymptotic predictions of Reynolds stresses in a turbulent channel flow. Data from Moser, Kim, and Mansour [49]: $\overline{R}_{11}$ (○), $\overline{R}_{22}$(△), $\overline{R}_{33}$(□), $\overline{R}_{12}$(◇); compared to results from the model (—). Note that the sign of $\overline{R}_{12}$ has been reversed to enable the use of a log plot.

stress tensor components matches data from Moser, Kim, and Mansour [49] quite well. Furthermore, very close to the wall the magnitudes of $\overline{R}_{22}$ and $\overline{R}_{12}$ (noting its sign has been reversed) agree reasonably well with DNS data. The magnitudes of $\overline{R}_{11}$ and $\overline{R}_{33}$, however, are clearly under-predicted. Achieving the proper separation of scales between $\overline{R}_{11}$, $\overline{R}_{22}$, $\overline{R}_{33}$, and $\overline{R}_{12}$ is difficult.

6.2 Discussion

The results presented above show that the Oriented-Eddy Collision turbulence model is capable of returning a stable, reasonable prediction for the Reynolds stresses which are the correct order of magnitude and exhibit the proper asymptotic approach to the channel wall. Attempts to improve the accuracy of the model once the near-wall reorientation schemes were developed and tested revealed many complications, some

of which are discussed at the end of Chapter 3. To begin with, while the standard diffusion model is employed, the performance of the model is very sensitive to the form of the turbulent viscosity and time scale. One or more additional production terms for the eddy orientation vectors are required, the form of which is not entirely known. The return-to-isotropy model for the eddy orientation vectors was also abandoned for a novel, albeit expensive approach which was not affected by the coupling between wall-normal eddy orientation vector production and wall-tangent eddy orientation dissipation.

These numerous and occasionally major changes to the basic Oriented-Eddy Collision turbulence model indicate that the original two-point correlation decomposition presented in Chapter 2 may require alteration, or an entirely new decomposition may be necessary. The crux of the issue lies in taking existing two-point correlation data for a channel flow from Moser, Kim, and Mansour [49] and translating it in to the decomposition employed for the Oriented-Eddy Collision turbulence model. This is an inverse operation which is difficult and may yield many possible solutions. It is no small undertaking, and is akin to the development of an entirely new turbulence model, which would require tuning and testing with the benchmarks outlined in Chapter 4.

CHAPTER 7

IMPLEMENTATION

7.1 Overview

The majority of the initial effort in this project focused on implementing the Oriented-Eddy Collision turbulence model in an open source collection of computational fluid dynamics libraries written in C++ called OpenFOAM. Rather than employing an in-house code, OpenFOAM was chosen to demonstrate that the Oriented-Eddy Collision turbulence model - a complex, structure-based model - can be implemented in a generic CFD framework with moderate effort. This stands in contrast to other structure-based turbulence models which often require complex, highly customized software operate. Not only does OpenFOAM allow the model to be distributed widely, but also simplifies validation and benchmarking.

FOAM is unique in that much of the mathematical and numerical framework required to perform advanced CFD is already in place, available for any user to copy and modify for their own needs. Despite having a vast assortment of CFD-related tools, solvers, and utilities, the latest versions of OpenFOAM have few Reynolds stress transport model implemented. In fact, they often only contain two: The Launder, Reece, and Rodi (1974) model and a variant, the Launder Gibson RSTM. Adding the Oriented-Eddy Collision turbulence model to FOAM was not trivial. An entire collection of transport equations must be carefully handled within FOAM, and the Oriented-Eddy Collision turbulence model is the first of its type to be implemented in any FOAM release. In its current form, the Oriented-Eddy Collision turbulence model employs anywhere from 22 to over 1,200 eddies for simulations. The number of

eddies available to the code is controlled by how the eddies may be arranged uniformly on a unit sphere. See Chartrand [10] for more details. Figure 7.1 illustrates the

```
fvm::ddt(qiINT)
- (1.0/3.0)*fvm::laplacian(dEff(), qiINT)
+ (1.0/3.0)*fvm::SuSp(((alpha*nu()*qsq + tauR)), qiINT)
==
- fvc::div(phi_, qiINT)
- ( qiINT & fvc::grad(U) )
- ( Ai + Bi )
```

Figure 7.1. FOAM provides a vast collection of operators.

power of OpenFOAM in that the software provides a wide variety of useful operators which eases the task of implementing a complex model such as the Oriented-Eddy Collision turbulence model. The entry in Figure 7.1 constructs the original evolution equation for q_i, and is contained within FOAM's "fvVectorMatrix" entity, the "fv" indicating "finite volume". Similar entities for tensors, "fvTensorMatrix" and scalars, "fvScalarMatrix" exist. All terms on the left hand side of the equation are cast implicitly, and as such are part of the matrix on the left hand side of the system to be solved. This can be thought of as $\underline{\underline{A}}\underline{x} = \underline{b}$ with $\underline{\underline{A}}$ a rank two tensor (matrix) which must be inverted, $\underline{x}$ the vector of unknowns, and $\underline{b}$ the vector of knowns on the right hand side. Operators such as"fvm::ddt" are easy to identify: "ddt" takes the time derivative of its argument, in this "qiINT" which is the current eddy vector. Note that transport equations such as this are constructed for eddy vectors, Reynolds stress tensors, and in some cases the scalar kinetic energy for every eddy at every cell location in the computational mesh. In FOAM, "fvm::" casts the operator in the "finite volume method", which essentially places the operator (and resulting term) on the left hand (implicit) side of the equation, in $\underline{\underline{A}}$. For example, the Laplacian operator (used for the viscous diffusion term) is cast implicitly for stability purposes. The "SuSp" operator makes a decision about the location of the source term (and thus whether it is cast explicitly or implicitly, placed in $\underline{b}$ or $\underline{\underline{A}}$) based on its sign. Alternatively,

operators may be cast using "fvc::", standing for "finite volume calculus", which is an explicit casting. This can be thought of as placing the resulting term in $\underline{b}$. For example, the convection term is handled with a call to "fvc::div", which performs an explicit divergence operation on the flux ϕ and the eddy vector. The eddy vector production term $-q_k \overline{u}_{k,i}$ employs an explicit gradient operator (there is no such thing as an implicit gradient operator) along with FOAM's inner product, "&". Finally, explicit source terms such as the return-to-isotropy A_i and rotation term B_i, which are constructed beforehand, can simply be added directly to the equation.

7.2 Storing eddy information

For every cell in a computational domain, there exists a collection of eddies in that cell. For every eddy, there is an associated eddy vector which has an evolution equation, an associated Reynolds stress tensor with an evolution equation, and a scalar kinetic energy which has an evolution equation if the "qkR*" or "LkR*" model variants are employed (see Appendix A). This concept is illustrated in Figure 7.2. Three pointer lists, of length N (where N is the number of eddies originally seeded

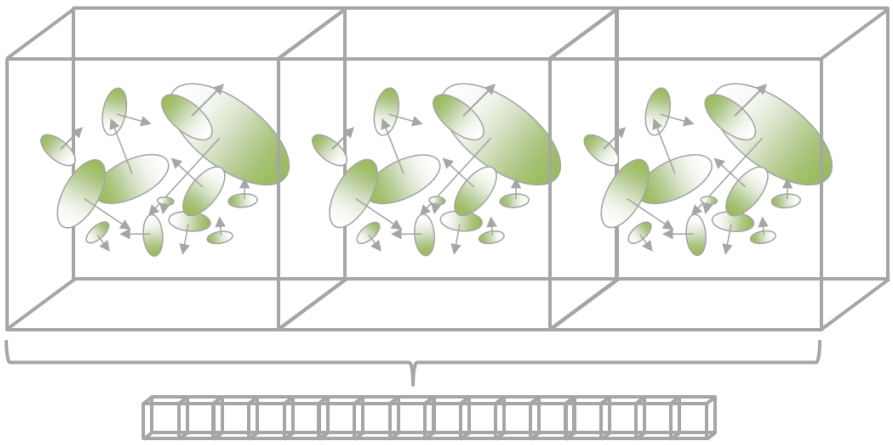

Figure 7.2. Schematic diagram of a collection of eddies that may exist in some turbulent flow. Note that each set of eddies exists at every cell in the computational mesh.

in the flow) are constructed. One is populated with FOAM's "volVectorField" entity, which stores a single vector at every cell location, responsible for handling the eddy orientation vectors. A second contains a "volSymmTensorField" array, which stores a six component symmetric tensor at every cell, handling the Reynolds stress tensor. The third (when needed) is a FOAM "volScalarField" which, not surprisingly, stores a scalar at every cell location, in this case containing the kinetic energy. A subtlety arises when considering the way in which this information is accessed. If each pointer list entry is assigned to a specific eddy, operations that span the entire computational domain are performed one eddy at a time because the pointer lists are iterated through on a per-eddy basis. To understand this, imagine selecting only the large, downward-pointing eddy in Figure 7.2 at every cell location and then manipulating one of this eddy's associated quantities. The alternative of course it to pick one cell (perhaps the center cell in Figure 7.2) and select every eddy at that cell, manipulating some eddy's associated value at that cell alone. This has advantages and disadvantages. Accounting for the many, many tensors, vectors, and scalars in any given flow is trivial, as each pointer list is of size N, each entry corresponding to the kinetic energy for one eddy at each cell, one eddy orientation vector at each cell, or one eddy's Reynolds stress tensor at each cell. This makes performing averages over all eddies as simple as a summation over all pointer list entries and a division by N. This choice makes operations that must be performed on every eddy at a given cell much more difficult, however. Such operations are rare but require extensive looping over each pointer list at each cell location which is an expensive operation. One of

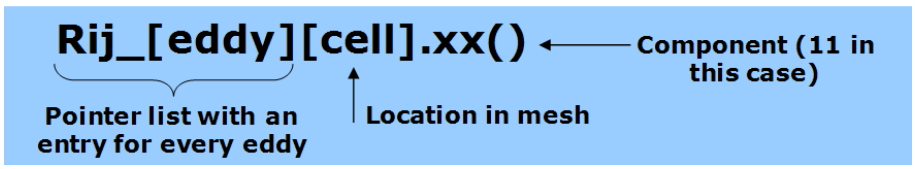

Figure 7.3. Using variable-sized pointer lists for per-eddy quantities in FOAM.

the most powerful and useful features of OpenFOAM is the ability to access and manipulate the components of a vector or tensor field across an entire mesh (*i.e.* across all cells and boundary patches) without the need to explicitly access each cell location. In fact, FOAM's namesake, "field operation and manipulation", betrays the power of this ability and makes the implementation of such a complex model much simpler in C++. Unfortunately, this feature may only be used if access to one eddy's components across the entire computational domain is required, and not the opposite, where the component of all eddies at a single cell is required. In Figure 7.3, the pointer list addressing is illustrated. If it is sufficient to access a given eddy's components (or other associated entities, such as "correctBoundaryConditions", a function that updates or recalculates a field's boundary values) the cell addressing may be omitted altogether, greatly increasing the efficiency of all such operations.

7.3 Going beyond rank two tensors

The evolution equation the Reynolds stress tensor may includes a term that involves the gradient of the Reynolds stress tensor, as shown in Equation (7.1). This is a rank two tensor, and its gradient produces a rank three tensor. Unfortunately rank three tensors are accommodated for in OpenFOAM. The templating is in place, but no operators can handle such an entity, including the gradient operator. As such, either the existing operator must be expanded to handle objects of the rank three tensor type, or a custom function written that could perform the calculation required in the model.

$$-D\left(\nu+\hat{\nu}_t\right)\left[\frac{R_{ij}}{K}\right]_{,k}(K)_{,k} \tag{7.1}$$

The first choice, extending the existing gradient operator to handle any rank two tensor would require immense effort (to make this operator sufficiently general and interface with the existing operator templates in OpenFOAM) and thus was deemed more effort than it was worth. The second option, writing a custom function to

perform the desired gradient in this model was instead completed. Specifically, the function was created to calculate the inner product of the stress tensor gradient (a rank three tensor) and the gradient of the kinetic energy (a rank one tensor) which results in a rank two tensor. A code snippet from the function is provided in Figure 7.4. Future work on the Oriented-Eddy Collision turbulence model in OpenFOAM may include the creation of a templated, generic gradient operator that can take a rank two tensor as an input and return a rank three tensor.

```
forAll (mesh_.C(), cell)       // internal cells
 {
      Rx[cell].x() = Rtmp[cell].xx();
      Rx[cell].y() = Rtmp[cell].xy();
      Rx[cell].z() = Rtmp[cell].xz();
      ...
      gradKgradR[cell].xx() = ( gradK[cell].x()*gradRx[cell].xx()
                              + gradK[cell].y()*gradRx[cell].xy()
                              + gradK[cell].z()*gradRx[cell].xz() );
      gradKgradR[cell].yy() = ( gradK[cell].x()*gradRy[cell].yx()
                              + gradK[cell].y()*gradRy[cell].yy()
                              + gradK[cell].z()*gradRy[cell].yz() );
      gradKgradR[cell].zz() = ( gradK[cell].x()*gradRz[cell].zx()
                              + gradK[cell].y()*gradRz[cell].zy()
                              + gradK[cell].z()*gradRz[cell].zz() );
```

Figure 7.4. An example of the custom function written for calculating the gradient term from Equation (7.1). Note that looping over all cell locations may be avoided in circumstances when access to one eddy at every cell is permissible.

7.4 Temporal stability

OpenFOAM has available a variety of time stepping schemes which are tied to the way in which the transport equations are posed within the code. Such schemes include simple Euler time stepping (which is by far the most commonly used option), Courant number limited Euler ("CoEuler"), Crank-Nicholson, stabilized local time-step ("SLTS"), the so-called "backward" scheme, and "local" Euler. Each will be described briefly below:

- "Euler" - The basic Euler scheme is a first-order Euler implicit/explicit time derivative using only the current and previous time-step values.

- “CoEuler” - This is the Courant number limited first-order Euler implicit/explicit time derivative. The time-step is adjusted locally so that the local Courant number does not exceed some specified value. This scheme is meant to be used for steady-state computations with transient codes where local time-stepping is preferable to under-relaxation.

- “Crank-Nicholson” - This is the classic second-order Crank Nicholson implicit scheme. It employs the current and previous time-step fields as well as the previous time-derivatives.

- “SLTS” - This is the stabilized local time-step first-order Euler implicit/explicit time scheme. In this case, the time-step is adjusted locally so that an advective equations remains diagonally dominant. Again, this scheme is meant to be used for steady-state computations which use transient codes. It is most appropriate for cases in which local time-stepping is preferable to under-relaxation.

- “Backward” - This is the second-order backward-differencing time derivative. The scheme uses the current and two previous time-step values.

- “Local Euler” - This is a local time-step first-order Euler implicit/explicit temporal derivative scheme. Once again this scheme is meant to be used for steady-state computations using transient codes.

The ”implicit/explicit” terminology can be somewhat obscure. How does a user dictate the whether, say, their Euler scheme is implicit or explicit? The key lies in the way in which the transport equation is cast inside FOAM, namely in the “fvScalarMatrix”, “fvVectorMatrix”, or “fvTensorMatrix” objects. These entities contain transport equations (for a scalar, vector, and tensor, respectively) in matrix form. These are the objects which are discretized spatially and temporally according to rules established by the user. Terms cast in “fvm::” (finite volume method), like

"fvm::ddt" or "fvm::Laplacian (the transient term and Laplacian operator, respectively) are on the left hand side of the "fv*Matrix" entity and are time-stepped using implicit Euler. The rest of the terms are either written directly or cast as explicit operators using "fvc::" (finite volume calculus) such as "fvc::grad", used to calculate gradients. These are time-stepped using explicit Euler. Most terms written directly can be made implicit source terms using "fvm::SuSp(α)" or "fvm::Sp(α)". The first makes a decision about implicit/explicit treatment based on the sign of its argument α; the second *always* casts its argument implicitly. Some operators, like the gradient, do not exist in an implicit form in FOAM, thus programmers are limited as to which terms in their transport equation can be cast implicitly.

At this point it may be appropriate to ask why OpenFOAM's time derivative schemes have been summarized, or at least why such a summary wasn't placed in an appendix. FOAM's built-in time schemes are suitable for many applications, but the Oriented-Eddy Collision turbulence model contains many numerically sensitive terms in its myriad transport equations that cannot be cast implicitly. As such, one seeks to increasing the stability of the *explicit* terms without resorting to a prohibitively small time step is desirable. Schemes such as Runge-Kutta time advancement [80, 34] are appealing as they are widely employed and provide enhanced accuracy and stability (depending on the order of the method). A low-storage, three step, second-order accurate, *mixed* implicit/explicit Runge-Kutta scheme, similar to the method employed by Martell [44] has been investigated as an alternative to schemes present in OpenFOAM. The goal is to both develop and implement such a scheme which can be folded into the existing FOAM time derivative schemes. Construction and implementation of such a scheme is not trivial in OpenFOAM.

A method identical to that outlined by Martell [44] was first implemented into OpenFOAM for use with the Oriented-Eddy Collision turbulence model. This method was soon abandoned, however, as it was revealed that the method was in fact only

first order accurate and may have handled implicitly cast terms incorrectly. A new three-step, second-order accurate method was sought that could handle both implicit and explicit terms properly. One possible solution is shown below:

- Step 1

$$\hat{u}^{n+1/2} = u^n$$

$$\left(I - \alpha_1 \tfrac{\Delta t}{2} L\right)\left(\tfrac{\tilde{u}^{n+1/2} - \hat{u}^{n+1/2}}{\Delta t/2}\right) = S + C\left(u^n\right) + L\left(u^n\right) - G\left(\tilde{p}^{n+1/2}\right) - \left(I - \alpha_1 \tfrac{\Delta t}{2} L\right)\left(\tfrac{\hat{u}^{n+1/2} - u^n}{\Delta t/2}\right)$$

- Step 2

$$\hat{\hat{u}}^{n+1} = 2\tilde{u}^{n+1/2} - u^n$$

$$\left(I - \alpha_2 \Delta t L\right)\left(\tfrac{\tilde{\hat{u}}^{n+1} - \hat{\hat{u}}^{n+1}}{\Delta t}\right) = S + C\left(\tilde{u}^{n+1/2}\right) + L\left(u^n\right) - G\left(\tilde{\hat{p}}^{n+1}\right) - \left(I - \alpha_2 \Delta t L\right)\left(\tfrac{\hat{\hat{u}}^{n+1} - u^n}{\Delta t}\right)$$

- Step 3

$$u^{*n+1} = \tilde{\tilde{u}}^{n+1}$$

$$\left(I - \alpha_3 \tfrac{\Delta t}{2} L\right)\left(\tfrac{u^{n+1} - u^{*n+1}}{\Delta t/2}\right) = S + C\left(\tilde{\tilde{u}}^{n+1}\right) + L\left(\tilde{u}^{n+1/2}\right) - G\left(p^{n+1}\right) - \left(I - \alpha_3 \tfrac{\Delta t}{2} L\right)\left(\tfrac{u^{*n+1} - \tilde{u}^{n+1/2}}{\Delta t/2}\right)$$

Note that u is the velocity (or other quantity being advanced in time). The superscript denotes the location of u in time: u^n is the known value at the previous time step, $\hat{u}^{n+1/2}, \tilde{u}^{n+1/2}, \hat{\hat{u}}^{n+1}$, and $\tilde{\tilde{u}}^{n+1}$ are intermediate quantities used by the RK3 scheme. The same nomenclature is employed for the pressure p. C can be considered any explicit term (in this case convection) with L any implicit term (in this case the Laplacian operator). G is the gradient operator (which is explicit) and S is some other source term. Δt is of course the time step, I the identity tensor, and α_{1-3} numerical constants. The complication arises from the fact that, for a given sub-step, C and L require *different arguments*. The method shown above should handle both

implicit and explicit terms properly, provide second-order accuracy, and continue to have a low storage profile.

There are generally two approaches to implementing a new feature in FOAM. The first is to spend the effort of creating a generic, templated entity (in this case a time derivative scheme), fold this code into the existing framework, and then call the method. While more attractive to the general user, the time required to do this is often not worth the reward. The initial RK3 scheme was directly coded in to the Oriented-Eddy Collision turbulence model and employs FOAM's Euler time derivative scheme for temporal sub-stepping. FOAM stores the previous values for a given entity (such as an eddy vector) making implementation easier. Old values can be easily recalled, and in certain circumstances FOAM's default behavior can be overridden using the ".storeOldTime()" function. This was especially useful when constructing the first RK3 schemes in OpenFOAM as there are a good number of intermediate arrays to be stored for the Reynolds stress tensor, eddy vector, kinetic energy, and velocity at each cell for every eddy. The close examination of near-wall damping and reorientation, boundary conditions, and diffusion in Chapter 5, and the subsequent changes made to the model and its implementation, halted development of the new three-step Runge-Kutta time marching method. Temporal stability of the model was greatly improved, allowing the basic Euler time marching scheme to be employed for all benchmark cases.

The Oriented-Eddy Collision turbulence model was also implemented into an in-house C++ code, "OEC++", as a means of increasing performance for wall-bounded flows and as an independent verification of the model outside of the OpenFOAM framework. A portion of the channel flow effort was done using OEC++. This work revealed that the difficulties experienced in capturing wall-bounded turbulent flows were independent of implementation, and therefore a result of the model itself.

CHAPTER 8

DISCUSSION & CONCLUSIONS

This work demonstrates the Oriented-Eddy collision turbulence model's ability to capture both equilibrium and non-equilibrium turbulent flows. In addition, the model remains stable at long times and when subjected to highly anisotropic flow conditions. The Oriented-Eddy Collision turbulence model precisely captures isotropic, homogeneous decaying turbulence as well as the rotating decay cases. Further refinement of the dissipation-like term which handles frame rotation may result in predictions even closer to experimental / direct numerical simulation data. The model is capable of returning the theoretical solution to turbulent flows in the rapid distortion theory limit, setting it apart from most other turbulence models. The inclusion of turbulent structure information is imperative to capturing linear turbulence, and this physical information is captured in the Oriented-Eddy Collision turbulence model by using turbulent eddy orientation information. While adding to the overall cost and complexity of the method, the benefits are obvious. Casting the Oriented-Eddy Collision turbulence model in a form similar to familiar Reynolds stress transport models aids comprehension and enables the user to employ traditional solution methods.

Basic turbulent flows over solid boundaries, including decaying turbulence near a wall and turbulent channel flow, have been investigated as a means of validating the theory developed in Chapter 5. Agreement was good for near-wall decay when compared to direct numerical simulation data from Perot and Moin [60] at short times, but limitations in the DNS domain size make long-time data difficult to assess. Larger-domain DNS is required to complete this validation. Simulations of turbulent channel

flow revealed weaknesses in the model which were not trivial nor related to tuning alone. Efforts to accurately predict channel flow discovered and addressed many issues with the Oriented-Eddy Collision turbulence model, but called into question the two-point correlation decomposition which constitutes the basis of the model.

It should be noted that the Oriented-Eddy Collision turbulence model is an order of magnitude more computationally demanding than existing Reynolds averaged Navier-Stokes models. This implies that in a turbulent Navier-Stokes calculation, the computational effort required to calculate the turbulence with the Oriented-Eddy Collision turbulence model is now roughly equal to the computational effort required to calculate the mean flow. This is not particularly expensive, and corresponds to the appropriate level of effort considering the turbulence physics represents roughly half of the total physics of most turbulent flow problems. The Oriented-Eddy collision modeling approach remains orders of magnitude less computationally demanding than large eddy simulation (LES). The Oriented-Eddy collision modeling approach therefore occupies a useful niche in the cost versus accuracy trade off, allowing much higher levels of predictive accuracy than traditional Reynolds averaged Navier-Stokes models at a cost significantly less than large eddy simulation.

Several modeling and development goals have been met, and are summarized here:

- The original Oriented-Eddy Collision turbulence model was evaluated for stability both far from and close to solid boundaries. Five different variants of the model were developed with varying success. Eventually, the more complex alternatives were abandoned for a simpler model which accounted for inhomogeneity. The final version is capable of performing well when subject to a battery of canonical turbulent flows as well as several simple wall-bounded flows.

- New theory as to the the behavior of the Oriented-Eddy Collision turbulence model near solid boundaries has been developed and tested. The model is capable of predicting various turbulent quantities such as Reynolds stresses,

kinetic energy, and dissipation with reasonable accuracy. It was discovered that near-wall damping and reorientation plays a vital role in energy redistribution amongst eddy orientation vectors and Reynolds stress tensors.

- Alternatives to the standard diffusion model, including statistical diffusion and "average eddy" diffusion were developed and tested, with varying success. Eventually, the standard model was employed, with lessons learned about the behavior of turbulent viscosity in the model.

- The turbulent viscosity was scrutinized and completely reformulated to more accurately capture near-wall physics.

- Boundary conditions for shear-free and no-slip surfaces were developed for the eddy orientation vectors and Reynolds stress tensors. Solid boundary treatments were tested using basic wall-bounded turbulent flows.

- Implementation of the Oriented-Eddy Collision turbulence model was refactored, increasing the code's efficiency and decreasing its length and code complexity.

- The basis for the homogeneous version of the model has been explicated, and the mathematical foundations of the new near-wall theory documented.

Several publications have directly resulted from this research, including *The Oriented-Eddy Collision Turbulence Model* by Michael B Martell Jr and J Blair Perot, which has been accepted for publication in the journal *Flow, Turbulence, and Combustion.* This paper is the first to introduce the Oriented-Eddy Collision turbulence model to the turbulence modeling community, and covers the basic formulation of the model as well as canonical benchmarks. A second paper, *The Oriented-Eddy Collision Turbulence Model in Wall-Bounded Flows*, is in progress for submission to the same journal.

This second paper aims to summarize the progress made toward creating a structure-based turbulence model which works in simple, wall-bounded flows. In addition, a talk, "The Oriented-Eddy Collision Model" was presented at American Physical Society's annual Division of Fluid Dynamics Meeting, in Baltimore, MD, in November of 2011.

Finally, several lessons have been learned throughout the course of this research:

- Turbulence modeling is difficult, and no model is ever perfect or complete. The Oriented-Eddy Collision turbulence model is no exception.

- Structure-based models, while more computationally expensive than classic Reynolds averaged Navier-Stokes models, offer new hope in an old and tired field of research. Although they fell out of fashion in the mid- to late 1990s, they are returning, with new publications from E. Akylas, S.C. Kassinos, and others. The ability to capture rapid pressure strain and non-local effects in wall-bounded flows goes a long way toward a truly generic model.

- While the OpenFOAM framework is an excellent tool for computational fluid dynamics, much effort was wasted in this project on implementation difficulties. When developing and testing a new turbulence model - especially one as complex as the Oriented-Eddy Collision turbulence model - it is best to use an in-house code. Efficiency, parallelism, and other "high-level" concerns should be addressed *after* the basic model is complete.

- If OpenFOAM is to become the *de facto* standard for research-level computational fluid dynamics, more effort must be placed on including higher-level time marching schemes as well as the ability to handle and operate on tensors above rank two.

- The quality and availability of either direct numerical simulation or experimental data for basic, canonical turbulent flows is severely lacking. Without

modern, well-documented, accurate benchmarks, turbulence modeling is greatly impeded.

- A negative result is often more useful than a positive result.

APPENDIX A

MODEL VARIANTS

A.1 The "qR" model

The original Oriented-Eddy Collision turbulence model is presented here, beginning with the transport equation for the eddy orientation vector q_i, as a means of comparison for variants considered later in this section:

$$q_{i,t} + \nabla \cdot (\overline{u}_j q_i) = \tag{A.1a}$$

$$- q_k \overline{u}_{k,i} \tag{A.1b}$$

$$- \frac{1}{3}\left(\alpha\nu\overline{q^2} + \frac{1}{\tau_R}\right) q_i \tag{A.1c}$$

$$- (A_i + C_\Omega q_i) \tag{A.1d}$$

$$+ \frac{1}{3}\left[(\nu + \nu_T)\, q_{i,k}\right]_{,k} \tag{A.1e}$$

$$+ W_i \tag{A.1f}$$

with Expression (A.1a) the material derivative of the eddy vector q_i, Expression (A.1b) the production term, Expression (A.1c) the dissipation with eddy turnover time,

$$\frac{1}{\tau_R} = \left(\overline{K}\overline{q^2}\right)^{1/2} \tag{A.2}$$

Expression (A.1d) is the return-to-isotropy model,

$$A_i = -\frac{1}{\tau_R}\left(\frac{C_Q}{1 + C_B\nu/\nu_T}\right)\left[3\frac{\overline{q_i q_k}}{\overline{q^2}} - \delta_{ki}\right] q_k \tag{A.3}$$

and the rotation model,

$$-\frac{1}{\tau_R}\left[\frac{\overline{(q_k\Omega_k^*)^2/q^2}}{20\overline{q^2}\,\overline{K}+0.25(\Omega_k^*)^2}\right]q_i \tag{A.4}$$

with $\Omega_k^* = \epsilon_{ijk}\overline{u}_{k,j} + \Omega_i$. Expression (A.1e) accounts for viscous diffusion, a troublesome term which will be discussed in detail later (§3.3). Turbulent viscosity is defined as

$$\nu_T = \left(\frac{\overline{K^2}}{\overline{Kq^2}}\right)^{1/2} \tag{A.5}$$

Note that W_i (Expression (A.1f)) was added to represent the near-wall reorientation necessary to achieve the proper asymptotic behavior of q_i and R_{ij} as they approach a solid boundary. This is discussed in §5.3.1.

The evolution equation for the Reynolds stress tensor is cast as:

$$R_{ij,t} + \nabla\cdot(\overline{u}_k R_{ij}) = \tag{A.6a}$$

$$\left[\overline{u}_{i,k} + \left(\frac{q_i q_l}{q^2} - \delta_{il}\right)2\overline{u}^*_{l,k}\right]R_{kj} + \left[\overline{u}_{j,k} + \left(\frac{q_j q_l}{q^2} - \delta_{jl}\right)2\overline{u}^*_{l,k}\right]R_{ki} \tag{A.6b}$$

$$-\left(\alpha\nu\overline{q^2} + \frac{1}{\tau_R}\right)R_{ij} \tag{A.6c}$$

$$-A_{ij} \tag{A.6d}$$

$$+M_{ij} \tag{A.6e}$$

$$+\left[(\nu+\nu_T)R_{ij,k}\right]_{,k} \tag{A.6f}$$

$$-D(\nu+\nu_t)\left[\frac{R_{ij}}{K}\right]_{,k}(K)_{,k} \tag{A.6g}$$

$$-E(\nu+\nu_t)\frac{(K)_{,k}}{K}\frac{(K)_{,k}}{K}R_{ij} \tag{A.6h}$$

$$+W_{ij} \tag{A.6i}$$

with return to isotropy and the orthogonality term defined as

$$A_{ij} = \frac{C_{A_{ij}}}{\tau_R}\left(\frac{\nu_T}{\nu_T + C_A^{Dn}\nu}\right)\left[R_{ij} - \overline{K}\left(\delta_{ij} - \frac{q_i q_j}{q^2}\right)\right] \tag{A.7}$$

$$M_{ij} = \left(R_{lj}\frac{q_i}{q^2} + R_{li}\frac{q_j}{q^2}\right)(A_l + C_\Omega q_l) \tag{A.8}$$

again noting that W_{ij} (Expression (A.6i)) has been added to the Reynolds stress equation to represent the wall reorientation applied to the tensor as a result of eddy vector rotation (W_i, Expression (A.1f)) and the orthogonality constraint. This term and its variants are discussed in §5.3.1. The expressions preceded by the constants D and E (terms (A.6g) and (A.6h), respectively) warrant discussion. The first involves the gradient of the Reynolds stress tensor. For models without normalized stress tensors these terms are

$$-D\left(\nu + \nu_t\right)\left[\frac{R_{ij}}{K}\right]_{,k}(K)_{,k} \tag{A.9}$$

and

$$-E\left(\nu + \nu_t\right)\frac{(K)_{,k}}{K}\frac{(K)_{,k}}{K}R_{ij} \tag{A.10}$$

in the Reynolds stress equation (for both models based on q_i and $q_i/q^2 = L_i$). For those involving the normalized Reynolds stress tensor $R^*_{ij} = R_{ij}/K$ (which will be introduced shortly), the term of interest in the Reynolds stress equation is

$$(2 - D)\left(\nu + \nu_t\right)\left[R^*_{ij}\right]_{,k}\frac{(K)_{,k}}{K} \tag{A.11}$$

The terms in the Reynolds stress equation (Expressions (A.9) and (A.10)) and by extension that in the normalized Reynolds stress equation (Equation (A.22)) come from expanding the last term in the original Oriented-Eddy Collision turbulence model model formulation and help ensure the near-wall asymptotic behavior of the model. Note that D is often chosen to be 2, thus eliminating the extra term in the R^*_{ij} evolution equation, which is desirable considering it can cause numerical difficulty near walls. E is chosen to be zero in an attempt to ensure that $\overline{q^2}$ (the average eddy vector magnitude) approaches a solid boundary like $(2/\alpha)/y^2$ where α is a tunable constant,

usually set to $\alpha = 15.0$. Note that OpenFOAM currently does not support tensors above rank two, the implementation of terms which employ such tensors is discussed in §7.3. This early version of the Oriented-Eddy Collision turbulence model differs little from the version used at present.

A.2 Moving from "q" to "L"

At a shear-free (slip) wall, turbulent eddies may align themselves to be tangential to (in the plane of) the wall and the magnitude of the eddy should remain unchanged, making this type of boundary condition somewhat easier to understand. No-slip wall boundary conditions for the eddy orientation vectors q_i present a conundrum. Intuitively, one might suspect that the size of a turbulent eddy approaches zero as the eddy approaches a no-slip wall. This, however, implies an infinite boundary condition on q_i (which, recall, has units of inverse length). This is of course not feasible. In an attempt to avoid this problem, the Oriented-Eddy Collision turbulence model was once again re-cast to evolve the eddy length itself, $L_i = q_i/q^2$, which has units of length and thus can be set to zero at no slip walls. It was suspected that this form of the Oriented-Eddy Collision turbulence model would be stable at solid boundaries and numerically tractable. Evolving a quantity like the eddy vector q_i is troublesome as the quantity goes to infinity at a solid boundary if the eddy length scale goes to zero. This is a problem separate from non-local pressure effects, which are addressed in Chapter 5.

The requirement of infinite boundary conditions applied to the eddy orientation vectors q_i led to the re-casting of the Oriented-Eddy Collision turbulence model in terms of $L_i = q_i/q^2$ which has solid boundary conditions of $L_i = 0$. Note that a hat $\hat{}$ indicates a model quantity based on L_i rather than q_i. The derived evolution equation for the new eddy vector:

$$\frac{DL_i}{Dt} = -\left(\delta_{in} - 2\frac{L_n L_i}{L^2}\right)(L_k \overline{u}_{k,n})$$
$$+ \frac{1}{3}\left(\alpha\nu\overline{\left(\frac{1}{L^2}\right)} - 2\nu\frac{|L|_{,k}|L|_{,k}}{L^2} + \frac{1}{\hat{\tau}_R}\right)L_i$$
$$- \left(\delta_{in} - 2\frac{L_n L_i}{L^2}\right)\left(\hat{A}_n + \hat{C}_\Omega L_n\right) + \frac{1}{3}[(\nu + \hat{\nu}_T)L_{i,k}]_{,k} + \hat{W}_n \quad \text{(A.12)}$$

with $\hat{W}_n$ once again representing the near wall rotation term, discussed later. Note the addition of $2\nu\frac{|L|_{,k}|L|_{,k}}{L^2}$ in the dissipation term of Equation (A.12) which comes from converting the q_i evolution equation to one which uses L_i. Similar to its original form, the return to isotropy model is written as:

$$\hat{A}_n = \frac{C_{A_i}}{\hat{\tau}_R}\left[\frac{\hat{\nu}_T}{\hat{\nu}_T + C_A^{Dn}\nu}\right]\left[3\hat{N}_{kn} - \delta_{kn}\right]L_k \quad \text{(A.13)}$$

with the isotropy tensor $\hat{N}_{kn}$ is now defined as

$$\hat{N}_{kn} = \frac{\overline{\left(\frac{L_n L_k}{(L^2)^2}\right)}}{\overline{\left(\frac{1}{L^2}\right)}} \quad \text{(A.14)}$$

and the turbulent viscosity is cast as

$$\hat{\nu}_T = \left(\frac{\overline{K^2}}{\overline{\left(K\frac{1}{L^2}\right)}}\right)^{\frac{1}{2}} \quad \text{(A.15)}$$

The time scale is now written

$$\frac{1}{\hat{\tau}_R} = \left(\overline{K}\overline{\left(\frac{1}{L^2}\right)}\right)^{\frac{1}{2}} \quad \text{(A.16)}$$

The system rotation term for the L_i-based model becomes

$$\hat{C}_\Omega = \frac{1}{\hat{\tau}_R}\left\{\frac{\overline{(L_k{\Omega_k}^*)^2/L^2}}{20.0\overline{\left(\frac{1}{L^2}\right)}\overline{K} + 0.25({\Omega_k}^*)^2}\right\} \quad \text{(A.17)}$$

Note that $\frac{1}{3}\left(\alpha\nu\overline{\left(\frac{1}{L^2}\right)} - 2\nu\frac{|L|_{,k}|L|_{,k}}{L^2} + \frac{1}{\hat{\tau}_R}\right) L_i$ in Equation (A.12) above is an approximation. The exact derivation (or conversion) from the q_i-based model to the L_i-based model returns a dissipation term similar to that in the original casting of the model, namely

$$\frac{1}{3}\left(\alpha\nu\overline{\left(\frac{1}{L^2}\right)} + \frac{1}{\hat{\tau}_R}\right) L_i$$

with several additional terms added the L_i evolution equation:

$$-\frac{2}{3}\left(\nu + \hat{\nu}_T\right)\frac{1}{L^2}\left(L^2\right)_{,k} L_{i,k} + \frac{2}{3}\left(\nu + \hat{\nu}_T\right) L^2 \left\{\left(\frac{L_n}{L^2}\right)_{,k}\left(\frac{L_n}{L^2}\right)_{,k}\right\} L_i \tag{A.18}$$

With the above model for the eddy length scale L_i, a corresponding model for the Reynolds stress tensor, now based on L_i, can be constructed:

$$\begin{aligned}\frac{D\hat{R}_{ij}}{Dt} &= \left[\overline{u}_{i,k} + \left(\frac{L_i L_l}{L^2} - \delta_{il}\right) 2\overline{u}^*_{l,k}\right]\hat{R}_{kj} + \left[\overline{u}_{j,k} + \left(\frac{L_i L_l}{L^2} - \delta_{jl}\right) 2\overline{u}^*_{l,k}\right]\hat{R}_{ki} \\ &- \left(\alpha\nu\overline{\left(\frac{1}{L^2}\right)} + \frac{1}{\hat{\tau}_R}\right)\hat{R}_{ij} - \hat{A}_{ij} + \hat{M}_{ij} + \left[\left(\nu + \hat{\nu}_t\right)\hat{R}_{ij,k}\right]_{,k} \\ &- D\left(\nu + \hat{\nu}_t\right)\left[\frac{\hat{R}_{ij}}{K}\right]_{,k}(K)_{,k} - E\left(\nu + \hat{\nu}_t\right)\left[\frac{\hat{R}_{ij}}{K}\right]_{,k}(K)_{,k} + \hat{W}_{ij}\end{aligned} \tag{A.19}$$

Note the similarities between the version of the stress tensor evolution equation based on the original eddy vector q_i and its current form. The return to isotropy of the Reynolds stresses based on L_i is written as

$$\hat{A}_{ij} = \frac{C_{A_{ij}}}{\hat{\tau}_R}\left\{\frac{\hat{\nu}_T}{\hat{\nu}_T + C_A^{Dn}\nu}\right\}\left[\hat{R}_{ij} - \overline{K}\left(\delta_{ij} - \frac{L_i L_j}{L^2}\right)\right] \tag{A.20}$$

and the corresponding orthogonality term

$$\hat{M}_{ij} = \left(\hat{R}_{lj}L_i + \hat{R}_{li}L_j\right)\left(\hat{A}_l + \hat{C}_\Omega L_n\right) \tag{A.21}$$

A.3 Adding kinetic energy

While the use of L_i in place of q_i avoided the infinite boundary condition conundrum, stability of the model in wall-bounded flows was still difficult to attain. In an attempt to ensure stability at solid boundaries, the Oriented-Eddy Collision turbulence model model was again recast to evolve the Reynolds stresses normalized by the kinetic energy, $R^*_{ij} = R_{ij}/K$. This necessitated an evolution equation for the kinetic energy K in addition to those for q_i and R^*_{ij}. The eddy orientation vector equation was unchanged by this operation and in addition was not suspected as the reason for near-wall instability. An evolution equation for the normalized Reynolds stress tensor R^*_{ij} was adopted:

$$\begin{aligned}\frac{\partial R^*_{ij}}{\partial t} + \nabla \cdot \left(\overline{u}_k R^*_{ij}\right) &= P^*_{ij} - A^*_{ij} + M^*_{ij} + \nabla \cdot (\nu + \nu_t) \nabla R^*_{ij} \\ &+ (2 - D)(\nu + \nu_t) \left[R^*_{ij}\right]_{,k} \frac{(K)_{,k}}{K} + W^*_{ij}\end{aligned} \tag{A.22}$$

and the evolution equation for the kinetic energy was derived as:

$$\begin{aligned}\frac{\partial K}{\partial t} + \nabla \cdot (\overline{u}_j K) &= \left[\overline{u}_{i,k} + \left(\frac{q_i q_l}{q^2} - \delta_{il}\right) 2\overline{u}^*_{l,k}\right] R_{ki} - \left(\alpha \nu \overline{q^2} + \frac{1}{\tau_R}\right) K \\ &- A^*_{kk} + M^*_{kk} + \left[(\nu + \nu_T) K_{,k}\right]_{,k} - E(\nu + \nu_T) \frac{(K)_{,k}(K)_{,k}}{K}\end{aligned} \tag{A.23}$$

noting again that the equation for q_i is unaltered. In Equation (A.22), P^*_{ij} a modified form of the production term:

$$\begin{aligned}P^*_{ij} &= \left[\overline{u}_{i,k} + \left(\frac{q_i q_l}{q^2} - \delta_{il}\right) 2\overline{u}^*_{l,k}\right] R^*_{kj} \\ &+ \left[\overline{u}_{j,k} + \left(\frac{q_j q_l}{q^2} - \delta_{jl}\right) 2\overline{u}^*_{l,k}\right] R^*_{ki}\end{aligned} \tag{A.24}$$

which is the same as P_{ij} (Expression (A.6b)) except it involves R^*_{ij} as opposed to R_{ij}. The same is true for the modified orthogonality term M^*_{ij}:

$$M^*_{ij} = \left(R^*_{lj}\frac{q_i}{q^2} + R^*_{li}\frac{q_j}{q^2} \right) (A_l + C_\Omega q_l) \tag{A.25}$$

which is simply the orthogonality term M_{ij} (Expression (A.6e)) operating on R^*_{ij}. The eddy orientation vector equation remains the same thus both the eddy orientation return-to-isotropy term and system rotation term $C_\Omega q_l$ are unchanged. The Reynolds stress return to isotropy term A^*_{ij} is slightly different from the one found in the original Oriented-Eddy Collision turbulence model model (Expression (A.6d)) and is shown below:

$$A^*_{ij} = \frac{C_{A_{ij}}}{\tau_R}\left[\frac{\nu_T}{\nu_T + C_A^{Dn}\nu}\right]\left[R^*_{ij} - \left(\delta_{ij} - \frac{q_i q_j}{q^2}\right)\right]\left(\frac{\overline{K}}{K}\right) \tag{A.26}$$

noting that the average kinetic energy $\overline{K}$ is normalized by the local (per-eddy) kinetic energy $K = \frac{1}{2}R_{ii}$. The "extra" term in the kinetic energy equation is

$$-E\left(\nu + \hat{\nu}_T\right)\frac{(K)_{,k}(K)_{,k}}{K} \tag{A.27}$$

and comes from the corresponding terms in the Reynolds stress evolution equation, Equations (A.9) and (A.10). The near-wall reorientation term W^*_{ij} is identical to W_{ij} except it now operates on R^*_{ij} rather than R_{ij}. Again, this term is addressed in §5.3.1. Evolving R^*_{ij} allows the per-eddy Reynolds stress R_{ij} to be calculated via $R_{ij} = R^*_{ij}K$ which does not present problems when $K = 0$. Once completed, the new q_i, K, R^*_{ij} ("qkR*") casting of the Oriented-Eddy Collision turbulence model was tested using the same basic cases that were employed for the original q_i, R_{ij} ("qR") model. Results from the two models matched closely for all benchmark cases (discussed in Chapter 4) and are presented later in this chapter (see Figure A.1).

A.4 Combining the two ideas

A fourth version of the Oriented-Eddy Collision turbulence model which combines the new eddy orientation vector L_i and the normalized Reynolds stress tensor ${R_{ij}}^*$

was created in hopes that the two variations would provide the most stability near solid boundaries. The equation for the evolution of L_i is again unchanged (as was the case with the transition from "qR" to "qkR*"), but the Reynolds stress and kinetic energy evolution equations are obviously affected. Note that terms which are both normalized by the kinetic energy K *and* are based on L_i carry both a hat ˆ and an asterisk. Keeping this in mind, the Reynolds stress evolution equation takes a familiar form:

$$\frac{D\hat{R}^*_{ij}}{Dt} = \left[\overline{u}_{i,k} + \left(\frac{L_i L_l}{L^2} - \delta_{il}\right) 2\overline{u}^*_{l,k}\right] \hat{R}^*_{kj} + \left[\overline{u}_{j,k} + \left(\frac{L_j L_l}{L^2} - \delta_{jl}\right) 2\overline{u}^*_{l,k}\right] \hat{R}^*_{ki} \quad \text{(A.28)}$$
$$- \hat{A}^*_{ij} + \hat{M}^*_{ij} + \left[(\nu + \hat{\nu}_t)\, \hat{R}^*_{ij,k}\right]_{,k} + (2 - D)\,(\nu + \hat{\nu}_t) \left[\hat{R}^*_{ij}\right]_{,k} \frac{(K)_{,k}}{K} + \hat{W}^*_{ij}$$

Once again D and is a numerical constant typically set to $D = 2$, thus zeroing second to last term in the evolution equation and avoiding potential numerical stability issues. The return to isotropy term for the Reynolds stresses corresponding to the normalized stress tensor model based on L_i:

$$\hat{A}^*_{ij} = \frac{C_{A_{ij}}}{\hat{\tau}_R} \left\{\frac{\hat{\nu}_T}{\hat{\nu}_T + C_A^{Dn}\nu}\right\} \left[\hat{R}^*_{ij} - \left(\delta_{ij} - \frac{L_i L_j}{L^2}\right)\right] \left(\frac{\overline{K}}{K}\right) \quad \text{(A.29)}$$

with the orthogonality term written as

$$\hat{M}^*_{ij} = \left(\hat{R}^*_{lj} L_i + \hat{R}^*_{li} L_j\right) (\hat{A}_l + \hat{C}_\Omega L_n) \quad \text{(A.30)}$$

As was the case with the previous normalized stress tensor variant of the Oriented-Eddy Collision turbulence model, an evolution equation for the kinetic energy K is required. In this case, this equation is constructed using the new eddy orientation vector L_i:

$$\frac{DK}{Dt} = \left[\overline{u}_{i,k} + \left(\frac{L_i L_l}{L^2} - \delta_{il}\right) 2\overline{u}^*_{l,k}\right] \hat{R}_{ki} - \left(\alpha\nu\overline{\left(\frac{1}{L^2}\right)} + \frac{1}{\hat{\tau}_R}\right) K - \hat{A}^* + \hat{M}^*$$
$$+ \left[\left(\nu + \hat{\nu}_T\right) K_{,k}\right]_{,k} - E\left(\nu + \hat{\nu}_T\right) \frac{(K)_{,k}(K)_{,k}}{K} \tag{A.31}$$

where $\hat{A}^* = (1/2)\hat{A}_{ii}^{\ *}$ and similarly $\hat{M}^* = (1/2)\hat{M}_{ii}^{\ *}$. Unfortunately, as was the case with the other forms of the Oriented-Eddy Collision turbulence model model variants, the "LkR*" version was also unstable when simulating simple wall bounded flows. The high Reynolds number shear flow of Matsumoto *et al.* [47] was employed to validate the derivations and implementations of the model variants. Figure A.1 shows a comparison of each model variants' performance: §4.6 presents additional

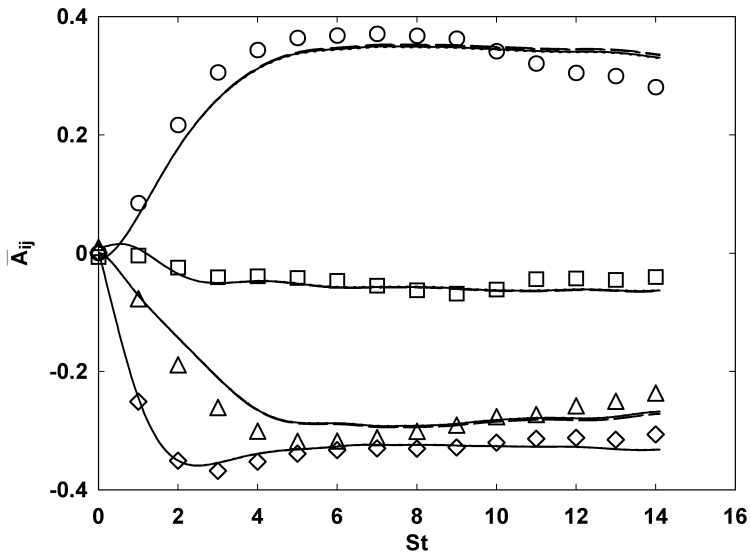

Figure A.1. Anisotropy data $\overline{A}_{ij} = \left(\overline{R}_{ij}/\overline{K}\right) - 2\delta_{ij}/3$ at $Re_T = 152$ from Matsumoto, Nagano, and Tsuji [47]. $\overline{A}_{11}$ (○), $\overline{A}_{22}$(△), $\overline{A}_{33}$(□), $\overline{A}_{12}$(◇); compared to results from the Oriented-Eddy Collision turbulence model: "qR" (—), "LR" (- - -), "qkR*" (· · ·), "LkR*" (–·–).

data from Matsumoto, *et al.* as a means of validating the current version of the Oriented-Eddy Collision turbulence model in the presence of shear. As seen in Figure A.1, the three additional models match the original "qR" variant: "qkR*", which normalizes the stress tensor by the kinetic energy and has a transport equation for

the kinetic energy, "LR" which used the eddy length vector L_i rather than the original q_i, and "LkR*" which employs both the eddy length vector L_i and the normalized stress tensor $R_{ij}* = R_{ij}/K$. The four model variants are stable (even over long periods of time) and return solutions within 2% of one another and within 5% of the shear data.

APPENDIX B

HOMOGENEOUS INITIAL CONDITIONS

The initial conditions for the eddy orientation vectors and stresses must be addressed. In theory, the more orientations used in the model, the better the representation of the underlying physics. Based on the number of eddies N, each cell in the computational domain is populated with N Reynolds stress tensors, and N eddy vectors. For isotropic initial conditions, the eddy orientations are sampled uniformly on a sphere. The magnitude of the eddy vectors governs the dissipation, so these vectors must initially be scaled to have the correct magnitude for a given initial kinetic energy and Reynolds number. The initial eddy vectors are scaled by the positive root to the following quadratic equation (with roots β):

$$\left[\nu\left(\overline{q^2K^0}\right)\alpha\right]\beta^2+\left[\left(\overline{K^0}\right)^{\frac{3}{2}}\overline{q^2}^{\frac{1}{2}}\right]\beta=\frac{\left(\overline{K^0}\right)^2}{\nu {Re_T}^0} \tag{B.1}$$

where $\overline{K^0}$ and ${Re_T}^0$ are the average initial kinetic energy and turbulent Reynolds number. Recall that the average eddy magnitude is calculated by $\overline{q^2}=\frac{1}{N}\sum q^2$.

The Reynolds stresses are set by the initial average Reynolds stress tensor $\overline{R^0_{ij}}$ and the corresponding eddy orientation by the equation

$${R_{ij}}^{IC}=3\left[\overline{R^0_{ij}}-\frac{q_kq_i}{q^2}\overline{R^0_{jk}}-\frac{q_kq_j}{q^2}\overline{R^0_{ik}}+\frac{q_s\overline{R^0_{st}}q_t}{q^2}\delta_{ij}\right]-\frac{3}{2}\left(\delta_{ij}-\frac{q_iq_j}{q^2}\right)\overline{R^0_{kk}} \tag{B.2}$$

These initial stresses are always orthogonal to the corresponding orientation. They have the correct kinetic energy for each orientation in as much as they sum to the

initial Reynolds stress ($\overline{R^0_{ij}}$) when the orientations are distributed on a sphere (that is, when they are isotropic).

For the model variants which employ the alternate length scale L_i (the "LR" and "LkR*" models), Equation (B.2) can be replaced by

$$\left[\nu\frac{1}{N}\sum\left(\overline{\left(\frac{1}{L^2}\right)}\overline{K^0}\right)\cdot\alpha\right]\beta^2+\left[\frac{\left(\overline{K^0}\right)^{\frac{3}{2}}}{\overline{|L_i|}}\right]\beta=\frac{\left(\overline{K^0}\right)^2}{\nu{\mathrm{Re}_T}^0} \tag{B.3}$$

again noting that with $\overline{|L_i|}=[(1/N)\sum(L^2)]^{\frac{1}{2}}$ similar to the equation for $\overline{q^2}$ above. If the orientations are initially isotropic then

$$N_{ik}=\frac{1}{N}\sum\frac{q_iq_k}{q^2}=\frac{1}{3}\delta_{ik} \tag{B.4}$$

and the desired Reynolds stress initial condition is recovered. If the orientations are *not* initially isotropic, the desired Reynolds stress initial condition is only approximately reproduced. Again for the for the "LR" and "LkR*" variants, the initial Reynolds stresses are:

$$\begin{aligned}{R_{ij}}^{IC}=3\left[\overline{R^0_{ij}}-L_i\cdot\left(\overline{R^0_{jk}}\cdot\tfrac{1}{L_k}\right)-L_j\cdot\left(\overline{R^0_{ik}}\cdot\tfrac{1}{L_k}\right)+L_s\cdot\left(\overline{R^0_{st}}\cdot\tfrac{1}{L_t}\right)\cdot\delta_{ij}\right]\\ -\tfrac{3}{2}\left(\delta_{ij}-\tfrac{L_iL_j}{L^2}\right)\cdot\left(\overline{R^0_{kk}}\right)\end{aligned} \tag{B.5}$$

The turbulent Reynolds number ${\mathrm{Re}_T}^*$ is recalculated once it is employed for the initial eddy vector and stress tensor scaling:

$${\mathrm{Re}_T}^*=\frac{\overline{K}^2}{\nu\epsilon}=\frac{\overline{K}^2}{\nu\left[\frac{1}{N}\sum(q^2K)\,\nu\alpha+\overline{K}^{\frac{3}{2}}\overline{|q_i|}\right]} \tag{B.6}$$

And for the "LR" and "LkR*" model variants:

$$\mathrm{Re}_T{}^* = \frac{\overline{K}^2}{\nu\epsilon} = \frac{\overline{K}^2}{\nu\left[\frac{1}{N}\sum\left(\frac{K}{L^2}\right)\nu\alpha + \frac{\overline{K}^{\frac{3}{2}}}{\overline{|L_i|}}\right]} \tag{B.7}$$

The somewhat unusual form of the turbulent Reynolds number formulations in Equations (B.6) and (B.7) comes from the fact that the Oriented-Eddy Collision turbulence model has no specific prescriptions for the dissipation ϵ, thus requiring the complex denominator that accounts for both the low and high Reynolds number expressions for the dissipation.

APPENDIX C

REYNOLDS AVERAGING

Reynolds [30] realized that the instantaneous turbulent velocity $\tilde{u}_i$ can be broken into two components, the *average* velocity $\overline{u}_i$ and the *fluctuating* velocity $u_i^{'}$ such that $\tilde{u}_i = \overline{u}_i + u_i^{'}$ [17, 66]. This definition can be substituted into Equations (1.1a) and (1.1b) (noting that a similar decomposition was performed with the pressure):

$$\frac{\partial(\overline{u}_i + u_i^{'})}{\partial t} + (\overline{u}_j + u_j^{'})\frac{\partial(\overline{u}_i + u_i^{'})}{\partial x_j} = -\frac{1}{\rho}\frac{\partial}{\partial x_i}(\overline{p} + p^{'}) + \nu\frac{\partial^2}{\partial x_i^2}(\overline{u}_j + u_j^{'}) \tag{C.1a}$$

$$\frac{\partial}{\partial x_i}(\overline{u}_i + u_i^{'}) = 0 \tag{C.1b}$$

After Reynolds decomposition, Equations (C.1a) and (C.1b) are then ensemble averaged. Ensemble averaging originates from averaging fields of variables. In this case, the fields of interest are velocity $\tilde{u}_i = \overline{u}_i + u_i^{'}$ and pressure $\tilde{p} = \overline{p} + p^{'}$. An ensemble average relies on the field being statistically stationary, meaning it is invariant in the statistics collected over time, space, or realizations [17, 66]. For example, if statistics collected at a given instant are independent of those taken at any other instant, time-averaging said field would be a form of ensemble averaging. It is important to note that the Navier-Stokes equations are not necessarily statistically stationary in time as they include an unsteady term, nor are they necessarily statistically "stationary" space [17]. As such, "averaging" Equations (C.1a) and (C.1b) does not necessarily imply simple temporal or volume (spatial) averaging. Instead, ensemble averaging can be defined as the average of discrete samples taken at different realizations of some experiment or simulation. Note that in most homogeneous, statistically steady

turbulent flows, the ergodic hypothesis applies, meaning that temporal, spatial, and ensemble averaging are equivalent [94, 105]. Due to the fact that most turbulent flows are in fact not homogeneous, temporal averaging is most often used.

APPENDIX D

GRADIENT DIFFUSION & TURBULENT VISCOSITY

D.1 Background

In order to understand zero-, one-, and two-equation models, it is necessary first to understand the underlying assumptions of these models. Returning to Equations (1.2a) and (1.2b), note that the Reynolds stress tensor, $R_{ij} = \overline{u_i' u_j'}$ is unclosed. The *turbulent viscosity hypothesis*, first introduced by Boussinesq in 1877 [6] (also called the Boussinesq hypothesis), stated that the shear (Reynolds) stress present in a boundary layer flow is simply the product of some eddy (turbulent) viscosity and the streamwise (in the x direction) mean velocity gradient normal to the wall (in the y direction):

$$R_{ij} = -\nu_T \frac{\partial \overline{u}_1}{\partial x_2} \tag{D.1}$$

Of course, at the time little was known about turbulence (it would be another twenty years before Osborne Reynolds proposed his famous decomposition of the Navier-Stokes equations [30]), and Boussinesq's idea stemmed from observations of shear stress in the flow, not about the (still-unnamed) Reynolds stress tensor. A coordinate-invariant version of the model claims the deviatoric portions of the Reynolds stresses are proportional to the mean strain rate:

$$R_{ij} - \frac{1}{3} R_{ii} \delta_{ij} = -2\nu_T \left(\frac{\partial \overline{u}_i}{\partial x_j} + \frac{\partial \overline{u}_j}{\partial x_i} \right) \tag{D.2}$$

recalling that U_i is the *average*, not fluctuating, velocity and δ_{ij} is the Kronecker delta. This implies that the transfer of momentum caused by turbulent flow could be

modeled by a so-called "eddy viscosity" ν_T, a rate-of-strain equation for the Reynolds stresses. The idea for such a relation stems from, and is similar to, the *gradient diffusion hypothesis* [66, 105], which states that, for some scalar in a flow, the velocity vectors and gradient vectors of that scalar are aligned. This assumption is false even for simple flows, but is a good place to begin describing turbulence. At the end of the 19th century, molecular transport was better understood than turbulent fluid flow, and it is no surprise that many in the then-fledgling field of turbulent research sought analogies between the two. This idea formed the basis for Boussinesq's hypothesis - essentially assuming that the behavior of unknown *turbulent* fluctuations could be replaced by better understood *random molecular* fluctuations [105]. The *eddy viscosity hypothesis* claims that the anisotropic part of the Reynolds stress tensor is aligned with the strain rate (also a tensor). The hypothesis states that all independent components of the anisotropy and strain tensors are simply related through the eddy (or turbulent) viscosity ν_T. Equation (D.2) establishes an equilibrium between the Reynolds stresses and the mean rate of strain, which is not always the case - R_{ij} and the mean strain can be temporally misaligned.

Eddy viscosity is assumed to be a combination of a length and time scale, or a length and velocity scale [71, 94, 66, 17, 105]:

$$\nu_T \propto \frac{l_0^2}{\tau_0} \tag{D.3a}$$

$$\nu_T \propto \tilde{u}_0 l_0 \tag{D.3b}$$

The eddy viscosity ν_T is prescribed before a simulation begins. More specifically, a turbulent length scale l_0 and turbulent time scale τ_0 are set by using knowledge from experimental results or previous simulations. Often, the eddy viscosity will be cast as a velocity scale and length scale [66] where the length and velocity scales l_0 and $\tilde{u}_0$ are known (or guessed) ahead of time for a given flow. Inherent to this is the assumption

that turbulence can be described by a *single* length and time scale. This is completely at odds with reality, as turbulent flows contain a multitude of relevant length and time scales. As a brief aside, one may wonder why such an approach may be sufficient for, say, molecular motion but not for turbulent flows. Specifically, collections of molecules (in a mixture of gasses, for example) can in fact have a variety of disparate length and time scales. Yet, an "eddy viscosity" approach can describe the physics of such a gas. The subtle but important key to understanding the difference lies not in the presence of many length and time (or velocity) scales, but in how those scales relate to the scale of the velocity gradients present. In the example gas mixture, the length and velocity scales over which the collection of molecules interacts is usually orders of magnitude smaller than the gradients present. Because of this, the molecules are always close to the flow's velocity in a local sense. This means that the molecular distribution is *Maxwellian* and shifted by the mean flow, but otherwise unaltered [66]. Turbulence, on the other hand, does not share this separation of scales enjoyed by molecular motion and thus assuming an equilibrium is physically wrong. Turbulent flows often have features (eddies, the surrogate for molecules in the analysis above) that are on the same order as the mean flow, meaning there is no massive separation of scale between the eddy interactions and the gradients present in the flow; the distribution describing a turbulent flow is decidedly not Maxwellian. Furthermore, assuming that turbulence may be described by its kinetic energy K, which is a scalar quantity, makes any model based on this assumption unable to capture anisotropy in the turbulence. Important physical phenomena, such as heat transfer and separation in boundaries rely on anisotropy, and cannot be captured by any model with such shortcomings. There are, however, flow situations where such assumptions can admit a reasonable description of the flow, such as high Reynolds number cases far from solid boundaries [66].

D.2 Zero-equation / Algebraic models

Zero-equation, or algebraic, models employ a partial differential equation (PDE) solely for the mean velocity field and do not contain any PDEs for turbulent quantities [71]. These models are commonly used by engineers due to their simplicity and speed. More popular in the 1960s and 1970s, they have been replaced in more recent years first by one- and two-equation models, and increasingly by large eddy simulation, Reynolds-stress models, and direct numerical simulation as computational resources increase in size and efficiency. These models use the Boussinesq approximation and solve for the Reynolds stresses by simply multiplying an eddy viscosity (of various forms) with the mean strain rate tensor [105]. Eddy viscosities, which are assumed to be a property of the turbulent flow in question, are constructed from a prescribed mixing length which must be known *a priori*. This makes any such model incomplete, as the equations cannot be solved by knowledge of their initial and boundary conditions alone. One of the simplest algebraic models is one which assumes uniform eddy viscosity throughout the flow in any direction other than the mean flow. Such models are often applied to planar free-shear flows [66], and pose the eddy viscosity as only a function of x, the streamwise direction:

$$\nu_T = \frac{\overline{u}_c l_c}{Re_T} \tag{D.4}$$

with $\overline{u}_c$ and l_c a characteristic velocity and length, and Re_T the turbulent Reynolds number. All three parameters must be specified, limiting the usefulness of this model to free shear flows and crippling it elsewhere.

Prandtl, who is credited with being the first to observe the boundary layer in 1904 [105], proposed one of the first zero-equation models in 1925 [91, 67]. He surmised that coherent "particles" of fluid would group together and move with the mean flow. In flows with shear present, he further believed that the momentum (in the shear

direction) of a given collection of particles would remain unchanged for some distance, which he called the mixing length [105]. Prandtl established the eddy viscosity as

$$\nu_T = l_m^2 \left| \frac{d\overline{u}_1}{dx_2} \right| \tag{D.5}$$

where in this case the model is applied to near-wall regions, x_2 is the wall normal direction, $\overline{u}_1$ the mean streamwise velocity, and the mixing length l_m is prescribed, usually as a function of position, in the viscous and mean flow regions over the solid boundary. The mixing length can be thought of as a counterpart to the mean-free path of a gaseous molecules, taken from the kinetic theory of gasses [105], and is representative of a "characteristic" turbulent structure (eddy) size or a lengthscale for turbulent dispersion [17]. The model is typically used for stationary boundary layer (two-dimensional) scenarios [66]. Van Driest [18] proposed a damping correction for the mixing-length model that is included in many algebraic models. To remove some of the difficulties in defining the turbulent length scale from the shear-layer thickness, Baldwin and Lomax [4] proposed an alternative algebraic model [105, 66] which replaces the mean normal velocity gradient in Equation (D.5) with the magnitude of the rate-of-rotation tensor, yielding $\nu_T = l_m^2 \Omega$ [66, 4]. Smagorinsky [87] proposed another alternative, whereby the magnitude of the rate of strain tensor was employed, such that $\nu_T = l_m^2 S$. Some zero-equation models find their greatest application in the flow of jets and wakes. They assume the eddy viscosity involves only some constant c, the width of the jet or wake l, and a mean velocity scale $\Delta\overline{u}$, which may be the difference between the center line and far field velocities. The turbulent viscosity becomes $\nu_T = c\Delta\overline{u}l$. In any case, such models are severely limited by the need to provide a length scale which reduces to *guessing* one for a given flow; they neglect history effects present in the flow; and they are unable to calculate the turbulent kinetic energy [94], not to mention more complex problems such as anisotropy. Furthermore, the lack of

scale separation between the eddy size and mean flow makes Prandtl's analogy to the kinetic theory of gasses unfounded [17].

D.3 One-equation models

One-equation models add to zero-equation models a PDE that describes the behavior of a turbulent velocity scale [71], thus having prescriptions for both the mean velocity and turbulent velocity scales. This is done in hopes of providing the ability to calculate the turbulent kinetic energy and to account for history effects in the calculation of the eddy viscosity [94]. Both Prandtl [68] and Kolmogorov [32] determined that the turbulent viscosity should be calculated using the turbulent kinetic energy, setting $\nu_T = lK^{1/2}$, where in this case the velocity scale is $K^{1/2}$. In order use the kinetic energy K in the definition of ν_T, it was necessary to introduce a means of determining the kinetic energy, and thus a transport equation for K was developed [94, 66]. The insight shared by both Prandtl and Kolmogorov was that the eddy viscosity was affected by the flow's history, information of which was contained in the turbulent kinetic energy [105]. One equation models suffer from several deficiencies, including a hold-over from algebraic models in that a turbulent lengthscale must still be defined. In addition, the models are not applicable to low Reynolds number flows and cannot be used at or close to solid walls [94].

The Spalart-Allmaras model is a relatively new and popular one-equation model used primarily for aeronautical flows, two-dimensional mixing layers, wakes, and other boundary layer applications [89, 88] that is unique in that it prescribes a transport equation for the eddy viscosity directly. This was done in an attempt to circumvent the problems of algebraic and other, older one-equation models while avoiding the computational cost and complexity of two-equation and stress transport models [66]. The model still relies on a length scale, in this case the distance from a solid boundary, in order to be fully specified. This distance is not prescribed but is in fact calculated,

making this length scale one which is set *automatically.* Although the model is capable of achieving good results near walls at high Reynolds numbers, it fails to predict several simple quantities, such as the decay of the turbulent viscosity in isotropic turbulence [66]. Clearly, improvements must be made to zero- and one-equation models.

D.4 Two-equation models

Two-equation models add an additional PDE for the turbulent length scale, thus having equations for the mean velocity, the turbulent velocity scale, and the turbulent length scale [71]. All models prior to two-equation models were incomplete, in that they required *a priori* knowledge of the flow in order to work, namely by the prescription of a mixing length or other length scale. Two equation models have no such requirements, as they are fully specified by their initial and boundary conditions (with some exceptions, noted below). The addition of a third PDE was driven by the desire to eliminate the need to prescribe an essentially *ad-hoc* length scale. Additionally, one requires at least two equations in a model in order to predict (rather than prescribe) a turbulent length scale [91]. The $K-\epsilon$ model and its myriad variants are the most widely used turbulence models to date [17]. With certain wall-prescriptions to handle solid boundaries, these models can provide fast, reasonable answers for a variety of turbulent flows. As with the previously considered models, $K-\epsilon$ must provide for the evolution of the eddy viscosity ν_T. The model makes several assumptions about turbulent flows, including the observation that at high Reynolds numbers, the dissipation and production rates are close in magnitude, and that the ratio of the Reynolds stresses to the kinetic energy $\overline{u_i'u_j'}/k \approx 0.3$. This yields a length scale $l_0 = K^{3/2}/\epsilon$ and time scale $\tau_0 = K/\epsilon$. From this, referring to Equation (D.3a), ν_T can be rewritten as [17, 29]:

$$\nu_T = C_\mu \frac{K^2}{\epsilon} \tag{D.6}$$

where C_μ is a given constant (usually $= 0.09$) and ϵ is the dissipation present in the flow. Thus, the $K - \epsilon$ model must describe the time and space evolution of the kinetic energy K and the dissipation ϵ which it does so through model equations, the details of which will not be covered here. The model was originally devised to improve solutions in regions of flow with low turbulent Reynolds numbers (such as turbulent boundary layers) [29], and it assumes that the production of dissipation is controlled by the anisotropy tensor and velocity gradients, while the destruction of dissipation is set by the turbulent length and time scales [94]. There are many shortcomings of such a model: those inherited from the eddy viscosity hypothesis, as well as the inability to integrate the K and ϵ equations to solid boundaries. Another deficiency is that the $K - \epsilon$ model assumes homogeneous turbulence, and specifically that K/ϵ, which is analogous to a turbulent time scale evolution equation, may be replaced in the model by a timescale itself and the evolution of the time scale modeled. In non-homogeneous flow, this assumption is not valid as there exists a non-trivial diffusion term which would need to be less than zero to satisfy the model [17]. The $K - \epsilon$ model suffers from other shortcomings, including a tendency to over predict skin friction [17] and a reliance on wall functions to handle physics near solid boundaries.

The $K - \omega$ model is similar to the $K - \epsilon$ model and was originally proposed by Wilcox [105]. It is based on the principle, mentioned above, that one may model the evolution of the turbulent time scale itself rather than dissipation. It overcomes the difficulties arising from non-homogeneous flow by instead considering the *inverse* time scale, $\omega = \epsilon/K$ [17, 105]. Wilcox's 1988 paper [104] sets the eddy viscosity as $\nu_T = K/\omega$. The $K - \omega$ model suffers from free-stream sensitivity, and also is unable to correctly predict shear stress present in flows with strong or adverse pressure gradients [17]. In some cases, the $K - \omega$ model and $K - \epsilon$ model are used in conjunction, the former being employed near solid boundaries (and away from free-stream conditions) and the latter employed away from solid boundaries. This approach is often used

to help model turbulence transition, and can be found in so-called SST (shear stress transport) models.

Finally, Kolmogorov proposed what may have been the first two-equation model in 1941 [91, 32, 105]. Amazingly, years before the advent of the $K - \epsilon$ and $K - \omega$ models (that is, $K - \omega$ models of the sort proposed by Wilcox, Speziale, and others [83, 85, 37, 107, 104]; Kolmogorov also used ω as a inverse time scale), Kolmogorov proposed a means of describing turbulent flows which employed an equation for two-thirds of the turbulent kinetic energy and an inverse time scale which was proportional to dissipation [91, 32]. Kolmogorov's model lacked a production term, which is based on the belief that the inverse time scale is only associated with small scale motions and is otherwise unaffected by the mean flow. This is not entirely correct, as it is in fact the *largest* scales present in a turbulent flow that govern relevant time scales [105, 66]. Kolmogorov's model also lacked molecular diffusion and, as is the case with many other two-equation models, it cannot be easily employed near a solid boundary.

D.5 Non-linear eddy viscosity models

Previous zero-, one-, and two-equation turbulence models, based on eddy viscosity, assumed a linear relationship between eddy viscosity and other turbulence quantities. Although able to capture certain important physics (especially in isotropic and homogeneous flows), these linear models have problems near solid boundaries, along streamline curvature, at high strain rates, and at stagnation points [11]. Models were proposed that incorporate a quadratic relationship between the strain and stress tensors such as the non-linear $K - l$ and $K - \epsilon$ proposed by Speziale [92], and others that incorporate a cubic relationship, so called "cubic eddy-viscosity" models [11]. Essentially, these models extend the Boussinesq approximation by adding to it "higher order terms" in a series expansion of the original relationship [105]. The cubic eddy-viscosity model developed by Craft, Launder, and Suga [11] worked *back-*

wards from a more complicated stress transport model (in this case, simplifying an algebraic stress transport model, the likes of which are not considered in this paper) in order to arrive at an approximation for the Reynolds stresses. Such models can be considered as more general versions of their linear cousins. The Craft, Launder, and Suga [11] model uses the aforementioned cubic stress-strain relationship which allows the model to capture physics that other linear models cannot while retaining the same level of computational cost. The authors tested the model on plane channel flow, curved channel flow, and a turbulent impinging jet. They discovered that the cubic model performed reasonably well for all cases considered even in the presence of dominant anisotropy, solid boundaries and curvilinear streamlines [11]. Although not as accurate as stress transport models, the cubic model showed promise as a viable alternative to the classic $K - \epsilon$ model for solving engineering flows in commercial software.

The $\overline{v^2} - f$ model transport equations have in them the previously-established K and ϵ equations, but with modifications that attempt to increase dissipation near walls and thus improve the solution for the kinetic energy returned by the model. This is done so by introducing two additional partial differential equations, one of which attempts to capture the elliptic behavior of pressure. Capturing the fluctuating parts of the pressure is crucial near solid boundaries, as this enforces important near-wall turbulent behavior. Any directional information is an improvement over the eddy-viscosity assumption which cannot account for anisotropy. Solid boundaries tend to damp wall-normal transport; this phenomena is crucial to the evolution of turbulence near walls. Any model that can (roughly) capture these physics without resorting to complicated tensor transport equations is very useful for engineers.

APPENDIX E

THE PISO ALGORITHM

The PISO, or Pressure Implicit with Splitting of Operators, algorithm was originally developed by Issa [25] as a pressure-velocity calculation method for *non-iterative* solutions to *unsteady, compressible* flows. Since its original form, it has been adapted for use as an iterative solution method for both steady and unsteady flows [102]. Many non-steady solvers in OpenFOAM employ the PISO algorithm. Before the method is described, however, it is necessary to discuss the Semi-Implicit Method for Pressure-Linked Equations, or "SIMPLE", algorithm originally developed by Patankar and Spalding [54]. The PISO algorithm is essentially an extension of the SIMPLE algorithm that includes one additional correction step [102]. To begin with, the SIMPLE algorithm is outlined below.

Patankar and Spalding's SIMPLE algorithm [54] is a guess and check method for evaluating pressure on a staggered grid. It evaluates the convective fluxes (per unit mass) though a cell's face using "guessed velocity components" [102, 54, 3]. In addition, a "guessed pressure field" is employed to solve both the momentum and pressure correction equations. This "guessed pressure" is obtained from the continuity equation and used to obtain a pressure correction field. This pressure correction field is finally used to update the velocity and pressure fields [102]. The algorithm begins with a guessed velocity and pressure field and aims to iteratively improve these guessed fields until convergence has been obtained. The basic SIMPLE procedure is outline below for a laminar, steady flow, adapted from [54, 102, 19]:

1. First, a pressure field p^* is guessed.

2. Then, the discretized momentum equation is solved using p^*. This results in u_i^*, the "guessed" velocity.

3. A similar procedure may be employed for any arbitrary field dependent on p^* or u_i^*, say the scalar ϕ^*.

4. At this point, all "guessed" quantities - p^*, u_i^*, ϕ^*, etc. - are available.

5. A pressure correction field $p^{'}$ is defined the difference between the "correct" pressure field p and the guessed field p^* as the "correct pressure" field p is defined as $p = p^* + p^{'}$.

6. Next define the velocity correction is the same manner: $u_i^{'} = u_i - u_i^*$.

7. Set up the momentum equation which describes the velocity correction.

   (a) Equations for the "correct" velocity u_i and "guessed" velocity u_i^* are known. Subtract these two momentum equations.

   (b) To obtain the equation for the velocity correction $u_i^{'}$, substitute its definition into the equation formed above. A momentum equation involving only the velocity correction $u_i^{'}$ is obtained.

   (c) SIMPLE's main approximation involves **arbitrarily discarding** contributions (to convection and diffusion) from neighboring cells' $u_i^{'}$ in the $u_i^{'}$ momentum equation as they are unknown. This is difficult to justify, and contributes to the slow convergence of the method [19].

   (d) The above approximation results in the $u_i^{'}$ "momentum equation" only containing known information about gradients in the pressure correction field $p^{'}$, cell areas, etc.

8. The simplified equation for $u_i^{'}$ is now substituted into $u_i = u_i^* + u_i^{'}$ to obtain u_i recalling u_i^* is known.

9. The corrected velocity u_i may now be employed in the continuity equation to obtain an expression for the pressure correction $p^{'}$.

10. Finally, the corrected pressure may be found via $p = p^* + p^{'}$ recalling p^* in known.

11. Now knowing p and u_i, any other unknown quantities may be found that depend on the velocity or pressure, such as ϕ.

12. The solution converges as $p^* \to p$ meaning $p^{'} \to 0$.

The procedure outlined above was originally employed for steady flows where each iteration corresponded to a time step. It can, however, be employed in some form at *each time step* for unsteady flows where accurate flow history matters. Note that several variations of the original SIMPLE algorithm exist, including "SIMPLE Revised" (SIMPLER) [53] and "SIMPLE-Consistent" (SIMPLEC) [99]. These alternatives

were created because step 7(c) above is quite drastic. Neglecting the unknown velocity corrections is hardly justified. An alternative approach involves performing *two* velocity corrector steps, one which neglects the unknown term and the second which approximates the unknown based on the previous velocity sub-step's information. This is the PISO algorithm.

The PISO algorithm begins with a predictor step in which, just as in SIMPLE, the discretized momentum equations are solved with a "guessed" pressure p^* yielding the intermediate velocities u_i^*. The algorithm then takes two corrector steps. The first step uses SIMPLE's corrector step to yield a second intermediate velocity, u_i^{**}, which, unlike the first intermediate velocity u_i^*, satisfies the discrete continuity equation [102]. In the simple algorithm, this step was denoted as $u_i = u_i^* + u_i^{'}$ (and also employed to find the pressure). Now, write this as $u_i^{**} = u_i^* + u_i^{'}$. This definition is then substituted into the continuity equation to yield the pressure correction equation. This is then solved for the pressure correction $p^{'}$. Finally, $p^{'}$ is employed to solve for u_i^{**}. In the SIMPLE approach, u_i^{**} would be considered the final velocity, and a new iteration would begin. In PISO, however, a second corrector step follows. The discretized momentum equation for the *twice-corrected* velocity u_i^{***} is formed using *twice-corrected* pressure p^{***} and the previous corrected velocity u_i^{**}. Herein lies the crux of the PISO algorithm: the second corrector step drastically improves the guessed velocity and pressure by employing the previously-corrected velocity value in the twice-corrected momentum equation rather than simply neglecting it.

The twice-corrected momentum equation involves the second pressure correction field $p^{''}$. The twice corrected pressure p^{***} can be found via $p^{***} = p^{**} + p^{''}$. Use of the twice-corrected velocity u_i^{***} in terms of u_i^{**} and $p^{''}$ (in the discretized continuity equation) yields an expression for $p^{''}$, which can then be solved to obtain $p^{''}$. Finally, the twice-corrected pressure can be solved via $p^{***} = p^{**} + p^{''} = p^* + p^{'} + p^{''}$ [102]. Now, everything needed is known to solve for the twice-corrected velocity u_i^{***} via its

momentum equation. u_i^{***} and p^{***} are considered the "correct" velocity and pressure at this iteration. The algorithm is outlined below, adapted from [102]:

1. Guess p^*, u_i^* and some ϕ^* if necessary.
2. Repeat the first three steps of the SIMPLE algorithm
   (a) Solve the momentum equation $\rightarrow u_i^{'}$
   (b) Solve the pressure correction equation $\rightarrow p^{'}$
   (c) Correct the pressure and velocity $\rightarrow u_i^{**}, p^{**}$
3. Solve the second pressure correction equation $\rightarrow p^{''}$
4. Correct the pressure and velocity
   (a) $p^{***} = p^* + p^{'} + p^{''}$
   (b) $u_i^{***} = f(u_i^*, p^{'}, u_i^{**}, p^{''})$, all of which are known.
5. The corrected pressure and velocity are the final answers, $p = p^{***}, u_i = u_i^{***}$.
6. Solve for any remaining quantities such as ϕ using new p, u_i. Repeat until convergence is satisfied *for* ϕ, if necessary. **No further iterations are considered necessary for** p **or** u_i [102, 25].

The methods outlined above were originally developed for steady, "boundary-layer" (*i.e.* parabolic) flows but may be altered to work in unsteady flows. The method outlined by Patankar and Spalding [54] purposefully uncoupled the lateral and longitudinal pressures but later forms of the algorithm do not do this. The discretized momentum and continuity equations mentioned above for the SIMPLE and PISO algorithms will of course include a transient term in addition to the spatial derivatives. In the case of the SIMPLE algorithm, the iterative method above is applied at every time step until convergence is reached. In contrast, PISO is a considered a non-iterative approach as the solutions for $p^{***} = p$ and $u_i = u_i^{***}$ are considered the final solutions for the pressure and velocity. For transient PISO, the non-iterative algorithm is applied at every time step in an unsteady flow until steady state (not to be confused with convergence) has been reached. Issa [25] pioneered this approach, showing the temporal accuracy for pressure is on the order of Δt^3 and momentum $O(\Delta t^4)$ [25, 102]. This is why the answers for pressure and velocity obtained by the

PISO algorithm at every time step (assuming a suitably small time step) are considered to be "accurate enough" to progress to the next time step. The PISO method has been employed extensively in OpenFOAM [27, 81] as it is less expensive than the implicit SIMPLE algorithm (or its variants) and has been tested extensively.

As is discussed by Jasak [27], Rusche [81] and others, alternatives exist to predictor-corrector methods such as PISO. Simultaneous algorithms exist (see, for example, Caretto *et al.* [7] and Vanka [101]) but are only feasible for simulations with small meshes and a limited number of unknown quantities. As such, PISO, SIMPLE and related methods are widely employed for handling coupled pressure-velocity systems. The Oriented-Eddy Collision turbulence model implementation in OpenFOAM makes use of the unsteady PISO algorithm as most flows of interest will be unsteady, turbulent flows.

APPENDIX F

A PRIMER ON TURBULENT TRANSITION

F.1 Introduction & Background

Fluids moving below a certain critical velocity are often steady and smooth. Their governing equations exhibit well-behaved, tractable solutions. Some unsteady fluid flows, such as Stokes' problems, are also well behaved and solvable. While rare, these laminar flows have been studied for over a century and are readily observable [106]. Most real-world flows are turbulent, however, and admit few closed solutions or simplistic descriptions. The phenomenon of a fluid passing from the laminar to turbulent regime - that is, turbulent transition - is complex. Transition is a function of many variables, including the velocity of the flow, the geometry of the surroundings, and fluid properties such as kinematic viscosity. Modern research efforts attempt to use stability analysis to understand the mathematics behind transition, characterize transition experimentally, and devise models to predict transition in a variety of flow circumstances. This section provides historical context and a brief overview of these three topics.

Prior to the 1930s, experimentalists lacked the tools necessary to observe rapid pressure and velocity fluctuations that are present in all turbulent flows [106]. As such, they aimed to predict the mean properties of a flow. They were successful up to the point where instabilities began to appear, after which they could not accurately predict the mean velocity profile, pressure drop, or other basic flow properties. Friction factors and boundary layer behavior were equally difficult to predict. When considering flow over a flat plate, for example, the Blasius solution for skin friction

drastically under predicts observed values during turbulent transition [106] - that is, in flows above a critical velocity. Furthermore, the Blasius solution fails to capture the velocity dependence of the skin friction in fully turbulent flows [106]. Abrupt changes can also be observed in the friction factor in a pipe (departing from the laminar prediction) as a result of turbulent transition.

The ability to understand and predict fluid behavior during and after transition is of paramount importance to the engineer. Early work by G.G. Stokes and others [17] showed that Poiseuille flow in a pipe was a solution to the Navier-Stokes equations up to some fluid velocity after which pressure drop versus flow rate predictions failed [17]. Rather than blaming the equations of his namesake, he argued an unsteady solution to the Navier-Stokes equations was needed [17]. Osborne Reynolds considered the odd phenomenon of the yet-unnamed turbulent transition in his 1883 paper on the subject [106, 69, 66]. Reynolds formulated a non-dimensional group proportional to the flow velocity, the pipe diameter, and the inverse of the fluid viscosity now called the Reynolds number. This parameter is used extensively in the analysis of transitional and turbulent flows [22]. He discovered that below a Reynolds number (based on pipe diameter) of $Re_D = 2300$, ink injected upstream of a contraction into a tube remained in a coherent stream centered in the pipe. Above this Reynolds number, Reynolds observed unsteady undulations in the ink. Further increasing the fluid velocity caused the ink to lose its coherent structure and diffuse throughout the pipe. This observation corresponded to the flow becoming fully turbulent [106]. Advances in measurement techniques after Reynolds' time enable high fidelity, instantaneous characterization of laminar, transitional, and fully turbulent flows. Such observations have revealed that within transitional flows, velocity measured at certain points exhibits sudden bursts separated by regions of stable flow [106]. This instability and 'burst' behavior is characteristic of turbulence itself - understanding the mechanisms of transitions aids in the characterization of the turbulence phenomenon.

In general, all fluid flows are laminar below a certain critical Reynolds number. This Reynolds number is geometrically dependent. As stated above, for pipe flow this Reynolds number is typically $2,100 \geq Re_C \geq 2,300$ [14]. For a flat plate, this number is typically higher, $Re_C \approx 60,000$, with the Reynolds number based on the distance from the leading edge [14], while for a sphere or cylinder this number is higher still, $Re_C \approx 200,000$ based on the object diameter [14]. Identifying turbulent transition is also geometry dependent. Pressure and skin friction measurements are common - transition in a pipe flow is associated with an increase in the drag and friction coefficient. The opposite is true for flow over a sphere or similar object - a transitional or fully turbulent flow shows a drop in these metrics [14]. As Deen [14] and others point out, these critical Reynolds numbers are approximate - it is impossible to exactly predict when transition will begin even in carefully controlled experiments, which is primarily due to both large- and small-scale flow perturbations 'tripping' turbulence. Care can be taken to reduce disturbances to the flow whereby an increase in the critical Reynolds number is affected for a given geometry by and order of magnitude or more [14]. Additionally, the exact transitional Reynolds number is difficult (or impossible) to determine due to the intermittent nature of transition. Transition does not occur all at once - instead, it is typical for several mechanisms to gradually force a laminar to turbulent switch. For example, while transition can be observed in a pipe at Reynolds numbers as low as $Re \approx 2,000$, typically such a flow is not fully turbulent until $Re \approx 3,000$ [14]. Different mechanisms dominate transition depending on the geometry, initial and boundary conditions, as well as secondary physics which may be relevant to a given flow.

F.2 Types of transition

Transition occurs as a result of the excitation of existing instabilities in a flow, summarized by Henningson and Alfredsson [22]. This phenomena is often referred to

as the "receptivity" problem, as it involves how receptive certain flow instabilities are to existing perturbations. As such, the flow environment is critical to understanding receptivity, and thus transition. The majority of the mathematical methods presented in §F.3 focus on linear stabilities; these suffice when the perturbations to flow are small. Large disturbances, however, lead to non-linear instabilities and, as such, more complex math. The growth of linear instabilities is thus modified and the instabilities become "saturated" [22]. This "saturated", non-linear condition makes the instabilities particularly susceptible to relatively small flow perturbations, which lead to so-called "secondary" instabilities, which eventually lead to turbulence. This three-stage process summarizes turbulent transition. Secondary instabilities are a function of their originating primary instabilities [22].

The concept of receptivity should not be understated. While most linear stability analysis is concerned with "internally perturbed" instability, in fact the majority of instability, and thus transition itself, is tripped by some external factor. A flow's sensitivity to these external perturbations is key to understanding the subsequent transition mechanism which evolves. As Henningson and Alfredsson point out, perturbations to the mean flow, roughness, sound and other vibration modes, and so forth, all affect the way in which an internal disturbance is entrained into a flow's boundary layer [22] . While some external disturbances are easy to quantify, one of the most common - free stream turbulence - is practically impossible to characterize in any form that could be employed for stability analysis. The so-called "PSE" method, discussed in §F.5, may be one solution to this problem [22].

In many situations, instabilities which lead to transition grow from a boundary layer. As such, it is instructive to examine a simple case of free-stream perturbation-induced instability in a boundary layer. Goldstein, as cited by Henningson and Alfredsson [22], derived an equation for disturbances in a laminar boundary layer subject to a"small amplitude free-stream disturbance" [22]:

$$\frac{\partial u_1^{'}}{\partial t} + \overline{u}_1 \frac{\partial u_1^{'}}{\partial x_1} + \overline{u}_2 \frac{\partial u_1^{'}}{\partial x_2} + u_1^{'} \frac{\partial \overline{u}_1}{\partial x_1} + u_2^{'} \frac{\partial \overline{u}_1}{\partial x_2} = -\frac{\partial p}{\partial x_1} + \frac{1}{R} \frac{\partial^2 u_1^{'}}{\partial x_2^2} \tag{F.1}$$

where $u_i^{'}$ and $\overline{u}_i$ are the disturbance and mean velocities, respectively, is physical space, p the pressure, and 1 and 2 the streamwise and wall-normal directions, respectively. Asymptotic solutions to Equation (F.1) can be formulated which interface with the Orr-Sommerfeld equations [22] , discussed in §F.3. While useful, Equation (F.1) is limited to two dimensions. In reality, all boundary layers exist in three dimensions and dimensionality effects may dominate. As Henningson and Alfredsson [22] discuss, there exists little work exploring fully three-dimensional effects. Below, transition due to exponential instabilities will be considered, where instabilities are contained within the flow in question (as opposed to external) and are modeled linearly. This will be followed by comments on bypass transition where the normal "slow" growth of instability is altogether avoided due to the presence of large amplitude perturbations to the flow.

F.2.1 Transition from Exponential Instabilities

For the most part, transition occurs due to primary instabilities becoming "saturated" and secondary instabilities forming within a given flow. The nature of these crucial secondary instabilities is in large part a function of the nature of the primary instability, the environment of the flow, and the nature of the perturbations present. When considering mathematical descriptions of instability, the underlying assumptions dictate the secondary behavior, which may be verified with carefully controlled experiments, discussed in §F.5. Observations of secondary instability in "Tollmien-Schlichting" (TS) waves [22] reveal a regular, three-dimensional peak and valley configuration is responsible for transition. The key lies in the velocity profiles which exhibit an inflection point. As will be discussed in §F.3, the presence of an inflection in the mean velocity profile is often an indication of instability, and in this

case high frequency instabilities are of primary interest [22]. In the case of TS-wave-like primary instability subjected to high-frequency perturbations, which are aligned in the streamwise direction, transition occurs rapidly and is referred to as "K-type" transition. "H-type" transition is similar to K-type except that it occurs more slowly. It is often associated with free (that is, not forced) transition found in nature [22]. The structure of H-type transition differs from K-type in that, which is composed of peak-and-valley features, they are not aligned with the mean flow but are instead staggered. The period of this staggered arrangement is interesting as it is actually lower than the frequency of the primary instability [22].

In the special case of vortical flows, secondary instabilities grow and subsequently dissociate. This breakdown leads to transition. These instabilities, which may be in the form of Görtler vortices, cross-flow vortices, and vortices in curved and rotating flows [22], tend to have both symmetric and anti-symmetric configurations. The nature of the instability configuration dictates the temporal evolution of the secondary instability. In the more complex cases of separated and shear flow transition scenarios, the concept of secondary instabilities still applies in most cases, and appears to be extremely sensitive to the nature of the "background" disturbance [22]. In some cases, the presence of fully three-dimensional disturbances dictates the growth of instability - if initially present, such disturbances may dominate the perturbation modes. If introduced after the primary instability has become established, however, they may play little to no role in transition, suggesting secondary instabilities are not important to transition in such cases [22]. It is interesting to note that some experiments observed instability waves which exhibited Kelvin-Helmholtz-like vortex roll up, resulting in so-called "ribs" and "rollers" [22].

F.2.2 Bypass Transition

Previously discussed transition mechanisms rely on a specific primary instability mode - Tollmein-Schlichting (TS) waves. These lead to secondary instabilities (for the most part), which lead to transition itself. There exists a class of transition scenarios where this instability path is avoided altogether, and transition occurs rapidly. In the context of §F.2.1, bypass transition is transition that emanates from linear instabilities other than those that are exponential in nature [22]. Following Henningson and Alfredsson [22], bypass transition will be considered in the context of four physical circumstances: streamwise vortices, or streaks; oblique waves; free-stream turbulence; and finally local perturbations and turbulent patches [22].

Instabilities resulting from streamwise vortices (streaks) are often studied in the context of plane Poiseuille flow with random perturbations (noise) present in the background [22]. Once a streak is established, a spanwise oscillation begins to form. Alternatively, oblique transition results from the generation of large amplitude streaks via oblique waves which exhibit the same secondary instability as the classic streamwise vortex case. In both cases, exponential growth of the secondary instability eventually trips transition [22]. Experiments studying oblique transition reveal large amplitude streaks are particularly sensitive to non-stationary perturbations [22]. In addition, such transition can occur at relatively low perturbation amplitudes when compared to similar TS instability scenarios [22]. Berlin, Lundbladh, and Henningson (as cited by Henningson and Alfredsson [22]) observed that oblique transition appears to be universal in nature; that is, all such transition in this regime is produced by transient growth of streaks and subsequent "lift up" and breakdown of said streaks due to secondary instability mechanisms [22].

Free stream turbulence plays an important role in many bypass transition scenarios. Numerous real-world flows transition due to free stream turbulence, including flow within turbo-machinery, in external aerodynamic flows, and flows within wind

tunnels [22]. This last case is of particular importance as often wind tunnel experiments require precise control over turbulence, which cannot be obtained without a basic understanding of transition. Characterizing the relationship between free stream turbulence and transition is very difficult. At "high" free stream turbulence levels, a Reynolds number based on "momentum loss thickness" [22] can be formulated and used to predict the minimum transition Reynolds number. This is not the case for lower levels of free stream turbulence, where there exists little experimental agreement and thus little theory [22]. Matsubara (as cited by Henningson and Alfredsson [22]) showed that initially, instability due to free stream turbulence takes the form of classic streamwise streaks inside the boundary layer with spanwise periodicity. They are unusual in their behavior and shape - they tend to grow downstream and be quite large. The presence of these streaks eventually lead to low-level perturbations within the mean flow and lead to a collapse to turbulence. Regions of strong streak activity tend to break down into turbulent patches or "spots" which grow in both size and number downstream and lead to a fully turbulent transition [22]. Despite these useful qualitative observations about the nature of free stream turbulent transition, there exists no clear mathematical relationship between the level of turbulence in the free stream and the nature of the resulting transition.

The last transition scenario considered is that of local perturbations and turbulent patches or "spots". These are directly related to the "lift up" behavior exhibited by streamwise streaks, and their behavior is often what leads to a fully turbulent boundary layer transition. Gustavsson (as cited by Henningson and Alfredsson [22]) was one of the first to characterize the nature of such instabilities, and separated them into a dispersive and convective portion, one which tended to spread perturbation waves and the other which tended to advect such waves [22]. Other observations of patches revealed strong linear growth across a range of disturbance scales in perturbations, which were aligned spanwise to the mean flow [22]. Additionally, the formation of

these turbulent spots can be described as a three phase process: initially, rapid redistribution occurs which tends to damp small scale perturbations. Second, streaks and other streamwise vortices develop according to linear theory. Third, these streaks break apart at local "peaks" and collapse into turbulence. While this and other descriptions of free stream and local patch turbulence transition modes are useful, much research is still required to gain a better understanding and characterization of this complex and ubiquitous process.

F.3 Mathematical concepts

The mathematical analysis of transition can be traced to Rayleigh and his contemporaries [22] who were concerned with characterizing instability in parallel flows [22]. While doing so, they devised a method of analyzing exponentially growing and decaying linear wave disturbances and discovered that in two-dimensional parallel inviscid flow, a mean velocity profile inflection point was necessary for a disturbance to grow and trip transition [22]. These ideas were later applied to the Navier-Stokes equations by Sommerfeld and Orr [22] to investigate dominant disturbance wavelengths and frequencies. These co-called "normal modes" were employed by Heisenberg, Tollmien, G.I. Taylor and others to understand instability in a limited number of flows. Early stability analysis showed reasonable agreement with experiments when predicting the dominant unstable mode (in a given flow situation) as well as the lowest possible critical Reynolds number at which transition could begin [22]. By the late 1940s the Tollmien solution to the Orr-Sommerfeld wave equations was validated experimentally, and fluid dynamicists had a basic mathematical representation of transition. Unfortunately, the linear nature of the Orr-Sommerfeld analysis makes it unsuitable to determine a precise transition Reynolds number, even for a simplified flow scenario [22]. To overcome this limitation, work by Ingen, Smith, and Gamberoni correlated linear wave theory with experimentally-observed transition to further characterize

and predict transition [22]. They determined that disturbances often grew as e^9 in certain "low-disturbance" environments [22]. While this early work was useful, it relied on simplified mathematical analysis and empirical observation, and provided only a basic tool for predicting transition.

The governing equations for fluid flows - that is, the Navier-Stokes equations - are repeated so often in existing literature that to do so here would be pointless. Instead, familiarity with these equations is assumed, and instead focus is placed on a few simple ideas regarding stability analysis. Begin with Reynolds decomposition applied to Navier-Stokes. The total velocities and pressures can be decomposed into mean and fluctuating components, or "laminar" and "disturbance" contributions to the flow [22]:

$$\tilde{u}_i = \overline{u}_i + u_i^{'} \ , \ \tilde{p} = \overline{p} + p^{'} \tag{F.2}$$

Then use this to obtain the "disturbance equation", that is the equation for the fluctuating velocity $u_i^{'}$, *viz.* [22]

$$\frac{\partial u_i^{'}}{\partial t} + \overline{u}_j \frac{\partial u_i^{'}}{\partial x_j} + u_j^{'} \frac{\partial \overline{u}_i}{\partial x_j} + \frac{1}{\rho} \frac{\partial p^{'}}{\partial x_i} - \nu \nabla^2 u_i^{'} = -u_j^{'} \frac{\partial u_i^{'}}{\partial x_j} \tag{F.3}$$

with ρ the fluid density and ν the kinematic viscosity. The corresponding continuity equation is [22]

$$\frac{\partial u_i^{'}}{\partial x_i} = 0 \tag{F.4}$$

Considering the energy is of critical importance to stability and transition analysis, the equation for "disturbance energy" can be derived by multiplying Equation (F.3) by the disturbance velocity $u_i^{'}$ and employing the continuity equation [22]:

$$\begin{aligned} \frac{1}{2}\left(\frac{\partial u_i^{'} u_i^{'}}{\partial t} + \overline{u}_j \frac{\partial u_i^{'} u_i^{'}}{\partial x_j}\right) &= -u_i^{'} u_j^{'} S_{ij} - 2\nu s_{ij}^{'} s_{ij}^{'} \\ - \frac{\partial}{\partial x_j}\left(\frac{1}{2} u_i^{'} u_i^{'} u_j^{'} - \frac{1}{\rho} u_j^{'} p - 2\nu u_i^{'} s_{ij}^{'}\right) & \end{aligned} \tag{F.5}$$

where the rate of strain tensors are defined as

$$S_{ij} \equiv \frac{1}{2}\left(\frac{\partial \overline{u}_i}{\partial x_j} + \frac{\partial \overline{u}_j}{\partial x_i}\right) \tag{F.6}$$

and

$$s'_{ij} \equiv \frac{1}{2}\left(\frac{\partial u'_i}{\partial x_j} + \frac{\partial u'_j}{\partial x_i}\right) \tag{F.7}$$

As is described by Hallbäck, *et al.* [22], the Reynolds-Orr equations for the total disturbance energy per unit volume $E_V = \int\limits_V \frac{1}{2} u'_i u'_i dV$ can be obtained from Equation (F.5) above by employing the divergence theorem, assuming no-slip boundary conditions and making some assumptions about the nature of the disturbances:

$$\frac{dE_V}{dt} = -\int\limits_V \tfrac{1}{2} u'_i u'_j S_{ij} dV - 2\nu \int_V s'_{ij} s'_{ij} dV \tag{F.8}$$

noting the integration is performed over the entire flow volume. Equation (F.8) above is important in the prediction and modeling of transition. It is currently impossible to completely characterize turbulent transition. As Henningson and Alfredsson point out [22], the equations of motion, an accurate description of the mean flow field, a complete description of the relevant geometry, and knowledge of all relevant disturbances (both within the flow and external) must be known. This, of course, is not possible. Even if it were, the interaction between disturbances and the flow field (specifically, the boundary layer, which is the focus of Henningson and Alfredsson's work) is unknown. As such, general descriptions of the flow, such as the ratio of the current to initial disturbance energy at time progresses, $\lim\limits_{t\to\infty} E_V(t)/E_V(0)$ are employed. In fact the disturbance energy can be used to categorize the stability of a general flow. If there exists some flow where $\lim\limits_{t\to\infty} E_V(t)/E_V(0) \to 0$, this flow is *stable* and will not transition. If, for some small perturbation, the flow remains stable when the initial perturbation energy is below some limit $E_V(0) < \delta$, then this flow is

conditionally stable. If the perturbation may grow to infinity without transition then the flow is *globally stable*. Finally, if the time derivative of the disturbance energy is always less than zero $dE_V(t)/dt < 0$ for all $t > 0$, the flow is *monotonically stable* [22]. Most often, the Reynolds number of the flow is associated with the stability. Much effort has been spent on determining the Reynolds numbers at which a given flow is monotonically stable, globally stable, and above which the flow is linearly unstable [22]. Unfortunately, this approach only provides a gross or ideal picture of transition, and only applies to disturbances which grow in time. While such cases are relevant for simple flow geometries, in the real world transition is often tripped by a physical feature, that is disturbances enter into the flow at a fixed location in space and further characterization is required [22].. In this case, the spatial growth, perhaps along with the temporal growth, is required. Describing the size and nature spatially is not well defined, especially if one employs kinetic (disturbance) energy. Often, simplistic measures such as the maximum streamwise velocity are employed [22].

The Reynolds-Orr equation is derived by neglecting non-linear terms [22]. As such, equation (F.8) represents the mean flow energy exchange and viscous dissipation. There is no linear energy growth term present. In order to represent this simplified case, such a term must be constructed. Henningson and Alfredsson outline the basic steps [22] based on the governing equations for infinitesimal perturbations to a mean flow. Ignoring their characterization of the equations in wave number space, they conclude that, for the normal velocity component $u_2^{'}$ and normal vorticity $\omega_2^{'} = \partial u_1^{'}/\partial x_3 - \partial u_3^{'}/\partial x_1$ in parallel flows, noting again 2 is the direction of variation and 1 the streamwise direction:

$$\left[\left(\frac{\partial}{\partial t} + \overline{u}_1 \frac{\partial}{\partial x_1}\right)\nabla^2 - \frac{\partial^2 \overline{u}_1}{\partial x_1^2}\frac{\partial}{\partial x_1} - \frac{1}{R}\nabla^4\right] u_2^{'} = 0 \tag{F.9}$$

and

$$\left[\frac{\partial}{\partial t} + U_1 \frac{\partial}{\partial x_1} - \frac{1}{R}\nabla^2\right]\omega_2 = 0 \tag{F.10}$$

Assuming the normal velocity $u_2^{'}$, the normal velocity derivative $\partial u_2^{'}/\partial x_2$, and the normal vorticity $\omega_2^{'}$ have zero (no-slip) boundary conditions and are bounded in the far field, and assuming prescribed initial conditions, the behavior of a linear perturbation to the flow is fully characterized. Henningson and Alfredsson describe interpretations of the forcing terms resulting from casting the vorticity equation (F.10) in wave number space and the use of inviscid linear stability theory to provide a kinematic description of this so-called "vortex tilting" [22]. Their analysis provides some clues as to solution methods for linear stability problems, and relies heavily on the Rayleigh equation. An important conclusion can be drawn from this effort: the mean velocity profile *must* include an inflection point (that is, $\partial^2\overline{u}_1/\partial x_2^2 = 0$) in the domain at hand in order to achieve exponential inviscid instability growth. Dispersive effects, so-called "wave packets", two-dimensional effects such as the "lift up effect", and algebraic instabilities are all considered within the realm of inviscid instabilities [22].

To consider viscous instabilities, Henningson and Alfredsson employ simple parallel flows keeping true to the work of Rayleigh and others. The Orr-Sommerfeld and Squire equations are used in wave number space once again along with complex arguments as to the eigenmodes of the given stability problem. While this provides an interesting delve into the vagaries of Fourier-space stability analysis, there is no clear advantage to this work except perhaps to highlight the deficiencies in the assumptions of the Orr-Sommerfeld equation. Of more interest to the engineer is the consideration of numerical solutions to stability problems, specifically of the Orr-Sommerfeld equation. For a simple case such as plane Poiseuille flow, only symmetric solutions become unstable, and only one unstable mode exists [22]. For three-dimensional cases, Squire's theorem may be employed to reduce the fully three-dimensional Orr-Sommerfeld equation to two dimensions. In fact, work by Squire concluded that stability in parallel flows is inherently two-dimensional [22]. When considering two-

dimensional boundary layer stability, the basic Orr-Sommerfeld equations, which describe temporal but not spatial instability growth, cannot be used directly. Normal mode analysis may be employed, but additional complications arise from the streamwise-direction dependence of the flow (*i.e.* the growth of the boundary layer). Modifying the Orr-Sommerfeld equation to account for streamwise dependence largely failed until the inception of the "PSE" method [22], which has enjoyed moderate success in predicting instability in more complex flows [22].

Three-dimensional flows, such as boundary layers over swept wings, rotating discs, cones, and spheres are also considered by Henningson and Alfredsson [22]. Velocity profiles for such flows may be approximated using similarity solutions such as the Falkner-Skan-Cooke solutions, the stability of which is considered by Henningson and Alfredsson. In essence, specialized solutions to the Orr-Sommerfeld equation can be successfully employed in certain regimes, such as the aforementioned swept wing [22]. Body forces are also important to the physics of instability, such as those present in curved or rotating channel or boundary layer flows. Streamline curvature with centrifugal forces and system rotation with Coriolis forces are of interest. For such flows, stability analysis relies on information from experiments, which indicates spatially growing streamwise vortices are the primary form of instability [22], whereas in rotating channel flow stratification occurs in the Coriolis force [22] leading to the primary instability mode. In the complex case of curved boundary layer flow that may also be rotating, Görtler vortices play a dominant role and necessitate non-local stability analysis [22]. The PSE method, outlined in section F.5, is required.

F.4 Experimental work

Capturing turbulent transition experimentally is difficult. Notwithstanding the trouble associated with collecting temporally and spatially accurate flow field information, the nature of transition and its extreme sensitively to flow conditions and

environmental perturbations makes controlling such experiments a monumental task. Much of the discussion in §F.2 hinted at experiments from which qualitative (and occasionally quantitative) assessments were made. Section F.5, which briefly outlines transition models, discusses the need for excellent empirical data. This section is brief, as nearly every experiment designed to characterize turbulence - whether for validation or design purposes - differs. Traditionally, data was collected with hot-wire apparatus. More recently, the use of laser-Doppler velocitometry, particle image velocitometry, and other similar optical methods has allowed experimentalists to resolve two-dimensional flow field data and in some cases three-dimensional data as well. Access to such rich data is only now being utilized in the transition modeling community.

The most basic experiments to study turbulence, such as those performed by Rayleigh, are mostly parallel flows such as plane Poiseuille flow. Here, simply increasing the Reynolds number will lead to reasonably well-ordered natural transition. Linear stability analysis captures this scenario well, and is an excellent first step. In a similar vein, Blasius boundary layer flow can be investigated to validate basic tenets of the Orr-Sommerfeld equations, as well as the work done by Squires [22]. Two dimensional boundary layers and flows with a constant pressure gradient have also been employed to test these basic linear theories. Separated flows, and three-dimensional boundary layers, are difficult to capture numerical or experimentally, but have nevertheless been employed to validate simple linear approaches [22]. Flow over a swept wing is a common case to consider, as are flows over rotating disks, cones, spheres, and cones at some angle of attack. Curved channel flow, as well as rotating channel flow, have been employed by many to investigate the relative stabilizing and destabilizing effects curvature tends to have on transition and the underlying primary and secondary stability modes.

Experimentally testing specific transition scenarios can be difficult. For example, analyzing the receptivity of a boundary layer to a two- or three-dimensional disturbance requires a precise description of all relevant, dominate perturbation modes. Only recently could the secondary instability in vortical flows be captured by numerical methods thus verifying both the flow and the model's ability to predict it [22]. Bubble flows have been employed often to understand transition in both separated and free shear turbulent flows. For bypass transition scenarios, clever apparatus have been devised to subject plane Poiseuille flow to oblique waves by means of "ribbons" which affect the mean flow [22]. Free stream turbulence is easier to achieve, but often such cases are riddled with uncharacterized, unknown external disturbances, which can have a drastic effect on the turbulence trip location and time. The recent availability of direct numerical simulation, especially of turbulence near a wall, has helped to characterize the vortices and streaks present there, and has aided in the understanding of so-called "lift up" scenarios which can lead to transition.

F.5 Models for transition

A complete survey of available transition models is impossible in this context considering the breadth of options, each which their own niche. In addition, the relationship between transition and turbulence models is complex, and a survey of turbulence models is impossible in this setting. Furthermore, the descriptions of turbulence transition scenarios provided in §F.2 would lead the astute reader to conclude that simple, accurate transition models are impossible to formulate, which is generally the case [22]. There is no universal turbulent transition model outside of numerical procedures such as direct numerical and large eddy simulation. While appropriate for simple flow geometries and lower Reynolds numbers, the computational cost associated with DNS and LES is prohibitive in many cases. Thus, models are required. As Henningson and Alfredsson [22] point out, all current modeling approaches (excluding

turbulence models that have been "enhanced" to capture transition, discussed later) require empirical input. Generally, models come in two categories. First, simplistic models employ information about boundary layer shapes and Reynolds numbers. At best, these predict transition location and perhaps a critical Reynolds number. The second category of models are often complex and rely heavily on experimental data. While they may provide better flow field predictions, they are limited in applicability and not useful for understanding transition mechanisms [22].

This section focuses on single point transitions models, with the noted exception of the PSE method, reserved for the end. As is summarized by Savill [22], most methods employ so-called "single point" transition models, where laminar flow is simply "switched off" and a turbulence model "switched on." It is understood that this is a drastic simplification, and assumed turbulence is tripped at one instant and at one physical location. Another approach uses experimental data to guess a location and time for transition to begin, and subsequently modifies the eddy viscosity empirically to roughly predict the onset of fully developed turbulence [22]. These simplistic methods are most often used in conjunction with equally simplistic algebraic turbulence models, and, similar to industry's use of basic turbulence models, represent the most widely used transition model type for design to date [22].

Two equation models, such as the Jones and Launder's popular $K - \epsilon$ as well as Wilcox's $K - \omega$ model (and their many variants), have been shown to predict turbulent transition quite well on their own [22]. Whenever employing traditionally high Reynolds number turbulence models to predict an inherently low Reynolds number transition case, it is necessary to either add terms to the model to account for low Reynolds number behavior or assume transition can be captured by essentially adding some scaled combination of a laminar and turbulent solution [22]. As is detailed by Savill [22], the first method assumes that transition is governed by the diffusion of free stream turbulence into the boundary layer or laminar region. This would essen-

tially model all transition as bypass transition, that is, transition which circumvents the natural stages of instability development and directly breaks down streaks and secondary instabilities into turbulence. While applicable in some scenarios, this is clearly not a universal case. Despite this limitation, single point methods are the most widely used in industry [22]. The second basic method is not inherently limited in its range of applicability, but requires experimental data and therefore loses some generality and is subject to the underlying empirical data upon which it may be based. Neither modeling scenario is capable of capturing the process of events that leads to transition. In addition, receptivity, growth, secondary effects, and patchiness are lost. Intermittency models attempt to make up for this deficiency specifically [22], and have enjoyed moderate success.

Another alternative are so-called "low Reynolds number" turbulence models, which were designed to model slow moving, near-wall flows. These models lack specific prescriptions for transition [22], and are not considered further. Yet other models attempt to linearly combine simpler models to account for intermittency, but experiments reveal these flow regimes to be much more than a simple addition of laminar and turbulent flows [22]. All of the models presented thus far suffer from several common problems. First, they assume that transition is governed by the diffusion of free stream turbulence in to a laminar boundary layer. Second, they cannot account for any non-local effects, and third, they cannot account for inviscid damping [22]. The use of second moment closures has advantages, especially when attempting to capture bypass transition. Reynolds stress transport approaches can capture free stream turbulence anisotropy, properly capture the effects of supplied strain, and predict the production of shear [22]. This being said, such models are still (mostly) single point closures, and cannot capture non-local information [22].

As discussed previously, the linear exponential model "e^N" models instability waves linearly. Despite its simplistic take on transition, it is quite successful in pre-

dicting transition for simple flows. It is a local method and therefore cannot account for strong directional dependence, which is often seen in free stream turbulence transition scenarios. It also fails to capture the non-linear wave behavior, which tends to occur just prior to a trip into turbulence. In addition, the reaction of a boundary layer to external perturbations (receptivity) cannot be accounted for. Some attempts to consider free stream turbulence have been made with varying success [22]. A non-local alternative to the e^N method is the PSE (parabolized stability equation) method of transition modeling [22]. This method predicts linear transition scenarios but outperforms the classic e^N method. In addition, it is capable of accurately capturing some non-parallel flow scenarios, where e^N cannot. As is often the case, the PSE method requires *a priori* knowledge of a transitional flow, often gathered from experimental data. As Bertolotti summarizes [22], this method contains a collection of nonlinear parabolic partial differential equations that smoothly transition a given flow into turbulence. Small disturbances are amplified similar to classical stability approaches. These methods are limited, however, to slowly changing disturbance and geometry regimes, and generally cannot predict temporal evolution of instability.

The PSE method requires a flow which is independent of the spanwise direction [22], similar to the Orr-Sommerfeld equations. In addition, the PSE contains all of the terms in the Navier-Stokes equations which vary slowly in the downstream direction and can be solved and integrated directly in the streamwise direction [22]. Steady disturbances can be captured directly, which includes distortions in the mean flow. Disturbance history is present, and can capture some receptivity behavior [22]. The methods is limited by the number of disturbance modes it can handle, more by numerical cost considerations than mathematical. Notably, PSE methods cannot capture bypass transition as they rely on the "natural" slow growth methods in classic instability analysis. In addition, flows which change rapidly in the streamwise direction, such as stagnation [22]. Non-linear versions of the PSE method are a recent addition

to the modeling tool chest [22]. These methods can capture both the linear and then non-linear growth present before collapse to turbulence occurs. This ability decouples the modeling approach from empirical tuning, but still requires detailed information about initial perturbation levels and a guess as the receptivity of the boundary layer to external influences [22].

A summary of the "state of the art" of turbulence modeling is provided by Savill [22]. Unsurprisingly, models used in industry cannot predict transition to any degree of accuracy. Low Reynolds number models must account the effects of solid boundaries on shear and dissipation in order to predict transition to any degree of accuracy. These models should provide damping that is not completely based upon wall distance, and should include streamwise position-based damping corrections as well. Low Reynolds number stress transport models are appealing as they capture more physics than their simpler zero-, one-, and two-equation counterparts. Initial and free-stream condition sensitivity plagues all modeling approaches, as does the necessity to employ large and expensive computational meshes to capture transition in complex flow geometries. Research directions should include hybrid modeling approaches and the use of PSE and intermittency transport approaches [22].

F.6 Summary

Transition is a complex, ubiquitous phenomenon that has enjoyed over 100 years of intense research. The limitations of current experimental methods make capturing empirical data difficult. The tightly coupled behavior of instability growth with external perturbations and eventually fully-turbulent flow makes a complete mathematical description impossible, at least currently. Advances in computational resources within the last 30 years has enabled numerical tools such as DNS and LES to step in and take the place of experiments in certain simple, low Reynolds number flows, but the need for comprehensive, accurate experimental data is still paramount. Interestingly,

LES has added support to the popular theory that instabilities do exist in wave-like configurations and streamwise free stream turbulent vortices and turbulent patches do form just prior to transition [22].

Modeling approaches vary widely when considering turbulent transition. They suffer from the same "pigeon hole" problem that many modern turbulence model exhibit - working well in a limited regime, and often horribly inaccurate outside of a small set of relatively simple flows. Modifications to Reynolds stress transport approaches, or the linear and non-linear PSE methods show the most promise, but still require much improvement. It is of questionable use, however, as LES is poised to become a dominate tool in the prediction of transition, despite its crippling reliance on inaccurate subgrid scale models and the need to capture the very physics that LES ignores or relegated to said simplistic SGS model. Overall, it is of no surprise that the topic of turbulent transition is covered little in graduate level fluid and turbulence texts considering the topic appears to still be in its infancy. As with some turbulence approaches, numerical solutions may be the ultimate tool for predicting and characterizing transition.

APPENDIX G

EDDY LOG LAYER ANALYSIS

Recall from §3.3.2 that the magnitude of the eddy viscosity ν_T was called into question, and an estimate for C_ν sought. An estimate for the coefficient scaling the second dissipation-like term in the q_i transport equation, C_p, can also be calculated. Similar log layer analysis for the dissipation can be found in multiple sources [66, 17]. A brief summary will be provided here. Begin with the transport equation for the eddy orientation vector q_i,

$$\begin{aligned}\frac{Dq_i}{Dt} = &-q_k\overline{u}_{k,i} + C_p(\frac{q_n q_m}{q^2}\overline{u}_{n,m})q_i - C_\Omega q_i - \frac{1}{3}\left(\alpha\nu\overline{q^2} + \frac{1}{\tau_R}\right)q_i \\ &- C_q\frac{1}{\tau_R}\left[3\frac{\overline{q_k q_i}}{\overline{q_j q_j}} - \delta_{ki}\right]q_k + \left[(\nu+\nu_t)q_{i,k}\right]_{,k} + C_g(\nu+\nu_t)\left(\frac{q_{n,k}q_{n,k}}{q^2}\right)q_i \quad \text{(G.1)}\end{aligned}$$

The evolution equation for the average eddy magnitude $\overline{q^2}$ is desired, as it is a direct corollary to dissipation and therefore useful in log layer analysis. Multiply through by $2q_k$,

$$\begin{aligned}\frac{Dq^2}{Dt} = &-(1-C_p)(2q_i q_k\overline{u}_{k,i}) - 2C_\Omega q_i q_k - \frac{2}{3}\left(\alpha\nu\overline{q^2} + \frac{1}{\tau_R}\right)q^2 \\ &- C_q\frac{2}{\tau_R}\left[3\frac{\overline{q_k q_i}}{\overline{q_j q_j}} - \delta_{ki}\right]q_k q_i + \left[(\nu+\nu_t){q^2}_{,k}\right]_{,k} \\ &- 2(\nu+\nu_t)q_{i,k}q_{i,k} + 2C_g(\nu+\nu_t)(q_{n,k}q_{n,k}) \quad \text{(G.2)}\end{aligned}$$

and then average over all eddies.

$$\frac{D\overline{q^2}}{Dt} = -(1-C_p)(2\overline{q_i q_k}\overline{u}_{k,i}) - 2C_\Omega \overline{q_k q_n} - \tfrac{2}{3}\left(\alpha\nu\overline{q^2} + \frac{1}{\tau_R}\right)\overline{q^2}$$
$$- C_q \frac{2}{\tau_R}\left[3\frac{\overline{q_i q_k q_i q_k}}{\overline{q^2}} - \overline{q^2}\right] + \left[(\nu+\nu_t)\overline{q^2}_{,k}\right]_{,k}$$
$$- 2(\nu+\nu_t)\overline{q_{i,k}q_{i,k}} + 2C_g(\nu+\nu_t)(\overline{q_{n,k}q_{n,k}}) \quad \text{(G.3)}$$

In the log layer $\overline{u}_{1,2} = \frac{u^*}{\kappa y}$, and $\overline{q^2} = \frac{A^2}{y^2}$. Recall the turbulent viscosity is defined as $\nu_T = C_\nu\left(\frac{\overline{K^2}}{\overline{Kq^2}}\right)^{\frac{1}{2}} = C_\nu\frac{(1.88u^*)y}{A}$ and the turbulent timescale $\frac{1}{\tau_R} = \left(\overline{Kq^2}\right)^{\frac{1}{2}} = \frac{1.88u^*A}{y}$. Note that $\overline{u}_{1,2} = \frac{u^*}{\kappa y} = 3.2\frac{1}{\tau}$ so $\frac{1}{\kappa} = 3.2*1.88A = 2.44$ and thus $A = 0.405$. Substituting in these values,

$$\frac{D\overline{q^2}}{Dt} = 0 = -(1-C_p)\left(2\overline{q_1q_2}\frac{u^*}{\kappa y}\right) - 2C_\Omega\frac{u^*}{\kappa y}\overline{q_3q_3} - \frac{2}{3}\left(\frac{0.762u^*}{y}\right)\overline{q^2}$$
$$- C_q 2\left(\frac{0.762u^*}{y}\right)\left[3\frac{\overline{q_iq_kq_iq_k}}{\overline{q^2}} - \overline{q^2}\right] + \left[(\nu+\nu_t)\overline{q^2}_{,k}\right]_{,k}$$
$$- 2C_\nu(4.64u^*y)\overline{q_{i,k}q_{i,k}} + 2C_\nu C_g(4.64u^*y)(\overline{q_{n,k}q_{n,k}}) \quad \text{(G.4)}$$

This reveals that that $\overline{q_1q_2} \propto \frac{1}{y^2}$ if the only production term in the $\overline{q^2}$ equation (the first term above) is large. Thus the other components of $\overline{q_iq_j}$ most likely behave in a similar manner, at least in the log layer. Using these assumptions,

$$0 = -(1-C_p)\left(\overline{q_1q_2}\frac{u^*}{\kappa y}\right) - C_\Omega\frac{u^*}{\kappa y}\overline{q_3q_3} - \frac{1}{3}\left(\frac{0.762u^*A^2}{y^3}\right)$$
$$- C_q\left(\frac{0.762u^*A^2}{y^3}\right)\left[3\frac{y^2\overline{q_iq_kq_iq_k}}{A^2\overline{q^2}} - z^*\right] + \left[C_\nu 2\left(4.64u^*\frac{A^2}{y^3}\right)\right]$$
$$+ C_\nu(C_g-1)(4.64u^*)\left(\frac{A^2}{y^3}\right) \quad \text{(G.5)}$$

Further simplifying,

$$
\begin{aligned}
0 = (1 - C_p)\frac{-\overline{q_1 q_2}}{\overline{q^2}}(0.4) - C_\Omega(0.4)\frac{\overline{q_3 q_3}}{\overline{q^2}} - 0.0417 \\
- C_q(0.125)\left[\frac{3\overline{q_i q_k q_i q_k}}{\overline{q^2 q^2}} - 1\right] - (0.0417)\left(\frac{3\overline{q_i q_k q_i q_k}}{\overline{q^2 q^2}}\right) \\
+ C_\nu\,(1.52) + C_\nu C_g(0.761)
\end{aligned}
\tag{G.6}
$$

Finally, this becomes

$$
0 = (1 - C_p)(0.1) - C_\Omega(0.13333) - 0.0417 + C_\nu(0.761)\,(C_g - 1) \tag{G.7}
$$

This suggests that the eddy viscosity ν_t should be smaller, with $C_\nu = \mathcal{O}(0.1)$. In addition, inspection of the corresponding log layer analysis for dissipation [66, 17] suggests $Cp \approx 0.4$. Note that several rotation models may be employed in the above analysis yielding similar results. For example, C_Ω could be represented by any of the rotation models defined previously with only minor changes to the values calculated.

APPENDIX H

NOTES ON "AVERAGE EDDY" DIFFUSION

Recall from §3.3.2 a diffusion scheme for the eddy orientation vectors q_i and local Reynolds stress tensors R_{ij} was sought as an alternative to the standard diffusion model $\nabla(\nu + \nu_T) \cdot \nabla\phi$. One such method proposed the construction of a so-called "average eddy ellipse", an ellipsoid which represents all of the eddy orientation vectors (and possibly all of the local Reynolds stress tensors) at a given location in physical space. This ellipsoid could be polled by neighboring cells in order to obtain the eddy vector magnitude in the direction of interest (*i.e.* the direction of the local q_i) even if the neighboring cell has no eddy pointing in the required direction. While this method was eventually abandoned for the classic diffusion model, the procedure to construct such an ellipsoid is still of interest. Given a discrete set of eddy orientation vectors, a "best fit" surface can be constructed around said vectors which roughly represents the eddy structure at any given cell. While theoretically possible, constructing such a surface representing the "average Reynolds stress tensor" surface is difficult as it exists in a higher dimension.

In general, an ellipsoid is given by the formula $\mathbf{x}^T A\mathbf{x} = 1$ where A is a symmetric, positive definite matrix. The goal is to solve for the "best-fit matrix" given data for $\mathbf{x}$. In this case, the data is in the form of the existing eddy orientation vectors q_i. This takes the form $x^i A_{xx} x^i + y^i A_{yy} y^i + z^i A_{zz} z^i + 2x^i A_{xy} y^i + 2x^i A_{xz} z^i + y^i A_{yz} z^i = 1$ for every data point i. Formulating the ideas above in matrix form,

$$\begin{bmatrix} x^1x^1 & y^1y^1 & z^1z^1 & x^1y^1 & x^1z^1 & y^1z^1 \\ x^2x^2 & y^2y^2 & z^2z^2 & x^2y^2 & x^2z^2 & y^2z^2 \\ \vdots & \vdots & \vdots & & & \vdots \end{bmatrix} \begin{pmatrix} A_{xx} \\ A_{yy} \\ A_{zz} \\ A_{xy} \\ A_{xz} \\ A_{yz} \end{pmatrix} = \begin{pmatrix} 1 \\ 1 \\ 1 \\ 1 \\ 1 \\ 1 \end{pmatrix} \tag{H.1}$$

where x^1, y^1, and z^1 are the three components of the "first" eddy orientation vector and the superscripts do not imply exponents. Note that dimensions of this matrix are $6 \times N$, where N is the number of eddy orientation vectors available for the best fit. Unfortunately, there are more equations than there are unknowns, and a least-squares fit must pre-multiply the transpose of the matrix in order to arrive at a square system which is solvable. Doing so results in,

$$\Im \begin{pmatrix} A_{xx} \\ A_{yy} \\ A_{zz} \\ A_{xy} \\ A_{xz} \\ A_{yz} \end{pmatrix} = \begin{pmatrix} \sum_i w^i x^i x^i \\ \sum_i w^i y^i y^i \\ \sum_i w^i z^i z^i \\ \sum_i w^i x^i y^i \\ \sum_i w^i x^i z^i \\ \sum_i w^i y^i z^i \end{pmatrix} \tag{H.2}$$

where

$$\Im = \begin{bmatrix} \sum_i w^i x^i x^i x^i x^i & \sum_i w^i x^i x^i y^i y^i & \sum_i w^i x^i x^i z^1 z^1 & \sum_i w^i x^i x^i x^1 y^1 & \sum_i w^i x^i x^i x^1 z^1 & \sum_i w^i x^i x^i y^1 z^1 \\ \sum_i w^i y^i y^i x^i x^i & \sum_i w^i y^i y^i y^i y^i & \sum_i w^i y^i y^i z^i z^i & \sum_i w^i y^i y^i x^i y^i & \sum_i w^i y^i y^i x^i z^i & \sum_i w^i y^i y^i y^i z^i \\ \vdots & \vdots & \vdots & & & \vdots \end{bmatrix} \tag{H.3}$$

This is essentially a 6×6 matrix problem which is symmetric and positive definite. Note that w^i are weighting factors which can be used to preferentially weight the ith orientation. This solution has the minimum error to the unsolvable problem above.

With the weights $w^i = 1$, the vector A becomes $N_{ij} = \overline{q_i q_j}/\overline{q^2}$. Note that $M_{ijnm}A_{nm} = N_{ij}$ where M_{ij} and N_{ij} are derived from summations. Let $\hat{N}_{(ij)} = q_i q_j$ be a vector of tensors and $N_{(ij)} = \sum \hat{N}_{(ij)}$ and $M_{(ij)(nm)} = \sum \hat{N}_{(ij)} \otimes \hat{N}_{(nm)}$. The goal is to solve $A_{nm} = [{M_{ijnm}}^{-1}]N_{ij}$. Given a vector q_i, another vector must be found which intersects the ellipse. That intersection will provide an estimate of the magnitude of the vector pointing in the direction of interest. This new vector, $q_n^* = \alpha q_n$ is the vector required to calculate diffusion for this method. The ellipse equation requires that q_n^* lies on the surface of the ellipse, thus $\alpha^2 q_n A_{nm} q_m = 1$ and therefore $\alpha = [q_n A_{nm} q_m]^{-1/2}$.

BIBLIOGRAPHY

[1] Akylas, E., and Kassinos, S.C. Advances in Particle Representation Modeling of Homogeneous Turbulence. From Linear PRM Version to the Interacting Viscoelastic IPRM. In *New Approaches in Modeling Multiphase Flows and Dispersion Turbulence, Fractal Methods, and Synthetic Turbulence* (2011), vol. 18, ERCOFTAC.

[2] Andeme, R. Development of an Oriented-eddy Collision Model for Turbulence. Master's thesis, The University of Massachusetts, Amherst, 2008.

[3] Anderson, J.R. *Computational Fluid Dynamics The Basics with Applications.* McGraw-Hill, New York, NY, 1995.

[4] Baldwin, B., and Lomax, H. Thin-layer approximation and algebraic model for separated turbulent flows. *American Institute of Aeronautics and Astronautics, Aerospace Sciences Meeting* (1978).

[5] Bhatnagar, P.L., Gross, E.P., and Krook, M. A Model for Collision Processes in Gases. I. Small Amplitude Processes in Charged and Neutral One-Component Systems. *Physical Review 94*, 3 (1954), 511–525.

[6] Boussinesq, J. Théorie de l'écoulement tourbillant. *Mem. Presentes par divers Savants Acad. Sci. Inst. Fr. 23* (1877), 46–50.

[7] Caretto, L., Curr, R.M., and Spalding, D.B. Two numerical methods for three-dimensional boundary layers. *Comp. Methods Appl. Mech. Eng. 1*, 1 (1972), 39–57.

[8] C.duP. Donaldson, and Rosenbaum, H. Calculation of the turbulent shear flows through closure of the Reynolds equations by invariant modeling. *Aeronautical Research Association Princeton, Princeton, NJ*, 127 (1968).

[9] Chang, W., Giraldo, F., and Perot, J.B. Analysis of an Exact Fractional Step Method. *Journal of Computational Physics 179* (2002), 1–17.

[10] Chartrand, C.C. Eddy Collision Models for Turbulence. Master's thesis, The University of Massachusetts, Amherst, 2005.

[11] Craft, T.J., Launder, B.E., and Suga, K. Development and application of a cubic eddy-viscosity model of turbulence. *International Journal of Heat and Fluid Flow 17* (1996), 108–115.

[12] de Bruyn Kops, S.M., and Riley, J.J. Direct numerical simulation of laboratory experiments in isotropic turbulence. *Physics of Fluids 10* (1998), 2125–2127.

[13] de Bruyn Kops, S.M., Riley, J.J., and Kos'aly, G. Direct numerical simulation of reacting scalar mixing layers. *Physics of Fluids 13* (2001), 1450–1465.

[14] Deen, W.M. *Analysis of Transport Phenomena*. Oxford University Press, New York, NY, USA, 1998.

[15] Deissler, R.G. Problem of steady state shear flow in turbulence. *Physics of Fluids 8*, 3 (1965), 391–398.

[16] Durbin, P.A. Separated Flow Computations with the $k - e - v^2$ Model. *AIAA J 33*, 4 (1995), 659–664.

[17] Durbin, P.A., and Reif, B.A.Pettersson. *Statistical Theory and Modeling for Turbulent Flows*. John Wiley and Sons, New York, NY, USA, 2001.

[18] E.R. van Driest. On Turbulent Flow Near a Wall. *Journal of the Aeronautical Sciences 23*, 11 (1956), 1007–1011.

[19] Ferziger, J.H., and Peric, M. *Computational Methods for Fluid Dynamics*. Springer, Berlin, 2002.

[20] Gadebusch, J. On the development of self-adapting (RANS/LES) turbulence models for fluid simulation at any mesh resolution. Master's thesis, The University of Massachusetts, Amherst, 2007.

[21] Girimaji, S.S., Jeong, E., and Poroseva, S.V. Pressure-strain correlation in homogeneous anisotropic turbulence subject to rapid strain-dominated distortion. *Physics of Fluids 15* (2003), 3209.

[22] Hallbäck, M., Henningson, D.S., Johansson, A.V., and Alfredsson, P.H. *Turbulence and Transition Modelling*. Kluwer Academic Publishers, London, 1996.

[23] Haworth, D.C., and Pope, S.B. A generalized Langevin model for turbulent flows. *Physics of Fluids 29*, 2 (1985), 387–405.

[24] Herrchen, M., and Öttinger, H.C. A detailed comparison of various FENE dumbbell models. *Journal of Non-Newtonian Fluid Mechanics 68*, 1 (1997), 17 – 42.

[25] Issa, R.I. Solution of the implicitly discretised fluid flow equations by operator-splitting. *Journal of Computational Physics 62*, 1 (1986), 40–65.

[26] Jacquin, L., Leuchter, O., Cambon, C., and Mathieu, J. Homogeneous turbulence in the presence of rotation. *Journal of Fluid Mechanics 220* (1990), 1–52.

[27] Jasak, H. *Error Analysis and Estimation for the Finite Volume Method with Applications to Fluid Flows.* PhD thesis, Imperial College of Science, Technology and Medicine, London, England, 1996.

[28] Jeong, E.H. *Selected problems in turbulence theory and modeling.* PhD thesis, Texas A&M University, College Station, TX, US, 2003.

[29] Jones, W.P., and Launder, B.E. The prediction of laminarization with a two-equation model of turbulence. *International Journal of Heat and Mass Transfer 15*, 2 (1972), 301–314.

[30] Kassinos, S.C., and Reynolds, W.C. One-point modeling of rapidly deformed homogeneous turbulence. *Proceedings of the Royal Society of London A 451* (1995), 87–104.

[31] Kim, John, Moin, Parviz, and Moser, Robert. Turbulence statistics in fully developed channel flow at low Reynolds number. *Journal of Fluid Mechanics 177* (1987), 133–166.

[32] Kolmogorov, A.N. Equations of turbulent motion of an incompressible fluid. *Izv. Akad. Nauk SSSR, Seria fizicheska VI*, 1-2 (1942), 56–58.

[33] Komminaho, J., and Skote, M. Reynolds Stress Budgets in Couette and Boundary Layer Flows. *Flow, Turbulence and Combustion 68* (2002), 167–192.

[34] Kutta, W. Beitrag zur naherungsweisen Integration von Differentialgleichungen. *Zeit. Math. Physik 46* (1901), 435–453.

[35] Launder, B.E., Reece, G.J., and Rodi, W. Progress in the development of a Reynolds-stress turbulence closure. *Journal of Fluid Mechanics 68*, 3 (1974), 537–566.

[36] Launder, B.E., and Shima, N. Second-moment closure for the near-wall sublayer: development and application. *AIAA J. 27* (1989), 1319–1325.

[37] Launder, B.E., and Spalding, D.B. *Mathematical Models of Turbulence.* London, 1972.

[38] Le, H., Moin, P., and Kim, J. Direct numerical simulation of turbulent flow over a backward-facing step. *Journal of Fluid Mechanics 330* (1997), 349–374.

[39] Le Penven, L., Gence, J.N., and Comte-Bellot, G. On the Approach to Isotropy of Homogeneous Turbulence: Effect of the Partition of Kinetic Energy Among the Velocity Components. In *Frontiers in Fluid Mechanics*, S.H. Davis and J.L. Lumley, Eds. Springer, New York, 1985, pp. 1–21.

[40] Lemons, D.S., and Gytheil, A. Paul Langevin's 1908 paper: On the Theory of Brownian Motion . *The American Journal of Physics 65*, 11 (1997), 1079–1081.

[41] Lumley, J.L. Computational Modeling of Turbulent Flows. *Advances in Applied Mechanics 18* (1978), 123–176.

[42] Lundgren, T.S. Distribution Functions in the Statistical Theory of Turbulence. *Physics of Fluids 10*, 5 (1967), 969–975.

[43] Mansour, N.N., Cambon, C., and Speziale, C.G. Theoretical and computational study of rotating isotropic turbulence. In *Studies in Turbulence*, T.B. Gatski, S. Sarkar, and C.G. Speziale, Eds. Springer-Verlag, 1992.

[44] Martell, M.B. Simulations of turbulence over superhydrophobic surfaces. Master's thesis, The University of Massachusetts, Amherst, 2009.

[45] Martell, M.B., Perot, J.B., and Rothstein, J.P. Direct numerical simulations of turbulent flows over superhydrophobic surfaces. *Journal of Fluid Mechanics 620* (2009), 31–41.

[46] Martell, M.B., Rothstein, J.P., and Perot, J.B. An analysis of superhydrophobic turbulent drag reduction mechanisms using direct numerical simulation. *Physics of Fluids 22* (2010), 065102:1–13.

[47] Matsumoto, A., Nagano, Y., and Tsuji, T. Direct numerical simulation of homogeneous turbulent shear flow. In *5th Symposium on Computational Fluid Dynamics* (1991), pp. 361–364.

[48] Mininni, P.D., and Teitelbaum, T. The decay of turbulence in rotating flows. *Physics of Fluids 23* (2011), 065105:1–15.

[49] Moser, R., Kim, J., and Mansour, N. Direct numerical simulation of turbulent channel flow up to Re_τ=590. *Physics of Fluids 11*, 4 (1998), 943–945.

[50] Naot, D., Shavit, A., and Wolfshtein, M. Interactions between components of the turbulent velocity correlation tensor due to pressure fluctuations. *Isr. J. Technol. 8* (1970), 259.

[51] Nilsson, M. Exploring fundamental turbulent physics using direct numerical simulation. Master's thesis, The University of Massachusetts, Amherst, 2009.

[52] Olroyd, J.G. On the Formulation of Rheological Equations of State. *Proceedings of the Royal Society of London. Series A, Mathematical and Physical Sciences 200*, 1063 (1950), 523–541.

[53] Patankar, S.V. *Numerical Heat Transfer and Fluid Flow.* Hemisphere Publising Corporation, New York, 1980.

[54] Patankar, S.V., and Spalding, D.B. A calculation procedure for heat, mass and momentum transfer in three-dimensional parabolic flows. *International Journal of Heat and Mass Transfer 15* (1972), 1787–1806.

[55] Perot, J.B. Determination of the decay exponent in mechanically stirred isotropic turbulence. *AIP Advances 1* (2011), 022104:1–18.

[56] Perot, J.B., and Chartrand, C. Modeling return to isotropy using kinetic equations. *Physics of Fluids 17* (2005), 035101–1:035101–18.

[57] Perot, J.B., and Chartrand, C. Modeling return to isotropy using kinetic equations. *Physics of Fluids 17* (2005), 035101–1 – 035101–18.

[58] Perot, J.B., and Gadebusch, J. A stress transport equation model for simulating turbulence at any mesh resolution. *Theoretical and Computational Fluid Dynamics 23* (2009), 271–286.

[59] Perot, J.B., and Moin, P. Shear-Free Turbulent Boundary Layers. Part I. Physical insights into near-wall turbulence. *Journal of Fluid Mechanics 295* (1995), 199.

[60] Perot, J.B., and Moin, P. Shear-Free Turbulent Boundary Layers, Part II: New Concepts for Reynolds Stress Transport Equation Modeling of Inhomogeneous Flows. *Journal of Fluid Mechanics 295* (1995).

[61] Perot, J.B., and Natu, S. A model for the dissipation rate tensor in inhomogeneous and anisotropic turbulence. *Physics of Fluids 16*, 11 (2004), 4053–4065.

[62] Perot, J.B., and S.M. de Bruyn Kops. Modeling turbulent dissipation at low and moderate Reynolds numbers. *Journal of Turbulence 7*, 69 (2006), 1–14.

[63] Pope, S.B. Consistent modeling of scalars in turbulent flows. *Physics of Fluids 26*, 2 (1982), 404–408.

[64] Pope, S.B. A Lagrangian two-time probability density function equation for inhomogeneous turbulent flows. *Physics of Fluids 26*, 12 (1983), 3448–3450.

[65] Pope, S.B. Lagrangian PDF methods for turbulent flows. *Annual Review of Fluids Mechanics 26* (1994), 23–63.

[66] Pope, S.B. *Turbulent Flows.* Cambridge University Press, New York, NY, USA, 2000.

[67] Prandtl, L. Bericht uber Untersuchungen zur ausgebildeten Turbulenz. Z. *angew. Math. Mech. 5* (1925), 136–139.

[68] Prandtl, L. Uber ein neues Formelsystem fur die ausgebildete Turbulenz. *Nachr. Akad. Wiss. Gottingen* (1945), 6–19.

[69] Reynolds, O. An experimental investigation of the circumstances which determine whether the motion of water shall be direct or sinuous, and of the law of resistance in parallel channels. *Philosophical Transactions of the Royal Society 174* (1883), 84–99.

[70] Reynolds, O. On the dynamical theory of incompressible viscous fluids and the determination of the criterion. *Philosophical Transactions of the Royal Society of London A 186* (1895), 123–164.

[71] Reynolds, W.C. Computation of Turbulent Flows. *Annual Review of Fluid Mechanics 8* (1976), 183–208.

[72] Reynolds, W.C. Effects of rotation on homogeneous turbulence. *Proceedings of the* 10th *Austrailian Fluid Mechanics Conference* (1989), KS1–KS2.6.

[73] Reynolds, W.C., and Kassinos, S.C. A particle representation model for the deformation of homogeneous turbulence. Tech. rep., Center for Turbulence Research, Stanford University, 1996.

[74] Reynolds, W.C., and Kassinos, S.C. A structure-based model with stropholysis effects. Tech. rep., Center for Turbulence Research Annual Research Briefs, Stanford University, 1998.

[75] Reynolds, W.C., and Lee, M.J. Numerical experiments on the structure of homogeneous turbulence. Tech. Rep. TF-24, Thermosciences, Department of Mechanical Engineering, Stanford University, 1985.

[76] Reynolds, W.C., Rogers, M.M., and Kassinos, S.C. One-point turbulence structure tensors. *Journal of Fluid Mechanics 428* (2001), 213–248.

[77] Richardson, L.F. *Weather Prediction by Numerical Process.* Cambridge University Press, Cambridge, UK, 1922.

[78] Rogers, M.M., and Moin, P. The structure of vorticity fields in homogeneous turbulent flows. *Journal of Fluid Mechanics 68* (1975), 537–566.

[79] Rotta, J. Statistische Theorie nichthomogener Turbulenz. *Zeitschrift für Physik A Hadrons and Nuclei 129* (1951), 547–572.

[80] Runge, C. Über die numerische Auflösung von Differential-gleichungen. *Math. Ann. 46* (1895), 167–178.

[81] Rusche, H. *Computational fluid dynamics of dispersed two-phase flows at high phase fractions.* PhD thesis, Imperial College of Science, Technology and Medicine, London, England, 2002.

[82] Saffman, P.G. The large-scale structure of homogeneous turbulence. *Journal of Fluid Mechanics 27*, 3 (1967), 581–593.

[83] Saffman, P.G. A Model for Inhomogeneous Turbulent Flow. *Proceedings of the Royal Society of London A 317* (1970), 417–433.

[84] Saffman, P.G. On the spectrum and decay of random two-dimensional vorticity distibutions at large Reynolds numbers. *Studies in Applied Mathematics 50* (1971), 377–383.

[85] Saffman, P.G., and Wilcox, D.C. Turbulence-Model Predictions for Turbulent Boundary Layers. *AIAA Journal 12*, 4 (1974), 541–546.

[86] Schumann, U. Realizability of Reynolds-stress turbulence models. *Physics of Fluids 20*, 5 (1977), 721–725.

[87] Smagorinsky, J. General circulation experiments with the primitive equations. *Monthly Weather Review 91*, 3 (1963), 99–164.

[88] Spalart, P.R. Strategies for turbulence modeling and simulations. *International Journal of Heat and Fluid Flow 21* (2000), 252–263.

[89] Spalart, P.R., and Allmaras, S.R. A one-equation turbulence model for aerodynamic flows. *La Recherche Aerospatiale 1*, 1 (1994), 5–21.

[90] Spalart, P.R., and Speziale, C.G. A note on constraints in turbulence modeling. *Journal of Fluid Mechanics 391* (1999), 373–376.

[91] Spalding, D.B. Kolmogorov's two-equation model of turbulence. *Proceedings of the Royal Society of London A 434* (1991), 211–216.

[92] Speziale, C.G. On nonlinear $k - l$ and $k - \epsilon$ models of turbulence. *Journal of Fluid Mechanics 178* (1987), 459–475.

[93] Speziale, C.G. Turbulence Modeling in Noninertial Frames of Reference. *Theoretical and Computational Fluid Dynamics 1* (1989), 3–19.

[94] Speziale, C.G. Analytical methods for the development of Reynolds-stress closures in turbulence. *Annual Review of Fluid Mechanics*, 23 (1991), 107–157.

[95] Speziale, C.G., Sarkar, S., and Gatski, T.B. Modeling the pressure strain correlation of turbulence: an invariant dynamical systems approach. *Journal of Fluid Mechanics*, 227 (1991), 245–272.

[96] Taylor, G.I. Diffusion by continuous movements. *Proceedings of the London Mathematics Society 20* (1921), 196–212.

[97] Taylor, G.I. Statistical theory of turbulence. *Proceedings of the Royal Society of London. Series A, Mathematical and Physical Sciences 151*, 873 (1935), 421–444.

[98] Tennekes, H., and Lumley, J.L. *A First Course in Turbulence*. Cambridge, Massachusetts, 1972.

[99] Van Doormaal, J.P., and Raithby, G.D. Enhancements of the simple method for predicting incompressible fluid flows. *Numerical Heat Transfer, Part A: Applications: An International Journal of Computation and Methodology 7*, 2 (1984), 147–163.

[100] Van Slooten, P.R., and Pope, S.B. PDF modeling for inhomogeneous turbulence with exact representation of rapid distortions. *Physics of Fluids 9*, 4 (1996), 1085–1105.

[101] Vanka, S.P. Block-implicit multigrid solution of navier-stokes equations in primitive variables. *J. Comp. Physics 65*, 1 (1986), 138–158.

[102] Versteeg, H.K., and Malalasekera, W. *An introduction to computational fluid dynamics: The finite volume method*. Longman Scientific and Technical, Essex, England, 1995.

[103] Wigeland, R.A., and Nagib, H.M. Effects of rotation on decay of turbulence. *Bull. Amer. Phys. Soc. 23* (1978), 998.

[104] Wilcox, D.C. Reassessment of the Scale Determining Equation for Advanced Turbulence Models. *AIAA Journal 26*, 11 (1988), 1299–1310.

[105] Wilcox, D.C. *Turbulence Modeling for CFD*. DCW Industries, La Canada, CA, USA, 1993.

[106] Wilcox, D.C. *Basic Fluid Mechanics*. DCW Industries, La Canada, CA, USA, 2000.

[107] Wilcox, D.C., and Alber, I.E. A Turbulence Model for High Speed Flows. *Proc. of the 1972 Heat Trans. & Fluid Mech.* (1972), 231–252.

[108] Winckelmans, G.S., Jeanmart, H., and Carati, D. On the modelling of the subgrid-scale and filtered-sale stress tensors in large-eddy simulation. *Journal of Fluid Mechanics 441* (2001), 119–138.

[109] Winckelmans, G.S., Jeanmart, H., and Carati, D. On the comparison of turbulence intensities from large-eddy simulation with those from experiment or direct numerical simulation. *Phys. Fluids 14* (2002), 1809–1811.